

Time-Dependent Deformations in Precast, Prestressed Bridge Girders

by

Brandon Ray Johnson

A thesis submitted to the Graduate Faculty of
Auburn University
in partial fulfillment of the
requirements for the Degree of
Master of Science

Auburn, Alabama
December 8, 2012

Keywords: camber, prestressed concrete, self-consolidating concrete, creep, shrinkage

Copyright 2012 by Brandon Ray Johnson

Approved by

Robert W. Barnes, Chair, James J. Mallett Associate Professor of Civil Engineering
Anton K. Schindler, Associate Professor of Civil Engineering
Justin D. Marshall, Assistant Professor of Civil Engineering

Abstract

Precast, prestressed girders are used across the state of Alabama for bridge construction. There has been a desire to allow self-consolidating concrete to be used to manufacture these bridge girders. The time-dependent deformation response of bridge girders that contain self-consolidating concrete is important information that must be gathered before the use of self-consolidating concrete in bridge girders can be widely used in the state of Alabama.

Twenty-eight bulb-tee girders were measured for internal strain and camber. Fourteen of the girders were composed of conventionally vibrated concrete while the remaining girders were composed of self-consolidating concrete. Predicted internal strains and cambers for these girders were found through the use of a time-step process. These predictions were formed based on creep and shrinkage methods allowed by the AASHTO LRFD 2010 Bridge Design Specification. These predictions were compared to the measured results in order to determine which prediction methods were the most accurate.

The comparison of time-dependent responses showed that girders constructed with self-consolidating concrete exhibit similar performance characteristics to those of girders constructed with conventionally vibrated concrete. The time-dependent deformation response can be accurately predicted if the concrete strength and stiffness is known at the time of prestress transfer. Predictions that use specified concrete strength and stiffness values that do not accurately represent actual strength and stiffness values will yield largely inaccurate predictions of time-dependent deformation.

Acknowledgements

I would like to thank Dr. Barnes for his great patience and wisdom in guiding me through this process. The engineering skills and life lessons that I have learned from him will serve me well in the future. I would also like to thank the Graduate Research Assistants who spent so many hours with me out in the field and in the lab: Wes Bullock, Emily Dunham, Morgan Ellis, Tom Hadzor, Sam Keske, Eric Miller, Will Minton, and Brian Rhett. This project would not have been possible without the support of the Auburn University Highway Research Center as well as the Alabama Department of Transportation. Finally, I would like to thank my friends and family. Their endless love and support continues to astound and humble me.

Table of Contents

Abstract.....	ii
Acknowledgements.....	iii
List of Tables	viii
List of Figures.....	ix
List of Abbreviations	xv
Chapter 1 Introduction	1
1.1 Background.....	1
1.2 Research Objectives.....	2
1.3 Research and Scope	3
1.4 Organization of Thesis.....	3
Chapter 2 Literature Review.....	5
2.1 Introduction.....	5
2.2 Principles of Time-Dependent Deformation.....	5
2.2.1 Incremental Strain.....	10
2.2.2 Incremental Curvature	11
2.3 Initial and Incremental Time-Step Calculations	12
2.3.1 Initial Prestress Losses and Time-Dependent Relaxation.....	12
2.3.2 Modulus of Elasticity of Concrete.....	14

2.3.3 Creep	15
2.3.3.1 ACI 209 Creep Prediction Method	16
2.3.3.2 AASHTO 2004 Creep Prediction Method	19
2.3.3.3 AASHTO 2010 Creep Prediction Method	21
2.3.3.4 MC 90 Creep Prediction Method	23
2.3.3.5 MC 90 – KAV Creep Prediction Method	27
2.3.4 Shrinkage	28
2.3.4.1 ACI 209 Shrinkage Prediction Method	28
2.3.4.2 AASHTO 2004 Shrinkage Prediction Method	32
2.3.4.3 AASHTO 2010 Shrinkage Prediction Method	33
2.3.4.4 MC 90 Shrinkage Prediction Method	35
2.3.4.5 MC 90 – KAV Shrinkage Prediction Method	36
2.4 Calculation of Camber and Stress in Prestressing Steel	37
2.5 Previous Research on Time-Dependent Deformations of SCC	37
2.6 Summary	40
Chapter 3 Design and Construction of Experimental Specimens	41
3.1 Introduction	41
3.2 Specimen Identification	41
3.3 Specimen Design	44
3.3.1 Strand Arrangement	45
3.3.2 Nonprestressed Reinforcement Arrangement	52
3.4 Material Properties	54
3.4.1 Concrete	54

3.4.2 Prestressing Strand.....	58
3.4.3 Nonprestressed Steel Reinforcement.....	59
3.5 Specimen Fabrication.....	60
3.5.1 Casting Configuration.....	60
3.5.2 Fabrication of Precast, Prestressed Bridge Girders.....	61
Chapter 4 Camber Measurement Program.....	76
4.1 Introduction.....	76
4.2 Surveying Method.....	76
4.3 Tensioned Wire Method.....	80
Chapter 5 Strain Measurement Program.....	85
5.1 Introduction.....	85
5.2 Vibrating Wire Strain Gauges.....	85
5.3 Vibrating Wire Strain Gauge Locations.....	86
5.4 Vibrating Wire Strain Gauge Installation.....	95
5.5 VWSG Data Acquisition System.....	97
Chapter 6 Results and Discussion.....	100
6.1 Introduction.....	100
6.2 Adjustment of Measurements to Account for Temperature.....	100
6.2.1 Temperature Correction for Camber.....	106
6.2.2 Temperature Correction for Internal Strain.....	111
6.3 Implementation of Prediction Methods.....	114
6.3.1 Concrete Strength and Modulus of Elasticity.....	115
6.3.2 Relative Humidity.....	116

6.3.3 Cement Class	117
6.3.4 Temperature History	117
6.3.5 ACI 209 Slump Correction Factor	118
6.3.6 ACI 209 Total Cement Content Correction Factor	119
6.3.7 MC 90 – KAV Cement Type Modification	119
6.3.8 Modifications to Schrantz (2012) VB Code	119
6.4 Ultimate Creep Coefficients and Ultimate Shrinkage Strains	120
6.5 Strains	124
6.6 Prestress Losses	137
6.7 Cambers	146
6.8 Predictions Using Design versus Measured Concrete Strengths	154
Chapter 7 Summary and Conclusions	158
7.1 Summary	158
7.2 Conclusions	159
7.3 Recommendations for Future Study	161
References	162
Appendix A: Notation	166
Appendix B: Prediction Program Input Values	167
Appendix C: Strain Predictions and Measurements	171
Appendix D: Camber Predictions and Measurements	189

List of Tables

Table 2-1: Kavanaugh Parameters Modified from MC 90 (Kavanaugh 2008)	27
Table 3-1: Casting Group Designations.....	43
Table 3-2: Summary of Concrete Mixtures	55
Table 3-3: Fresh Concrete Properties	57
Table 3-4: Hardened Concrete Properties.....	58
Table 6-1: Predicted Ultimate Creep Coefficients.....	121
Table 6-2: Predicted Ultimate Shrinkage Strains (in./in.).....	122
Table 6-3: Unbiased Estimate of the Standard Deviation of the Prediction Errors for Bottom-Flange Strains.....	136
Table 6-4: Unbiased Estimate of the Standard Deviation of the Prediction Errors for Camber Growth	153
Table 6-5: Hardened Concrete Properties 72-8C.....	155
Table B-1: Section Geometric Property Prediction Program Inputs	167
Table B-2: Concrete Strength and Modulus of Elasticity.....	168
Table B-3: Concrete Mixture Properties.....	169
Table B-4: Time of Events, Curing, and Maturity Information.....	169
Table B-5: Analysis Intervals	170
Table C-1: Measured Gauge 1 Strains and AASHTO 2004 Predicted Strains.....	172
Table C-2: Predicted Gauge 1 Strains AASHTO 2010 and ACI 209.....	173
Table C-3: Predicted Gauge 1 Strains MC 90 and MC 90-KAV	174
Table D-1: Measured Camber and AASHTO 2004 Predicted Cambers	189
Table D-2: AASHTO 2010 and ACI 209 Predicted Cambers.....	190
Table D-3: MC 90 and MC 90-KAV Predicted Cambers.....	191

List of Figures

Figure 2-1: Concrete Modulus of Elasticity Development Using Two-Point Method.....	15
Figure 3-1: Girder Identification Scheme (Dunham 2011).....	42
Figure 3-2: BT-54 Cross Section	44
Figure 3-3: BT-72 Cross Section	45
Figure 3-4: Profile and Hold-Down of Draped Strands for the BT-54 Girders.....	46
Figure 3-5: Profile and Hold-Down of Draped Strands for the BT-72 Girders.....	46
Figure 3-6: Mild Steel and Strand Arrangement for BT-54 Girder at Midspan	48
Figure 3-7: Mild Steel and Strand Arrangement for BT-54 Girder at End of Span	49
Figure 3-8: Mild Steel and Strand Arrangement for BT-72 Girder at Midspan	50
Figure 3-9: Mild Steel and Strand Arrangement for BT-72 Girder at End of Span	51
Figure 3-10: Mild Steel Spacing in BT-54 Girders	53
Figure 3-11: Mild Steel Spacing in BT-72 Girders	53
Figure 3-12: Prestressing Wire Surface Condition	59
Figure 3-13: Casting Configuration of Three BT-54 Girders.....	60
Figure 3-14: Casting Configuration of Two BT-54 Girders.....	61
Figure 3-15: Casting Configuration of BT-72 Girders	61
Figure 3-16: Strand Debonding	63
Figure 3-17: Side Form Installation.....	64
Figure 3-18: Concrete Delivery Truck.....	65

Figure 3-19: Internal Vibration used in CVC Placement.....	66
Figure 3-20: External Vibration.....	67
Figure 3-21: Surface Roughening of SCC Bridge Girders	68
Figure 3-22: Camber Measurement Marker	69
Figure 3-23: Curing Blanket and Tarp Covering.....	70
Figure 3-24: Crack in BT-54 Girder Prior to Prestress Transfer	71
Figure 3-25: Crack Width in BT-54 Girder Prior to Prestress Transfer	72
Figure 3-26: Flame-Cutting Sequence for BT-54 Girders	73
Figure 3-27: Flame-Cutting Sequence for BT-72 Girders.....	74
Figure 3-28: Support Conditions in Storage	75
Figure 4-1: Surveying Target in Place	77
Figure 4-2: Surveying Method Camber Measurements.....	79
Figure 4-3: Tensioned Wire System Schematic.....	80
Figure 4-4: Drilling Holes for Tensioned Wire Anchors.....	81
Figure 4-5: Tensioned Wire Measurement Rulers.....	82
Figure 4-6: Hanging Weight for Tensioned Wire Camber Measurement	83
Figure 4-7: Camber Measurement using the Tensioned Wire	84
Figure 5-1: VCE-4200 Vibrating Wire Strain Gauge Schematic	86
Figure 5-2: VWSG Layout Plan View.....	87
Figure 5-3: Single VWSG at Midspan for a BT-54.....	89
Figure 5-4: Single VWSG at Midspan for a BT-72.....	90
Figure 5-5: Full Depth VWSG Profile at Midspan for a BT-54	91
Figure 5-6: Full Depth VWSG Profile at Midspan for a BT-72.....	92

Figure 5-7: Full Depth VWSG Profile at Quarterspan for a BT-54	93
Figure 5-8: Full Depth VWSG Profile at Quarterspan for a BT-72	94
Figure 5-9: Full Depth VWSG Profile at Midspan for 54-7S and 54-8C	95
Figure 5-10: VWSG Secured in Bottom Bulb	96
Figure 5-11: VWSG Secured in Web of a Bulb-Tee Girder	97
Figure 5-12: VWSG Data Acquisition System Schematic	98
Figure 6-1: Simplified BT-54 Section	101
Figure 6-2: Simplified BT-72 Section	102
Figure 6-3: Temperature Gradients for 54-4S at Times of Camber Measurement	110
Figure 6-4: Casting Group C Cambers (0 to 225 days)	110
Figure 6-5: Casting Group C Cambers (0 to 7 days)	111
Figure 6-6: Adjusted Strains for 54-4S	114
Figure 6-7: Annual Average Ambient Relative Humidity in Percent (AASHTO 2010, Fig. 5.4.3.2.3.3-1)	116
Figure 6-8: Early-Age Concrete Temperatures for 54-5S	118
Figure 6-9: Predicted Ultimate Creep Coefficients	121
Figure 6-10: Predicted Ultimate Shrinkage Strains	123
Figure 6-11: Measured Versus Predicted Internal Strains – SCC BT-54 Gauge 1	125
Figure 6-12: Measured Versus Predicted Internal Strains – CVC BT-54 Gauge 1	125
Figure 6-13: Measured Versus Predicted Internal Strains – SCC BT-72 Gauge 1	126
Figure 6-14: Measured Versus Predicted Internal Strains – CVC BT-72 Gauge 1	126
Figure 6-15: Measured Versus Predicted Internal Strains – SCC BT-54 Gauge 2	128
Figure 6-16: Measured Versus Predicted Internal Strains – CVC BT-54 Gauge 2	128
Figure 6-17: Measured Versus Predicted Internal Strains – SCC BT-72 Gauge 2	129

Figure 6-18: Measured Versus Predicted Internal Strains – CVC BT-72 Gauge 2	129
Figure 6-19: Measured Versus Predicted Internal Strains – SCC BT-54 Gauge 3	130
Figure 6-20: Measured Versus Predicted Internal Strains – CVC BT-54 Gauge 3	131
Figure 6-21: Measured Versus Predicted Internal Strains – SCC BT-72 Gauge 3	131
Figure 6-22: Measured Versus Predicted Internal Strains – CVC BT-72 Gauge 3	132
Figure 6-23: Measured Versus Predicted Internal Strains – SCC BT-54 Gauge 4	133
Figure 6-24: Measured Versus Predicted Internal Strains – CVC BT-54 Gauge 4	133
Figure 6-25: Measured Versus Predicted Internal Strains – SCC BT-72 Gauge 4	134
Figure 6-26: Measured Versus Predicted Internal Strains – CVC BT-72 Gauge 4	134
Figure 6-27: Prestress in Casting Group A (SCC)	138
Figure 6-28: Prestress in Casting Group B (CVC)	139
Figure 6-29: Prestress in Casting Group C (SCC)	139
Figure 6-30: Prestress in Casting Group D (CVC)	140
Figure 6-31: Prestress in Casting Group E (CVC)	140
Figure 6-32: Prestress in Casting Group E (SCC)	141
Figure 6-33: Prestress in Casting Group F (SCC)	141
Figure 6-34: Prestress in Casting Group G (CVC)	142
Figure 6-35: Prestress in Casting Group H (SCC)	142
Figure 6-36: Prestress in Casting Group I (CVC)	143
Figure 6-37: Prestress in Casting Group J (SCC)	143
Figure 6-38: Prestress in Casting Group K (CVC)	144
Figure 6-39: Prestress in Casting Group L (CVC)	144
Figure 6-40: Prestress in Casting Group L (SCC)	145

Figure 6-41: SCC BT-54 Measured Midspan Cambers.....	147
Figure 6-42: CVC BT-54 Measured Midspan Cambers.....	147
Figure 6-43: SCC BT-72 Measured Midspan Cambers.....	148
Figure 6-44: CVC BT-72 Measured Midspan Cambers.....	148
Figure 6-45: Measured Versus Predicted Camber – SCC BT-54.....	150
Figure 6-46: Measured Versus Predicted Camber – CVC BT-54.....	150
Figure 6-47: Measured Versus Predicted Camber – SCC BT-72.....	151
Figure 6-48: Measured Versus Predicted Camber – CVC BT-72.....	151
Figure 6-49: Predicted and Measured Camber of 72-8C.....	156
Figure 6-50: Predicted and Measured Effective Prestress for 72-8C.....	157
Figure C-1: Measured Strain 54-1S.....	175
Figure C-2: Measured Strain 54-2S.....	175
Figure C-3: Measured Strain 54-3S.....	176
Figure C-4: Measured Strain 54-4S.....	176
Figure C-5: Measured Strain 54-5S.....	177
Figure C-6: Measured Strain 54-6S.....	177
Figure C-7: Measured Strain 54-7S.....	178
Figure C-8: Measured Strain 54-8C.....	178
Figure C-9: Measured Strain 54-9C.....	179
Figure C-10: Measured Strain 54-10C.....	179
Figure C-11: Measured Strain 54-11C.....	180
Figure C-12: Measured Strain 54-12C.....	180
Figure C-13: Measured Strain 54-13C.....	181

Figure C-14: Measured Strain 72-1S	181
Figure C-15: Measured Strain 72-2S	182
Figure C-16: Measured Strain 72-3S	182
Figure C-17: Measured Strain 72-4S	183
Figure C-18: Measured Strain 72-5S	183
Figure C-19: Measured Strain 72-6S	184
Figure C-20: Measured Strain 72-7S	184
Figure C-21: Measured Strain 72-8C.....	185
Figure C-22: Measured Strain 72-9C.....	185
Figure C-23: Measured Strain 72-10C.....	186
Figure C-24: Measured Strain 72-11C.....	186
Figure C-25: Measured Strain 72-12C.....	187
Figure C-26: Measured Strain 72-13C.....	187
Figure C-27: Measured Strain 72-14C.....	188

List of Abbreviations

AASHTO	American Association of State Highway and Transportation Officials
ACI	American Concrete Institute
ALDOT	Alabama Department of Transportation
BT-54	Bulb-tee girder 54 in. in height
BT-72	Bulb-tee girder 72 in. in height
CVC	Conventionally vibrated concrete
SCC	Self-consolidating concrete
VB	Visual Basic

Chapter 1 Introduction

1.1 Background

Precast, prestressed girders are used across the state of Alabama for bridge construction. As improvements to materials continue, new types of concrete have been introduced into the precast industry including high-strength concrete and self-consolidating concrete (SCC). Although these new materials are currently being used in bridge construction, the development of updated methods to predict time-dependent deformations for these new materials has lagged behind. Time-dependent deformations must be accurately predicted so that prestress losses and camber can be accurately predicted in precast, prestressed bridge girders.

Time-dependent deformations occur because of many different factors, but two of the most difficult to predict accurately are creep and shrinkage. The *AASHTO LRFD 2010 Bridge Design Specifications* allow for the use of various methods to predict the creep and shrinkage response of concrete in bridge girders. One of the main objectives of this research was to determine which of these methods most accurately predicted deformations for both conventionally vibrated concrete (CVC) and SCC. The creep and shrinkage models used in this research include the *AASHTO LRFD Bridge Design Specifications* 2004 and 2010 editions, ACI Committee Report 209, and CEB-FIP Model Code 1990. Also included was a modification to the CEB-FIP Model Code recommended for SCC by Kavanaugh (2008).

The accuracy of the creep and shrinkage response for a particular girder is important because the creep and shrinkage predictions relate directly to prestress loss and camber prediction. Incorrectly predicting the amount of prestress loss occurring over the service-life of a

girder might cause a significant increase in the amount of prestressing placed in the girder, driving up the cost of that girder. In a similar fashion, the significant over-prediction of camber can cause issues during the construction of the bridge including extra deck concrete being required and in extreme cases may result in a bridge that sags under superimposed dead loads.

In order to address the issue of predicting time-dependent deformations in precast, prestressed bridge girders in the state of Alabama, the Alabama Department of Transportation (ALDOT) sponsored an investigation to be performed by Auburn University researchers. In a past investigation by Schrantz (2012), the Auburn University Highway Research Center developed a time-step prediction procedure to predict time-dependent deformations. This program was used to develop predictions for twenty-eight bulb-tee girders for use in a replacement bridge constructed on State Route 22 over Hillabee Creek in Tallapoosa County, Alabama. Two of the spans of the bridge were constructed using girders composed of SCC while the remaining two spans were constructed using girders containing CVC. These girders were instrumented for internal strain as well as camber over an extended period of time in order to compare the measured to the predicted response.

1.2 Research Objectives

Specific research objectives are stated below:

1. Compare measured time-dependent deformations of PCI bulb-tee girders constructed with CVC to those of PCI bulb-tee girders constructed with SCC.
2. Compare the time-dependent deformations measured in SCC and CVC girders to predicted deformations developed from widely used creep and shrinkage models.
3. Demonstrate the importance of using accurate material parameters when predicting time-dependent deformations in precast, prestressed concrete members.

1.3 Research Scope

Predicted time-dependent deformations were found for each of the twenty-eight girders manufactured for use in this project. These predicted time-dependent deformations were found by using the time-step program developed by Schrantz (2012). Vibrating-wire strain gauges were used to measure internal strains in the girders and two different methods of camber measurement were used to track the time-dependent deformations of the girders.

1.4 Organization of Thesis

Chapter 2 outlines the principles of predicting time-dependent deformations in precast, prestressed bridge girders. These principles include the calculation of the initial and incremental strains and curvatures of cross sections. An overview of the creep and shrinkage prediction models used in this project is included. A review of previous studies regarding time-dependent deformations in bridge girders follows.

Chapter 3 discusses the design and fabrication of the bulb-tee girders used in this study. The dimensions of the girders along with the material properties for the concrete, prestressing steel, and nonprestressed reinforcement are provided. Finally, a detailed description of the process used to fabricate the girders is provided.

The camber measurement program is presented in Chapter 4. Both the surveying and tensioned wire methods used are outlined in detail.

Chapter 5 discusses the process used to measure the internal strain in the girders. Included in this section are the type of gauge used, the location of the gauges within the girders, and the data acquisition system used to record the measurements.

Chapter 6 is a presentation of the results of this study. It begins with a discussion of how the measured results were modified to account for the effects of temperature in the girders. The

implementation of the prediction models is then presented, with an emphasis on inconsistencies discovered in the time-step program used. Finally, the predicted and measured time-dependent deformations including strains, prestress losses, and cambers are presented.

In conclusion, Chapter 7 presents a brief overview of the study along with final conclusions drawn from the results.

Chapter 2 Literature Review

2.1 Introduction

A major portion of this research project involved the comparison of predicted time-dependent deformations to actual measured deformations in bulb-tee girders constructed with self-consolidating concrete (SCC) and conventionally vibrated concrete (CVC). The predictions were developed by the use of a computer program written by Schrantz (2012). This Visual Basic (VB) program was able to take input from the user including geometric properties, material properties, and curing information to determine time-dependent deformations at specified time-steps using a variety of material models. The final output of the program included strains in the concrete and effective prestress force at various cross sections along the member as well as the camber at midspan at different concrete ages. Subsequent sections in this chapter explain the theory used in achieving these predictions including outlining the various creep and shrinkage models used in the program. The chapter ends with a discussion of previous studies relating to the time-dependent deformation of prestressed, precast concrete girders containing SCC.

2.2 Principles of Time-Dependent Deformation

The time-step procedure developed by Schrantz (2012) to predict time-dependent deformations in prestressed members is based on the principles of compatibility, linear-elastic stress-strain material behavior, and equilibrium. These fundamental principles provide the framework in which complicated cross-sectional deformations may be calculated for each time step. The process implemented by Schrantz (2012) is summarized here. Transformed-section

properties are used for instantaneous computations at each time step to determine the cross-sectional deformations and stresses at that time step. The time-dependent material properties and total deformations and stresses are then updated, and the analysis continues to the next time step.

One of the most important assumptions throughout the prediction methodology is that plane sections remain plane. This means that the change in strain at any level can be determined if the change in strain at the centroid and the change in curvature of the cross section is known, as shown in Equation 2-1 and Equation 2-2. It is inherent within these equations that strain compatibility between materials is followed, meaning that the change in strain in prestressing steel is equal to that of the concrete surrounding it after bond is achieved.

$$\Delta\varepsilon_c = \Delta\varepsilon_{cen} + (\Delta\phi)y \quad \text{Equation 2-1}$$

$$\Delta\varepsilon_p = \Delta\varepsilon_{cen} + (\Delta\phi)y_p + \Delta\varepsilon_{p,i} \quad \text{Equation 2-2}$$

Where

$\Delta\varepsilon_c$ is the change in strain in the concrete (in./in.),

$\Delta\varepsilon_{cen}$ is the change in strain at the centroid of the cross-section (in./in.),

$\Delta\phi$ is the change in curvature of the cross section,

y is the distance from the centroid (positive down) to the concrete being considered (in.),

$\Delta\varepsilon_p$ is the change in strain in the prestressing steel (in./in.),

y_p is the distance from the centroid to the prestressing steel (positive down) (in.),

$\Delta\varepsilon_{p,i}$ is the initial difference in prestressing steel strain and strain in adjacent bonded concrete (in./in.).

Linear-elastic stress-strain material behavior requires that the stress and its accompanying strain at a location are related through a constant of proportionality, the modulus of elasticity, E . The modulus of elasticity is assumed to remain constant through the time step being analyzed. This is shown in Equation 2-3 below. For the purposes of this prediction program, non-linear material responses at or near ultimate stress limits are not considered. These types of responses would include the cracking of concrete and the yielding of steel reinforcement.

$$\varepsilon = \frac{f}{E} \quad \text{Equation 2-3}$$

Where

ε is the portion of total strain (in./in.), that corresponds to an induced stress f (ksi),

and

E is the modulus of elasticity for the material (ksi).

The integral of all of the changes in normal stress integrated over the cross-sectional area must be equal to the change in axial force for a time step, as indicated in Equation 2-4. The girders investigated in this research were all statically determinate, simply supported beams. There were no externally applied axial loads, and the only vertical load present was the self-weight of the member. Thus, the cross-sectional axial force, N , remained zero throughout the analysis.

$$\int_{A_c} \Delta f_c dA_c + \sum (\Delta f_p A_p) = \Delta N \quad \text{Equation 2-4}$$

Where

Δf_c is the change in stress in the concrete (ksi),

A_c is the cross-sectional area (in²),

Δf_p is the change in stress in a layer of prestressing steel (ksi),

A_p is the cross-sectional area of prestressing steel layer (in²), and

ΔN is the change in applied axial load.

Equilibrium also requires that the integral of the changes in stress integrated over the cross section and multiplied by the distance from the centroidal axis must equal the applied moment, M , at the cross section in that time step, as indicated in Equation 2-5. The externally applied moment, which is caused only by the girder's self-weight in this program, will not change across the time step, so the increment is set to zero after the initial prestress is applied.

$$\int_{A_c} \Delta f_c y dA_c + \sum (\Delta f_p y_p A_p) = \Delta M \quad \text{Equation 2-5}$$

Where

y is the distance from the centroidal axis (downward positive) (in.),

y_p is the distance from the centroidal axis to the prestressing steel (in.), and

ΔM is the change in externally applied moment.

The changes in strain at the centroid of a cross section and cross-sectional curvature can be attributed to two different types of strain changes. The first type of strain is stress-dependent strain. These strain changes result directly from the linear-elastic response to changes in the state of stress on the material. The second type of strain includes the strain components that occur independently of stress changes, such as thermal, shrinkage, and creep strains. The shrinkage

strains are considered constant over the depth of the cross section when unrestrained. The creep strain, however, varies with depth. This is because the creep strain for the time step is proportional to the state of stress at the *beginning* of the time step, and these stresses vary linearly over the depth of the cross section. Therefore, the creep strains can be described by an axial component combined with an associated curvature component that describes their variation through the depth. The total strain change in the concrete is the sum of the stress-dependent strain and the stress-independent strains, i.e. the creep, shrinkage, and thermal strains that would occur without change in stress, as shown in Equation 2-6.

$$\Delta\varepsilon_c = \frac{\Delta f_c}{E_c} + \Delta\varepsilon_{c,cr} + \Delta\varepsilon_{c,sh} + \Delta\varepsilon_{c,T} \quad \text{Equation 2-6}$$

Where

$\Delta\varepsilon_c$ is the total change in strain in the concrete during the time step (in./in.),

E_c is the modulus of elasticity of the concrete (ksi),

$\Delta\varepsilon_{c,cr}$ is the change in concrete strain due to creep (in./in.),

$\Delta\varepsilon_{c,sh}$ is the change in concrete strain due to shrinkage (in./in.), and

$\Delta\varepsilon_{c,T}$ is the change in concrete strain due to temperature (in./in.).

Because temperature changes are transient, they were neglected in the prediction models used for this research. Experimental results were later corrected to address thermal changes, as described in Section 6.2. Rearranging Equation 2-6 to solve for the change in concrete stress yields:

$$\Delta f_c = E_c [\Delta\varepsilon_c - (\Delta\varepsilon_{c,cr} + \Delta\varepsilon_{c,sh})] \quad \text{Equation 2-7}$$

Because the prestressing reinforcement does not shrink and its viscoelastic response is usually described as stress relaxation rather than creep strain, the change in stress in the reinforcement over a time step can be computed from Equation 2-8:

$$\Delta f_p = E_p(\Delta \varepsilon_p) + \Delta f_{p,R} \quad \text{Equation 2-8}$$

Where

$\Delta f_{p,R}$ is the change in stress due to relaxation (ksi).

2.2.1 Incremental Strain

The relationships defined above in Equation 2-7 and Equation 2-8 are combined and substituted into the equilibrium relationship of Equation 2-4. The strain change resulting from temperature is ignored in this program, so that term is not be present. The resulting equation is solved for the change in strain at the centroid of the cross section and is shown as Equation 2-9:

$$\Delta \varepsilon_{cen} = \frac{E_c A_c (\Delta \varepsilon_{cen,cr} + \Delta \varepsilon_{c,sh}) + E_c \Delta \phi_{cr} \int_{A_c} y dA_c - \sum (A_p \Delta f_{p,R})}{E_c A_c + E_p \sum A_p} \quad \text{Equation 2-9}$$

Applying the principles of transformed-section analysis, Equation 2-9 for determining the incremental strain at the centroid of the cross section can be rewritten as Equation 2-10:

$$\Delta \varepsilon_{cen} = \frac{A_c}{A_{tr}} (\Delta \varepsilon_{cen,cr} + \Delta \varepsilon_{c,sh}) - \left[\frac{\Delta \phi_{c,cr} \{ \sum (n_p y_p A_p) \} + \frac{1}{E_c} \sum (A_p \Delta f_{p,R})}{A_{tr}} \right] \quad \text{Equation 2-10}$$

Where

A_{tr} is the area of the transformed section (in²).

Careful examination of this equation reveals that the centroidal strain change is primarily a result of the shrinkage strain and the axial component of the creep strain. However, the change in curvature due to creep and the steel relaxation also contribute slightly if the section is eccentrically reinforced.

2.2.2 Incremental Curvature

The change in curvature for each time step is found in a similar fashion as the change in strain at the centroid of the section. The same relationships are substituted into Equation 2-5, and then the equation is solved for the change in curvature. Transformed-section analysis is again taken into account. Equation 2-11 is the resulting equation used to calculate the change in curvature in each time-step.

$$\Delta\phi = \Delta\phi_{cr} \left[1 - \frac{\sum n_p y_p^2 A_p}{I_{tr}} \right] - \left[\frac{\left\{ (\Delta\varepsilon_{cen,cr} + \Delta\varepsilon_{c,sh}) (\sum n_p y_p A_p) + \sum n_p \left(\frac{\Delta f_{p,R}}{E_p} \right) y_p A_p \right\}}{I_{tr}} \right]$$

Equation 2-11

Where

n_p is the modular ratio for the prestressing steel and concrete (E_p/E_c),

E_p is the modulus of elasticity of the prestressing steel (ksi), and

I_{tr} is the area moment of inertia of the transformed cross section (in^4).

Careful examination of this equation reveals that the curvature change is primarily a result of the bending (curvature) component of the creep strain. However, the shrinkage, steel relaxation, and axial component of the creep also contribute slightly to the curvature change if the section is eccentrically reinforced.

2.3 Initial and Incremental Time-Step Calculations

Many inputs need to be determined in each time step in order to calculate the centroidal strain and cross-section curvature by the above equations. This section will describe both the calculations that occur before and immediately following prestress transfer, and the calculations that occur in each time step that determine the inputs into Equation 2-10 and Equation 2-11.

2.3.1 Initial Prestress Losses and Time-Dependent Relaxation

Prestress losses can be separated into two different categories: initial losses and time-dependent losses. For the purpose of this study, the initial prestress losses include the relaxation of the steel prestressing reinforcement prior to transfer and the elastic shortening of these strands during transfer. The initial prestress loss due to relaxation prior to release is calculated by Equation 2-12 (Nilson 1987).

$$\Delta f_{p,R} = f_{pj} \left[\frac{(\log t_i)}{K_L} \right] \times \left[\left(\frac{f_{pj}}{f_{py}} \right) - 0.55 \right] \quad \text{Equation 2-12}$$

Where

$\Delta f_{p,R}$ is the change in prestress force due to relaxation (ksi),

f_{pj} is the jacking stress (ksi),

f_{py} is the yield strength of the prestressing reinforcement (ksi),

t_i is the time between jacking and prestress transfer (hours), and

K_L is 10 for stress-relieved strands; 45 for low-relaxation strands.

At the time of transfer, the prestressing force applied to the concrete member causes axial compression and results in an axial shortening of the member. This causes the strands to simultaneously shorten because of their bond to the concrete. The prestress loss due to the elastic

shortening of the concrete can be calculated using the incremental concrete strain and modulus of elasticity of the prestressing strand.

$$\Delta f_{p,ES} = E_p [\Delta \varepsilon_{cen} + \Delta \phi y] \quad \text{Equation 2-13}$$

Where

E_p is the modulus of elasticity of the prestressing steel (ksi),

$$\Delta \varepsilon_{cen} = \frac{-N_o}{E_c I_{tr,initial}} = \text{change in strain at the centroid of the cross section (in/in)}$$

$N_o = \sum E_p \varepsilon_{p,initial} A_p = \text{axial load on cross section due to prestress transfer (kips),}$

$$\varepsilon_{p,initial} = \frac{f_{pbt}}{E_p} = \frac{f_{pj} + \Delta f_{p,R}}{E_p} = \text{strain in prestressing steel immediately before transfer (in/in),}$$

$$\Delta \phi = \frac{M_G - M_o}{E_c I_{tr,initial}} = \text{change in cross-sectional curvature,}$$

$M_o = \sum N_o y_{p,cen} = \text{moment on cross section due to prestress transfer (kip-in),}$

M_G is the moment due to self-weight (kip-in), and

y is the distance from centroid to the point being considered (positive downward) (in.).

The effective stress in the prestressing strands just prior to transfer for this program is found by subtracting the relaxation before transfer and the elastic-shortening stress loss from the jacking stress.

$$f_{p,t=0} = f_{pj} - \Delta f_{p,R} - \Delta f_{p,ES} \quad \text{Equation 2-14}$$

Where

$f_{p,t=0}$ is the stress in the prestressing steel at the initial time step (ksi), and
 f_{pj} is the jacking stress (ksi).

The incremental time-step strand relaxation calculation is similar to Equation 2-12. The time from jacking to transfer is replaced by the time interval from the beginning of the time step to the end of the time step. Also, the jacking stress is replaced by the stress in the prestressing strands at the beginning of the time step.

$$\Delta f_{p,R} = f_{pi} \left[\frac{(\log t_2 - \log t_1)}{K_L} \right] \times \left[\left(\frac{f_{pi}}{f_{py}} \right) - 0.55 \right] \quad \text{Equation 2-15}$$

Where

t_1 is the time at the beginning of the interval (relative to jacking), and

t_2 is the time at the end of the interval (relative to jacking).

2.3.2 Modulus of Elasticity of Concrete

The VB program developed by Schrantz (2012) used for this project allows for different ways to account for the change in the modulus of elasticity of the concrete, E_c . The user can select a constant E_c , or select a two-point method in which measured or assumed modulus values at transfer ($E_{c,initial}$), and at 28 days ($E_{c,28}$) are used to establish a growth curve over time.

Equations 2-16 and 2-17 shown below were developed based on the time-dependent coefficient $\beta_{cc}(t)$ found in the MC 90 equation for development of concrete strength with time (CEB 1990).

The modulus of elasticity of the concrete is a function of the concrete age at the beginning of each interval, the modulus of elasticity at 28 days, and the growth rate, s . The two-point system described below was used for all of the predictions developed in this study.

$$E_{c,i} = E_{c,28} \exp \left\{ s \left[1 - \left(\frac{28}{age_{i-1}} \right)^{1/2} \right] \right\} \quad \text{Equation 2-16}$$

Where

age_{i-1} is the concrete age at the beginning of the interval (days), and

$$s = \frac{\ln \left(\frac{E_{c,initial}}{E_{c,28}} \right)}{\left[1 - \left(\frac{28}{t_{initial}} \right)^{1/2} \right]} \quad \text{Equation 2-17}$$

A typical growth curve for the concrete modulus of elasticity developed using Equation 2-16 and 2-17 is shown in Figure 2-1.

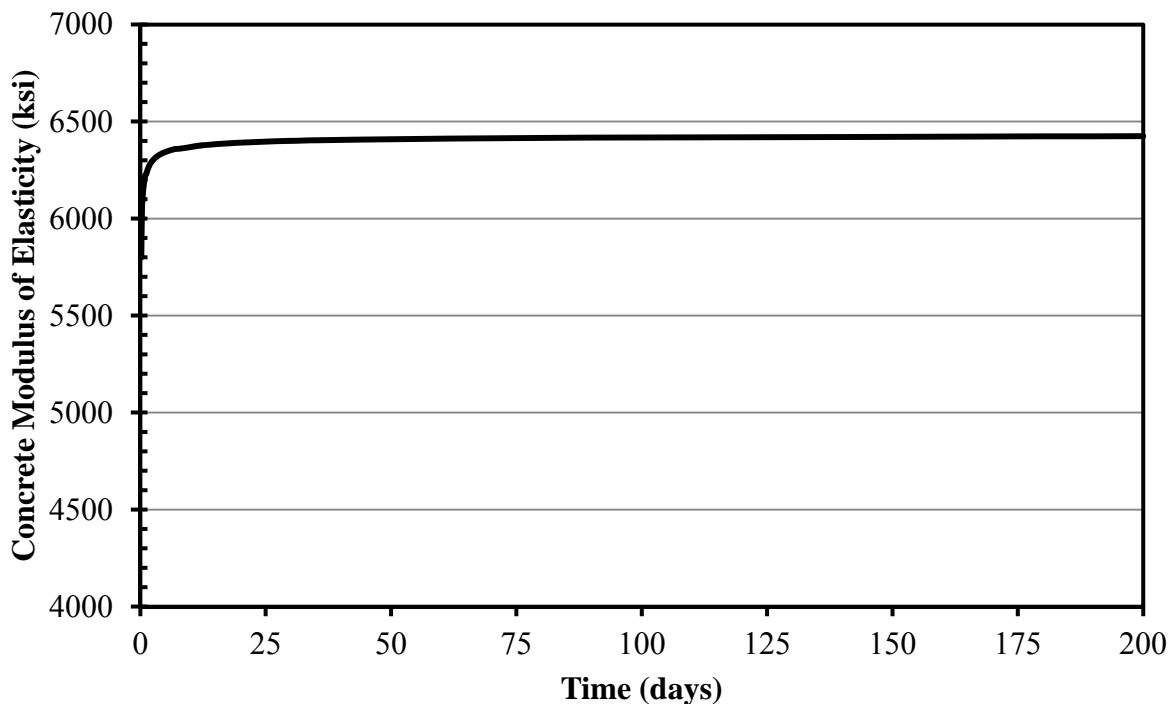


Figure 2-1: Concrete Modulus of Elasticity Development Using the Two-Point Method

2.3.3 Creep

Creep is defined as “the time-dependent increase of strain in hardened concrete subjected to sustained stress” (ACI 209 1992). Many studies have been conducted to determine the creep

characteristics of different types of concrete. Neville (1997) concluded that creep in concrete that underwent accelerated curing can be thirty to fifty percent lower than creep in concrete that underwent non-accelerated curing. When hard coarse aggregates are used in concrete mixtures, creep was found to be reduced when compared to mixtures using soft coarse aggregates (Mokhtarzadeh and French 2000). Studies have also shown that concrete with a higher compressive strength will exhibit less creep than concrete with a lower compressive strength (Hinkle 2006). The AASHTO LRFD 2010 Bridge Design Specification Section 5.4.2.3.1 allows for the use of a variety of creep and shrinkage prediction models for the time-dependent behavior of concrete bridge components. In the sections below, each prediction model's approach to predicting creep in pretensioned members is discussed.

2.3.3.1 ACI 209 Creep Prediction Method

The ACI Committee 209 (1992) proposed a creep prediction model that uses an ultimate creep coefficient computed using mixture-specific characteristics, element geometry, and loading parameters as well as environmental conditions. A time-rate function to account for the growth of creep over time is used in conjunction with the ultimate creep coefficient. To find the creep strain at a given concrete age, the ultimate creep coefficient is multiplied by the time factor, which is then multiplied by the elastic strain that resulted at the time of loading the concrete. The ultimate creep coefficient, ν_u , is computed by the following equation:

$$\nu_u = 2.35(\gamma_{la} \cdot \gamma_{\lambda} \cdot \gamma_{vs} \cdot \gamma_{\psi} \cdot \gamma_s \cdot \gamma_a) \quad \text{Equation 2-18}$$

Where

γ_{la} is the loading age correction factor,

γ_{λ} is the relative humidity correction factor,

γ_{vs} is the volume-to-surface area ratio correction factor,

γ_ψ is the fine aggregate percentage correction factor,

γ_s is the slump correction factor, and

γ_a is the air content correction factor.

The calculations used to obtain these correction factors are outlined in Equation 2-19 through Equation 2-26.

The loading age factor, γ_{la} , is calculated only for loading ages greater than 7 days for non-accelerated-cured concrete or 1-3 days for accelerated-cured concrete. Equation 2-19 outlines the equation used for non-accelerated-cured concrete and Equation 2-20 shows the equation used for accelerated-cured concrete.

$$\gamma_{la} = 1.25(t_{la})^{-0.118} \quad \text{Equation 2-19}$$

$$\gamma_{la} = 1.13(t_{la})^{-0.094} \quad \text{Equation 2-20}$$

Where t_{la} is the concrete age at which the load is applied (days).

When the ambient relative humidity is greater than 40 percent, the correction factor γ_λ is calculated by Equation 2-21:

$$\gamma_\lambda = 1.27 - 0.0067\lambda \quad \text{Equation 2-21}$$

Where λ is the relative humidity (%).

Equation 2-22 shows the calculation for the volume-to-surface area ratio correction factor:

$$\gamma_{vs} = \frac{2}{3} [1 + 1.13(e^{-.54(v/s)})] \quad \text{Equation 2-22}$$

Where v_s is the volume-to-surface area ratio of the cross section (in.).

The fine aggregate percentage correction factor is calculated using Equation 2-23 only when the ratio of fine aggregate to total aggregate by weight does not fall between 40 and 60 percent. When the percentage of fine aggregate to total aggregate by weight does fall between 40 and 60 percent, the correction factor is equal to 1.0.

$$\gamma_\psi = 0.88 + 0.0024\psi \quad \text{Equation 2-23}$$

Where ψ is the ratio of fine aggregate to total aggregate by weight (%).

The slump correction factor is calculated according to Equation 2-24 shown below. For slump values less than 5 inches, the correction factor is equal to 1.0.

$$\gamma_s = 0.82 + 0.067s \quad \text{Equation 2-24}$$

Where s is the slump (in.).

The air content correction factor calculation is shown below. When air contents of less than 8 percent are observed the factor is equal to 1.0.

$$\gamma_\alpha = 0.46 + 0.09\alpha \geq 1.0 \quad \text{Equation 2-25}$$

Where α is the air content (%).

In order to calculate the creep coefficient at a particular time step of interest, the ultimate creep coefficient must be multiplied by the time factor, v_t , associated with that age as shown in Equation 2-26.

$$\nu_u(t) = \nu_u \times \nu_t \quad \text{Equation 2-26}$$

Where ν_t is the time factor.

The time factor is a ratio of the creep strain to the initial strain based on the time after loading the concrete. Equation 2-27 is valid for both normal weight and lightweight concretes, using accelerated and non-accelerated curing, and Types I and III cements, under standard conditions. This equation is only valid for loading ages later than 7 days for non-accelerated-cured concrete and later than 1-3 days for accelerated-cured concrete.

$$\nu_t = \frac{t^{0.6}}{10 + t^{0.6}} \quad \text{Equation 2-27}$$

Where t is the length of time after loading (days).

Once the creep coefficient is determined for a particular time step, the creep strain at that time step can be predicted by multiplying the creep coefficient by the elastic strain at loading.

$$\text{Predicted Creep, } \varepsilon_{cr}(t) = \text{creep coef.} \times \text{elastic strain at loading} \quad \text{Equation 2-28}$$

2.3.3.2 AASHTO 2004 Creep Prediction Method

This creep prediction model should be used to determine the effects of creep on the loss of prestressing force in bridges other than those that are segmentally constructed (AASHTO 2004). The methods of predicting creep and shrinkage in AASHTO 2004 were taken from Collins and Mitchell (1991), and are based on recommendations from ACI 209 and other published data (AASHTO 2004). The creep coefficient is calculated using Equation 2-29:

$$\psi(t, t_i) = 3.5k_c \cdot k_f \left(1.58 - \frac{H}{120}\right) t_i^{-0.118} \left(\frac{(t - t_i)^{0.6}}{10 + (t - t_i)^{0.6}}\right) \quad \text{Equation 2-29}$$

Where

k_c is the volume-to-surface ratio correction factor,

k_f is the concrete strength correction factor,

H is the relative humidity (%),

t is the maturity of concrete (days), and

t_i is the concrete age at time of load application (days).

For creep calculations, the AASHTO 2004 code does not specify which type of curing (accelerated or non-accelerated) is the basis for the loading age term, t_i . The code does state that “one day of accelerated curing by steam or radiant heat may be taken as equal to seven days of normal curing,” which implies that any accelerated curing would require modification of the t_i term. In order to compensate for accelerated curing, in the time-step procedure employed for this project, the accelerated-curing loading age is multiplied by seven to get an equivalent number of non-accelerated curing days. Collins and Mitchell (1991), however, refer to *adding* days to compensate for accelerated curing as opposed to multiplying by 7 days. For accelerated-curing periods of 18 to 24 hours, such as employed in this study, the difference in the loading age factor found by adding days or multiplying by 7 days is less than 3 percent. It should be noted that the time factor portion of Equation 2-29 is the same as in Equation 2-27, which is the time factor for the ACI 209 method.

The volume-to-surface ratio correction factor, k_c , is calculated using Equation 2-30 shown below. This equation was developed based on a maximum volume-to-surface ratio of 6.0 inches (PCI 1977).

$$k_c = \left[\frac{\frac{t}{26e^{0.36(V/S)} + t}}{\frac{t}{45 + t}} \right] \left[\frac{1.8 - 1.77e^{-0.54(V/S)}}{2.587} \right] \quad \text{Equation 2-30}$$

Where V/S is the volume-to-surface area ratio (in.).

The concrete strength correction factor in Equation 2-29, k_f , is calculated by:

$$k_f = \frac{1}{0.67 + \left(\frac{f'_c}{9} \right)} \quad \text{Equation 2-31}$$

Where f'_c is the specified compressive strength of concrete at 28 days (ksi).

To determine the predicted strain due to creep, the creep coefficient $\psi(t, t_i)$ is multiplied by the compressive strain caused by permanent loads. This process is similar to Equation 2-28.

2.3.3.3 AASHTO 2010 Creep Prediction Method

Similar to the AASHTO 2004 creep prediction method, the newer AASHTO LRFD 2010 method should be used for determining the effects of creep on the loss of prestressing force in bridges other than segmentally constructed ones. This method was created based on the findings of Huo et al. (2001), Al-Omaishi (2001), Tadros (2003), Collins and Mitchell (1991), recommendations by ACI Committee 209, and other recently published data (AASHTO 2010). The provisions of AASHTO 2010 are valid for concrete strengths up to 15.0 ksi.

The creep coefficient is computed using the following equation:

$$\psi(t, t_i) = 1.9(k_{hc} \cdot k_s \cdot k_f \cdot k_{td})t_i^{-.118} \quad \text{Equation 2-32}$$

Where

k_{hc} is the relative humidity correction factor,

k_s is the volume-to-surface area ratio correction factor,

k_f is the concrete strength correction factor,

k_{td} is the time development correction factor, and

t_i is the concrete age at time of load application (days).

The relative humidity correction factor is calculated by:

$$k_{hc} = 1.56 - 0.008H \quad \text{Equation 2-33}$$

Where H is the relative humidity (%).

The volume-to-surface area correction factor is calculated using Equation 2-34 shown below. The surface area used in determining k_s should only include the area exposed to atmospheric drying.

$$k_s = 1.45 - .13(V/S) \geq 1 \quad \text{Equation 2-34}$$

Where V/S is the volume-to-surface area ratio (in.).

The concrete strength correction factor is calculated by:

$$k_f = \frac{5}{1 + f'_{ci}} \quad \text{Equation 2-35}$$

Where

f'_{ci} is the specified compressive strength at prestressing for pretensioned members and at time of initial loading for non-prestressed members (ksi). If the age of concrete at initial loading is unknown, f'_{ci} may be taken as $0.8 f'_c$.

The time development correction factor is calculated using Equation 2-36. It is valid for both precast and cast-in-place concrete as well as accelerated and non-accelerated curing conditions.

$$k_{td} = \frac{t}{61 - 4f'_{ci} + t} \quad \text{Equation 2-36}$$

Where t is the concrete maturity (days).

As with the creep prediction methods mentioned previously, the creep coefficient can be multiplied by the elastic strain due to permanent loads in order to determine the predicted strain due to creep.

2.3.3.4 MC 90 Creep Prediction Method

The CEB-FIP Model Code 1990 was developed as a European design code applicable to concrete mixtures subjected to normal conditions (Al-Manaseer and Lam 2005). The MC 90 creep prediction model contains provisions that allow for cement type, curing temperature, and high stress levels to be incorporated into the prediction (CEB 1990). The MC 90 prediction model is not valid for mixtures subjected to extreme high or low temperatures, low relative humidities, or mixtures using structural lightweight aggregate (CEB 1990). The procedure involved in this creep prediction model is outlined below.

A creep coefficient is calculated by Equation 2-37:

$$\Phi(t, t_o) = \Phi_o \cdot \beta_c(t - t_o) \quad \text{Equation 2-37}$$

Where

$\Phi(t, t_o)$ is the creep coefficient,

Φ_o is the notional creep coefficient,

β_c is the coefficient describing development of creep with time after loading,

t is the age of concrete at the moment considered (days), and

t_o is the age of concrete at loading.

The notional creep coefficient in Equation 2-37 can be calculated using Equation 2-38 shown below:

$$\Phi(t, t_o) = \Phi_o \cdot \beta_c(t - t_o) \quad \text{Equation 2-38}$$

With

$$\Phi_{RH} = 1 + \frac{1 - \left(\frac{RH}{RH_o}\right)}{.46 \left(\frac{h}{h_o}\right)^{1/3}} \quad \text{Equation 2-39}$$

$$\beta(f_{cm}) = \frac{5.3}{\left(\frac{f_{cm}}{f_{cmo}}\right)^{.5}} \quad \text{Equation 2-40}$$

$$\beta(t_o) = \frac{1}{.1 + \left(\frac{t_o}{t_1}\right)^{.2}} \quad \text{Equation 2-41}$$

Where

RH is the relative humidity of the environment (%),

$$RH_o = 100\%,$$

$$h = \frac{2A_c}{u}$$

Equation 2-42

A_c is the cross-sectional area (mm²),

u is the perimeter (mm),

$$h_o = 100 \text{ mm},$$

f_{cm} is the mean compressive strength at 28 days (MPa),

$f_{cmo} = 10$ MPa, and

$$t_1 = 1 \text{ day}.$$

The notional creep coefficient must be multiplied by a time factor. The time factor formulation is shown below:

$$\beta_c(t - t_o) = \left[\frac{\frac{(t - t_o)}{t_1}}{\beta_H + \frac{(t - t_o)}{t_1}} \right]^{0.3}$$

Equation 2-43

Where

$$\beta_H = 150 \left[1 + \left(1.2 \frac{RH}{RH_o} \right)^{18} \right] \frac{h}{h_o} + 250 \leq 1500$$

Equation 2-44

and all other factors previously defined.

Once again, after the creep coefficient for each time step is found, the predicted creep strain at that time step is calculated by multiplying the creep coefficient by the elastic strain resulting from loading as in Equation 2-28.

The research done for this project was performed on pretensioned girders that were cured using steam curing. The Model Code 1990 accounts for elevated temperatures during curing by requiring a maturity calculation to be done using the temperature history of the concrete during curing to find an equivalent age at loading. The temperature adjusted t_o term that is used in Equation 2-41 should be found using the equations below when curing temperatures are elevated:

$$t_o = t_{o,T} \left[\frac{9}{2 + \left(\frac{t_{o,T}}{t_{1,T}} \right)^{1.2}} + 1 \right]^\alpha \geq 0.5 \text{ days} \quad \text{Equation 2-45}$$

Where

$t_{o,T}$ is the temperature adjusted age according to Equation 2-39 (days)

$t_{1,T} = 1$ day, and

α is the cement type;

$\alpha = -1$ for slowly hardening cements (SL), 0 for normal or rapid-hardening cements (N and R), and 1 for rapid-hardening high-strength cements (RS).

The temperature adjusted age $t_{o,T}$ is calculated using Equation 2-46:

$$t_{o,T} = \sum_{i=1}^n \Delta t_i \cdot \exp \left[13.65 - \frac{4000}{273 + \left(\frac{T(\Delta t_i)}{T_o} \right)} \right] \quad \text{Equation 2-46}$$

Where

Δt_i is the number of days where temperature T prevails,

$T(\Delta t_i)$ is the temperature ($^{\circ}\text{C}$) during the time period Δt_i , and

$$T_o = 1^\circ\text{C}.$$

The temperature adjusted t_o term should only be used in Equation 2-41 when finding the notional creep coefficient. The actual age of the concrete t_o should be used when computing the time factor as in Equation 2-43. This calculation assumes that t_o represents that actual time that the concrete is under load.

2.3.3.5 MC 90 – KAV Creep Prediction Method

The final creep prediction model utilized in this research was a modified version of the MC 90 model. Research conducted by Kavanaugh (2008) at Auburn University yielded a variation of the MC 90 that was adapted to research conducted on creep performance of both conventional and SCC concrete mixtures. Non-accelerated curing formulas and accelerated curing formulas were derived to modify specific creep parameters. Table 2-1 summarizes the modified MC 90 functions.

Table 2-1: Kavanaugh Parameters Modified from MC 90 (Kavanaugh 2008)

Parameter	Original Formulation	KAV Modification
$\beta(f_{cm})$	$\frac{5.3}{(f_{cm}/f_{cmo})^{.5}}$	$\frac{4.65}{(f_{cm}/f_{cmo})^{.5}}$
$\beta(t_o)$	$\frac{1}{.1 + (t_o/t_1)^2}$	$\frac{1}{.26 + (t_o/t_1)^{.18}}$
$\beta_c(t - t_o)$	$\left[\frac{(t - t_o)/t_1}{\beta_H + (t - t_o)/t_1} \right]^{0.3}$	$\left[\frac{(t - t_o)/t_1}{\beta_H + (t - t_o)/t_1} \right]^{0.35}$
$t_{o,T}$	$\sum_{i=1}^n \Delta t_i \exp \left[13.65 - \frac{4000}{273 + \left(\frac{T(\Delta t_i)}{T_o} \right)} \right]$	$\sum_{i=1}^n \Delta t_i \exp \left[18.47 - \frac{5410}{273 + \left(\frac{T(\Delta t_i)}{T_o} \right)} \right]$

The temperature adjusted t_o term calculated in Equation 2-46 in the MC 90 creep prediction method accounts for the cement type used in the concrete mixture. Kavanaugh (2008) accounted for the cement type modification by modifying Equation 2-47 to include the effects of cement type. Therefore, the $t_{o,T}$ term found by using the MC 90-KAV should be substituted directly in place of t_o where applicable without the modification of Equation 2-46. The ramifications of this difference between these two methods and their implementation is discussed further in Section 6.3.6.

2.3.4 Shrinkage

Shrinkage is defined as the time-dependent strain measured from an unloaded and unrestrained concrete specimen. The two major types of shrinkage accounted for in prediction models are drying shrinkage and autogenous shrinkage. Drying shrinkage occurs primarily because of moisture loss during the drying or curing process. Autogenous shrinkage results from self-densification occurring in the concrete as a result of hydration.

Shrinkage, like creep, causes a shortening in the overall length of the member, and in the case of a prestressed member, this would cause a loss of prestress force. Therefore, it is important to identify the shrinkage properties of a concrete mixture so that an accurate shrinkage strain prediction can be made. The following sections outline the approach to predicting shrinkage strain for each of the prediction models included in this research project.

2.3.4.1 ACI 209 Shrinkage Prediction Method

The ACI 209 shrinkage prediction method uses a process similar to that of the ACI 209 creep prediction method, in which an ultimate shrinkage value is calculated and is modified by a

time-dependent factor for predictions over time. First, a notional ultimate shrinkage strain is calculated using modification factors for non-standard conditions.

$$(\varepsilon_{sh})_u = 780 \times 10^{-6} (\gamma_\lambda \cdot \gamma_{vs} \cdot \gamma_\psi \cdot \gamma_s \cdot \gamma_\alpha \cdot \gamma_c) \quad \text{Equation 2-47}$$

Where

γ_λ is the relative humidity correction factor,

γ_{vs} is the volume-to-surface area ratio correction factor,

γ_ψ is the fine aggregate percentage correction factor,

γ_s is the slump correction factor,

γ_α is the air content correction factor, and

γ_c is the cement content correction factor.

Each of the correction factors in Equation 2-47 must be calculated based on the equations that follow.

The relative humidity correction factor is equal to 1.0 if the ambient relative humidity is less than 40 percent. If the relative humidity is between 40 and 80 percent, Equation 2-48 should be used to calculate the correction factor. If the relative humidity is greater than 80 percent, Equation 2-49 is used.

$$\gamma_\lambda = 1.4 - .0102\lambda \quad \text{for } 40\% \leq \lambda \leq 80\% \quad \text{Equation 2-48}$$

$$\gamma_\lambda = 3 - .03\lambda \quad \text{for } 80\% < \lambda \leq 100\% \quad \text{Equation 2-49}$$

Where λ is the relative humidity (%).

The volume-to-surface area ratio correction factor is computed using Equation 2-50:

$$\gamma_{vs} = 1.2(e^{-.12(v/s)}) \quad \text{Equation 2-50}$$

Where v/s is the volume-to-surface area ratio (in.).

The fine aggregate percentage correction factor is computed using Equation 2-51 for percentages less than or equal to 50 percent, and Equation 2-52 for percentages greater than 50 percent.

$$\gamma_{\psi} = .3 + .014\psi \quad \text{for } \psi \leq 50\% \quad \text{Equation 2-51}$$

$$\gamma_{\psi} = .9 + .002\psi \quad \text{for } \psi > 50\% \quad \text{Equation 2-52}$$

Where Ψ is the ratio of fine aggregate to total aggregate by weight (%).

The slump correction factor is calculated using Equation 2-54. When the observed slump is less than 5 inches, the factor is approximately equal to 1.0. While this method calls for the observed slump to be used, Schrantz (2012) concluded that a modified slump value should be used in this equation when water-reducing admixtures are used in the concrete mixture. This is discussed further in Section 6.3.5.

$$\gamma_s = .89 + .041s \quad \text{Equation 2-53}$$

Where s is the slump (in.).

The air content correction factor, γ_{α} , is computed using Equation 2-54:

$$\gamma_{\alpha} = .95 + .008\alpha \quad \text{Equation 2-54}$$

Where α is the air content (%).

The cement content correction factor is calculated by using Equation 2-55.

$$\gamma_c = .75 + .00036c \quad \text{Equation 2-55}$$

Where c is the cement content (lb/yd³).

There are two different equations for the shrinkage time factor depending on the type of curing. Equation 2-56 is used in situations that involve 7 days of non-accelerated curing while Equation 2-57 is used for 1 to 3 days of accelerated curing. These equations are only applicable after 7 days of non-accelerated curing or 1 to 3 days of accelerated curing.

$$(\varepsilon_{sh})_t = \frac{t}{35 + t} \quad \text{Equation 2-56}$$

$$(\varepsilon_{sh})_t = \frac{t}{55 + t} \quad \text{Equation 2-57}$$

Where t is the time from the end of initial curing (days).

The total shrinkage strain at a certain concrete age can be predicted by multiplying the ultimate shrinkage strain by the time factor.

$$\text{Predicted Shrinkage, } \varepsilon_{sh}(t) = (\varepsilon_{sh})_t \times (\varepsilon_{sh})_u \quad \text{Equation 2-58}$$

2.3.4.2 AASHTO 2004 Shrinkage Prediction Method

The AASHTO 2004 shrinkage prediction method takes into account aggregate characteristics, relative ambient humidity, volume-to-surface area ratio, concrete age, and curing type. While recommended for predicting shrinkage strains in bridges other than those that are segmentally constructed, AASHTO 2004 suggests that large concrete members might experience significantly less shrinkage than smaller members in a laboratory setting even if the concrete mixtures are the same.

Equation 2-59 predicts shrinkage strains in non-accelerated cured concretes that do not contain shrinkage-prone aggregates. The resulting predicted strain from Equation 2-59 should be increased by 20 percent if the non-accelerated cured concrete is exposed to drying before five days of curing has passed. The code does not specify if this curing period consists of non-accelerated-cured days or accelerated-cured days. Therefore, in the case of the accelerated-cured concrete, the critical curing period is adjusted by dividing the “normal” five-day period by a factor of seven. Therefore, for accelerated-curing periods less than 5/7 day (17 hours), the shrinkage is increased by 20 percent. Equation 2-60 should be used for concretes undergoing accelerated curing.

$$\varepsilon_{sh} = -k_s \cdot k_h \left(\frac{t}{35 + t} \right) 0.51 \times 10^{-3} \quad \text{Equation 2-59}$$

$$\varepsilon_{sh} = -k_s \cdot k_h \left(\frac{t}{55 + t} \right) 0.56 \times 10^{-3} \quad \text{Equation 2-60}$$

Where

k_s is the volume-to-surface area ratio correction factor,

k_h is the relative humidity correction factor, and

t is the maturity of concrete (days).

The volume-to-surface ratio correction factor should be calculated by Equation 2-61. The maximum V/S ratio considered in the development of this equation was 6.0 inches. Also, the surface area used for this calculation should only include the area that will be exposed to drying.

$$k_s = \left[\frac{\frac{t}{26e^{0.36(V/S)} + t}}{\frac{t}{45 + t}} \right] \left[\frac{1064 - 94(V/S)}{923} \right] \quad \text{Equation 2-61}$$

Where

V/S is the volume-to-surface area ratio (in.), and

t is the maturity of concrete (days).

The relative humidity correction factor can be calculated by the following equations:

$$k_h = \frac{140-H}{70} \quad \text{for } H < 80\% \quad \text{Equation 2-62}$$

$$k_h = \frac{3(100-H)}{70} \quad \text{for } H \geq 80\% \quad \text{Equation 2-63}$$

Where H is the relative humidity (%).

2.3.4.3 AASHTO 2010 Shrinkage Prediction Method

Similar to the AASHTO 2004 shrinkage prediction method, this method should be used for determining the effects of shrinkage on the loss of prestressing force in bridges other than segmentally constructed ones. This method was created with a basis on the findings of Huo et al. (2001), Al-Omaishi (2001), Tadros (2003), Collins and Mitchell (1991), recommendations by

ACI Committee 209 and other recently published data (AASHTO 2010). Shrinkage prediction for this method is based on aggregate characteristics, concrete strength, curing method, average humidity, volume-to-surface area ratio, duration of drying, and the age at the start of drying. Equation 2-64 predicts the shrinkage strain in concretes that do not contain shrinkage-prone aggregates.

$$\varepsilon_{sh} = k_{hc} \cdot k_s \cdot k_f \cdot k_{td} \cdot 0.48 \times 10^{-3} \quad \text{Equation 2-64}$$

Where

k_{hc} is the relative humidity correction factor,

k_s is the volume-to-surface area ratio correction factor,

k_f is the concrete strength correction factor, and

k_{td} is the time development correction factor.

The relative humidity correction factor may be taken as:

$$k_{hc} = 2.0 - 0.014H \quad \text{Equation 2-65}$$

Where H is the relative humidity (%).

The remaining factors used in Equation 2-64, the volume-to-surface area ratio correction factor, the concrete strength correction factor, and the time development factor are calculated in the exact same manner as the creep prediction method outlined in Section 2.3.3 above. The specific equations for these factors are Equation 2-34 Equation 2-35, and Equation 2-36 respectively. The 20 percent increase to shrinkage predictions to concrete exposed to drying before five days of curing used in the AASHTO 2004 method is applied in the same manner in the AASHTO 2010 method.

2.3.4.4 MC 90 Shrinkage Prediction Method

The MC 90 shrinkage prediction uses a notional shrinkage value multiplied by a time factor to determine total shrinkage strain at a given concrete age. Factors that are used in this method include concrete strength, cement type, member geometry, age of the concrete, and relative humidity. The total shrinkage strain may be calculated by:

$$\varepsilon_{cs}(t, t_s) = \varepsilon_{cso} \cdot \beta_s(t - t_s) \quad \text{Equation 2-66}$$

Where

ε_{cso} is the notional shrinkage coefficient,

β_s is the coefficient that describes shrinkage with time,

t is the age of the concrete at the moment considered (days), and

t_s is the age at the start of shrinkage (days); normally at the end of curing.

The notional shrinkage coefficient, ε_{cso} , is given by :

$$\varepsilon_{cso} = \varepsilon_s(f_{cm})\beta_{RH} \quad \text{Equation 2-67}$$

With,

$$\varepsilon_s(f_{cm}) = \left[160 + 10 \cdot \beta_{sc} \left(9 - \frac{f_{cm}}{f_{cmo}} \right) \right] 10^6 \quad \text{Equation 2-68}$$

Where

f_{cm} is the mean compressive strength at 28 days (MPa),

$f_{cmo} = 10$ MPa,

β_{sc} is the cement type coefficient:

$\beta_{sc} = 4$ for slow-hardening concrete (SL)

= 5 for normal or rapid-hardening concrete (N or R)

= 8 for rapid-hardening high-strength concrete (RS)

And

$$\beta_{RH} = -1.55\beta_{SRH} \quad \text{for } 40\% \leq RH < 99\% \quad \text{Equation 2-69}$$

$$\beta_{RH} = .25 \quad \text{for } RH \geq 99\% \quad \text{Equation 2-70}$$

With

$$\beta_{SRH} = 1 - \left(\frac{RH}{RH_o} \right)^3 \quad \text{Equation 2-71}$$

Where

RH is the ambient relative humidity (%), and

$RH_o = 100\%$.

The time development of shrinkage is given by:

$$\beta_s(t - t_s) = \left[\frac{(t - t_s)/t_1}{350 \left(h/h_o \right)^2 + (t - t_s)/t_1} \right]^{0.5} \quad \text{Equation 2-72}$$

Where

h is the notional size of the member (mm), defined in Equation 2-42

$t_1 = 1$ day, and

$h_o = 100$ mm.

2.3.4.5 MC 90 – KAV Shrinkage Prediction Method

The Kavanaugh modified method did not recommend any changes to the MC 90 shrinkage prediction model. Therefore, shrinkage predictions for this method are identical to those predicted by the MC 90 prediction method.

2.4 Calculation of Camber and Stress in Prestressing Steel

After determining the incremental strain change at the centroid of the cross section and the incremental change in curvature of the cross section by Equation 2-9 and Equation 2-10 respectively, the time-dependent deformations of camber and change in strain of the prestressing steel may be calculated. The incremental strain in the prestressing steel and incremental relaxation is then used to directly calculate the change in stress in the prestressing steel for each time interval in accordance with Equation 2-8.

The camber calculations are based on the moment-area method and assume the use of a simply-supported, symmetrical beam with a uniformly distributed self-weight. The camber is only determined at the midspan of the girder. Curvatures are determined for a user-specified number of cross sections along the girder length in each time-step, and these curvatures are used to compute the midspan deflection by the moment-area method described in detail by Schrantz (2012). An increase in the number of cross sections analyzed corresponds to an increase in the accuracy of the camber prediction.

The effective stress in the prestressing steel at the end of each time step is computed by accumulating the stress changes over all of the previous time steps.

2.5 Previous Research on Time-Dependent Deformations of SCC

One of the questions surrounding the issue of using SCC in prestressed bridge girders is how the time-dependent deformations in the girder will differ from those of CVC prestressed bridge girders. Some research projects have been conducted throughout North America that sought to compare prestressed bridge girders constructed with SCC to those constructed with CVC. Labonte et al. (2005) studied AASHTO Type II beams, some of which were composed of SCC and others composed of CVC. No notable differences were found in mean camber growth

between the girders. Trent (2007) evaluated prestress losses in girders constructed with SCC and CVC. It was found that the girders containing CVC experienced greater prestress losses than ones containing SCC mixtures. Schrantz (2012) found no significant differences in camber or camber growth between girders composed of SCC and CVC.

Another concern that arises from using SCC in prestressed bridge girder applications is the ability to accurately predict time-dependent deformations. Schrantz (2012) analyzed various types of girders using different SCC and CVC mixtures. Prediction models were developed based on accurate material parameters used in real bridge girders. This means that values predicted by Schrantz using accurate material properties were compared to *measured* values. The girders analyzed by Schrantz included AASHTO Type I girders and BT-54 girders. However, the predictions developed for the BT-54 girders were incorrect because of an error in the program used to develop the predictions. The ½ in. diameter strands were neglected in the analysis. This is discussed further in Section 6.3.7. Also, the MC-90 KAV prediction for creep predictions reported by Schrantz (2012) were incorrect. In Section 2.3.3.5 the modification to the temperature-adjusted age is shown to be included in the modifications to the MC 90 made by Kavanaugh, but Schrantz (2012) included the modification separately according to the MC 90 method. It was determined that the MC 90 and MC 90-KAV creep and shrinkage models are the best predictors of camber in SCC girders. Furthermore, the AASHTO 2004, AASHTO 2010, and ACI 209 models were found to drastically over-predict long-term camber (Schrantz 2012).

These results were found by using the most accurate concrete material properties available as opposed to estimated design values. Stallings et al. (2003) determined that accurate predictions require the use of accurate material parameters. Cambers that were calculated using standard material parameters consistently exceeded measured values, and these errors resulted

primarily from overestimating creep and shrinkage characteristics of the concrete (Stallings 2003). These findings were from bridge girders that contained high-performance CVC girders. Barr et al. (2008) found that the AASHTO prediction methods over-predicted the average prestress losses for highly stressed girders by 20%. The error seems to be occurring in the creep and shrinkage prediction models, so most of the research conducted recently has been geared toward comparing the creep and shrinkage characteristics of SCC and CVC.

Levy et al. (2010) determined that creep and shrinkage strains of SCC elements were no larger than conventional-slump concrete at similar levels of concrete strength and applied prestress force. Similarly, Kavanaugh (2008) found that all of the SCC mixtures tested exhibited creep values similar to or less than CVC mixtures. In accelerated-cured specimens, the creep strains of all of the SCC mixtures were less than those of CVC concretes (Kavanaugh 2008). Shrinkage strains in the SCC mixtures were found to be similar in magnitude to the shrinkage strains of the CVC mixtures (Kavanaugh 2008).

The various creep and shrinkage prediction models used in this study have been used in past studies to determine which methods are most accurate in predicting long-term strain changes in both high-performance CVC and SCC concretes. Levy et al. (2010) found that ACI 209 and AASHTO long-term creep and shrinkage predictions of SCC mixtures including slag cement as a supplementary cementing material (SCM) were much larger than measured values. The same result was found for high-strength SCC mixtures (Levy et al. 2010) with slag cement or fly ash as SCMs. Kavanaugh (2008) concurred with Levy about the ACI 209 prediction model, concluding that it could not accurately predict the creep strain of high-strength concrete. Levy et al. (2010) concluded that the AASHTO 2010 model provided better shrinkage strain predictions than AASHTO 2004 predictions, but the creep predictions were very similar. Kavanaugh (2008)

concluded that the AASHTO 2010 method overestimated creep in accelerated-cured concrete. The MC 90 was found to be the most accurate model to predict creep strains for both CVC and SCC mixtures (Kavanaugh 2008). However, the MC 90 models evaluated were updated in 1999, and comparisons were not made to the newer models.

2.6 Summary

The AASHTO 2010 Bridge Design Specification allows for the use of many different prediction models to develop predictions for creep and shrinkage strains. These predictions are used to develop predicted time-dependent deformations including camber and prestress losses. While various studies have sought to determine which of these prediction models produces the most accurate predictions, the results of these studies are largely inconclusive. Many of the models do not provide predictions that correspond to measured deformations in full-scale girders. Therefore, the research described below seeks to compare predicted time-dependent deformations to actual measured deformations in large, full-scale girders manufactured using SCC and CVC concrete.

Chapter 3 Design and Construction of Experimental Specimens

3.1 Introduction

The girders used in this research were fabricated in the fall of 2010 at Hanson Pipe and Precast in Pelham, Alabama. All twenty-eight girders were PCI Bulb-Tee girders. Spans 1 and 4 contained seven BT-54 girders 97 ft 10 in. in length and spans 2 and 3 contained seven BT-72 girders 134 ft 2 in. in length. Two different types of concrete were used to manufacture these girders. The girders in spans 1 and 2 were cast using a self-consolidating concrete (SCC) while the girders in spans 3 and 4 were cast using a conventionally vibrated concrete (CVC). Details concerning both the design and fabrication of all twenty-eight girders are discussed below.

3.2 Specimen Identification

A specimen identification scheme was developed for this project by Dunham (2011), and adapted for use in this report. Figure 3-1 illustrates the specimen identification scheme used in this project. This scheme was adapted from the precast concrete producer's numbering scheme in order to more readily relate information about the girder being identified. By adapting an identification scheme similar to the precast concrete producer's identification scheme, researchers and the workers at the precast concrete plant were able to communicate efficiently.

In addition to labeling each specific girder with a unique number, it was necessary to group girders according to their casting group. For the 54 in. girders, three girders were able to be cast on the same casting line, while only two 72 in. girders could be cast on the same line. Table 3-1 groups the specific girders into casting groups, which aids in reporting the properties

of the concrete used in each girder. The girders in each casting group were all cast on the same day.

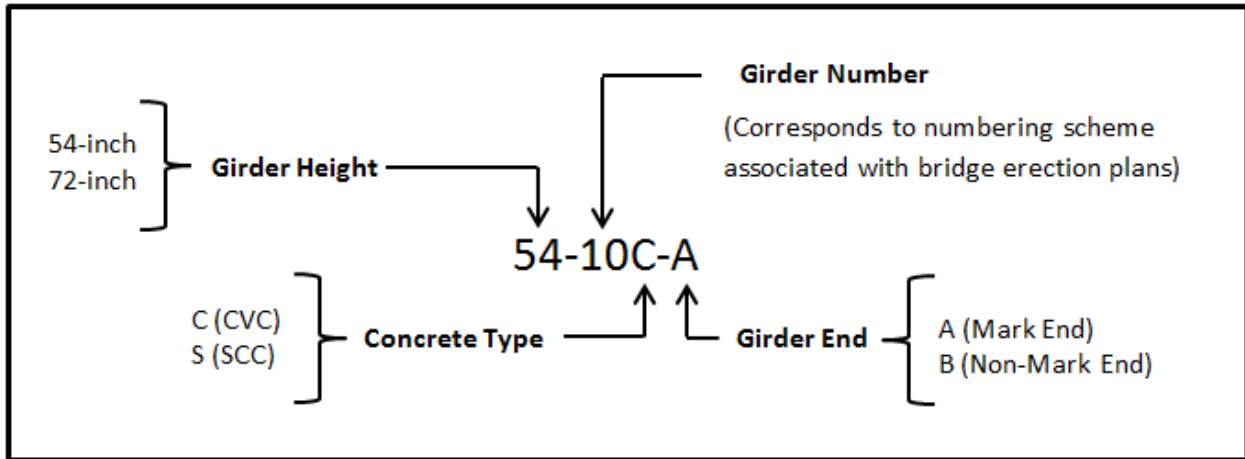


Figure 3-1: Girder Identification Scheme (Dunham 2011)

Two different PCI Bulb-Tee sections were used in this project, half of the girders had heights of 54 in. and the other half had heights of 72 in. The specimen heights are the first number in the specimen identification scheme. The girder number corresponds to the numbering system set forth on the bridge erection plan. The girder numbers range from 1 to 14. The letter immediately following the girder number indicates the type of concrete used in the girder. Girders 1 through 7 of the 54 in. and 72 in. girders were cast using SCC. Girders 8 through 14 of both the 54 in. and 72 in. girders were cast using CVC. Finally, the last letter in the identification scheme indicates which end of the girder is being referred to. The mark end refers to a specific end of the girder upon which the manufacturer marked its own information after the girders were cast. The mark end of all twenty-eight girders was the east end of the girder when it was on the casting line and was the southwest end of the girder when it was placed in the bridge.

Table 3-1: Casting Group Designations

Casting Group	Girders
A	54-2S 54-5S 54-6S
B	54-9C 54-10C 54-13C
C	54-1S 54-3S 54-4S
D	54-11C 54-12C 54-14C
E	54-7S 54-8C
F	72-1S 72-7S
G	72-8C 72-14C
H	72-3S 72-4S
I	72-10C 72-13C
J	72-2S 72-5S
K	72-11C 72-12C
L	72-6S 72-9C

3.3 Specimen Design

Two different sizes of PCI Bulb-Tee girders were used for this bridge because of the different span lengths. Span 1 and Span 4 of the bridge each used seven girders that were BT-54 sections 97 ft 10 in. in length. The cross-sectional dimensions of a BT-54 section can be seen in Figure 3-2. Span 2 and Span 3 also used seven girders each, but they were BT-72 sections 134 ft 2 in. in length. The cross-sectional dimensions for a BT-72 section can be seen in Figure 3-3. The bridge incorporated a 15 degree skew to provide proper alignment for the approaches to the bridge; this resulted in all twenty-eight girders being fabricated with a 15 degree skew.

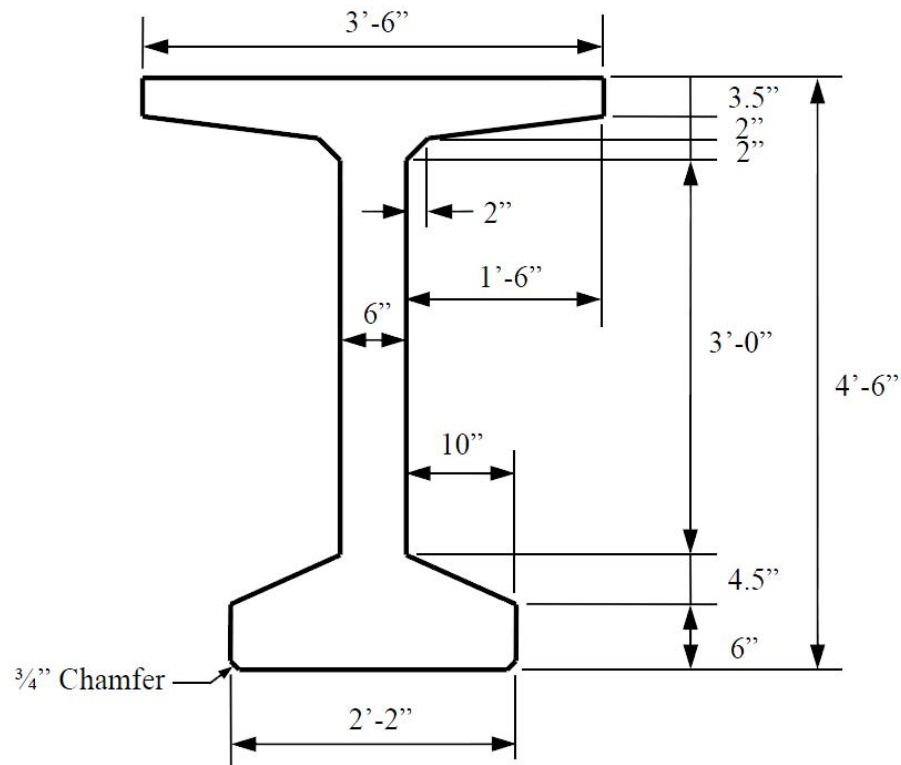


Figure 3-2: BT-54 Cross Section

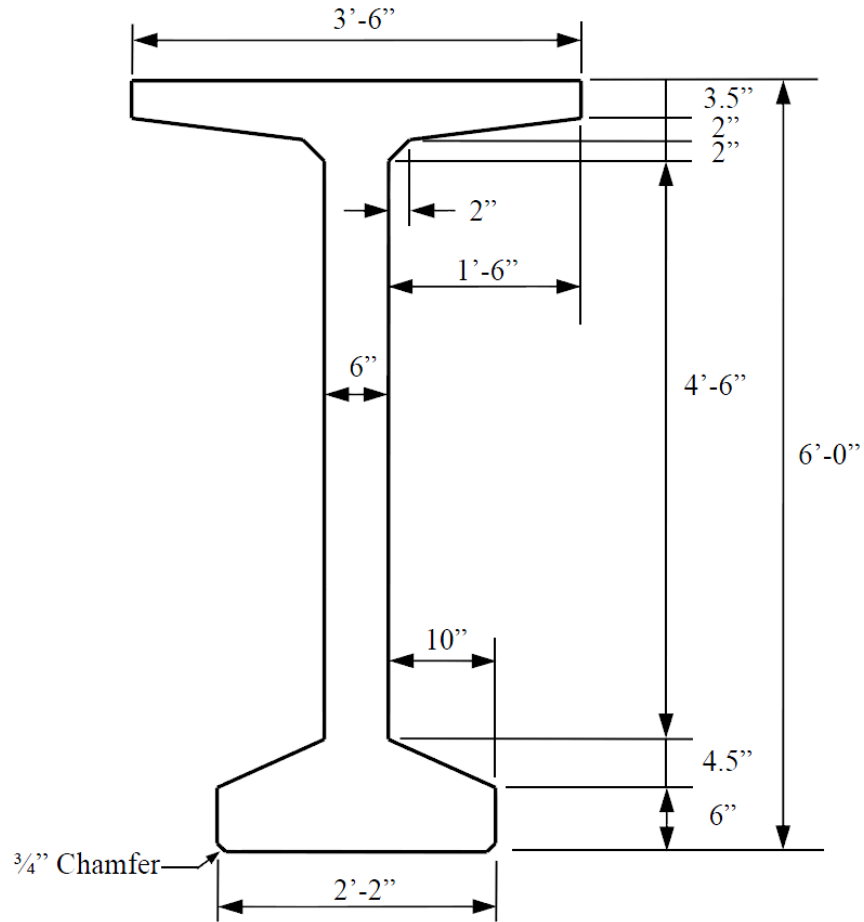


Figure 3-3: BT-72 Cross Section

3.3.1 Strand Arrangement

Two different strand arrangements were used for the girders depending on the section size. Seven-wire, Grade 270, low-relaxation, 1/2 -inch diameter strands were used in the BT-54 girders. Seven-wire, Grade 270, low-relaxation, 1/2 -inch “special” diameter strands were used in the BT-72 girders. The specified jacking stress (f_{pj}) was 202.5 ksi for the bottom strands and draped strands and 32.7 ksi for the lightly tensioned top strands in all of the girders. A two-point draping configuration was used in both the BT-54 girders and BT-72 girders as shown in Figures 3-4 and 3-5.

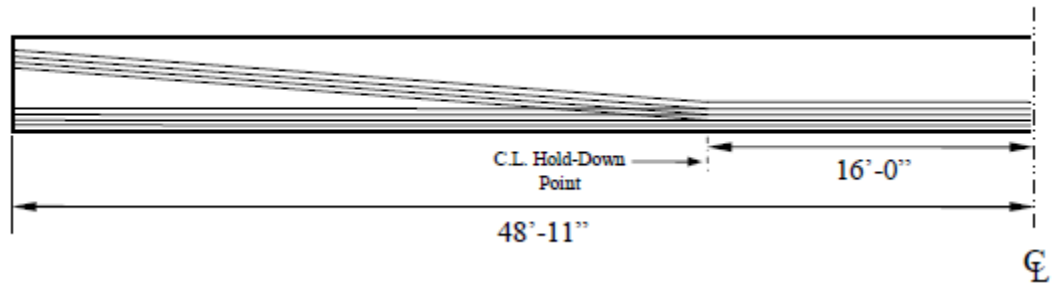


Figure 3-4: Profile and Hold-Down of Draped Strands for the BT-54 Girders

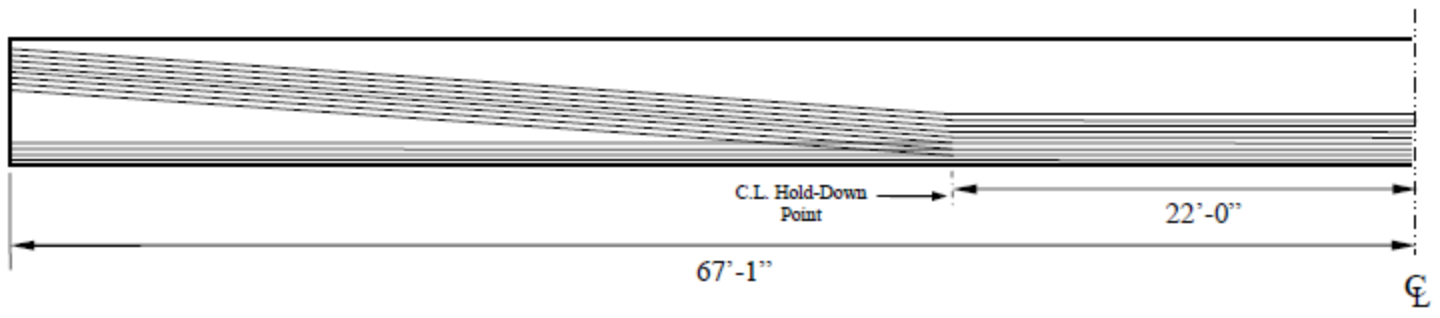


Figure 3-5: Profile and Hold-Down of Draped Strands for the BT-72 Girders

The BT-54 girders contained forty strands including twenty-eight ½ -inch diameter strands in the bottom of the section, eight ½ -inch diameter strands draped along the length of the member, and four ½ -inch diameter lightly tensioned strands in the top of the member. The strands in the bottom of the section as well as the draped strands were tensioned to 30,980 pounds each while the lightly tensioned top strands were tensioned to 5,000 pounds each. The locations of each strand in the BT-54 members at midspan are shown in Figure 3-6 and the locations at the ends of each section are shown in Figure 3-7.

The BT-72 girders contained 50 strands including twenty eight ½ -inch “special” diameter strands in the bottom of the section, eighteen ½ -inch “special” diameter strands draped along the member, and four ½ -inch diameter lightly tensioned strands. The bottom strands and draped strands were tensioned to 33,800 pounds each while the top strands were tensioned to 5,000 pounds each. The locations of the strands at both midspan and the end of the section are illustrated in Figure 3-8 and Figure 3-9.

Figures 3-7 and 3-9 indicate the presence of debonded strands in the girder ends of both the BT-54 girders and the BT-72 girders. The debonding of strands was accomplished by encasing the strand in plastic casing and sealing it with tape. This was done for four strands in the BT-54 girders and six strands for the BT-72 girders for 10 feet from each girder end.

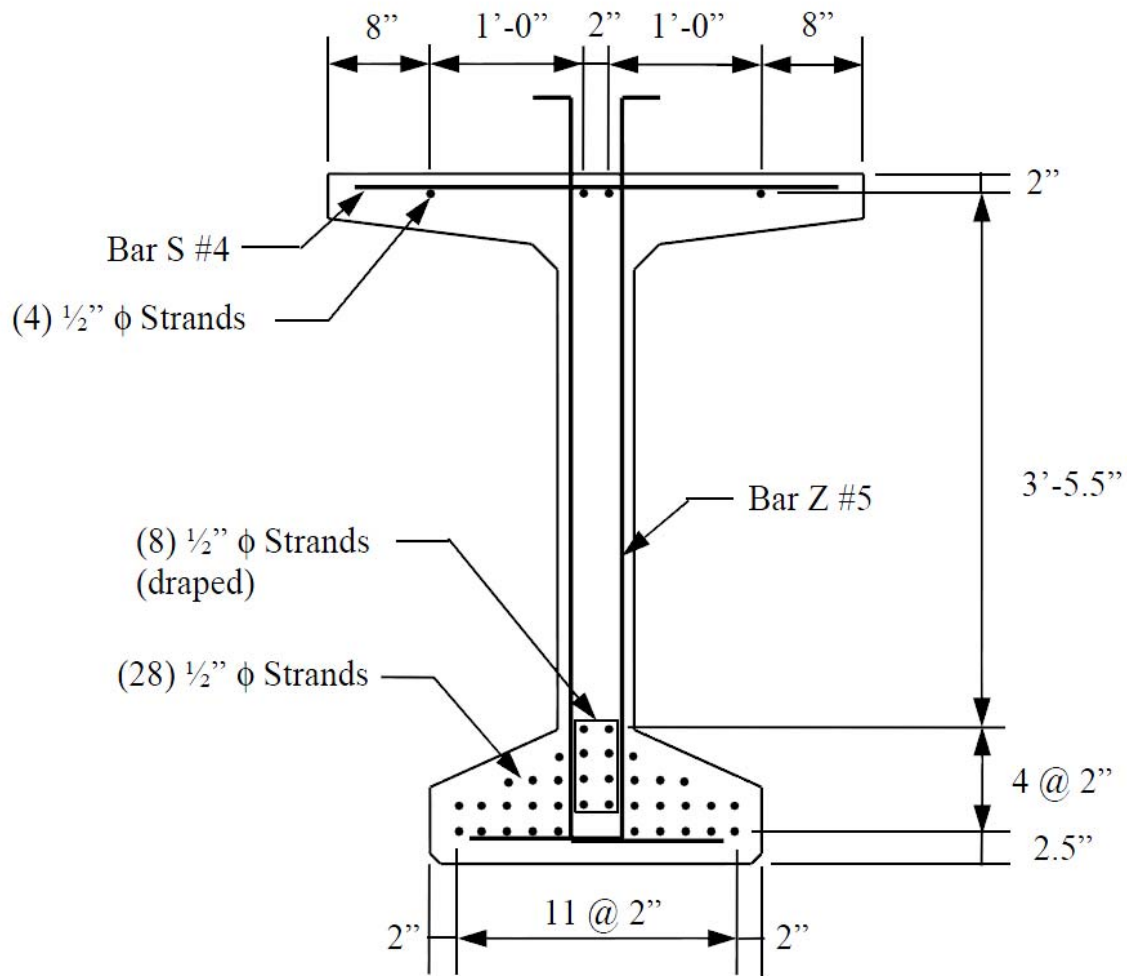


Figure 3-6: Mild Steel and Strand Arrangement for BT-54 Girder at Midspan

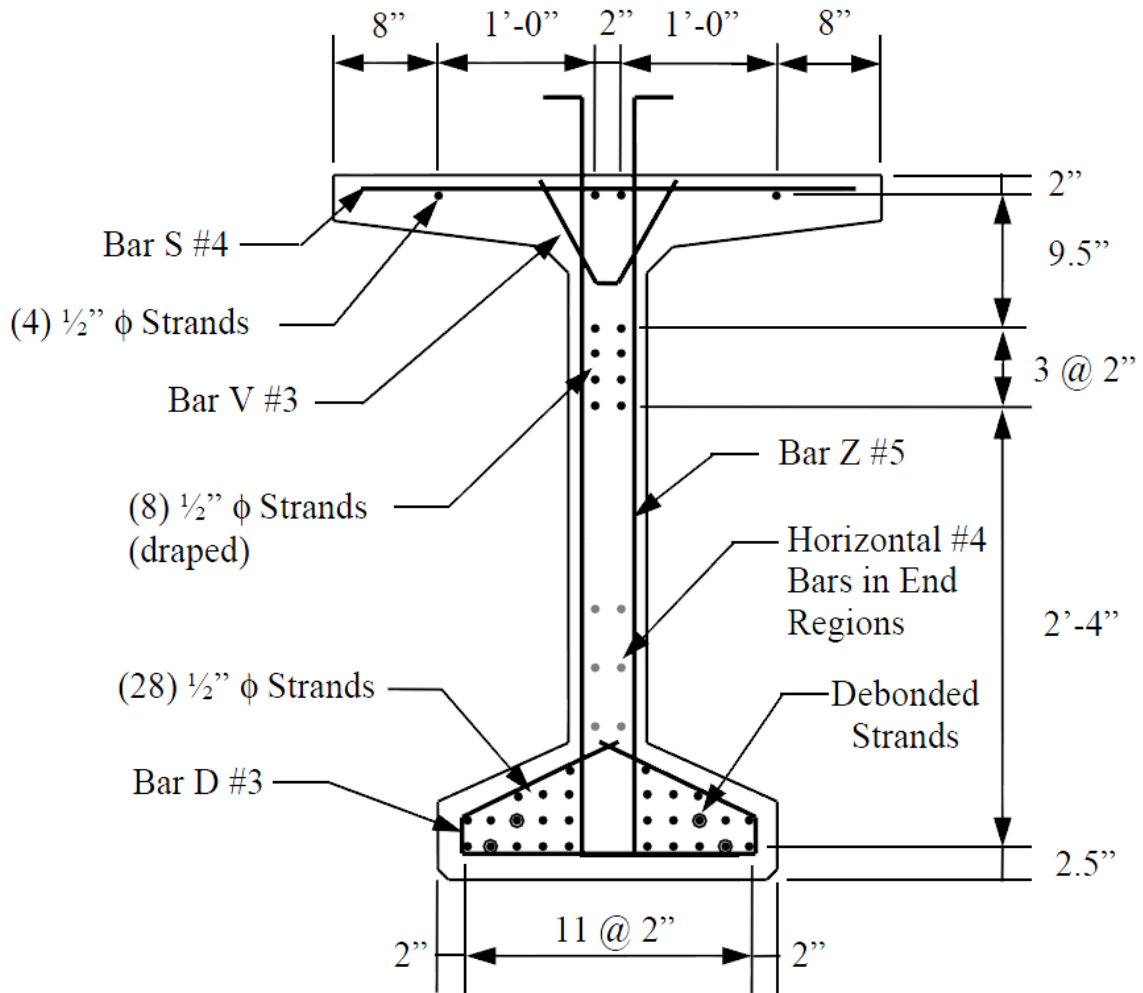


Figure 3-7: Mild Steel and Strand Arrangement for BT-54 Girder at End of Span

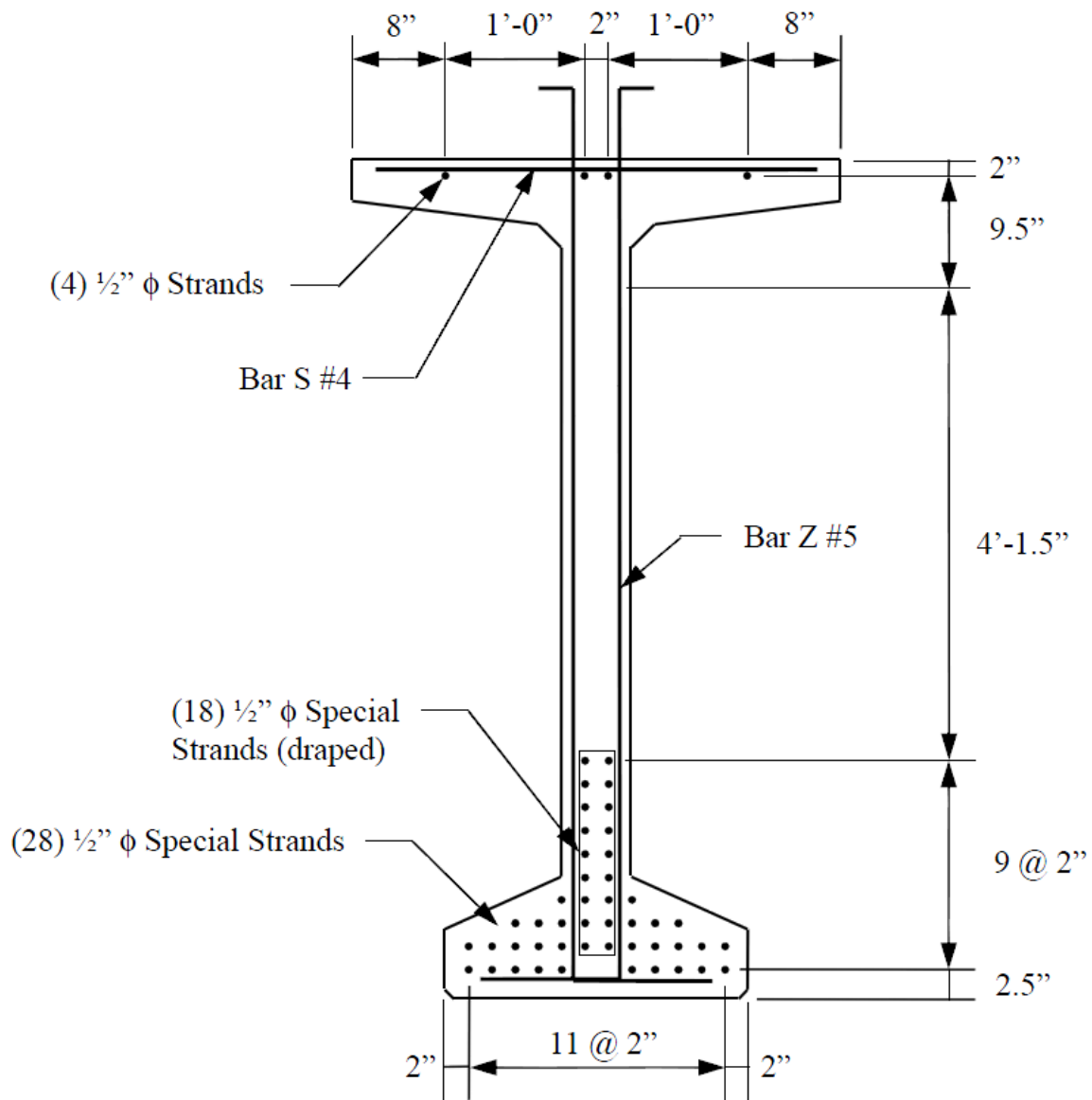


Figure 3-8: Mild Steel and Strand Arrangement for BT-72 Girder at Midspan

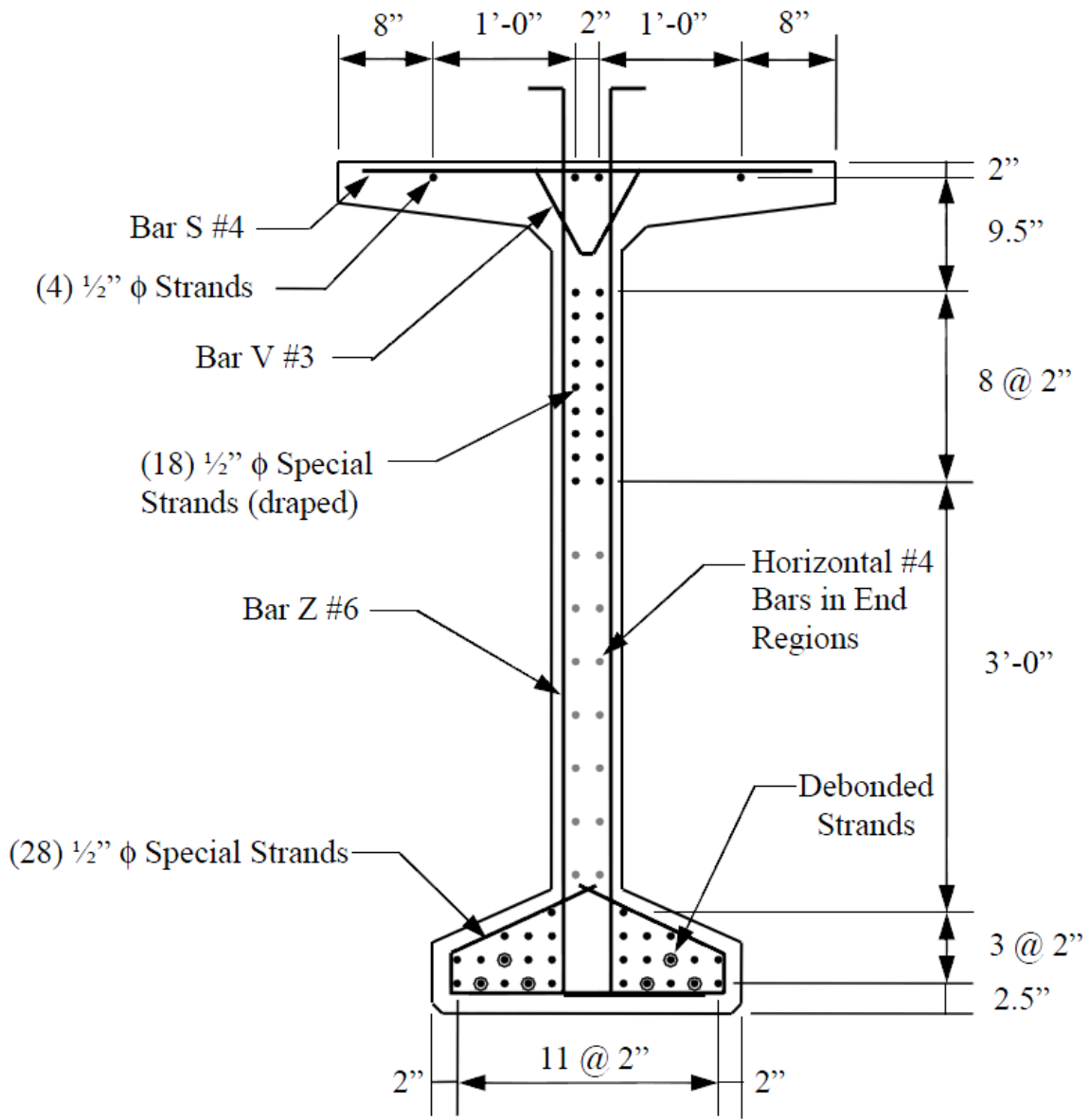


Figure 3-9: Mild Steel and Strand Arrangement for BT-72 Girder at End of Span

3.3.2 Nonprestressed Reinforcement Arrangement

Nonprestressed reinforcement was needed in the girders to resist shear forces over the girder length as well as anchorage zone forces in the girder ends. The configuration of the mild steel reinforcement in the girders is depicted in Figure 3-5 through Figure 3-8. The four different bar shapes used in both the BT-54 girders and BT-72 girders include Z-bars, bottom steel confinement bars (D-bars), straight bars (S-bars), and V-bars. Bar spacing along the girder length changed for the BT-54 girders as compared to the bar spacing for the BT-72 girders, as illustrated in Figure 3-10 and 3-11.

At the girder ends, additional horizontal reinforcement in the form of S-bars was required in both the BT-54 and BT-72 girders. The vertical locations of these horizontal bars are shown in Figure 3-7 and Figure 3-9, and their location along the span of the girders is shown in Figure 3-10 and Figure 3-11. It should also be noted that the nonprestressed reinforcement was heavily concentrated at the girder ends. This was due to both the higher shear forces at the ends of the simply-supported girders as well as the spalling and bursting stresses in the girder ends due to the anchorage of the prestressing strands. The bottom steel confinement bars (D-bars) and V-bars were only located at the girder ends, none were required along the girder length closer to midspan.

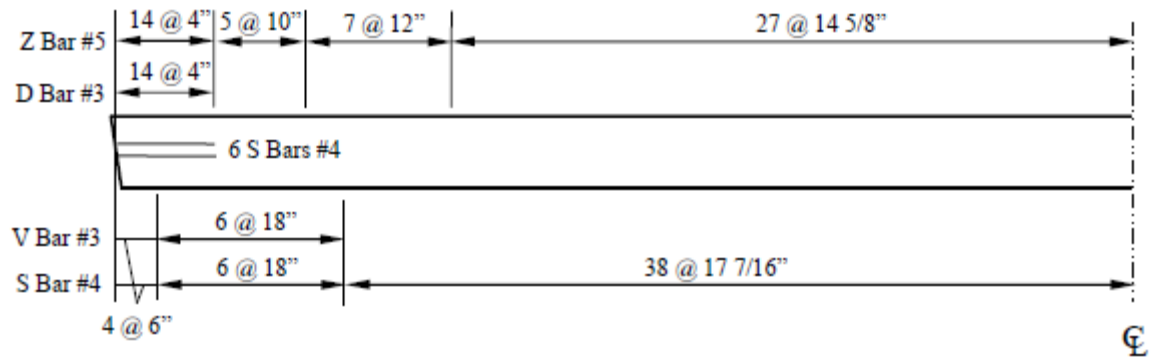


Figure 3-10: Mild Steel Spacing in BT-54 Girders

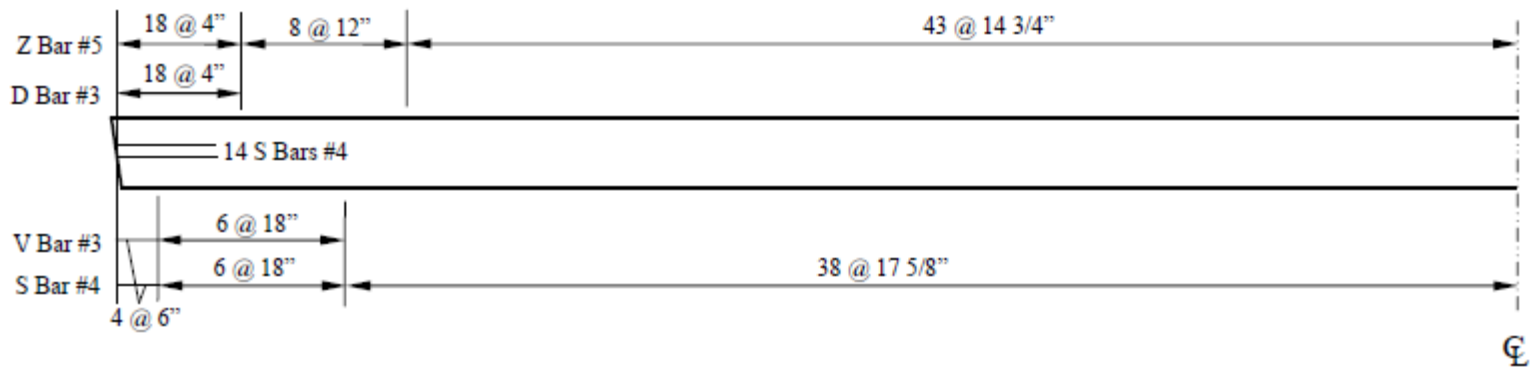


Figure 3-11: Mild Steel Spacing in BT-72 Girders

3.4 Material Properties

The materials used to construct the bulb tee girders included conventionally vibrated concrete, self-consolidating concrete, prestressing strand, and nonprestressed reinforcement. The material properties for all of these materials are discussed below.

3.4.1 Concrete

One of the main goals for this research project was the direct comparison of the performance of precast, prestressed bridge girders fabricated with conventionally vibrated concrete (CVC) to the performance of those fabricated with self-consolidating concrete (SCC). Therefore, two different concrete mixtures were used in the girders in this project. All concrete used in the girders was mixed on site at the Hanson Pipe & Precast prestressing plant in Pelham, AL. Both mixtures utilized Type III portland cement as well as slag cement. Chemical admixtures were necessary to achieve the desired concrete properties in both mixes. These chemical admixtures included an air-entraining admixture (Darex AEA EH), a high-range water-reducing admixture (ADVA Cast 575), a viscosity-modifying admixture (V-Mar 3), and a hydration-stabilizing mixture (Recover). All admixtures were supplied by W.R. Grace.

There are two key differences between the CVC and SCC mixtures. First, the amount and type of admixtures used in each mixture had to be different to bring about the desired properties for each mixture. Second, the SCC mixture used #78 limestone as coarse aggregate whereas the CVC mixture utilized #67 limestone as coarse aggregate. Third, the sand-to-total aggregate ratio for the SCC was much higher than that of the CVC. The components used in each mixture are summarized in Table 3-2.

Table 3-2: Summary of Concrete Mixtures

Item	BT-54		BT-72	
	SCC	CVC	SCC	CVC
Water Content (pcy)	266	238	265	234
Cement Content (pcy)	758	696	760	708
GGBF Slag Content (pcy)	134	124	135	125
w/cm	0.30	0.29	0.30	0.28
SSD Coarse Agg. #78 (pcy)	1528	0	1550	0
SSD Coarse Agg. #67 (pcy)	0	1923	0	1950
SSD Fine Agg. (pcy)	1384	1163	1370	1179
s/agg (by weight)	0.48	0.38	0.47	0.38
Air-Entraining Admixture (oz/cy)	0.3	0.3	0.2	0.2
HRWR Admixture (oz/cy)	11	8	11	7
Viscosity-Modifying Admixture (oz/cy)	2	0	4	0
Hydration-Stabilizing Admixture (oz/cy)	2	1	2	1
Total Air Content (%)*	4.1	4.2	4	3.2

*Average of air content determined from fresh test results.

During the casting process fresh concrete samples were taken in order to determine various fresh properties of the concrete mixtures. The first sample was taken from the first batch of concrete that was to be placed in the girder. The second sample was taken from a batch close to the halfway point of concrete casting for that mixture for that day. The third and final sample was taken towards then end of casting of that mixture for that day. These samples were all taken from the concrete trucks just after mixing. This was done to ensure that the concrete mixture maintained consistent properties throughout the casting process. For the CVC mixture, the fresh properties tested included the slump, air content, and unit weight of the concrete. The SCC mixtures were tested to determine their slump flow, air content, unit weight, visual stability index (VSI), and the T-50 test result. The values reported in Table 3-3 were determined by Auburn University researchers, but these values were not used in determining whether or not a

specific batch of concrete was suitable for placement in the girder. ALDOT inspectors performed their own fresh tests to determine if the concrete mixture was acceptable according to the project specifications.

In addition to fresh tests, concrete cylinders were made by Auburn University researchers to determine hardened concrete properties for each casting group. The 6-inch by 12-inch cylinders were steam-cured alongside the girders under the curing tarp. The cylinders were tested at specific ages in order to determine the concrete strength and modulus of elasticity at those ages. The strength testing was done according to ASTM C 39 (2005) and the modulus of elasticity was found according to ASTM C 469 (2002). The averaged results for both strength and modulus of elasticity as well as the number of hours that elapsed between concrete placement and the prestressing strand release are summarized in Table 3-4.

Table 3-3: Fresh Concrete Properties

Casting Group	Sample No.	Unit Weight (lb/ft³)	Slump (in.)	Slump Flow (in.)	Air (%)	T50 (sec.)	VSI
A	1	149.1	-	28.0	3.3	-	1.5
	2	-	-	27.5	4.4	-	1.0
	3	-	-	26.0	4.5	-	1.0
B	1	152.3	9.00	-	3.9	-	-
	2	153.2	10.00	-	4.0	-	-
	3	-	8.75	-	4.0	-	-
C	1	-	-	27.0	2.6	7	1.0
	2	-	-	26.0	3.0	6	1.0
	3	-	-	27.0	4.6	8	1.0
D	1	-	8.50	-	4.2	-	-
	2	-	9.00	-	4.5	-	-
	3	-	8.75	-	4.4	-	-
E (SCC)	1	-	-	26.0	5.5	7	1.5
	2	-	-	26.0	4.2	8	1.5
E (CVC)	1	-	9.00	-	4.5	-	-
	2	-	8.75	-	3.9	-	-
F	1	150.1	-	25.0	3.7	10	0.0
	2	-	-	23.0	4.5	10	0.0
	3	-	-	24.0	3.8	11	0.0
G	1	-	8.50	-	4.0	-	-
	2	-	9.00	-	4.3	-	-
	3	-	8.75	-	3.5	-	-
H	1	-	-	26.0	3.3	8	1.0
	2	-	-	26.0	4.3	9	0.0
	3	-	-	23.0	4.8	14	0.0
I	1	-	9.00	-	3.1	-	-
	2	-	9.00	-	2.5	-	-
	3	-	9.25	-	3.1	-	-
J	1	149.8	-	22.5	4.2	9	1.0
	2	-	-	24.0	3.7	10	1.0
	3	-	-	22.0	3.8	15	1.0
K	1	153.4	8.50	-	3.6	-	-
	2	-	9.00	-	3.1	-	-
	3	-	9.00	-	3.5	-	-
L (SCC)	1	148.1	-	26.0	3.8	7	1.0
	2	-	-	28.0	3.7	5	1.5
L (CVC)	1	153.3	9.00	-	2.2	-	-
	2	-	8.25	-	3.2	-	-

Table 3-4: Hardened Concrete Properties

Casting Group	Release			28 Days	
	Age (hrs)	f' _{ci} (psi)	E _{ci} (ksi)	f' _c (psi)	E _c (ksi)
A (SCC)	24	9010	6200	10240	6400
B (CVC)	23	8790	7100	10590	7400
C (SCC)	24	8680	6300	10800	6600
D (CVC)	24	7860	6700	9670	6900
E (SCC)	24	7940	6100	10180	6200
E (CVC)	25	8760	6400	10360	6800
Specified BT-54	-	5200	-	6000	-
F (SCC)	24	8120	5800	10490	6300
G (CVC)	23	8290	6700	10770	7000
H (SCC)	19	7860	5900	10770	6400
I (CVC)	22	8770	7100	10850	7300
J (SCC)	22	8220	5800	10550	6400
K (CVC)	20	8320	6800	11050	7700
L (SCC)	19	6930	5700	10070	6000
L (CVC)	20	7710	6600	10510	6900
Specified BT-72	-	5800	-	8000	-

3.4.2 Prestressing Strand

As mentioned earlier, the prestressing strand used in this project was low-relaxation, Grade 270, seven-wire strand. The strand used in the BT-54 sections was ½-inch diameter strand provided by Strand-Tech Martin, Inc. from Summerville, South Carolina. The BT-72 girders used ½-inch “special” strand provided by American Spring Wire from Houston, Texas. Prior to being used in the girders, the strand was stored outdoors in accordance with standard ALDOT procedure. As evident in Figure 3-12, the prestressing strand exhibited slight weathering effects.



Figure 3-12: Prestressing Wire Surface Condition

Prior to girder fabrication, strand pull-out testing was performed on samples of the strand that would be used in the project. This testing was done to ensure that the bond between the concrete and strand would be adequate but not excessively strong. The pull-out tests were performed on September 14, 2010 at Hanson Pipe and Precast in Pelham, Alabama. The bond quality of both the ½-inch and ½-inch “special” strands was found to be adequate, as reported in Dunham (2011, Appendix C).

3.4.3 Nonprestressed Steel Reinforcement

Nonprestressed steel reinforcement was used in the girders to reinforce against shear forces and anchorage zone forces. ASTM A615 Grade 60 steel was used. Figures 3-6 through 3-

9 show the shape and locations of the nonprestressed reinforcement and Figures 3-10 and 3-11 show the spacings along the girder for this reinforcement.

3.5 Specimen Fabrication

This section will detail the fabrication process used in making the twenty-eight prestressed, precast girders for the bridge on State Route 22 over Hillabee Creek. There are some key differences in the way that the girders fabricated with CVC were made versus those that were made using SCC. The process for making BT-54 girders is very similar to that for making BT-72 girders, and that process is detailed below.

3.5.1 Casting Configuration

Two adjacent casting lines were utilized at the plant for to help complete fabrication more efficiently. The BT-54 sections were 97 ft 10 in. in length, and therefore could be cast with three girders on the same line at the same time, as shown in Figure 3-13. Casting began on September 21, 2010 with the first three SCC girders and then alternated between CVC and SCC girders. Four total castings were performed with three BT-54 girders each to yield twelve girders. On the last day of casting the BT-54 girders, only two were cast on the line as shown in Figure 3-14. This pair consisted of a CVC girder and an SCC girder, with the CVC being cast first so that the vibration during placement wouldn't affect the fresh SCC. All of the BT-54 girders were completed before work began on the BT-72 girders.



Figure 3-13: Casting Configuration of Three BT-54 Girders



Figure 3-14: Casting Configuration of Two BT-54 Girders

The BT-72 girders were 134 ft 2in. in length, and so only two could be cast on the same casting line at one time. Figure 3-15 depicts the casting line for the BT-72 girders. The casting for the BT-72 girders began on October 14, 2010 with the casting of two SCC girders. Pairs of SCC and CVC girders were cast alternating between the types of concrete, which was similar to the process used for the BT-54 girders. On the final day of casting for the BT-72 girders, which was October 28, 2010, one CVC girder and one SCC girder were cast on the same line, again placing the CVC first to avoid vibrating the SCC.

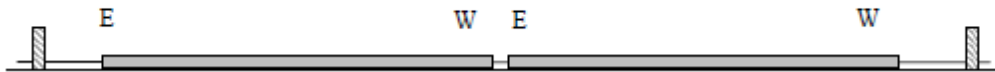


Figure 3-15: Casting Configuration of BT-72 Girders

3.5.2 Fabrication of Precast, Prestressed Bridge Girders

The test specimens used in this project were designed and built to be used in an actual bridge on State Route 22 over Hillabee Creek near Alexander City, Alabama. Care had to be taken to ensure that experimental testing equipment and procedures did not interfere with the standard plant operations during fabrication. While some standard procedures did have to be altered in small ways, these alterations were deemed to be acceptable and to not have any adverse effects on girder performance.

The first step in the process involved aligning and cleaning the casting bed. Next, wooden headers with holes for the prestressing strands were placed on the casting lines to form the girder

ends so that the girders would be the correct length. Hold-down anchors used for the draped strands were positioned and secured to the casting bed. Hold-up anchors were located in a lowered position so that after the strands were tensioned, they could be raised up to drape the strands. Strands were then pulled through all of the headers and hold-up/down anchors.

After all of the strands were positioned properly, they were tensioned to a specified jacking stress using a hydraulic jack and checked according to ALDOT standards for the proper tension and elongation. The strands were partially stressed at first in order to straighten them and detect potential flaws. Once it was determined that the strand did not have any major flaws, the full jacking stress was imparted to the strand. Once all of the strands were properly tensioned, the hold-up anchors were raised to the correct elevation for draping using a crane. After tensioning the strands, insulating foam was applied on the outside holes in the wooden headers through which the strands had been run in order to prevent concrete and bleed water from leaking out of the formwork.

At the ends of each girder some strands were designed to be debonded for a length of 10 feet. Figure 3-7 shows that four total strands would be debonded at the ends of the BT-54 girders and Figure 3-9 shows that six total strands would be debonded at the ends of the BT-72 girders. Debonding was achieved by securing a plastic sheath around the specific strands as shown in Figure 3-16. The plastic sheath prevented the concrete from coming into contact with the strand and bonding to it.



Figure 3-16: Strand Debonding

After the prestressing strands were positioned and tensioned, the mild steel reinforcement discussed in section 3.3.2 above was tied into place. The pre-bent reinforcing bars were secured to the prestressing strands with wire ties at the specified locations and spacing. Once the nonprestressed steel was securely in place, the vibrating-wire strain gauges (VWSGs) that were used in each girder were installed by Auburn University researchers. The gauges were installed at midspan or at quarterspan of the girders using wire ties, zip-ties, and in some cases small pieces of reinforcing bar for proper alignment. This process is discussed in detail in the next chapter.

The final preparations before concrete placement could begin included applying form release agent to the bottom of the casting bed. Care had to be taken to avoid getting the release agent on the prestressing strands, as this would compromise their bond to the concrete and have detrimental effects to the performance of the girder. The release agent was also sprayed onto the side forms before they were installed. The side forms were then put into place and secured, again making sure that the release agent did not come into contact with any of the prestressing strand or nonprestressed reinforcement. Figure 3-17 depicts the installation of a side form. Cables

connecting the VWSGs to the data acquisition system had to be run over the top of the side forms, and behind the vibrator tracks located on the outside of the side forms. This was done to ensure that the VWSG cables would not interfere with or be damaged by the vibration of the CVC.



Figure 3-17: Side Form Installation

All concrete used in the girders was batched on site at the plant. Specialized concrete delivery trucks with a 4 yd³ capacity transported concrete from the mixing tower to the casting

line. The concrete was placed in the girder forms from the trucks through the use of an auger-driven chute attached to the front of the truck, as seen in Figure 3-18. Throughout the casting process each day, trucks would be stopped periodically to perform tests on the fresh concrete, the results of which are discussed in section 3.4.1. The same trucks would also be stopped to obtain concrete samples to use in making test cylinders to determine hardened concrete properties. These samples were taken from the trucks after they had discharged roughly half of their concrete into the girder.



Figure 3-18: Concrete Delivery Truck

The process used to place the CVC was different than the process used to place the SCC because of the physical differences in the fresh concrete. To place the CVC, the delivery trucks positioned the chute over the girder starting at one end of the girder and discharged enough

concrete to fill up the bottom bulb and web of the girder in that area before moving down the girder a few feet and discharging more concrete. The CVC was not able to flow through the reinforcement, causing the trucks to have to discharge concrete every few feet along the girder. Then a second truck would come behind the first one and fill the top flange with concrete. The placement began at one end of the girder and progressed down to the other end.

As the forms were filled with concrete, vibration needed to be introduced to the concrete in order to adequately consolidate the CVC. Internal and external vibration techniques were used. Figure 3-19 shows the internal vibration applied by a worker walking along the top of the formwork. Figure 3-20 shows the external vibrator in a track on the side of the formwork as concrete is being placed in the girder.



Figure 3-19: Internal Vibration used in CVC Placement



Figure 3-20: External Vibration

For girders that were made with the SCC, the concrete placement process was more simple than the CVC placement process. The placement of SCC did not involve as many laborers because it did not require any external or internal vibration. When the delivery trucks placed the concrete into the forms, it flowed easily around the reinforcement. This allowed the delivery trucks to not be as precise as to where they placed the concrete because the SCC would simply flow around the reinforcement and level itself.

There were two casting days in which both a CVC girder and an SCC girder were cast on the same line. When this was done, the CVC was always placed first. This was due to the internal and external vibration that was necessary in the CVC placement process. Placement of the SCC only began after all of the vibration of the CVC had been completed so as to avoid adversely affecting the SCC with external vibration.

Once a girder was completely filled with concrete, and all vibration had been completed in the case of the CVC girders, the top surface of each girder was roughened by the use of a wire

rake. In the case of the SCC girders, the top surface was roughened using the wire rake after some time was allowed to pass so that the SCC would stay in a roughened state as opposed to consolidating back down into a smooth top surface. Figure 3-21 shows the surface roughening process. After surface roughening had been accomplished in accordance with ALDOT specifications, metal deck clips and overhang brackets were installed on the top flanges of the girder by inserting them into the fresh concrete. These accessories would be used later to facilitate installation of formwork for the bridge deck. As the deck clips and overhang brackets were being installed, steel bolts were inserted into the tops of the girders as part of the camber measurement system discussed in detail in the next chapter. Figure 3-22 shows one of these bolts installed in the girder and illustrates the surface roughness of an SCC girder.



Figure 3-21: Surface Roughening of SCC Bridge Girders



Figure 3-22: Camber Measurement Marker

After the top of the girder was roughened and the accessories and camber measurement bolts had been installed, a curing blanket and protective tarp were prepared to cover the girders during curing. Prior to the blanket and tarp covering, the concrete cylinders that had been prepared from the concrete used in the girders were placed beside the formwork for the girders so that they would be subjected to the same steam curing as the girders. Once the cylinders were positioned, the curing blanket and tarp were pulled over the formwork by the use of a crane as seen in Figure 3-23. The curing blanket and tarp remained on the girders for one night and were removed the following morning.



Figure 3-23: Curing Blanket and Tarp Covering

The morning after concrete placement, the curing blanket and protective tarp were removed from the formwork and the forms were stripped off of the sides of the girders. Care was taken to disconnect the VWSG cables from the data acquisition system while the forms were being stripped because the wires had been run underneath the vibrator track on the forms. Once the forms had been removed, the gauges were reconnected in order to collect data before and during prestress transfer.

Some cracking in the girders occurred after the removal of the formwork prior to prestress transfer. The girders had two or three cracks that ran from the top surface down to the web. There did not seem to be any difference between CVC or SCC girders in the cracking pattern or number of cracks. In Figure 3-24, a typical crack that has been highlighted by marker ink can be seen. Cracks were widest at the top of the girder. The width of this crack (in a CVC girder) can be seen in Figure 3-25. Most of the cracks were approximately 0.02 in. wide, with the

largest crack 0.04 in. wide. The cracks closed during prestress transfer. Some possible reasons for why these cracks developed as well as their possible influence on the research for this project are discussed in Chapter 6.



Figure 3-24: Crack in BT-54 Girder Prior to Prestress Transfer

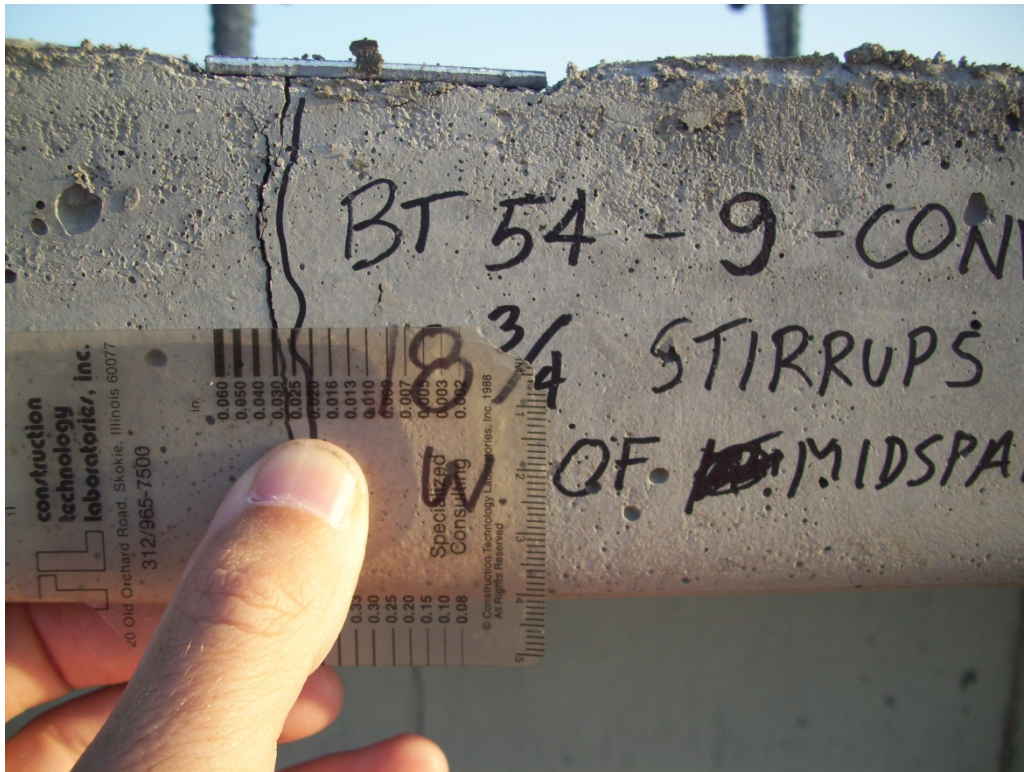


Figure 3-25: Crack Width in BT-54 Girder Prior to Prestress Transfer

After the forms were stripped, installation of the tensioned-wire camber measurement system began. This camber measurement system is discussed in detail in the next chapter. After the tensioned-wire system was installed, baseline readings were taken. Baseline readings were also taken using the surveying camber measurement system.

As the camber baseline readings were taken, concrete cylinders that had been steam-cured alongside of the girders were tested in order to verify that the girder concrete had reached the minimum strength required to transfer the prestress force through strand release. Releasing the strands was accomplished by cutting them with oxyacetylene torches. Flame-cutting the strands required a worker at each end of the casting line as well as between each girder. The strands and hold-downs were cut in a specific order. Each individual strand was cut by each worker with the torch before moving on to the next strand. First, the bottom-most outside strands were cut. Next, the top strands were cut. These were followed by the draped strands. Finally, the

remaining strands in the bottom flange were cut. Figure 3-26 shows the flame-cutting sequence for the BT-54 girders and Figure 3-27 shows the flame-cutting sequence for the BT-72 girders.

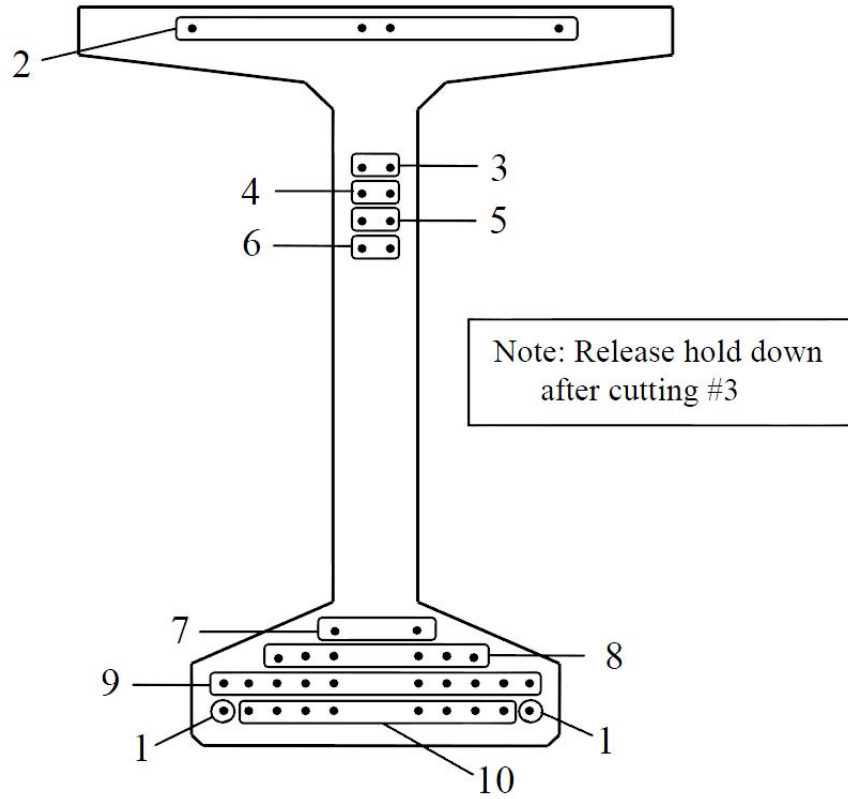


Figure 3-26: Flame-Cutting Sequence for BT-54 Girders

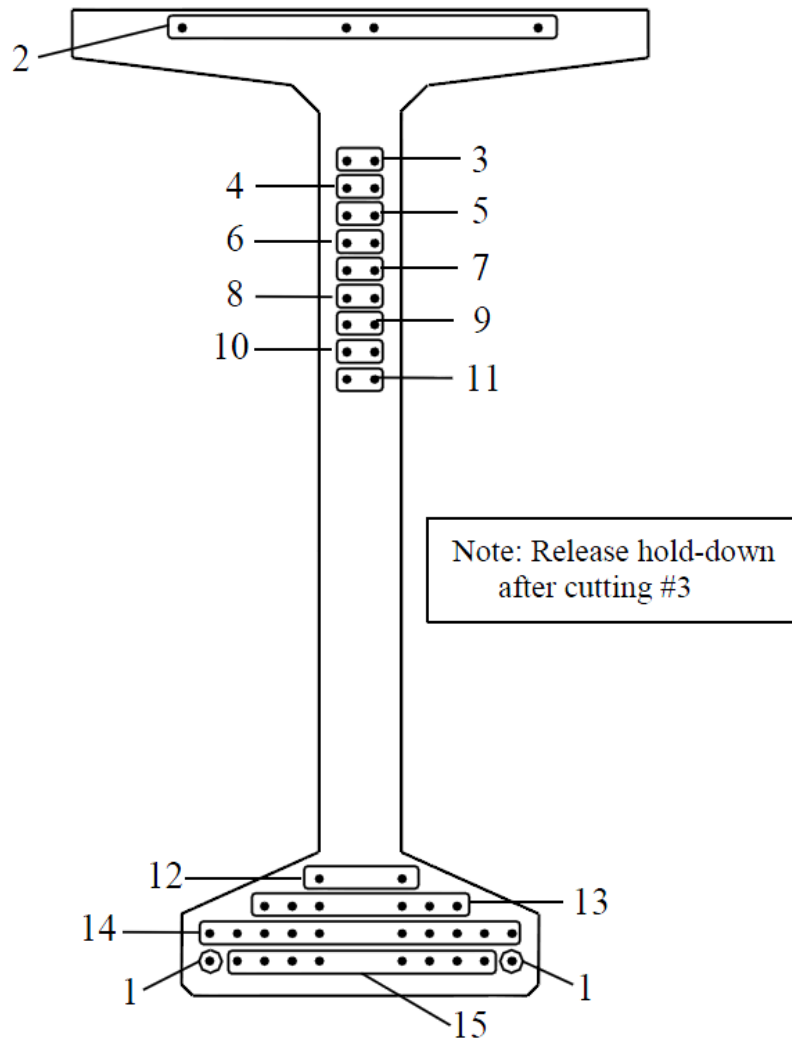


Figure 3-27: Flame-Cutting Sequence for BT-72 Girders

Immediately after all of the strands and hold-downs were released, camber measurements were taken using both the tensioned-wire system and surveying system. After these measurements were recorded, the girders were ready to be moved to storage. Once again, the VWSG wires had to be disconnected while the girders were transported to storage. One crane was used to move each BT-54 girder while two cranes were used to move each BT-72 girder. Storage conditions were arranged so that the girders would be supported with the same span length that they would have in the bridge. This meant that a length of 9 inches of the girder

should be resting on the support. The support conditions are shown in Figure 3-28. After being placed in storage, the VWSG cables were reconnected to the data collection system and another set of camber measurements were taken.



Figure 3-28: Support Conditions in Storage

Chapter 4 Camber Measurement Program

4.1 Introduction

The precast, prestressed bridge girders used in this study were measured for camber using two different methods. All twenty-eight girders were measured for camber over an extended period of time using surveying equipment. In addition to the surveying method, twelve of the girders were measured for camber using a tensioned-wire system. Part of the scope of this study was to compare the results of these two methods to each other. This chapter will describe in detail the implementation of both methods.

4.2 Surveying Method

The twenty-eight girders that were studied in this project were measured for camber using the surveying method. This method involved the use of specific targets placed on the surface of each girder, a prism rod with an attached prism, and a total station. The targets provided a specific and consistent location for prism rod placement for each total station reading. These targets consisted of hexagonal bolts that were embedded in the top of the fresh concrete at specific locations along the length of each girder after the concrete surface had been roughened. Then, each bolt was marked on top with a sharpie to provide a more specific target to place the tip of the prism pole. One of these bolts embedded in the concrete is shown in Figure 4-1. These targets were placed on specific points along the girder surface: 9 inches from each end, the 1/6th and 5/6th span locations, and midspan.



Figure 4-1: Surveying Target in Place

Camber measurements were taken at specific times as the girders aged. The baseline set of readings were taken after the concrete had cured just prior to prestress transfer. The first true cambers were measured just after transfer had taken place. Camber was measured again after the girders were moved from the casting bed to their storage location in the plant. Camber measurements were then taken when the girders reached ages of 7 days, 14 days, and 28 days. After the girders reached 28 days, intermittent readings were taken while the girders remained in storage. In most cases, cambers were measured every two weeks after the girders reached an age of 28 days. These measurements were taken as early in the day as possible so as to minimize temperature effects due to sunlight. Discussion regarding temperature effects and associated corrections are discussed in Chapter 6.

The first step in the measurement of camber using the surveying method involved the setup of the total station. An effort was made to set up the total station in locations that were not too close to the girders, as large horizontal angle changes between the end targets might have decreased accuracy in the measurements. Furthermore, when measurements were taken on girders in storage, a single setup location was often used to make measurements on multiple girders. On many occasions, the location of the total station was constrained by plant operations.

Once the total station was set up and leveled, measurements were taken. First, the prism pole was placed on the bolt installed at the mark end of the girder. Once the prism was correctly positioned on the bolt and held level, the total station measured the horizontal angle, the horizontal distance, and the vertical distance to the prism. This is shown in Figure 4-2. Once this was completed, the values were manually recorded, and the prism pole was moved to the 1/6th - span location. The measurement process was then repeated for every location on the girder, ending with the far end. All of the calculations to determine camber were relative to the endspan target locations. Specifically, the horizontal angle measured and recorded for the mark end target for each set of measurements was the baseline angle for that set of measurements. The change in horizontal angle from the mark end target to the other targets was the important value to calculate the camber change, the absolute angle reading did not matter. In many cases, the horizontal angle for the first reading was set to 0°0'0" in order to simplify the other angle measurements for that girder.



Figure 4-2: Surveying Method Camber Measurements

A computer spreadsheet was developed to determine the camber values for each girder based on the surveying method measurements. The first set of measurements taken for each girder were taken just prior to transfer. The computer program used these first measurements as baseline readings. The offset of the $1/6^{\text{th}}$ -span, midspan, and $5/6^{\text{th}}$ -span targets off of an imaginary straight line drawn between the two end span targets was calculated. If the target was above the imaginary straight line, then the offset was a negative value. If the target was below the line, the offset was positive. After transfer, the offsets of the interior targets were again calculated from an imaginary straight line drawn between the end span targets. These measured offsets were subtracted from the initial offsets in order to determine the change in camber during the measurement time interval.

4.3 Tensioned Wire Method

In addition to measuring camber using the surveying method, some of the girders in this study were measured for camber using the tensioned wire method. All of the girders in this study were not measured for camber using the tensioned wire system because of the time that it takes to set the system in place while the girders are sitting on the casting bed just prior to transfer. The labor involved in installing the system would have delayed plant operations significantly if multiple girders were to be measured for camber using this system. For this reason, only one girder in a casting group was measured for camber using the tensioned wire method. The only exception to this was casting group E, which consisted of girders 54-7S and 54-8C. Both of these girders were measured for camber using the tensioned wire system in order to have a direct comparison between the CVC and SCC girders. A schematic illustration of the tensioned wire system is shown in Figure 4-3. This method is based on a camber measurement method reported by Gross (2000).

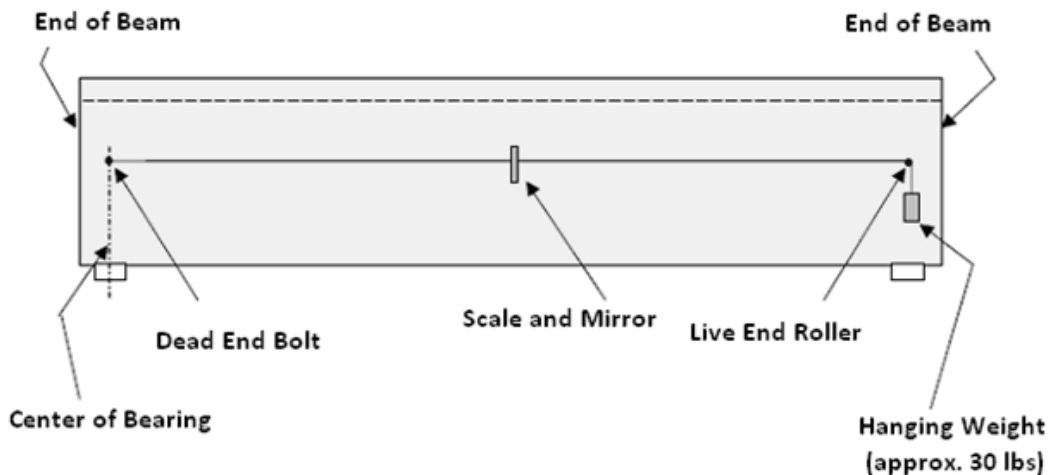


Figure 4-3: Tensioned Wire System Schematic

The first step in the installation of the tensioned wire system occurred after the forms had been stripped off of the girders, but prior to transfer. One 2 in. deep hole was drilled into the web

of the girder 9 inches from each end of the girder using a 3/8 in. drill bit as shown in Figure 4-4. Once these holes were drilled, wedge stud anchor bolts were inserted into the holes and anchored in place. After the bolts were installed and secured, the measurement rulers were secured onto the web surface of the girder at midspan as well as 1/6th span. These rulers had been cut into six-inch sections and these were glued onto mirrors as shown in Figure 4-5. The ruler and mirror assemblies were secured to the girder using epoxy using special care to make sure that the rulers were installed perfectly level and at the correct height so that the tensioned wired would cross the ruler.



Figure 4-4: Drilling Holes for Tensioned Wire Anchors



Figure 4-5: Tensioned Wire Measurement Rulers

After the rulers were securely in place, 0.016 in. diameter stainless steel wire was tied securely to one of the bolts that had been installed close to the end of the girder. The wire was stretched along the girder so that it would just reach the other bolt. A pulley was installed on the other bolt so that the wire could rest on the pulley and be able to slide freely over it. A carabiner was tied to the end of the piano wire to allow for the weight being used to be quickly attached and unattached.

To take a measurement, a cylindrical 30-pound weight was hung from the carabiner making sure that the wire was resting on the pulley so that it could be drawn tight by the freely hanging weight as shown in Figure 4-6. A reading was taken by simply recording the value on the ruler that the wire crossed to the nearest 0.01 in. Parallax error in the readings was minimized through the use of the mirror behind the ruler. The value on the ruler at which the wire completely covered its own reflection was the value recorded as shown in Figure 4-7. This ensured that the researcher taking the readings was always reading from the same vantage point.

In addition, two researchers would independently take the readings, and the average of those was the reported result.

A baseline measurement was taken just prior to transfer. The height that the tensioned wire crossed the ruler both at midspan and at $1/6^{\text{th}}$ span was recorded. Then, after transfer, a measurement was taken again. The difference in the readings was recorded as the initial camber. Tensioned wire camber measurements were taken every time that the surveying method was used to measure camber until the girders were transported to the bridge site and set into place.



Figure 4-6: Hanging Weight for Tensioned Wire Camber Measurement



Figure 4-7: Camber Measurement using the Tensioned Wire

Chapter 5 Strain Measurement Program

5.1 Introduction

Vibrating-wire strain gauges (VWSGs) were installed in various cross sections and locations within the girders in order to measure internal strains and temperatures. The measurement of internal strain was important in this project for two reasons. First, the gauges were positioned within the CVC and SCC girders in such a way as to provide a direct comparison between the strains measured in each. Second, predicted internal strains for the girders were calculated using various material property models. Part of the scope of the project was making comparisons between the measured internal strains to the predicted strains based on various prediction models.

5.2 Vibrating-Wire Strain Gauges

The vibrating-wire strain gauges used in this project were Geokon, Inc. VCE-4200 gauges. According to the Geokon manual, these gauges are ideally suited for long-term strain measurements in mass concrete. The strain measurement was accomplished through the vibrating wire. A steel wire is tensioned between the two end blocks of the gauge. Once the gauge is embedded in the hardened concrete the gauge will undergo shortening and lengthening along with the concrete, which will increase or decrease the tension in the wire accordingly. Electromagnets incorporated into the gauge pluck the wire and subsequently measure the wire's natural frequency of vibration. The change in the natural frequency of the wire reflects the change in tension that the wire has undergone, which can in turn yield the change in strain of the wire. Figure 5-1 is a detailed drawing showing the various components of these gauges.

Along with the vibrating wire scheme, a thermistor is incorporated into each gauge. The thermistor measures the temperature of the gauge at the same time that the strain measurement is being taken using the vibrating wire assembly. The temperature of the gauge at the time of a strain reading was important information to record, as corrections due to temperature were calculated and applied to the strain readings. These corrections will be discussed in the following chapter.

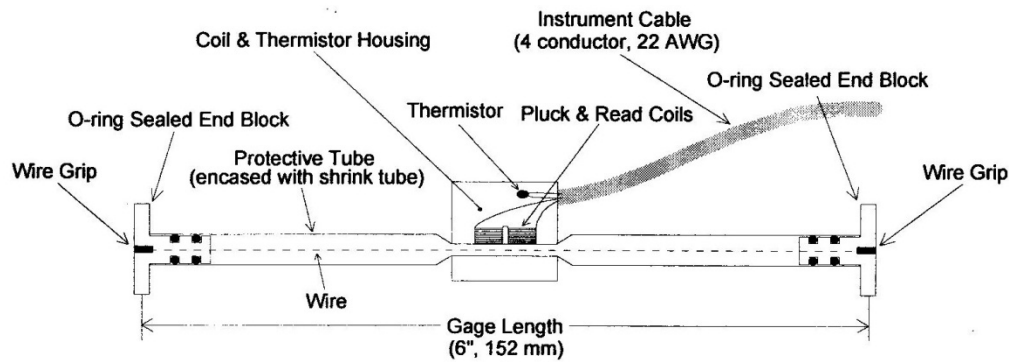


Figure 5-1: VCE-4200 Vibrating Wire Strain Gauge Schematic (Geokon 2010)

5.3 Vibrating-Wire Strain Gauge Locations

The bridge that was to be built over Hillabee Creek in Tallapoosa County, AL was designed to have four spans. The two end spans (Span 1 and Span 4) were designed to use BT-54 girders, while Span 2 and Span 3 were designed to utilize BT-72 girders. This symmetry allowed for a girder layout conducive to direct comparisons between those composed of CVC to those composed of SCC. Therefore, Span 1 and Span 2 consisted of SCC girders while Span 3 and Span 4 contained CVC girders.

Special consideration was taken when placing the VWSGs within the girders to allow for strain comparisons between girders undergoing similar loading but composed of different types of concrete. Specifically, more strain gauges were placed in girders with numbers from 4 to 7 on

Spans 1 and 2, and from 8 to 11 on Spans 3 and 4. This was done to allow for a more direct comparison between girders of different spans under load testing and traffic loads due to the bridge skew. Figure 5-2 is a schematic illustration of the girder configuration in the bridge. This view also shows the gauge layouts that were used in each girder.

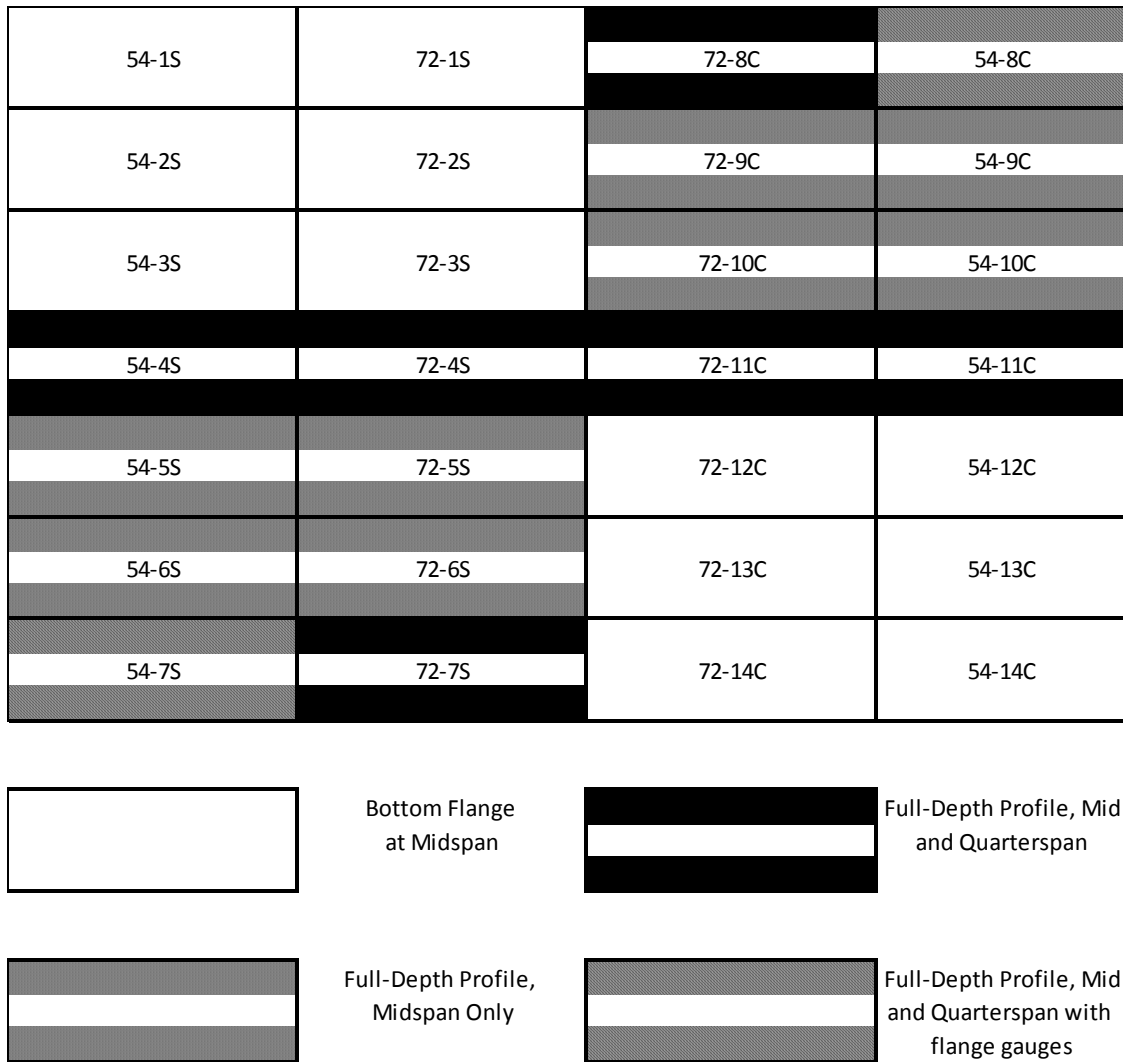


Figure 5-2: VWSG Layout Plan View

The VWSGs that were placed in girders containing only one gauge were placed at the centroid of the prestressing strands that were contained within the bottom bulb. This included the draped strands because they were located in the bottom bulb at the midspan of the girder. These

centroids, shown in Figures 5-3 and 5-4, were located at a height of 6 in. for the BT-54 girders and a height of 8.8 in. for the BT-72 girders. Figures 5-5 and 5-6 depict the gauge locations for the girders that contained gauges to measure strains across a full depth profile at midspan. The bottom-flange gauges were again placed at the centroid of the bottom prestressing steel. The gauges in the web were placed one quarter of the web height above the bottom bulb as well as below the top flange. Finally, the top gauge was placed at the centroid of the prestressing steel that ran through the top flange.

When full-depth profile measurements were required at both the midspan and quarterspan of a girder, the gauge heights at the quarterspan locations were identical to those at midspan and are shown in Figures 5-7 and 5-8. In the case of girder 54-7S and 54-8C, extra gauges were placed at the midspan cross section in addition to those used for the full-depth profile. One gauge was placed in the bottom bulb at a height of 6 in. along the prestressing strand that ran on the outside of the layer and would be located near the outside edge of the girder once it was placed at the bridge site. Another gauge was placed in the top flange along the outside prestressing strand on the same side so that it would also be near the outside edge of the bridge. These gauge locations are depicted in Figure 5-9.

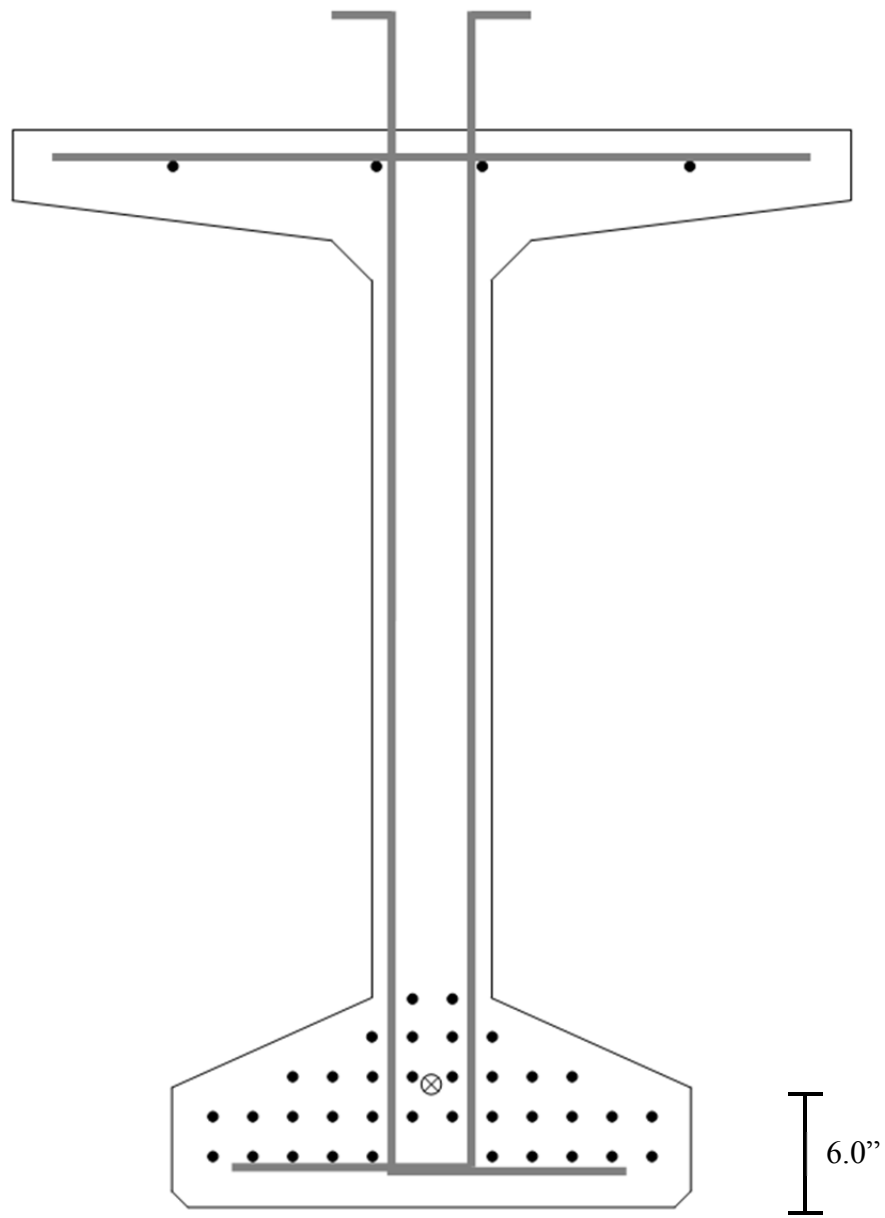


Figure 5-3: Single VWSG at Midspan for a BT-54

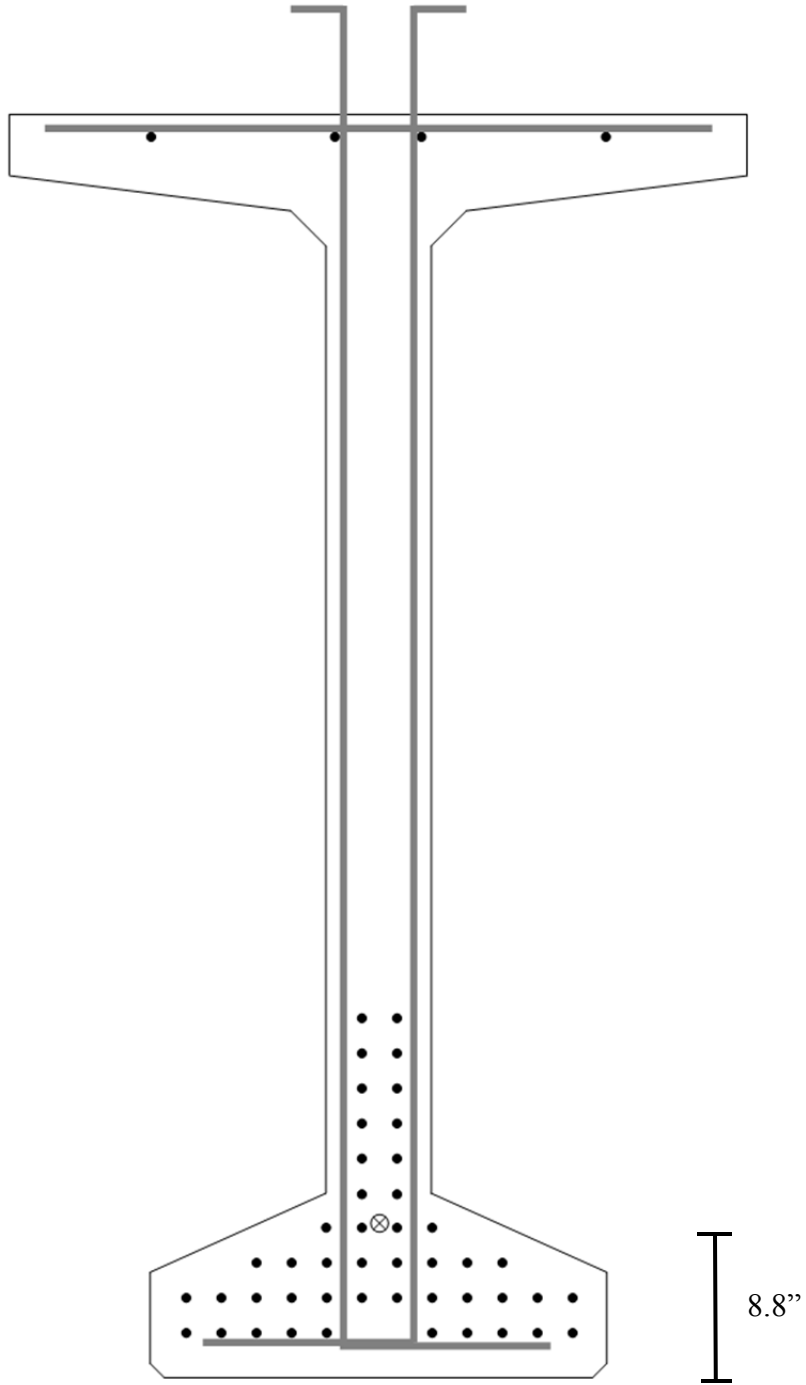


Figure 5-4: Single VWSG at Midspan for a BT-72

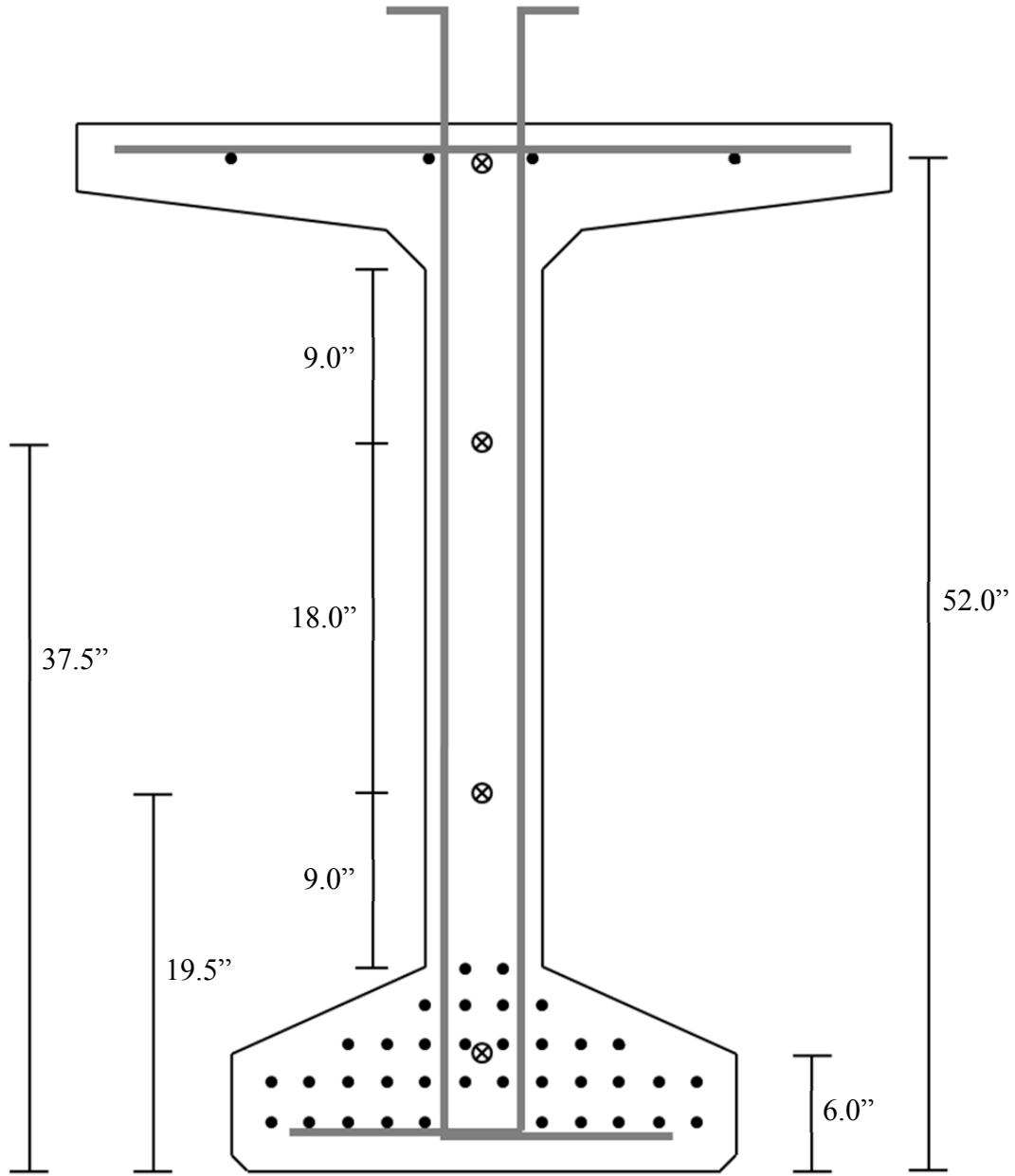


Figure 5-5: Full-Depth VWSG Profile at Midspan for a BT-54

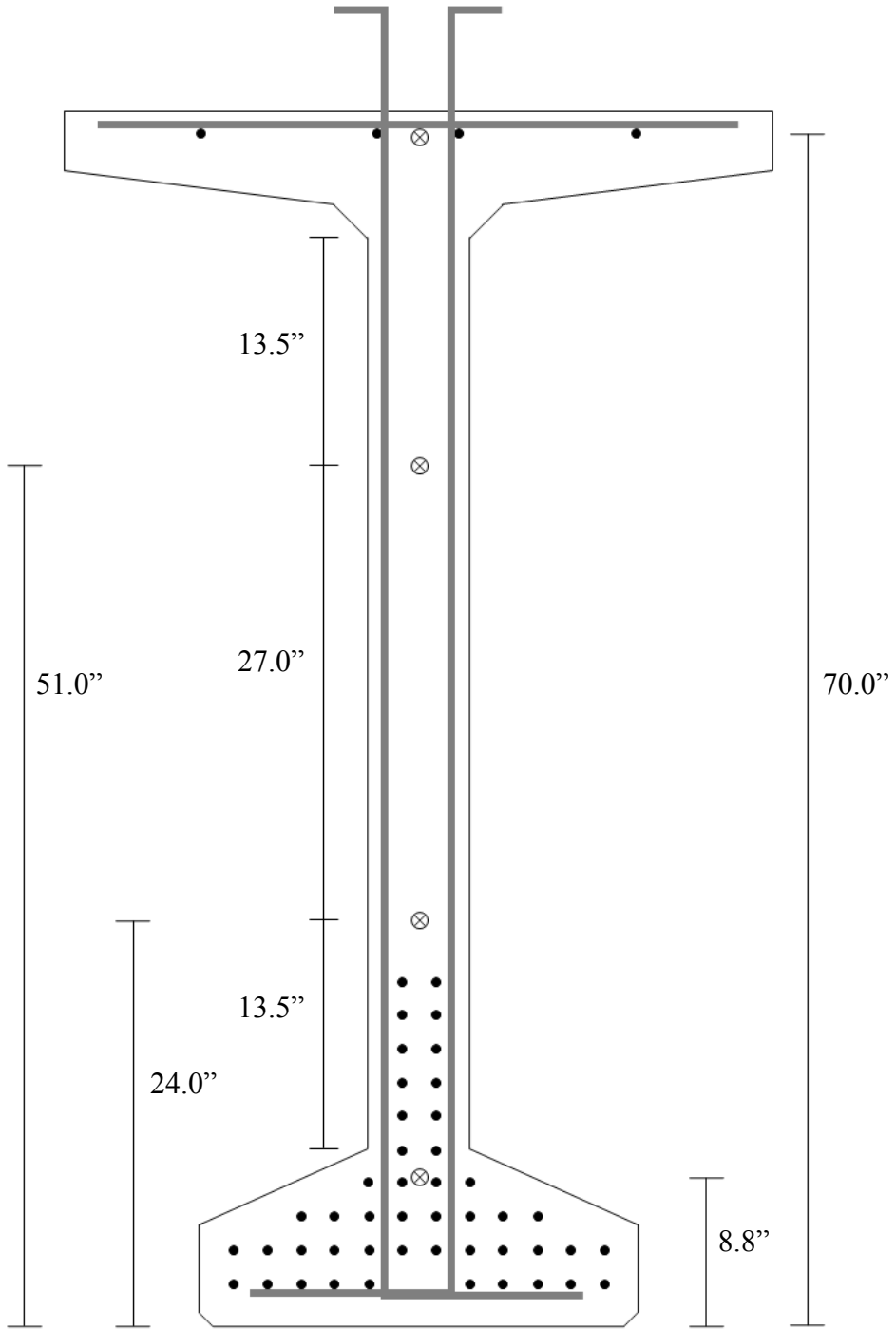


Figure 5-6: Full-Depth VWSG Profile at Midspan for a BT-72

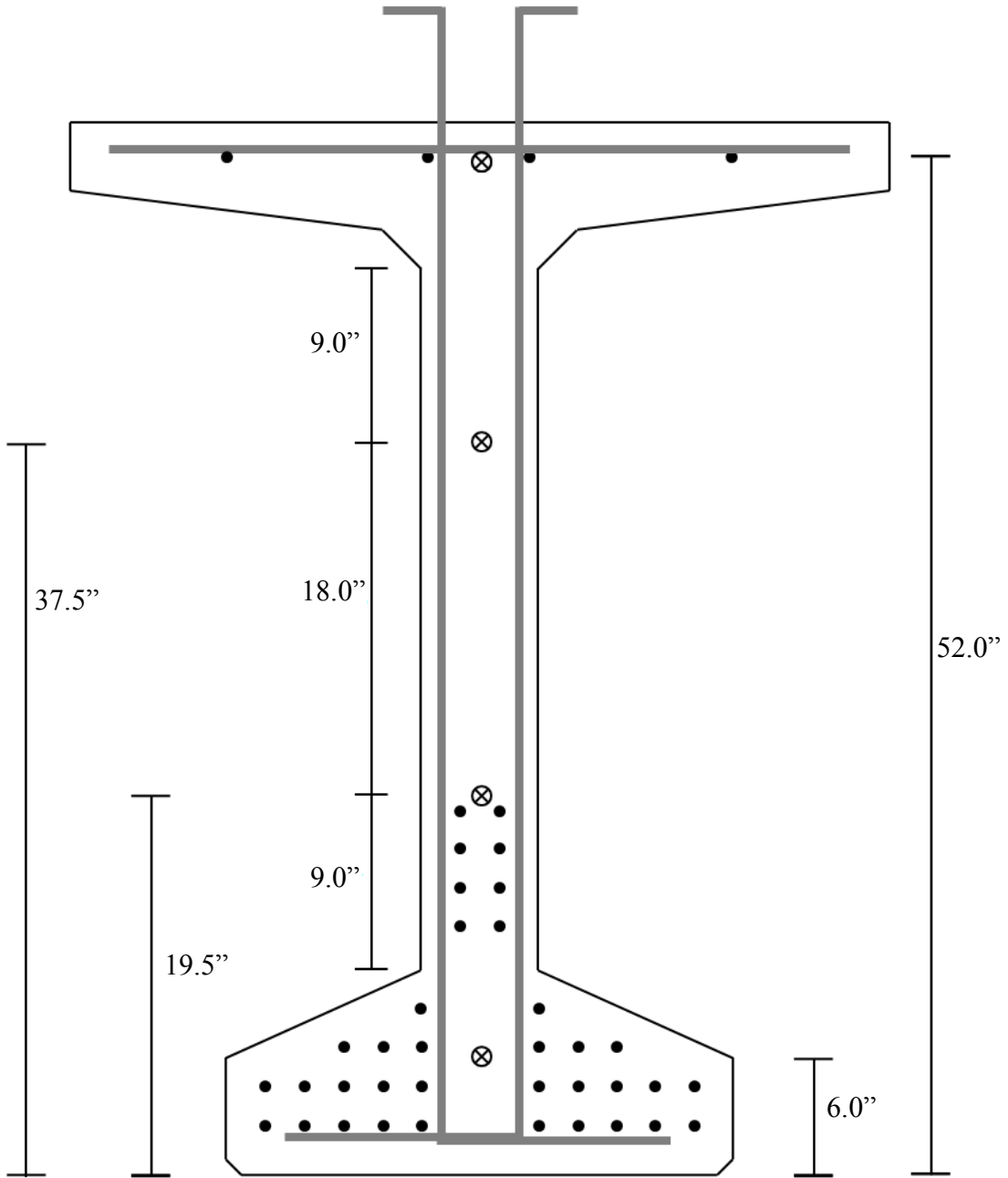


Figure 5-7: Full-Depth VWSG Profile at Quarterspan for a BT-54

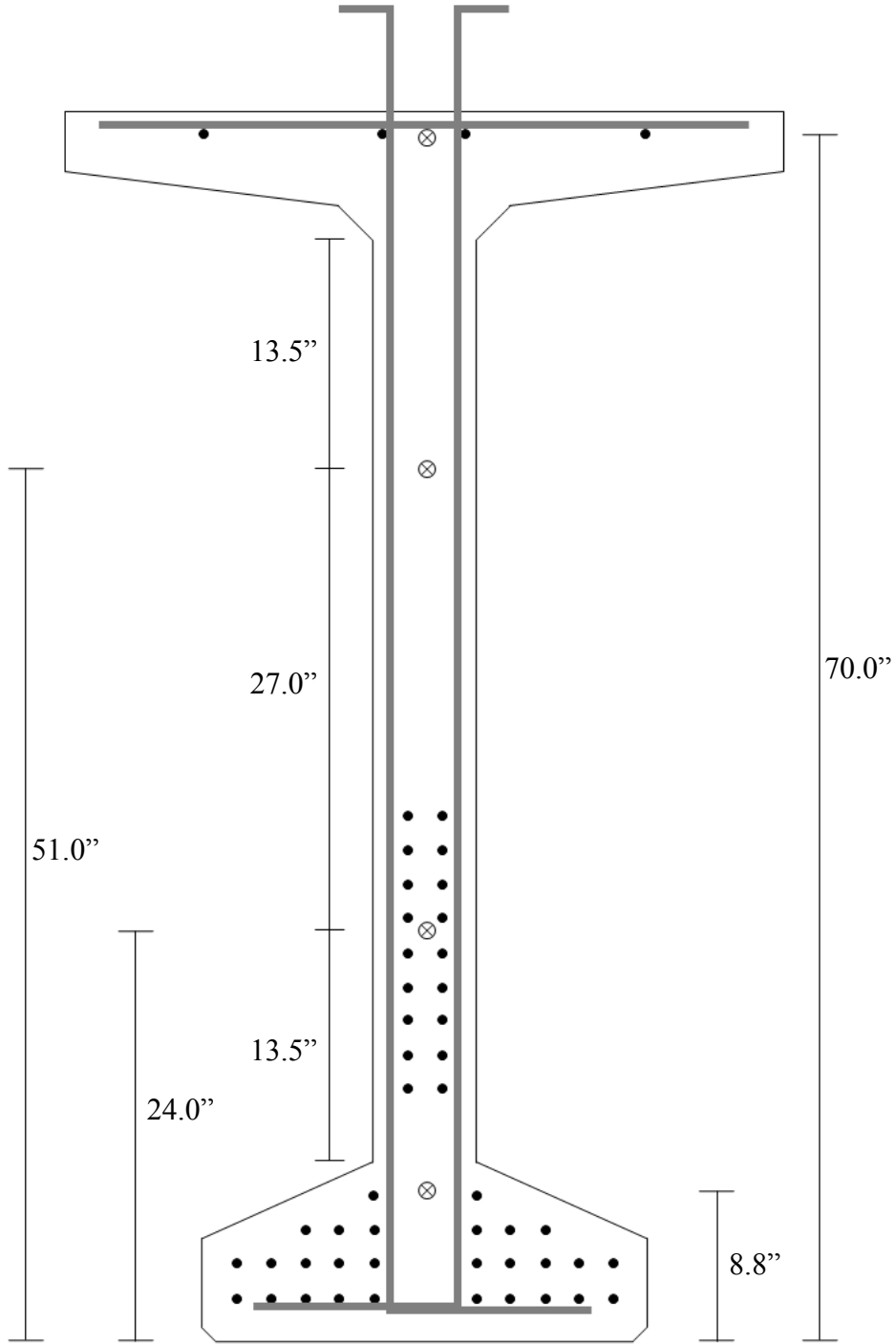


Figure 5-8: Full-Depth VWSG Profile at Quarterspan for a BT-72

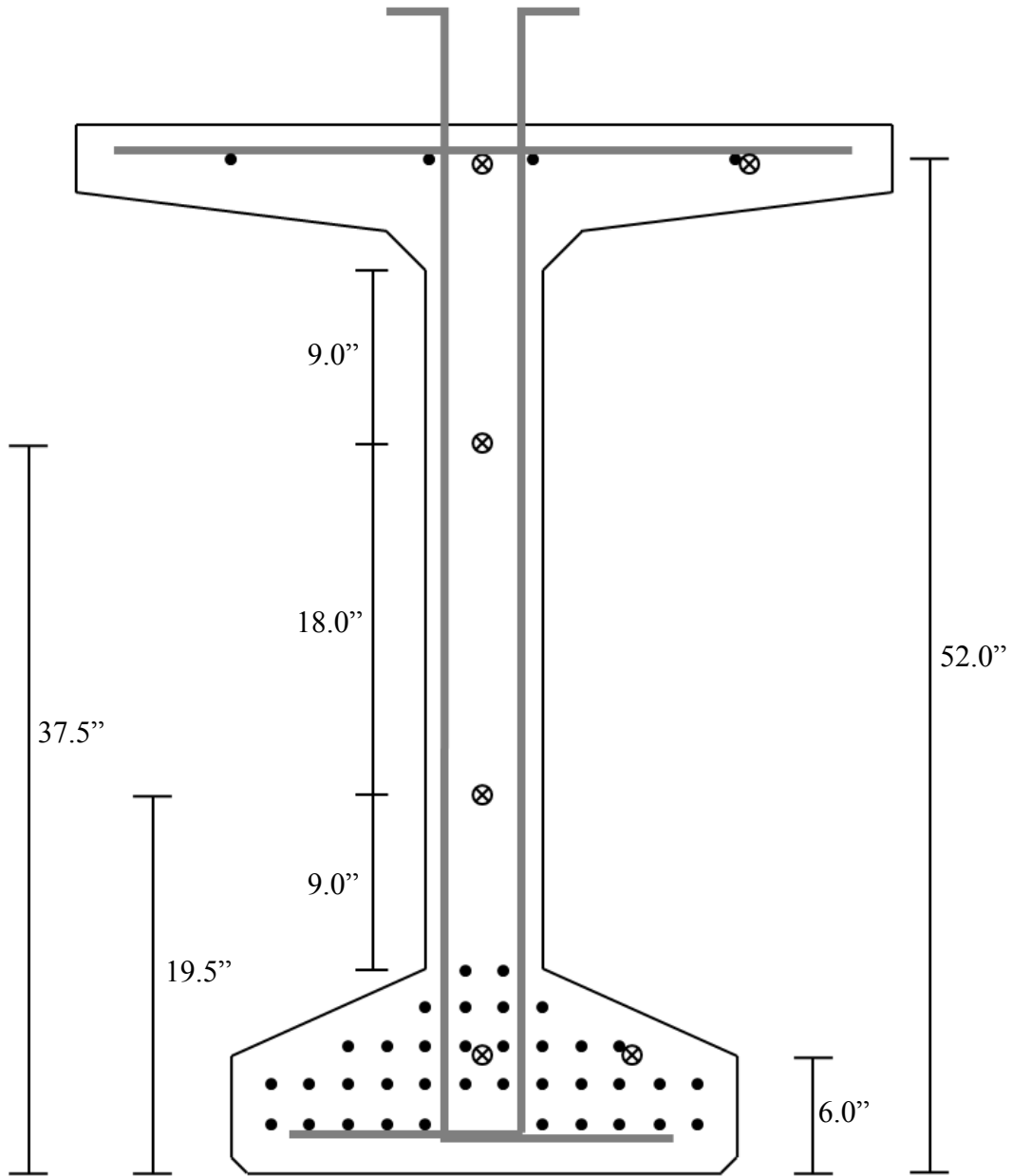


Figure 5-9: Full-Depth VWSG Profile at Midspan for 54-7S and 54-8C

5.4 Vibrating-Wire Strain Gauge Installation

Great care was taken to place the VWSGs in a manner in which they were secured at the proper location and would be able to bond with the concrete. The gauges were secured into place

using various materials including plastic zip cable-ties, steel wire, and small segments of reinforcing steel. Gauges located in the bulb section of the girder were secured into place using zip-ties tied around the prestressing strand. Figure 5-10 shows a gauge located in the bottom bulb of a girder. Gauges placed in the top flange of a girder were secured in the same manner.



Figure 5-10: VWSG Secured in Bottom Bulb

Gauges that were to be placed within the web of a girder were more difficult to secure because there were no prestressing strands to tie directly to. An assembly of small sections of reinforcing bar along with steel wire was fabricated in order to provide a stable suspension system without adding significant longitudinal reinforcement to the cross sections. Figure 5-11 shows a typical example of this method of securing the VWSGs. Wire ties were used to tie small sections of reinforcing steel to the stirrup sections used as reinforcement in the girder. Next, steel wire was wound around the steel sections to connect them together. Finally, zip-ties were used to secure the VWSG to the steel wire.

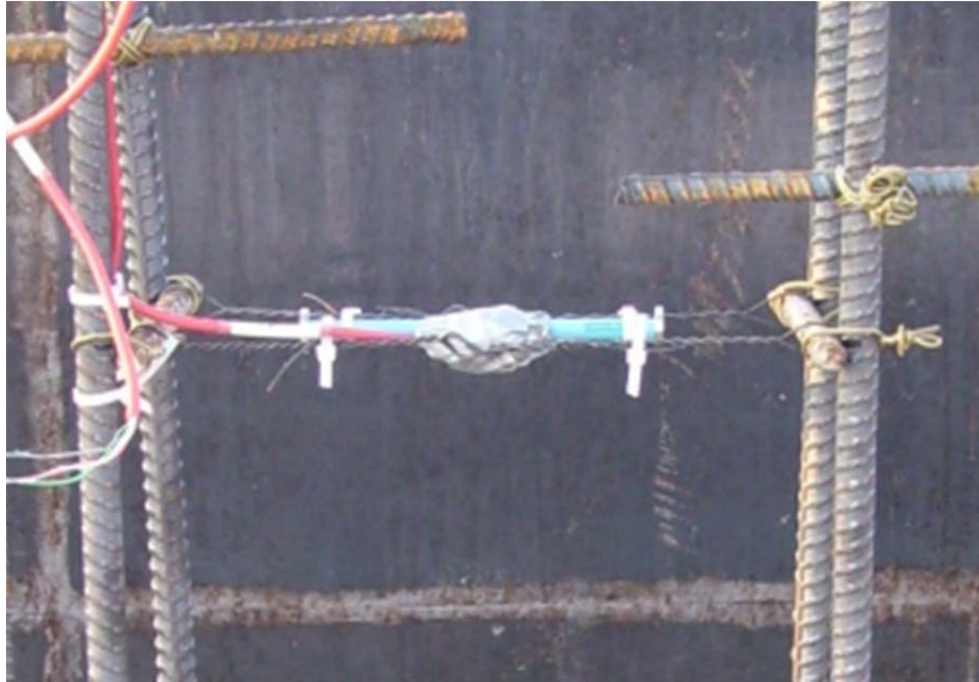


Figure 5-11: VWSG Secured in Web of a Bulb Tee Girder

5.5 VWSG Data Acquisition System

Two data acquisition systems (DAS) were used in this research. Each DAS was designed to be a stand-alone system that could be used to collect data at the prestressing plant as well as on-site at the bridge. The boxes containing the DAS equipment were designed to withstand the rigors of being exposed to the environment for extended periods of time while recording measurements. The design and configuration of the DAS were based on a similar setup by Gross (2000). Each DAS unit contained a CR1000 datalogger, two multiplexers, and a battery system. Figure 5-12 provides a schematic for the layout of each DAS unit.

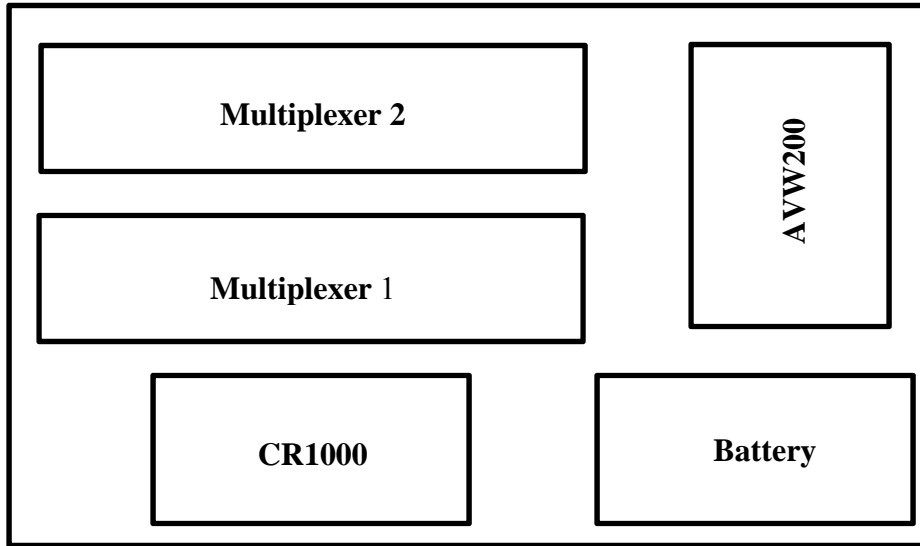


Figure 5-12: VWSG Data Acquisition System Schematic

The CR1000 was programmed to activate each VWSG every six minutes and record the resonant frequency of vibration and thermistor resistance as discussed in Section 5.2. Each multiplexer used had the capacity to record 16 separate VWSGs. This means that each DAS had the capacity to read 32 VWSGs simultaneously. The program calculated the temperature of the gauge using the recorded thermistor resistance by Equation 5-1. The constants A , B , and C were provided in the instruction manual included with the gauges, and Equation 5-1 is located in Appendix C of the Geokon Instruction Manual (2010).

$$T = \frac{1}{A + B(\ln R) + C(\ln R)^3} - 273.15 \quad \text{Equation 5-1}$$

Where

T is the gauge temperature ($^{\circ}\text{C}$),

R is the thermistor resistance,

$A = 1.4051 \times 10^{-3}$,

$B = 2.369 \times 10^{-4}$, and

$C = 1.019 \times 10^{-7}$

The gauge strain was determined in a similar manner using the recorded natural frequency of vibration. The process outlined below is found in Appendix B of the Geokon Instruction Manual (2010) that was included with the gauges. The natural frequency of vibration of a wire is related to its tension, length, and mass by Equation 5-2.

$$f = \frac{1}{2L_w} \sqrt{\frac{F}{m}} \quad \text{Equation 5-2}$$

Where

f is the natural frequency of the wire (Hz),

L_w is the length of the wire (in.),

F is the wire tension (lbs), and

m is the mass of the wire per unit length (pounds, sec.²/in.²).

Re-arranging Equation 5-2, using the relationship that the force in the wire is related to the strain in the wire through the modulus of elasticity of the wire, and using the correct values for length and mass of the wire, Equation 5-3 can be used to determine the strain in the wire directly from the natural frequency measured.

$$\varepsilon_w = 3.304 \times 10^{-3} * f^2 \quad \text{Equation 5-3}$$

Where

ε_w is the measured strain in the gauge (10^{-6} in./in.), and

f is the frequency (Hz).

Chapter 6 Results and Discussion

6.1 Introduction

This chapter includes both the predicted and measured results for the studied specimens. In order to make comparisons between the prediction models, the values measured in the field needed to be adjusted to account for varying temperatures. A discussion of the implementation of the VB program developed by Schrantz (2012) is also included, to address noteworthy issues. Finally, the predicted and measured results are presented and discussed.

6.2 Adjustment of Measurements to Account for Temperature

The predicted internal strains and cambers for the specimens in this study were computed assuming a constant temperature throughout the girder cross section. However, the actual test specimens were stored outdoors and exposed to environmental conditions including sunlight and wind. These environmental conditions caused non-uniform temperature distributions throughout the girder cross sections during the measurement of internal strains and cambers. Because both steel and concrete are susceptible to thermal expansion, measured internal strains and cambers reflected these temperature gradients. It was necessary to take these thermal gradients into account and adjust the strains and cambers measured in order to minimize the influence of thermal effects on the readings. Adjustments to the camber and strain readings were made so that adjusted readings were relative to a uniform internal temperature of 68 degrees Fahrenheit (20 °C).

The first step in the process of accounting for the thermal gradients in the girder cross sections was to use an assumed cross section that was simpler to analyze than the standard BT-54 and BT-72 cross-sections. The idealized BT-54 section and BT-72 section are shown below in Figure 6-1 and Figure 6-2, respectively. These idealized shapes were dimensioned in order to very closely resemble the BT-54 section and BT-72 section in such geometric properties as the location of the centroid, the area of the cross section, and the moment of inertia of the cross section.

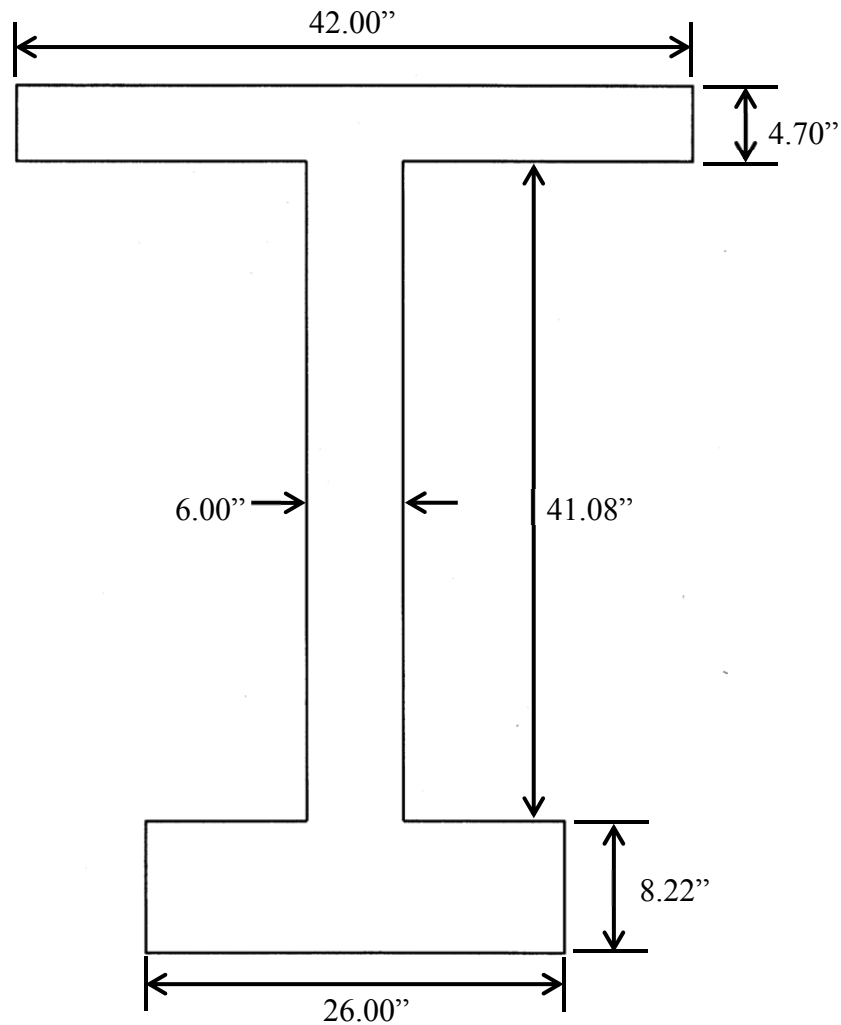


Figure 6-1: Simplified BT-54 Section

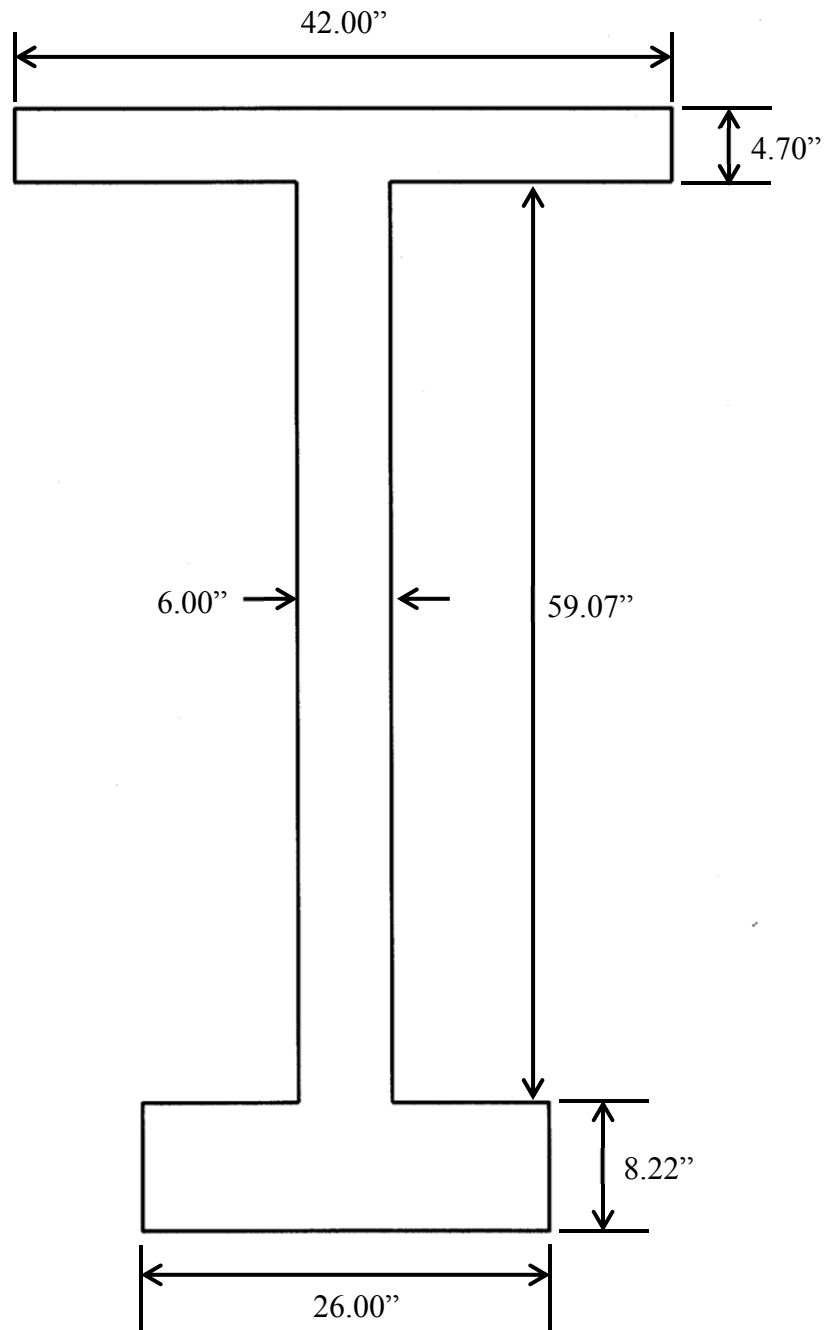


Figure 6-2: Simplified BT-72 Section

As discussed previously, the VWSG gauges installed in the girders measured strain and temperature. Therefore, whenever a strain reading was recorded, the corresponding temperature of the gauge and consequently the temperature of the concrete around the gauge was recorded. This allowed temperature gradients at the time of strain measurements to be constructed based on

these temperature measurements. Temperature gradients were assumed to be constant throughout the bottom and top rectangles of the idealized girder cross sections. The temperature gradient through the middle rectangle, which idealized the web of the girder, was assumed to be linear. This was due to the placement of the VWSG within the actual girders. There was only one gauge in the bottom bulb or top flange to record temperature while there were two gauges in the web of a fully-instrumented cross section. Gauge locations were discussed above in Section 5.3. Trial analyses were also conducted assuming linear gradients in both the bottom bulb and the top flange, but results from those models did not differ significantly from the constant temperature assumption in the bottom bulb and top flange.

In order to make accurate comparisons to predicted values, the measured strains and cambers needed to be adjusted so that they would represent what the measured strain or camber would have been if the girder was a constant 68°F (20°C) throughout its cross section at the time of measurement. These adjustments can be made assuming that the concrete behaved in a linear-elastic manner and that plane sections remain plane at all times. Along with this, the relationship defined in Equation 2-1 regarding the strain at any height in a cross section as a function of the curvature of the cross section holds true.

The change in total strain at any depth of a cross section is the sum of the change in stress-dependent strain and the change in stress-independent strain. Stress-independent strain includes strain due to shrinkage and temperature. For the purposes of this temperature correction process, only the strain due to the temperature gradient is considered, as evidenced in Equation 6-1.

$$\Delta\varepsilon = \frac{\Delta f}{E_c} + \alpha_T \Delta T \qquad \text{Equation 6-1}$$

Furthermore, as long as there is no externally applied axial force and no axial restraint of the member, then the sum of the axial forces on any cross section must equal zero. This means that the change in stresses on a cross section integrated over the area of that cross section must equal zero, as shown in Equation 6-2.

$$\int_A \Delta f dA = 0 \quad \text{Equation 6-2}$$

Solving Equation 6-1 for the change in stress, using the relationship for the strain at any height as a function of the curvature, and substituting into Equation 6-2 yields the relationship shown in Equation 6-3.

$$\int_A E_c \left[(\Delta \varepsilon_{cen,t} + (\Delta \phi \times y)) - \alpha_T \Delta T \right] dA = 0 \quad \text{Equation 6-3}$$

Finally, Equation 6-3 is rearranged to solve for the change in strain at the centroid of the cross section due to a change in the non-linear temperature gradient. The value used for the coefficient of thermal expansion for concrete was obtained from Section 5.4.2.2 of the AASHTO LRFD Bridge Design Manual (2010).

$$\Delta \varepsilon_{cen,t} = \frac{\alpha_T \int T dA}{A} \quad \text{Equation 6-4}$$

Where

$\Delta \varepsilon_{cen,t}$ is the strain change at the centroid of the cross section due to temperature change in the concrete ($\mu\varepsilon$),

α_T is the coefficient of thermal expansion of concrete = 6.0 ($\mu\epsilon/^\circ\text{F}$),

T is the non-linear temperature gradient of the cross section ($^\circ\text{F}$), and

A is the cross-sectional area (in^2).

For a simply-supported flexural member, the sum of the change in moments on any cross section must also be equal to zero. This assumption was used to determine the change in curvature of each cross section due to a change in the non-linear temperature gradient. This means that the integral of the change in stress times the distance from the centroid y integrated over the area must equal zero.

$$\int_A (\Delta f \times y) dA = 0 \quad \text{Equation 6-5}$$

Again, the equation is rewritten in terms of strain change at the centroid and curvature, resulting in Equation 6-6. Notice that the equation below is similar to Equation 6-3 with the exception of the addition of the y term.

$$\int_A E_c [(\Delta \epsilon_{cen} + (\Delta \phi \times y)) - \alpha_T \Delta T] y dA = 0 \quad \text{Equation 6-6}$$

Distributing the integration to each term yields:

$$\left(E_c \Delta \epsilon_{cen} \int y dA \right) + \left(E_c \Delta \phi \int y^2 dA \right) - \left(E_c \alpha_T \int T y dA \right) = 0 \quad \text{Equation 6-7}$$

The first term in Equation 6-7 is equal to zero. In the second term of Equation 6-7, the integral of the y^2 term is equivalent to I , the area moment-of-inertia of the cross section.

Therefore, Equation 6-7 is rearranged to solve for the change in curvature of the cross section.

$$\Delta\phi_t = \frac{\alpha_T \int (\Delta T \times y) dA}{I} \quad \text{Equation 6-8}$$

Where

$\Delta\phi_t$ is the change in curvature of a concrete cross section due to temperature

changes on the cross section (in./in.),

α_T is the coefficient of thermal expansion of concrete 6.0 ($\mu\epsilon/^\circ\text{F}$),

ΔT is the change in the non-linear temperature gradient,

y is the distance from the centroid (in.),

A is the cross-sectional area (in^2), and

I is the cross-sectional moment of inertia (in^4).

6.2.1 Temperature Correction for Camber

The first step in correcting the measured cambers for temperature was to correct the baseline camber reading for temperature gradient. These baseline readings were taken just prior to prestress transfer. However, because steam curing had recently ended, there were significantly elevated temperatures (relative to 68°F) throughout the cross section, and a gradient due to elevated temperatures in the bulb section of the girder. The baseline camber reading was corrected by calculating the curvature due to this original temperature gradient and transforming it into a deflection with Equation 6-9. The girder was assumed to be simply supported at the ends

and the curvature due to the non-linear temperature gradient was assumed to be constant for every cross section along the girder length.

$$\delta_{i,t} = \frac{\Delta\phi_{i,t}(L^2)}{8} \quad \text{Equation 6-9}$$

Where

$\delta_{i,t}$ is the initial deflection at midspan due to temperature gradient (in.),

$\Delta\phi_{i,t}$ is the change in initial curvature due to temperature gradient (in./in.), and

L is the length of the girder (in.).

Because the bottom flange was initially the hottest portion of the girder, this initial temperature-induced deflection was always a negative value, meaning that the temperature gradient was causing the ends of the girder to be slightly elevated relative to midspan. After prestress transfer, camber readings were taken at various times as the girders were in storage at the prestressing plant. Each time that a camber measurement was taken the temperature readings across the midspan of that girder were recorded. Girders that were only instrumented with one VWSG were assumed to have similar gradients as those in the same casting groups that were fully instrumented. The change in deflection due to temperature gradient at the time of camber measurement, δ_t , is calculated by Equation 6-10, which is similar to Equation 6-9 above.

$$\delta_t = \frac{\Delta\phi_t(L^2)}{8} \quad \text{Equation 6-10}$$

Where

δ_t is the deflection at midspan due to temperature gradient (in.),

$\Delta\phi_t$ is the change in curvature due to temperature gradient (in./in.), and

L is the length of the girder (in.).

The adjusted camber for each girder at the time of each camber measurement was calculated by Equation 6-11 shown below:

$$\Delta_{adj} = \Delta_{meas} - (\delta_t + -\delta_{i,t}) \quad \textbf{Equation 6-11}$$

Where

Δ_{adj} is the adjusted camber (in.),

Δ_{meas} is the unadjusted, measured camber (in.),

$\delta_{i,t}$ is the initial deflection as calculated in Equation 6-9, (in.), and

δ_t is the deflection due to temperature gradient at the time of camber measurement (in.).

The adjustments discussed above were applied to every camber measurement taken using the surveying method. Occasionally camber readings were taken when temperature data from the VWSGs were not recorded. In these instances, gradients from the same time of day for either the day before or the day after the camber measurement were used to provide a close approximation. Furthermore, gradients were assumed for girders that had only one VWSG in the midspan cross section by using companion girders that were fully instrumented. There was at least one girder in each casting group that had a fully instrumented midspan, and the gradients from those girders were used for the other girders in that group.

Camber measurements were most often taken early in the morning, just after sunrise. This was done because at this time of day the temperature gradients across the girder are usually the most constant, meaning that the entire cross section should be close to the same temperature.

Figure 6-3 shows some temperature gradients for Girder 54-4S. These are the gradients measured at the time of camber measurement. It is apparent that the temperature gradient was most severe at the time of prestress transfer, with the bottom bulb of the girder significantly warmer than the web and top flange. This temperature distribution was likely the main cause for the cracks observed in the girders prior to prestress transfer discussed in Chapter 3. The earliest camber measurements were most affected by the temperature gradients, as evidenced in Figure 6-4 and Figure 6-5. Figure 6-4 shows camber measurements for Casting Group C from an age of zero days to an age of 212 days. All of the adjusted values are lower than the measured values. This is due to the initial offset calculated by Equation 6-2 above and applied to every successive measurement. Figure 6-5 shows the first seven days of the same plot. The adjustments were largest in the initial camber readings that took place just after transfer and when the girders were moved from the casting bed to their storage location. During these measurements, the temperature gradient across the girder was not constant, whereas during later measurements it was much closer to constant.

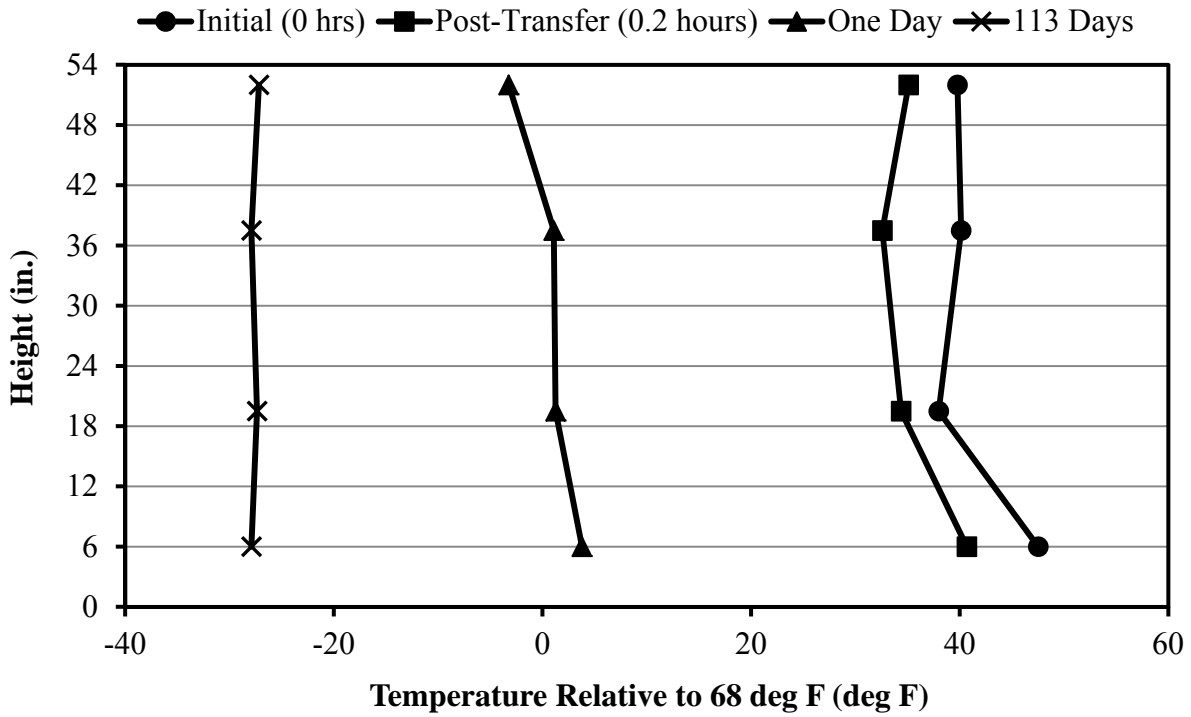


Figure 6-3: Temperature Gradients for 54-4S at Times of Camber Measurement

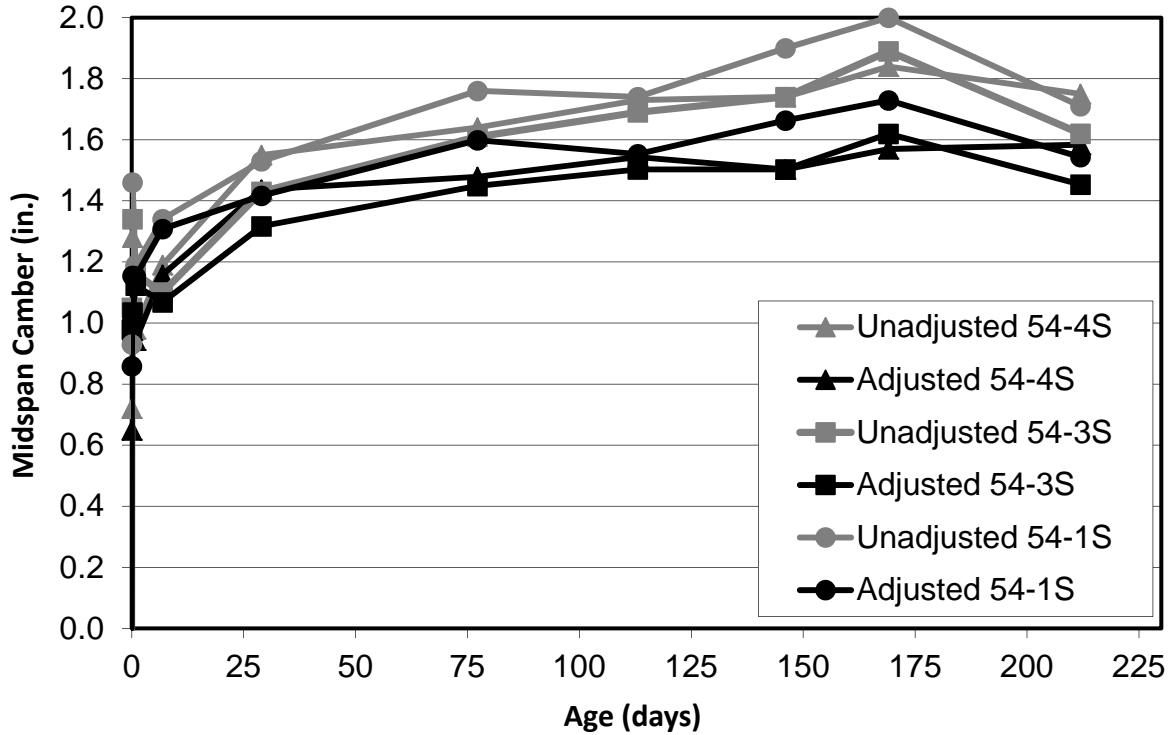


Figure 6-4: Casting Group C Cambers (0 to 225 days)

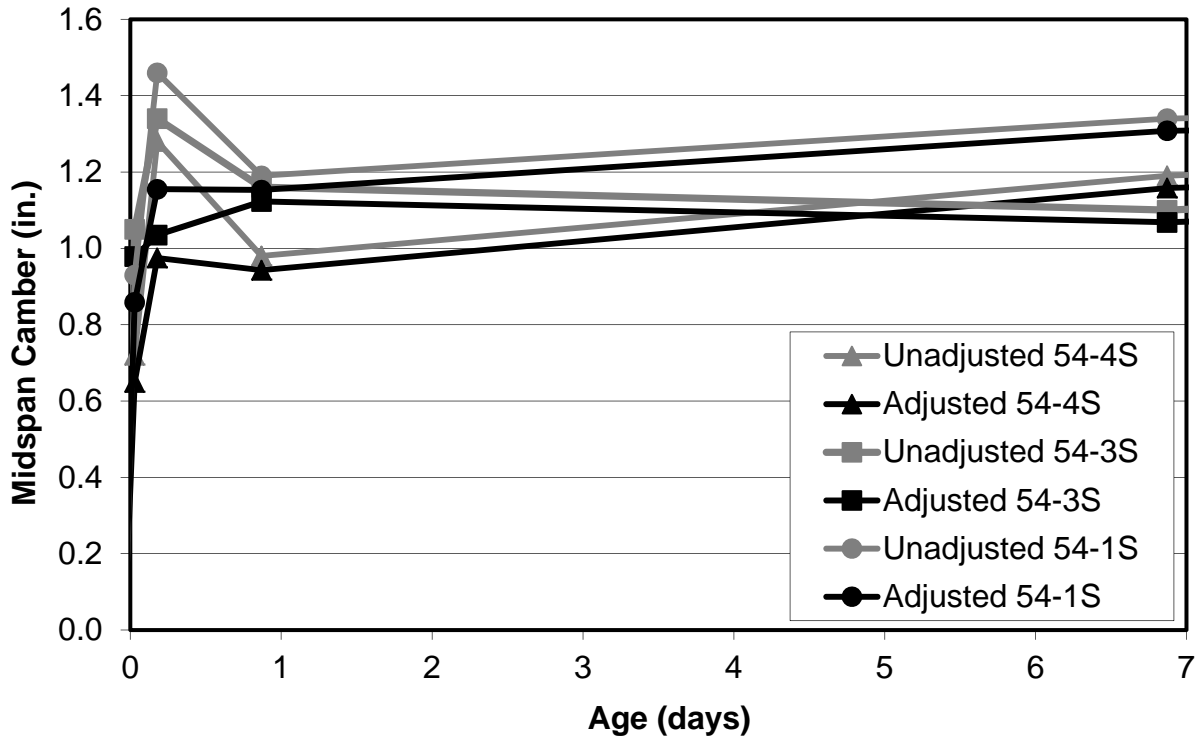


Figure 6-5: Casting Group C Cambers (0 to 7 days)

6.2.2 Temperature Correction for Internal Strain

In order to make accurate comparisons to predicted strain values, measured strain values needed to be adjusted so that they would represent what the measured strain would have been if the girder was a constant 68°F throughout its cross section at the time of measurement. The correction was a two-step process. The first correction was due to the temperature of the VWSG itself, and the second correction dealt with the nonlinear temperature gradient across the cross section.

The very nature of the VWSG itself caused the need for a temperature correction to every strain reading recorded from the VWSG. The gauge measures strains by essentially measuring the tension of a steel wire anchored at each end of the gauge. The steel wire itself is susceptible to temperature deformations. This means that even if the gauge was completely restrained against movement, a temperature change within the gauge would cause a change in the strain

reading simply because the wire tension would be altered by the temperature change. The strain reading was corrected for the temperature of the gauge (relative to 68°F) by Equation 6-12 shown below:

$$\varepsilon_{rec,gt} = \varepsilon_{rec} + (T_g * \alpha_g) \quad \text{Equation 6-12}$$

Where

$\varepsilon_{rec,gt}$ is the recorded strain corrected for gauge temperature ($\mu\varepsilon$),

ε_{rec} is the recorded strain ($\mu\varepsilon$),

T_g is the gauge temperature relative to 68°F(°F), and

α_g is the coefficient of thermal expansion for the VWSG ($\mu\varepsilon/^\circ\text{F}$).

After the recorded strains were corrected to account for gauge temperature, the recorded strains were corrected for the temperature gradient over the cross section of the girder. This was done in a manner similar to that of the camber correction for temperature gradient. First, a strain change at the centroid of the cross section due to temperature was computed by Equation 6-4.

The strain change at any height within the cross section is the algebraic sum of the strain change at the centroid and the change in strain at that height due to the change in curvature of the section. The change in curvature of the cross section was calculated as a part of the camber correction procedure discussed above.

$$\Delta\varepsilon_T = \Delta\varepsilon_{cen,t} + (\Delta\phi_t \times y) \quad \text{Equation 6-13}$$

Where

$\Delta\varepsilon_T$ is the strain due to the temperature gradient ($\mu\varepsilon$),

$\Delta\varepsilon_{cen,t}$ is the strain change at the centroid of the cross section due to temperature ($\mu\varepsilon$),

$\Delta\phi_t$ is the change in curvature of the cross section due to the temperature gradient,

and

y is the distance from the centroid to the strain reading (positive downward), (in.).

These internal strain corrections were applied to every recorded strain reading reported. Some of the girders only had one VWSG, which was located in the bottom bulb of the girder. However, changes in the curvature of the midspan cross section are required in order to correct the strain reading. Therefore, curvature values for each time step for the girders containing one gauge were assumed by using curvatures from companion girders. Each casting group contained at least one girder with a “fully-instrumented” midspan cross section. The changes in curvature resulting from the temperature gradient measured in these girders were used to correct the strains in the other girders in the casting group that were not “fully-instrumented.” Figure 6-6 is an example of the effect that the temperature corrections had on the recorded strains for girder 54-4S. The temperature gradients altered the reported strain slightly over time.

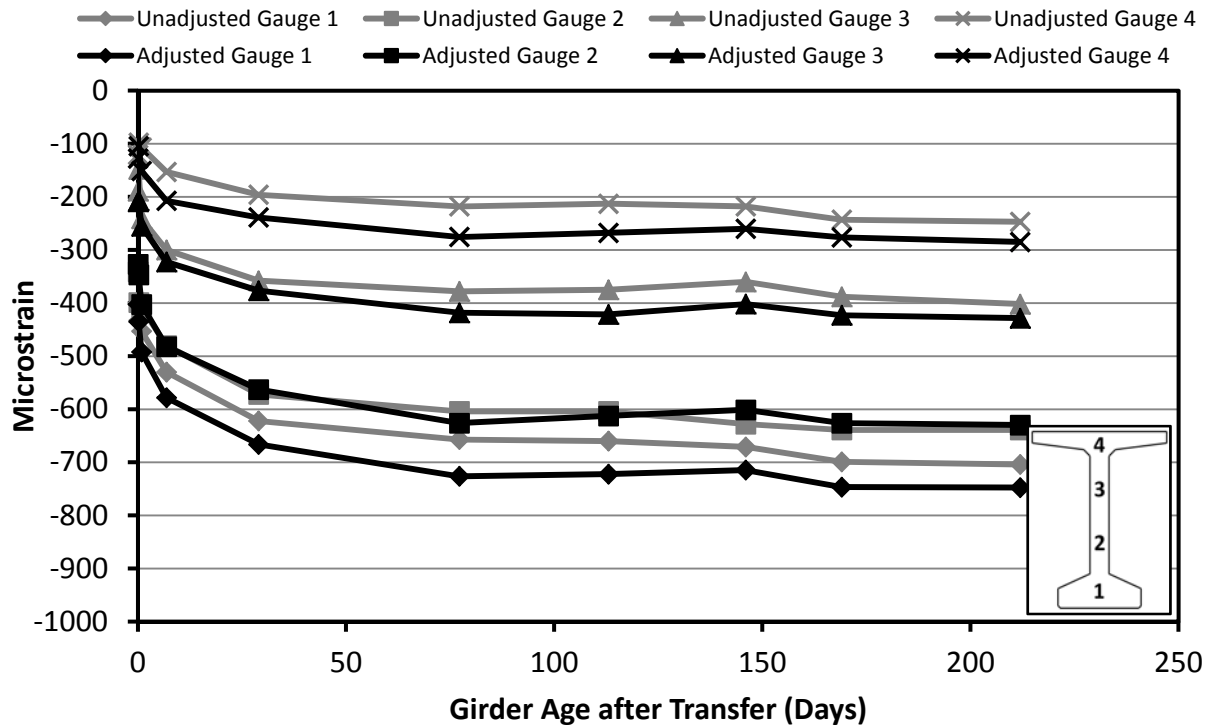


Figure 6-6: Adjusted Strains for 54-4S

6.3 Implementation of Prediction Methods

One of the main objectives of this project was to compare predicted strains, prestress losses, and cambers of prestressed bridge girders manufactured with CVC and SCC to measured values. Correct application of prediction models was a necessity to this process. In many instances, the codes required assumptions to be made about concrete properties, environmental conditions, and other factors impacting those predictions. A full table of the inputs used in the prediction models for each casting group can be found in Appendix B. First, this section will outline some general considerations involved in the prediction models that applied to all of the models discussed in Chapter 2. Next, some specific considerations for certain models are discussed. Finally, errors that were discovered and fixed in the program developed by Schrantz (2012) are discussed.

6.3.1 Concrete Strength and Modulus of Elasticity

The very nature of prediction models allows for the use of actual measured strength and modulus of elasticity values as opposed to design values. For this research, both concrete strength and modulus of elasticity values were tested at prestress release and at 28 days for each casting group. The use of measured strength and modulus of elasticity values allowed more accurate design predictions than those that used only design strengths. The difference in prediction models using design and measured strength values is discussed later in this chapter.

A direct substitution of measured strengths and modulus of elasticity values were used in all of the prediction models with the exception of the MC 90 and MC 90-KAV models. These models incorporate a mean compressive strength, which is determined using Equation 6-14 from the specified characteristic (design) strength (CEB 1990). This increase reflects the tendency for concrete producers to provide concrete at a higher strength than the required design strengths. Therefore, when the MC 90 and MC 90-KAV predictions were developed for this project, a reduced concrete strength value calculated by Equation 6-15 was input into the program so that the strength actually generated and used in the internal calculations within the program reflected the actual measured concrete strength. Note that 6.5 MPa is equivalent to 943 psi. The strengths used as input into the program are displayed in Appendix B.

$$f_{cm} = f'_c + 6.5 \quad \text{Equation 6-14}$$

Where

f_{cm} is the mean compressive strength (MPa), and

f'_c is the design compressive strength (MPa).

$$f'_{c,inp} = f'_{c,meas} - 943 \quad \text{Equation 6-15}$$

Where

$f'_{c,inp}$ is the concrete strength input into VB program (psi), and

$f'_{c,meas}$ is the measured compressive strength (psi).

6.3.2 Relative Humidity

The girders that were studied in this research, along with the cylinders that were used to determine the properties of the concrete, were stored outside and exposed to environmental conditions close to Birmingham, AL. The AASHTO 2010 code provides a relative humidity map in which annual average values can be used in prediction models based on the location in the United States. The map, shown in Figure 6-7, calls for the use of a relative humidity value of between 70 and 75 percent for Birmingham, AL. Local weather data for the first two months of curing for the specimens in this research reflected an average relative humidity of 70 percent for Birmingham, AL. Therefore, an average relative humidity value of 70 percent was used for all prediction models.



Figure 6-7: Annual Average Ambient Relative Humidity in Percent (AASHTO 2010, Fig. 5.4.3.2.3.3-1)

6.3.3 Cement Class

Both the MC 90 and the MC 90-KAV require the use of a cement class in order to determine a cement type coefficient for use in predicting the notional shrinkage coefficient, as discussed in Section 2.6.4 and 2.6.5. Because of the use of ASTM C 150 Type III cement, the cement class used was the rapid-hardening, high-strength cement, designated “RS” in the MC 90 and MC 90-KAV prediction models according to Table 4.1 in ACI 209 (2008).

6.3.4 Temperature History

The MC 90 and MC 90-KAV models incorporate the use of the maturity of the concrete at release in their creep prediction models. The maturity of the concrete, $t_{o,T}$, is determined by Equation 2-45 for the MC 90 model, and the corresponding modified equation for the MC 90-KAV model. This time-step calculation uses the concrete temperature at each given time period to calculate an adjusted age. This calculation is performed from the time the concrete is mixed until the time of prestress transfer. Recorded temperature data are only available for the concrete when it is placed in the formwork for the girder. Therefore, an assumption was made based on observation that the concrete was mixed approximately 18 minutes before it was placed in the girder, and that the temperature at mixing was constant and equal to the first recorded concrete temperature. Temperatures were recorded every six minutes after concrete placement up until the forms were being removed just prior to prestress transfer. The wires connecting the VWSG to the data recording system had to be unplugged for a period of time to allow for the removal of the formwork. During this time period, which varied for each girder, a linear cooling of the concrete was assumed. Figure 6-8 shows the resulting temperature history for Girder 54-5S from the start of casting up to prestress transfer.

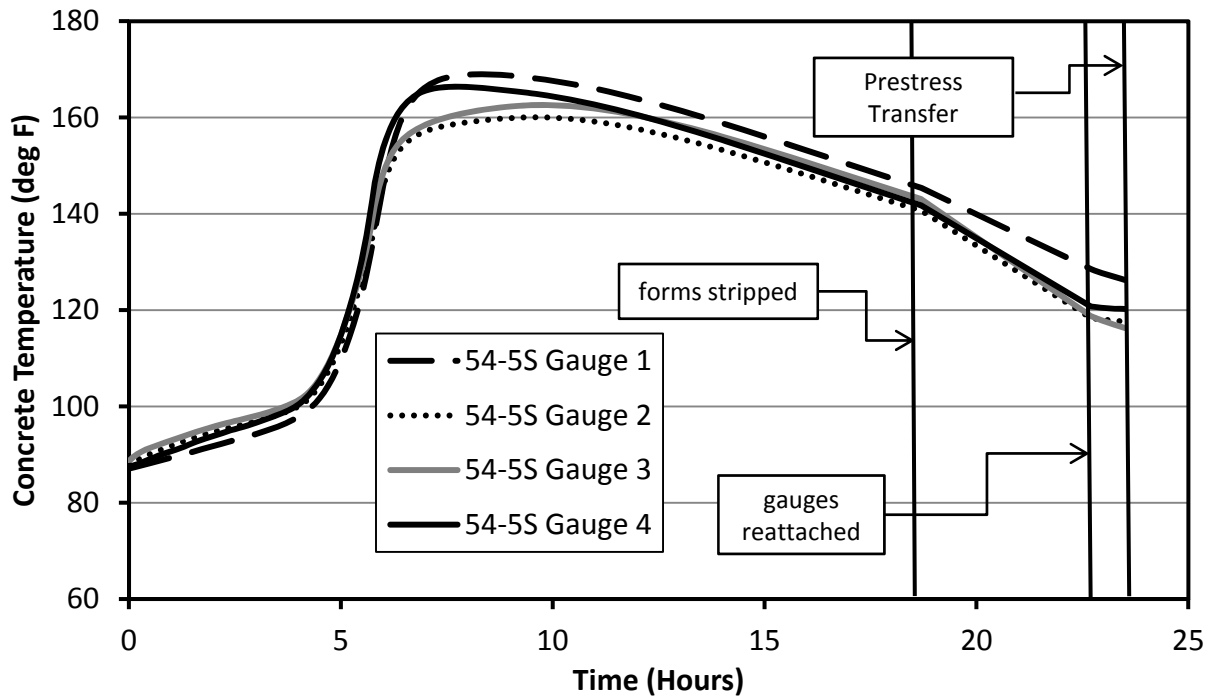


Figure 6-8: Early-Age Concrete Temperatures for 54-5S

6.3.5 ACI 209 Slump Correction Factor

A modification factor based on the slump of a concrete mixture is incorporated into the ACI 209 creep and shrinkage prediction model, as shown in Equation 2-24 and Equation 2-53. The ACI 209 method was developed before concrete mixtures started including significant amounts of water-reducing admixtures. Therefore, as Roberts (2005) shows, if the actual field-measured slump values for concrete mixtures are used in the predictions for mixtures that contain water-reducing admixtures, the result would be the significant over-prediction of concrete strain and camber. A corrected slump value should be used; one that reflects the expected slump of the concrete mixture without the water-reducing admixtures (Roberts 2005). Accordingly, corrected slump values of 0 in. for SCC and a slump value of 0.5 in. for CVC were used for the ACI 209 predictions for the concretes involved in this research project.

6.3.6 ACI 209 Total Cement Content Correction Factor

The ACI 209 shrinkage prediction model also includes a modification factor based on total cement content. An assumption was made by Ellis (2012) to include the total weight of supplementary cementitious materials (SCM) when determining this factor using Equation 2-46. The concrete mixtures used in this project included slag cement as an SCM. Therefore, the total weight of portland cement and the slag cement was included when calculating the cement content modification factor.

6.3.7 MC 90-KAV Cement Type Modification

Modifications made to the MC 90 by Kavanaugh (2008) are discussed in Section 2.5.5. It was noted that the equation used to calculate the temperature-adjusted concrete age, $t_{o,T}$, included the effect of cement type. This means that when using the MC 90-KAV method, the temperature-adjusted age should not be modified by Equation 2-46, but rather used directly in place of t_o where applicable.

6.3.8 Modifications to Schrantz (2012) VB Code

Throughout the process of developing predictions for each casting group in this study, two errors were found in the VB code written by Schrantz (2012). These errors were fixed and the prediction models developed using the updated code reflected these changes. The first error that was discovered involved the input of the size of prestressing strand used in the girder being analyzed. A mistake in the code caused the program to be unable to recognize the ½ -inch strand input. When the ½ in. strand was selected, the program assumed a strand area of 0 in², meaning that it behaved as though the strand was not present. Thus, the predictions for the bulb-tee girders documented by Schrantz (2012) are incorrect because they did not include any lightly stressed ½ in. strands in the top flange.

The second error involved the implementation of the MC 90-KAV prediction model. Section 6.3.6 outlines the fact that the Kavanaugh (2008) modification includes the modification for cement type in the adjusted age calculation. In the original Schrantz (2012) VB code, however, both the MC 90 and the MC 90-KAV adjusted ages were modified using the cement type modification equation. The code reflected the thesis of Kavanaugh (2008). Therefore, the predictions made by Schrantz (2012) using the MC 90-KAV method were incorrect. The change was made in the code for this study so that the temperature-adjusted age was calculated correctly as originally intended for the MC 90-KAV prediction model.

6.4 Ultimate Creep Coefficients and Ultimate Shrinkage Strains

Each prediction method in this project utilized an ultimate creep coefficient and an ultimate shrinkage value to predict the growth of strain over time. One of the ways to compare the prediction methods involves comparing the creep coefficients and ultimate shrinkage values. Table 6-1 contains the predicted ultimate creep coefficients for each casting group. The ultimate creep coefficients are compared in a graphical form in Figure 6-9. Table 6-2 contains the predicted ultimate shrinkage strains for each casting group. The predicted ultimate shrinkage strains are presented in graphical form in Figure 6-10.

Table 6-1: Predicted Ultimate Creep Coefficients

Casting Group	AASHTO ('04)	AASHTO ('10)	ACI 209	MC 90	MC 90-KAV
A	1.283	1.012	1.252	1.590	1.362
B	1.255	1.034	1.222	1.560	1.337
C	1.236	1.043	1.252	1.540	1.320
D	1.320	1.240	1.272	1.556	1.408
E (SCC)	1.282	1.128	1.252	1.583	1.358
E (CVC)	1.263	1.029	1.222	1.559	1.339
F	1.256	1.104	1.249	1.557	1.336
G	1.244	1.092	1.272	1.553	1.330
H	1.269	1.167	1.249	1.603	1.365
I	1.242	1.041	1.272	1.554	1.330
J	1.261	1.100	1.249	1.549	1.345
K	1.240	1.103	1.272	1.568	1.338
L (SCC)	1.328	1.308	1.249	1.589	1.417
L (CVC)	1.281	1.180	1.272	1.608	1.372

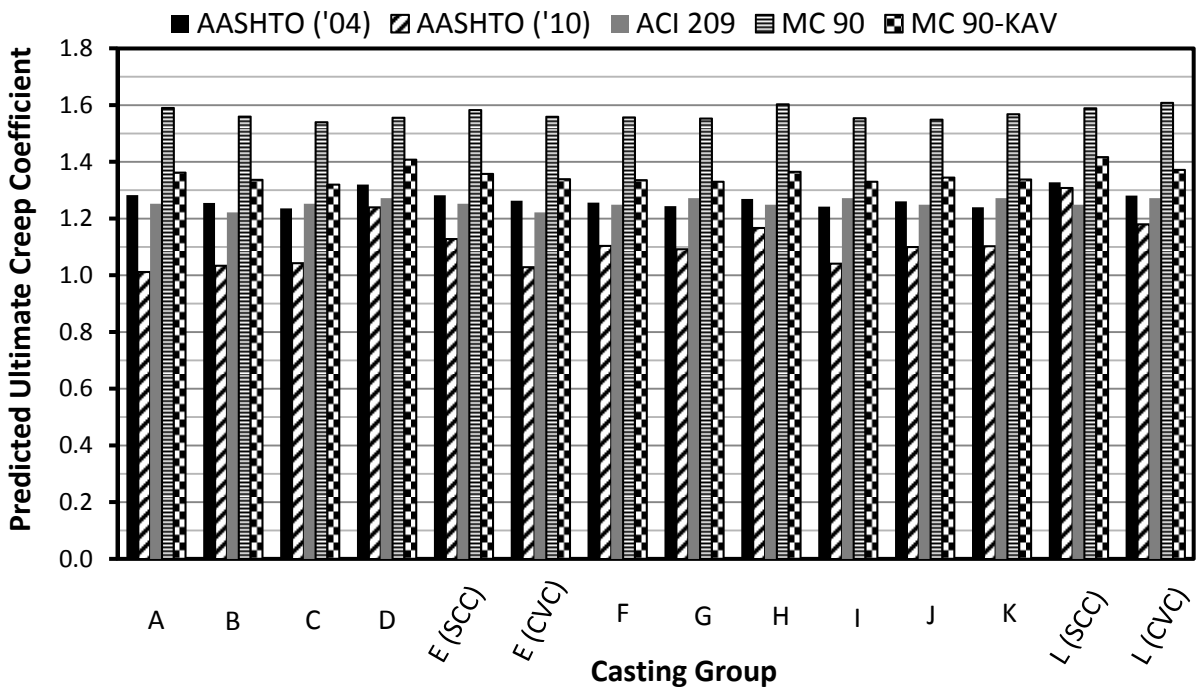


Figure 6-9: Predicted Ultimate Creep Coefficients

A number of observations can be made regarding the differences in the prediction models as they pertain to the girders used in this research based on the ultimate creep coefficients. The first observation is that the MC 90 predicts significantly higher ultimate creep coefficients compared to all of the other models. The MC 90-KAV model predicts the next highest creep coefficients, followed closely by the AASHTO 2004 and AASHTO 2010 models. For all but one casting group, the AASHTO 2010 model predicted the lowest ultimate creep coefficient.

Table 6-2: Predicted Ultimate Shrinkage Strains (in./in.)

Casting Group	AASHTO ('04)	AASHTO ('10)	ACI 209	MC 90	MC 90-KAV
A	-0.000567	-0.000311	-0.000416	-0.000321	-0.000321
B	-0.000567	-0.000318	-0.000347	-0.000301	-0.000301
C	-0.000567	-0.000321	-0.000413	-0.000290	-0.000290
D	-0.000567	-0.000383	-0.000356	-0.000353	-0.000353
E (SCC)	-0.000567	-0.000348	-0.000348	-0.000324	-0.000324
E (CVC)	-0.000567	-0.000319	-0.000348	-0.000314	-0.000314
F	-0.000567	-0.000341	-0.000410	-0.000307	-0.000307
G	-0.000567	-0.000335	-0.000356	-0.000291	-0.000291
H	-0.000567	-0.000351	-0.000410	-0.000291	-0.000291
I	-0.000567	-0.000318	-0.000353	-0.000287	-0.000287
J	-0.000567	-0.000337	-0.000410	-0.000304	-0.000304
K	-0.000567	-0.000334	-0.000353	-0.000275	-0.000275
L (SCC)	-0.000567	-0.000392	-0.000409	-0.000331	-0.000331
L (CVC)	-0.000567	-0.000357	-0.000351	-0.000306	-0.000306

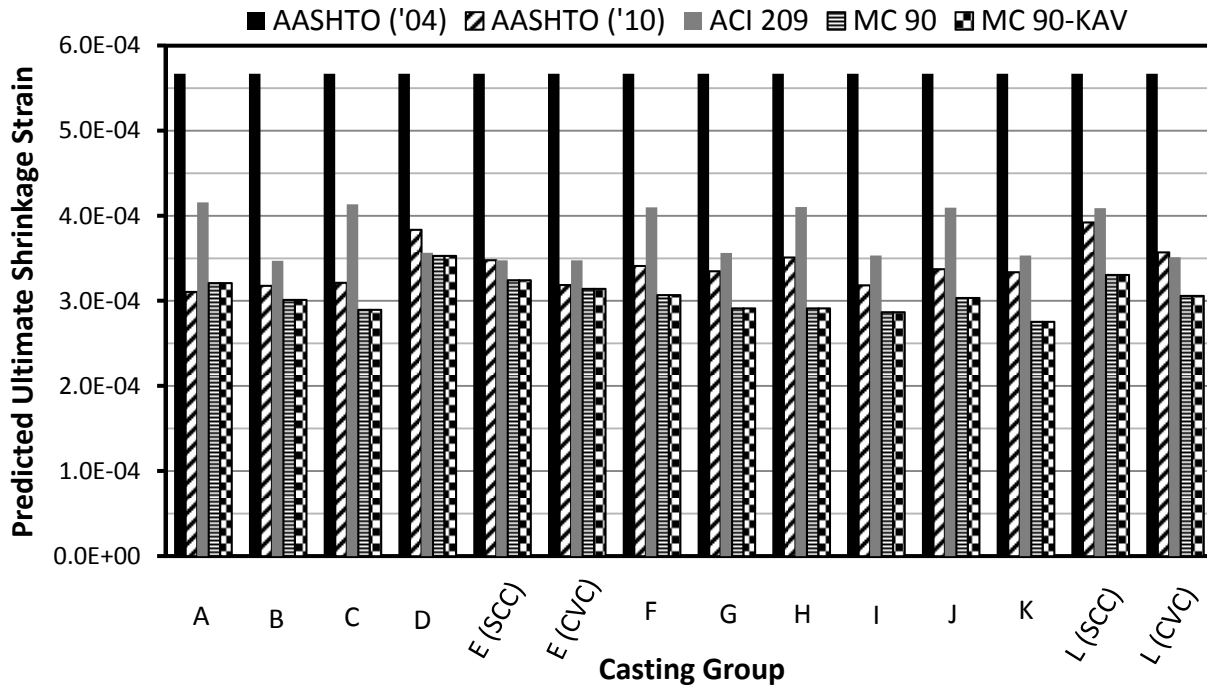


Figure 6-10: Predicted Ultimate Shrinkage Strains

The AASHTO 2004 prediction method predicted the most shrinkage strain for all casting groups. The prediction was the same for each casting group because the AASHTO 2004 method only takes volume-to-surface area and relative humidity into account. The ACI 209 method predicted the second-highest shrinkage strains for most of the casting groups. The MC 90 and MC 90-KAV had the lowest ultimate shrinkage predictions for most of the casting groups. These two models predicted the same ultimate shrinkage strains because they used the same shrinkage prediction equations.

While it can be useful to compare the ultimate creep coefficients and ultimate shrinkage strains predicted for each casting group in this research, the varying material properties of each group mean that a direct comparison of these ultimate values across casting groups is not entirely equitable. However, the prediction methods can be compared to each other within each casting

group, as discussed above. Definitive conclusions about the accuracy of the prediction models must be determined from comparisons to measured values.

6.5 Strains

As outlined in Chapter 4, VWSGs were used in each girder in this project to measure internal strains. The complete results of these measurements at midspan for each girder are located in Appendix C. Predicted values based on each prediction model were also developed for each casting group. A plot showing both the measured and predicted strains over time does not yield comparisons that are readily apparent. However, a plot of measured versus predicted strain values for certain ages of specific girders is more useful. These plots are shown below followed by an explanation of results that can be seen in these figures. The figures show measured values versus predicted values for three concrete ages. These ages are immediately after prestress transfer, 56 days after prestress transfer, and the age at actual erection in the bridge.

Figure 6-11, Figure 6-12, Figure 6-13, and Figure 6-14 contain the measured values versus predicted values for the VWSG in the bottom bulb of each girder at midspan, which was located at a height of 6 in. in the BT-54 girders and 8.8 in. in the BT-72 girders. In general, most of the values on these plots fall within the 20% error range. This indicates that for the most part, all of the models are doing at least a decent job of predicting the bottom-flange strains in these girders, regardless of concrete type and the size of the girder. The values at prestress transfer are indicated in Figure 6-11. These values are found in similar locations on the other figures.

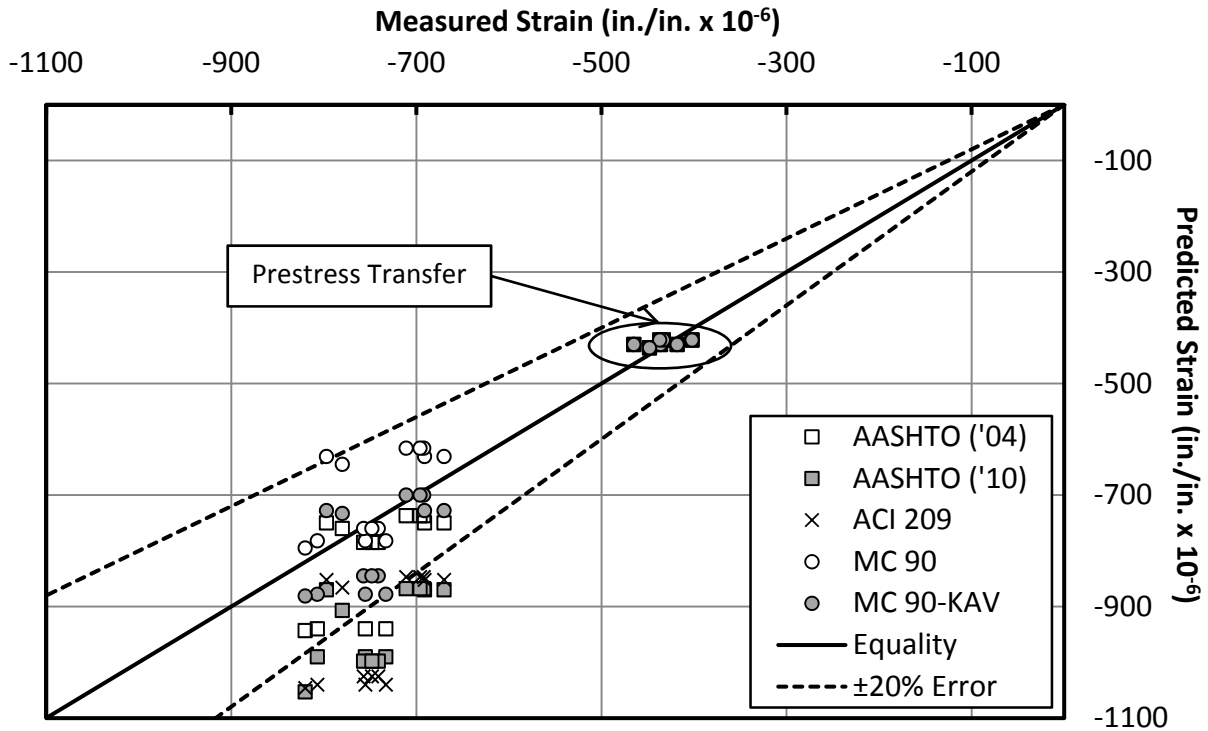


Figure 6-11: Measured Versus Predicted Internal Strains – SCC BT-54 Gauge 1

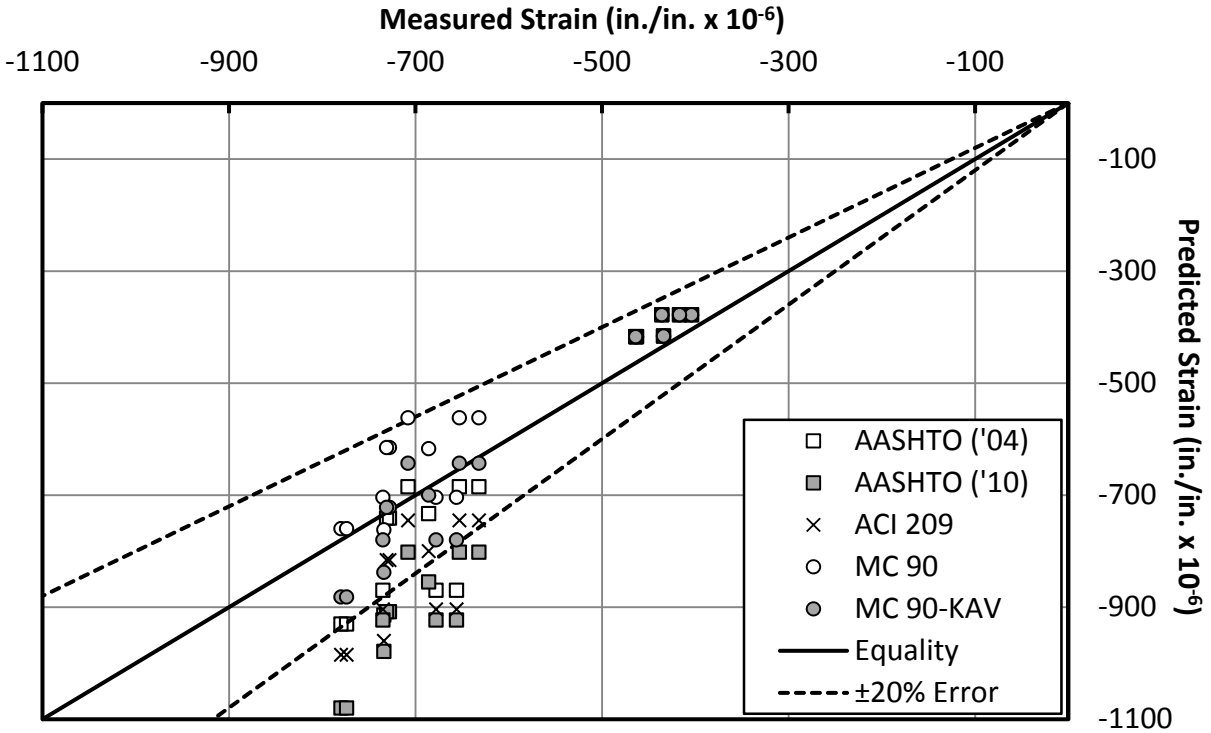


Figure 6-12: Measured Versus Predicted Internal Strains – CVC BT-54 Gauge 1

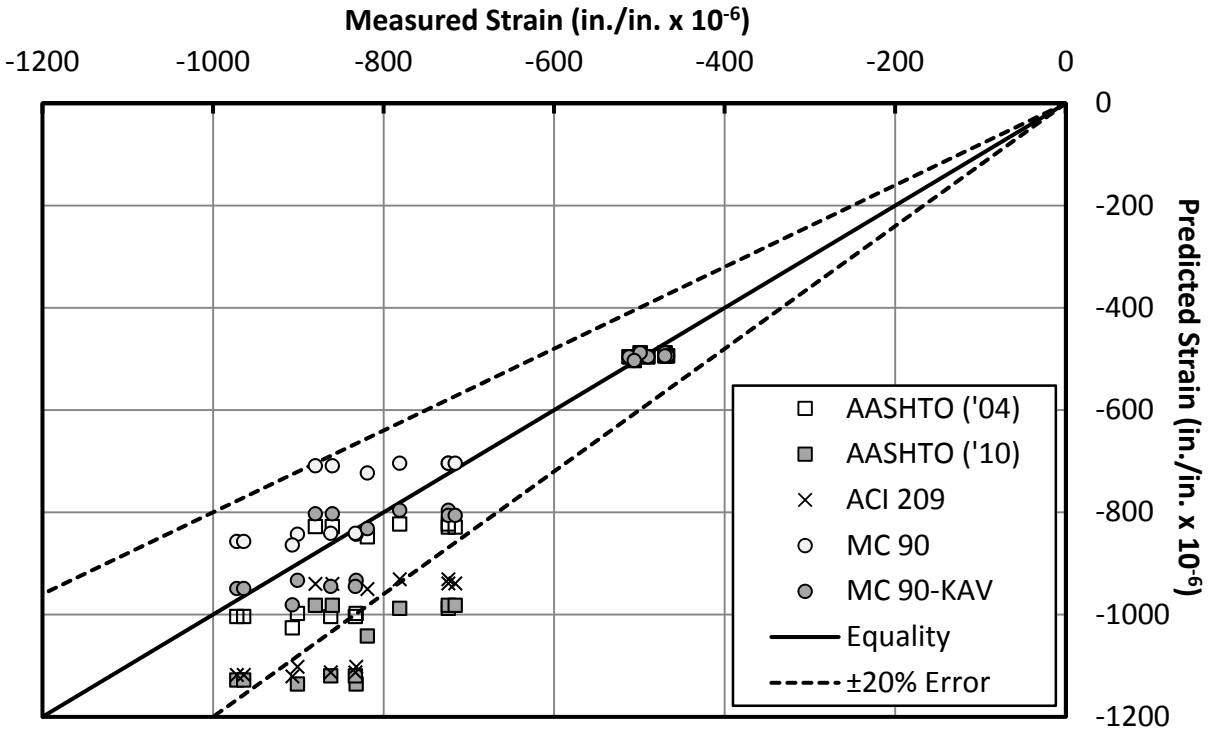


Figure 6-13: Measured Versus Predicted Internal Strains – SCC BT-72 Gauge 1

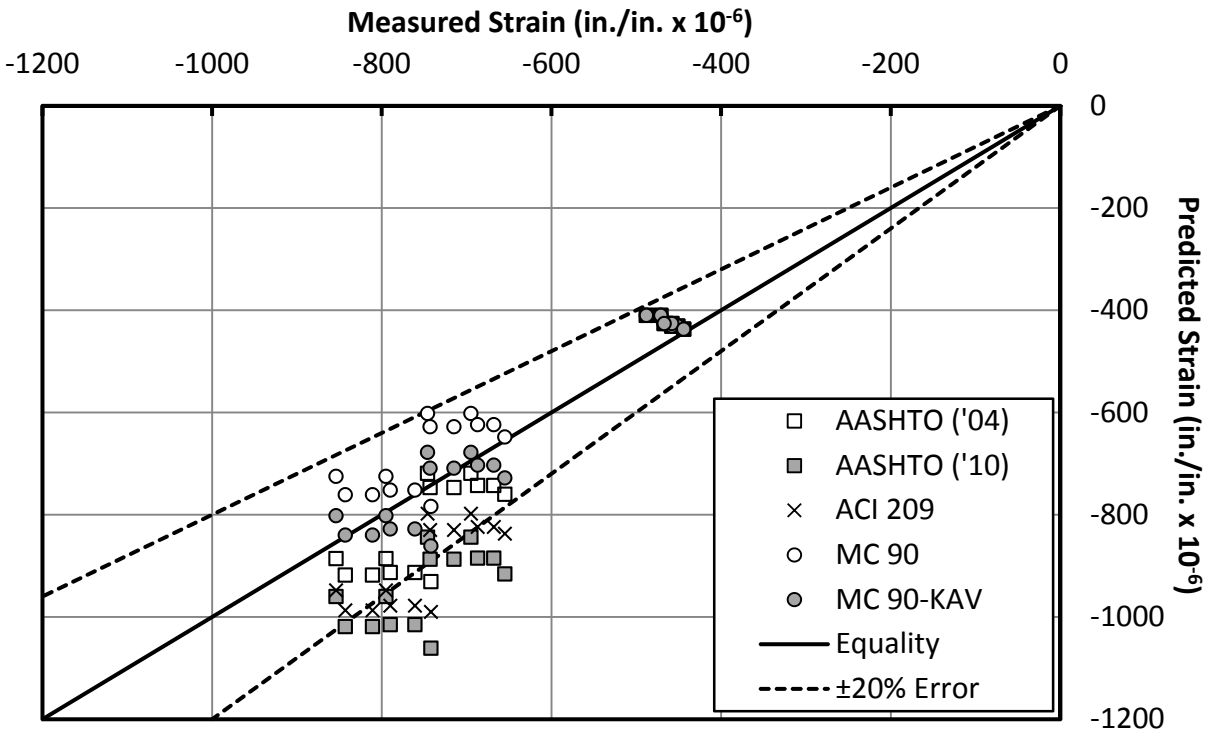


Figure 6-14: Measured Versus Predicted Internal Strains – CVC BT-72 Gauge 1

All of the values that represent the strains just after transfer fall very close to equality. This is due to the fact that at the time of transfer, strand relaxation is the only time-dependent behavior that is acting. Creep and shrinkage do not have a significant effect until later time steps. There are marked differences in the models for time-dependent behavior that takes place after prestress transfer. For example, the AASHTO 2004 model accurately predicted strains at 56 days, but over-predicted strains at later ages. The AASHTO 2010 and ACI 209 models both consistently over-predicted strains, while the MC 90 model consistently under-predicted strains, although all of the predictions were within the $\pm 20\%$ error lines. All of the predictions using the MC 90-KAV model were within the $\pm 20\%$ error lines.

Figure 6-15, Figure 6-16, Figure 6-17, and Figure 6-18 contain strain values corresponding to “Gauge 2” which was located low in the web at a height of 19.5 in. in the BT-54 girders and 24 in. in the BT-72 girders. Trends that were observed in the plots for Gauge 1 seem to continue in these plots, and the predictions from the MC 90 and MC 90-KAV are all still within the $\pm 20\%$ error lines. However, there is overall more scatter of the data points, with more strains falling outside of the $\pm 20\%$ error lines.

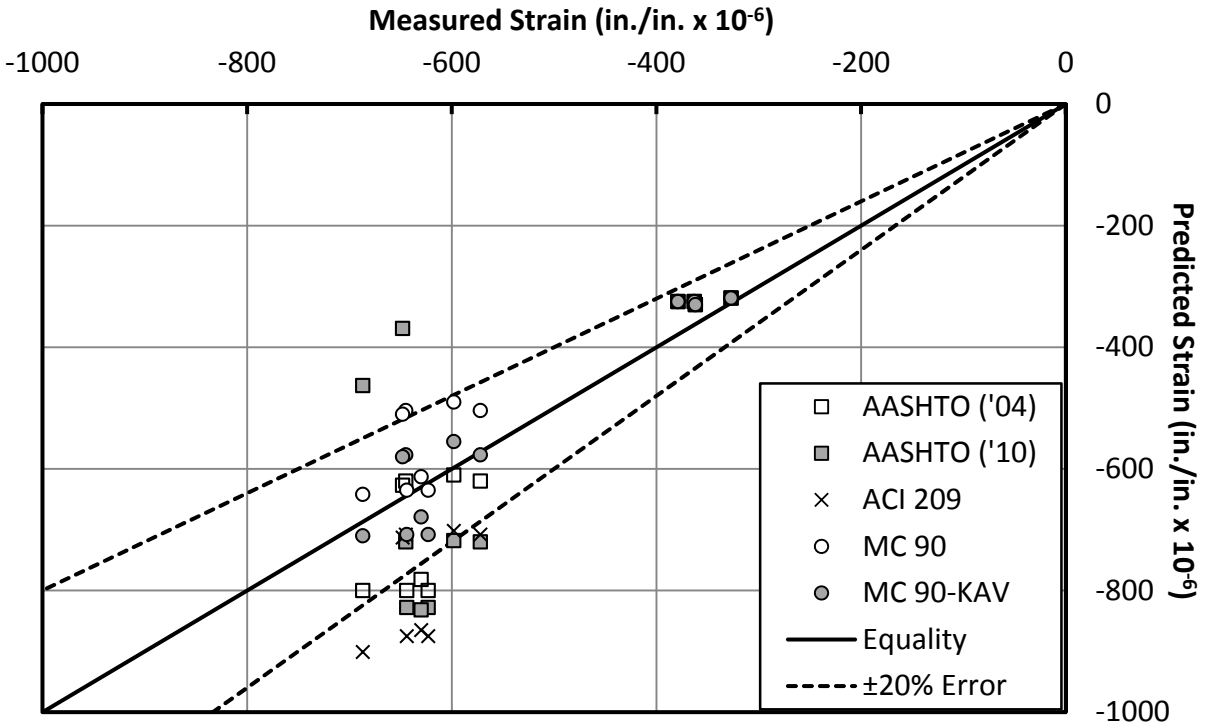


Figure 6-15: Measured Versus Predicted Internal Strains – SCC BT-54 Gauge 2

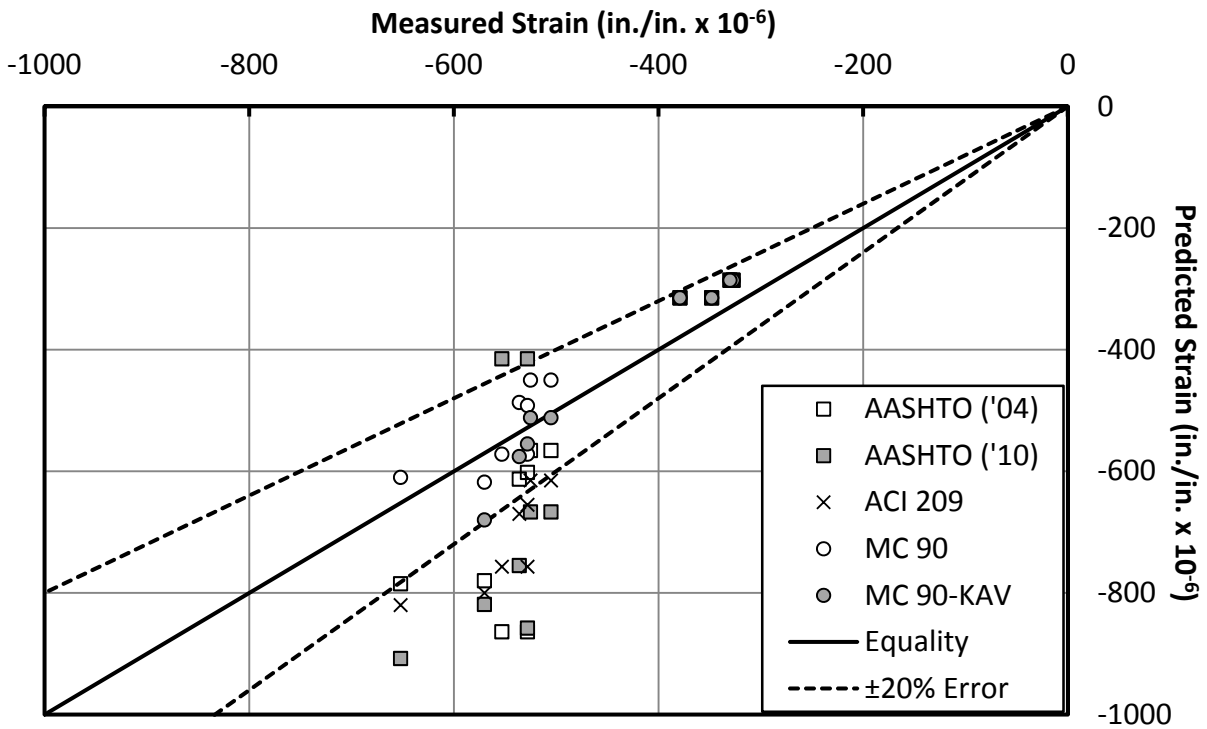


Figure 6-16: Measured Versus Predicted Internal Strains – CVC BT-54 Gauge 2

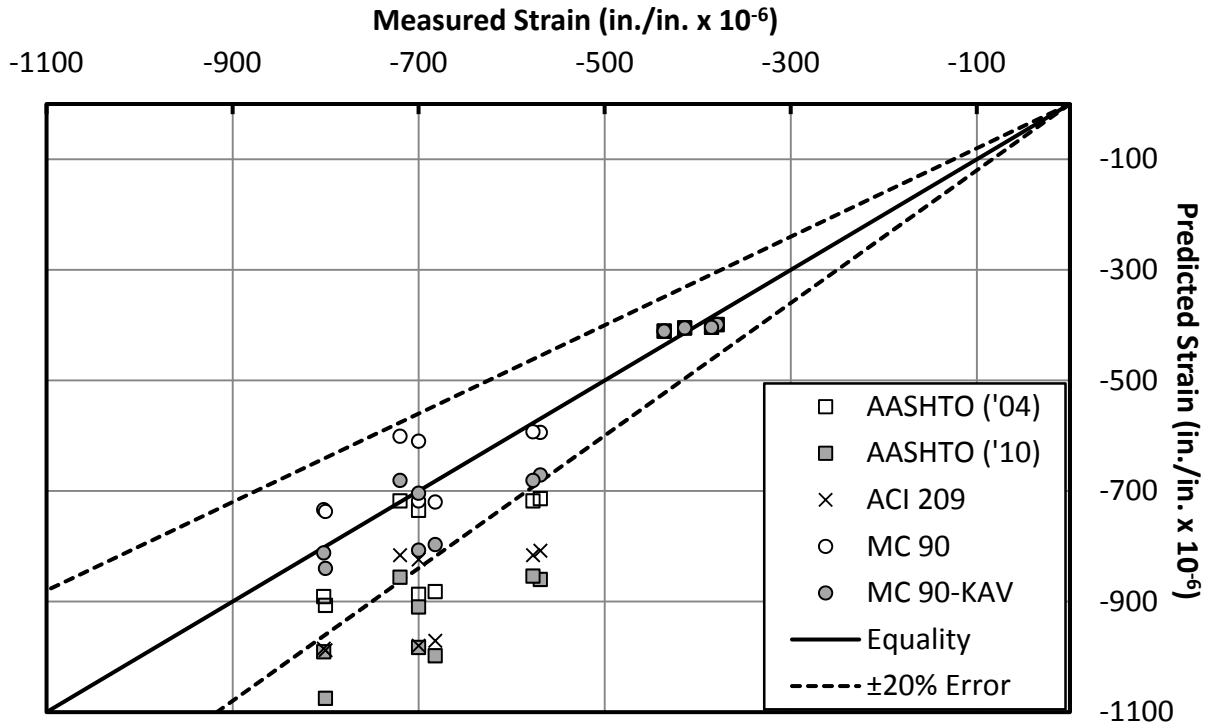


Figure 6-17: Measured Versus Predicted Internal Strains – SCC BT-72 Gauge 2

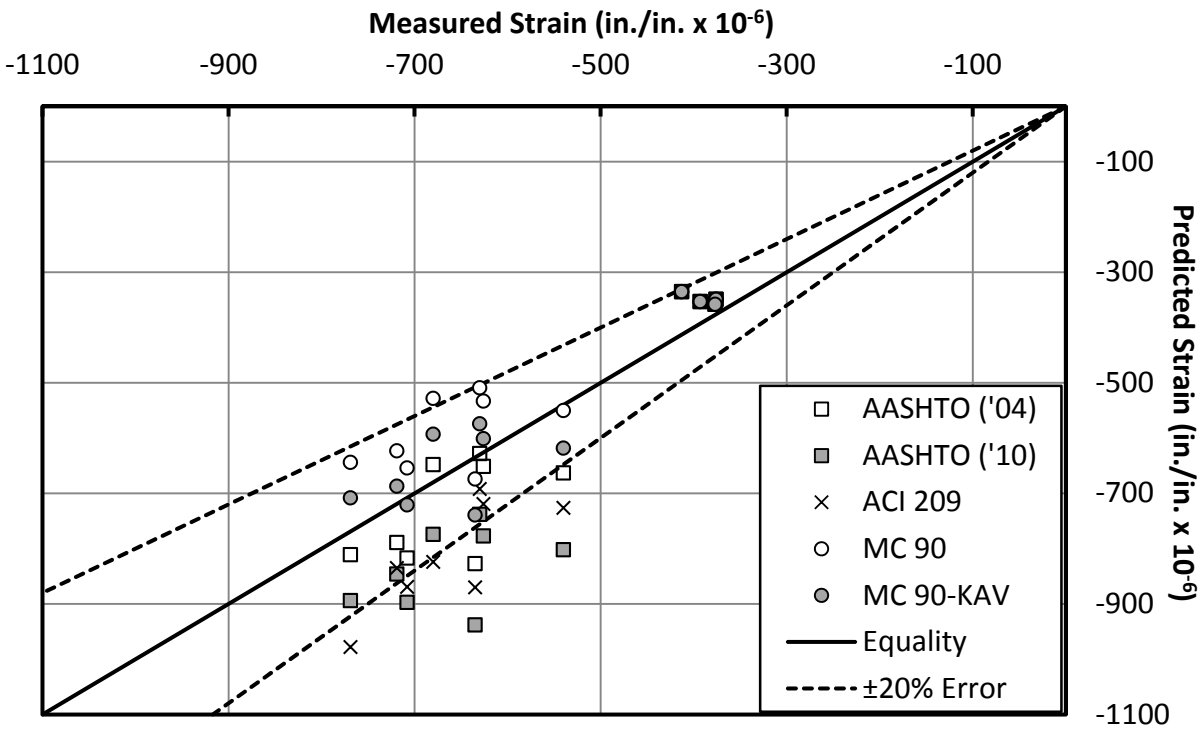


Figure 6-18: Measured Versus Predicted Internal Strains – CVC BT-72 Gauge 2

Figure 6-19, Figure 6-20, Figure 6-21, and Figure 6-22 contain strain values for “Gauge 3,” located high in the web at a height of 37.5 in. in the BT-54 girders and 51 in. in the BT-72 girders. Again, the trends observed in the previous plots apply to these Gauge 3 plots as well. However, the scatter in the data continues to increase, with a significant proportion of the predictions falling outside of the $\pm 20\%$ error lines, with most being over-predictions. Also, the values representing strains just after transfer are slightly under-predicted in all of the girders.

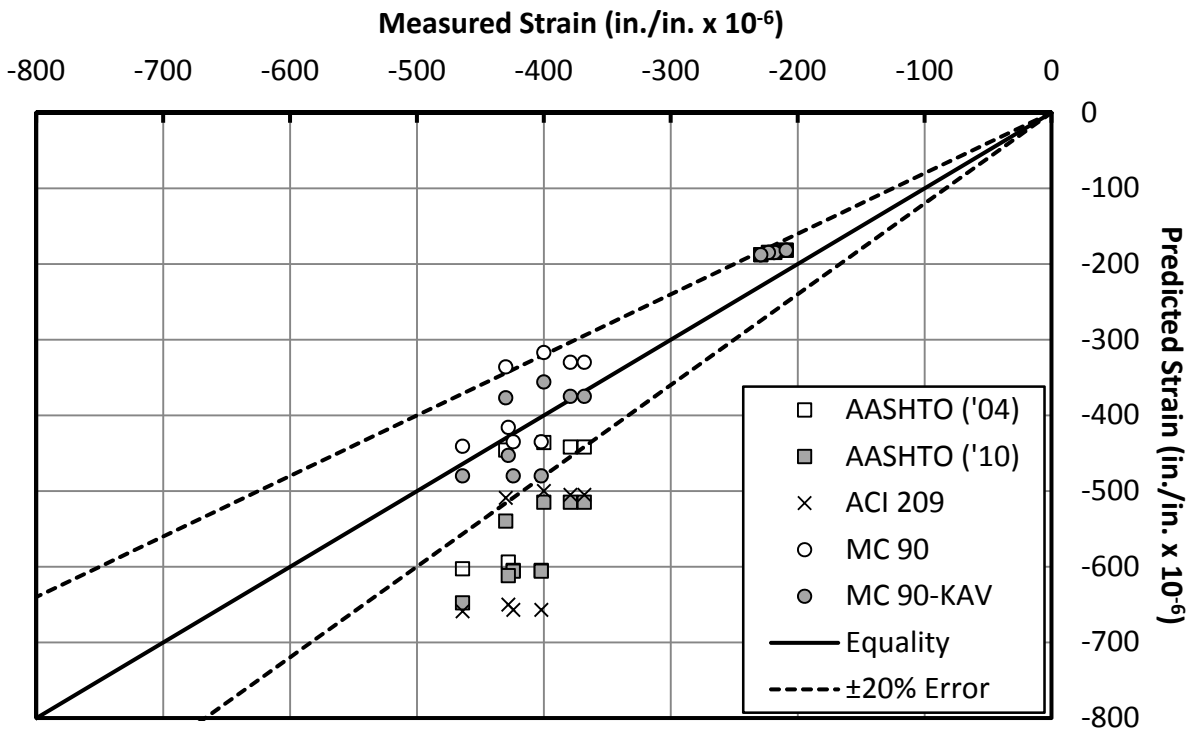


Figure 6-19: Measured Versus Predicted Internal Strains – SCC BT-54 Gauge 3

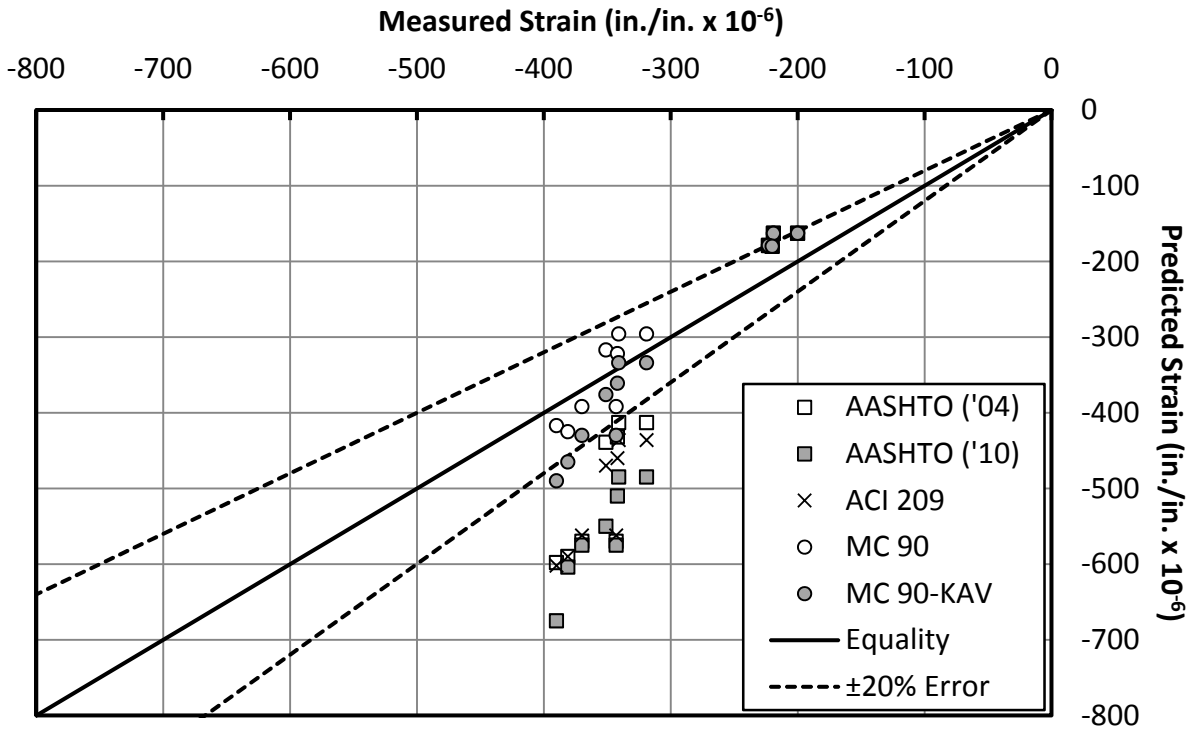


Figure 6-20: Measured Versus Predicted Internal Strains – CVC BT-54 Gauge 3

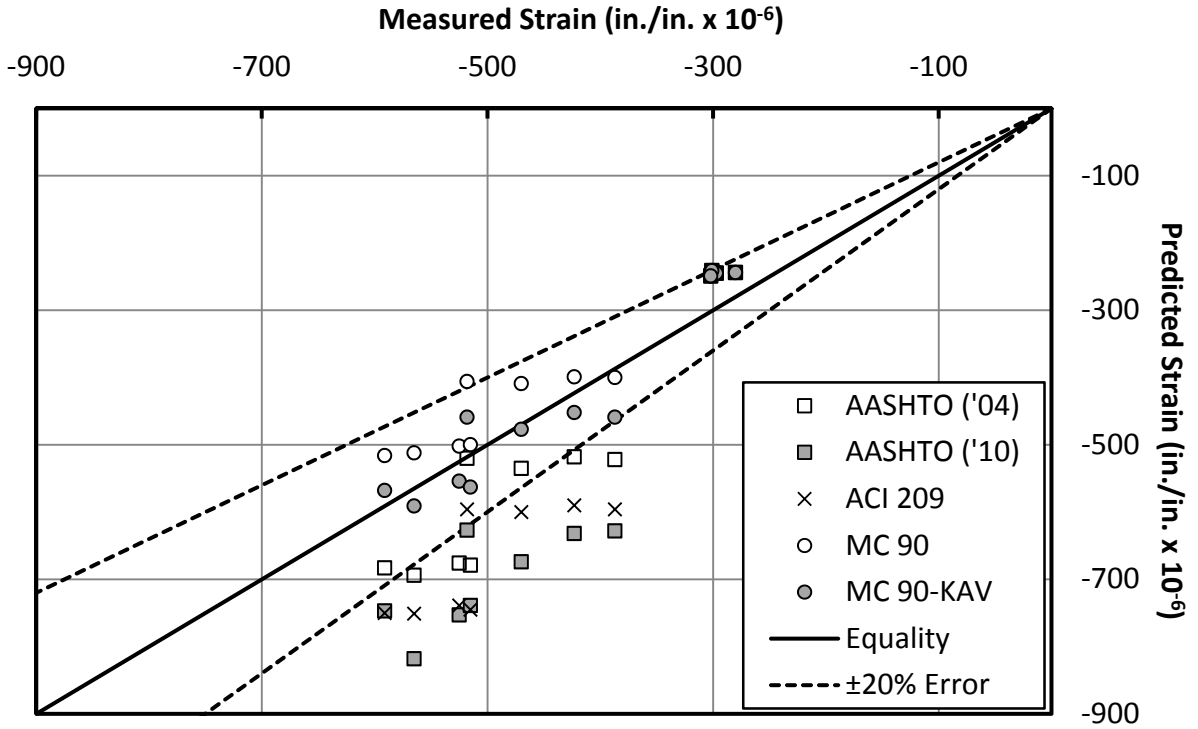


Figure 6-21: Measured Versus Predicted Internal Strains – SCC BT-72 Gauge 3

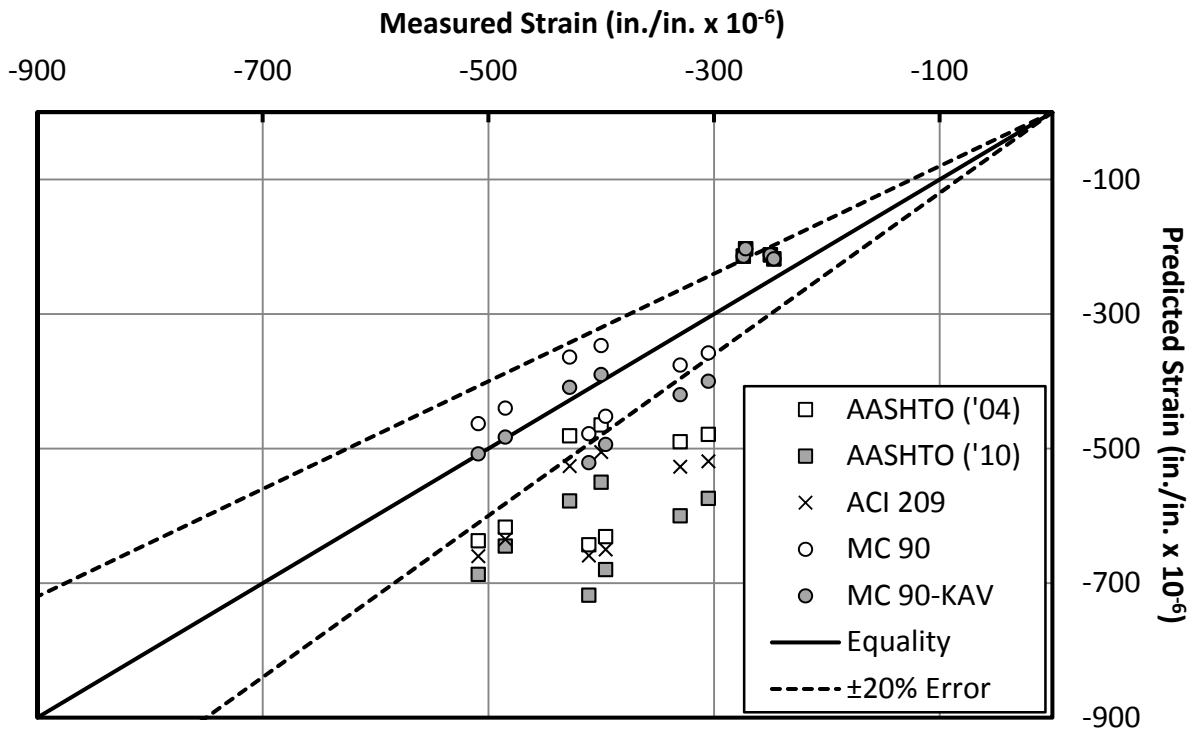


Figure 6-22: Measured Versus Predicted Internal Strains – CVC BT-72 Gauge 3

Finally, Figure 6-23, Figure 6-24, Figure 6-25, and Figure 6-26 contain the measured versus predicted strain values for the top-flange VWSG located at a height of 52 in. and 70 in. in the BT-54 and BT-72 girders respectively. These plots contain the most error, with a large number of predictions falling outside the error lines. One of the probable sources for this error is the presence of a temperature gradient that is rapidly changing during prestress transfer. The method used to correct for the temperature gradient may not be an accurate representation of what is actually present in the cross section. Inaccuracies in later ages might be due to the different accuracies of the creep and shrinkage models.

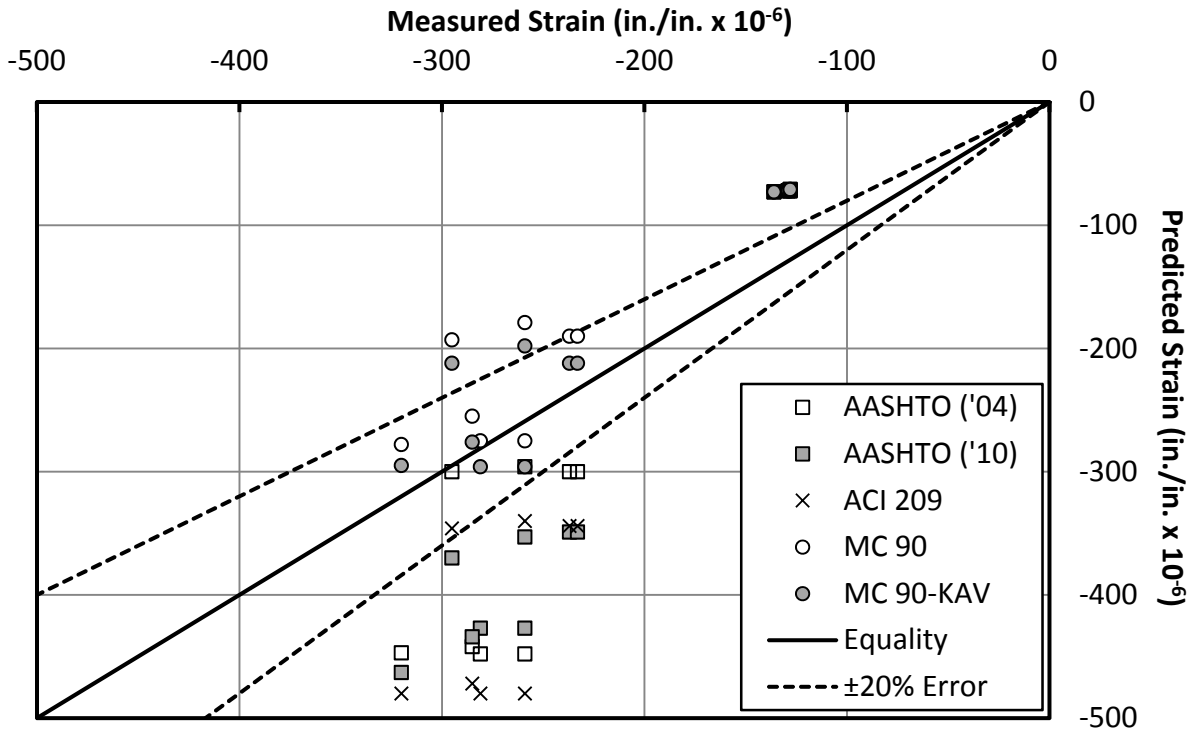


Figure 6-23: Measured Versus Predicted Internal Strain – SCC BT-54 Gauge 4

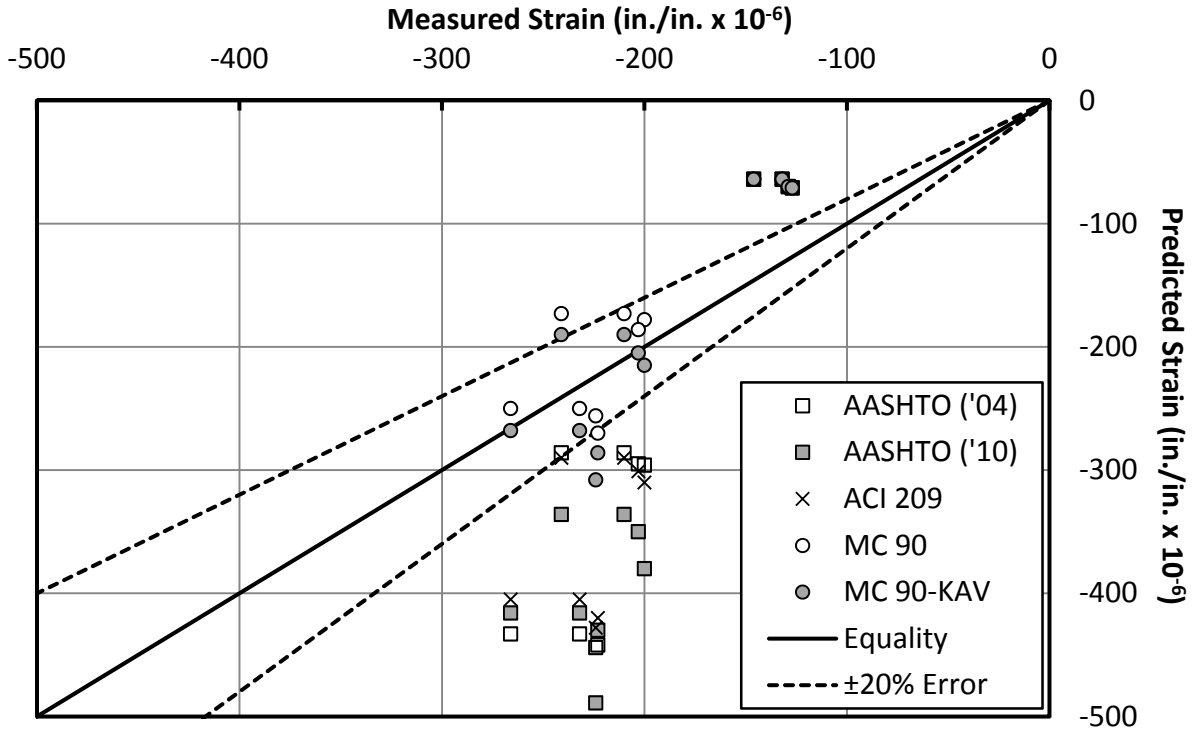


Figure 6-24: Measured Versus Predicted Internal Strain – CVC BT-54 Gauge 4

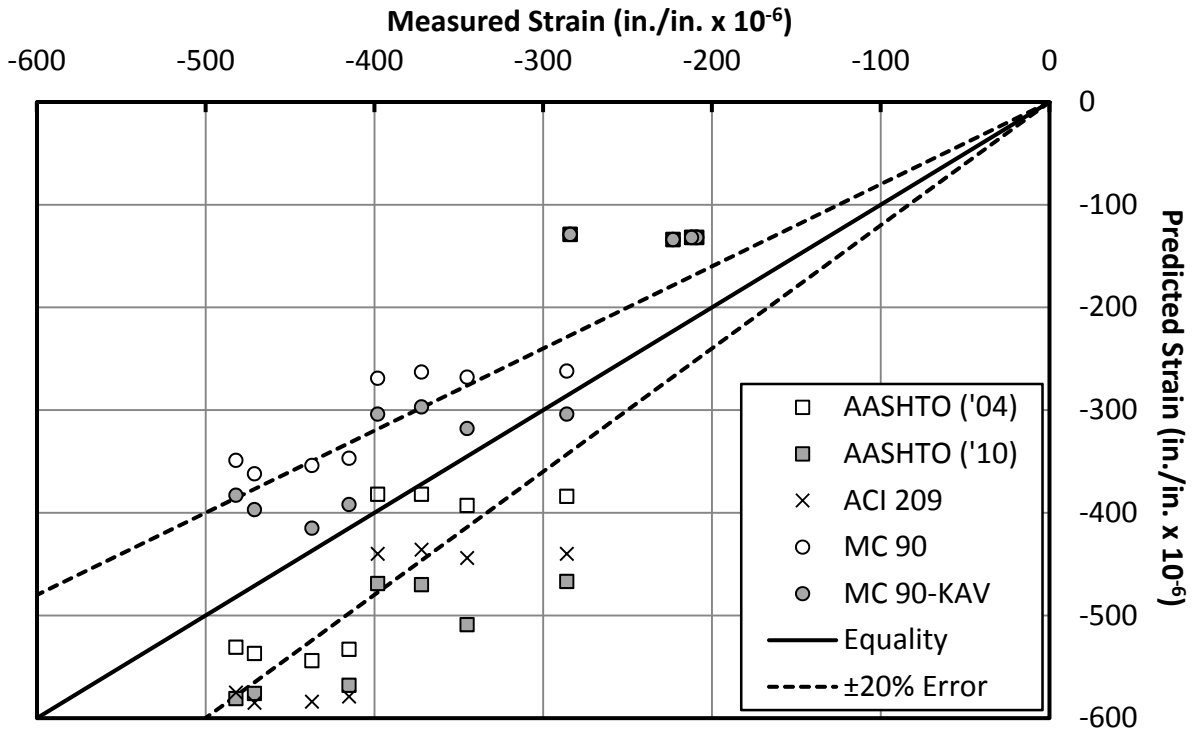


Figure 6-25: Measured Versus Predicted Internal Strain – SCC BT-72 Gauge 4

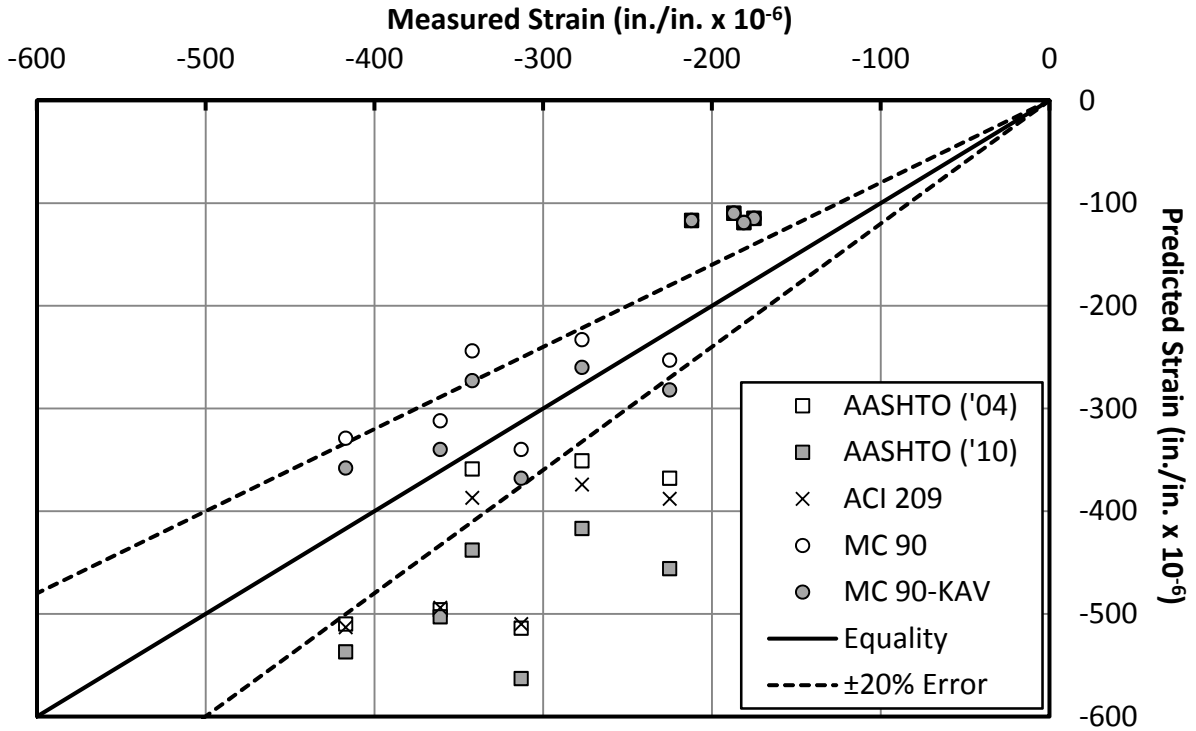


Figure 6-26: Measured Versus Predicted Internal Strain – CVC BT-72 Gauge 4

The most accurate predictions occur at the bottom of the girder, where the prestressing force is concentrated most heavily. While there is some prestressing at the top of the girder, it is only lightly stressed. This means that the creep strains in the concrete would be much more dominant at the bottom of the girder as opposed to the top. The shrinkage models will be much more influential at the top of the girders where creep does not have as much of an effect. This could point to the conclusion that the creep predictions are more accurately predicting the girder response to creep than the shrinkage models are predicting shrinkage strains. This finding agrees with the results of the laboratory research performed by Ellis (2012) on the creep and shrinkage characteristics of the concrete used in these girders.

A statistical evaluation of the error between the predicted and measured values was performed for the bottom-flange (gauge 1) strains by determining the unbiased estimate of the standard deviation of the fractional error of the predicted time-dependent strains according to Equation 6-16 (McCuen 1985). The fractional error between the predicted and measured values at 56 days and at erection was calculated using Equation 6-17 in order to account for variation in the initial predictions and initial measurements.

$$S = \sqrt{\frac{1}{n-1} \sum_i^n \Delta_i^2} \quad \text{Equation 6-16}$$

Where

S is the unbiased estimate of the standard deviation of the fractional error,

n is the number of data points, and

Δ is the fractional error.

$$\Delta = \frac{(\varepsilon - \varepsilon_{initial})_{predicted} - (\varepsilon - \varepsilon_{initial})_{measured}}{(\varepsilon - \varepsilon_{initial})_{measured}} \quad \text{Equation 6-17}$$

Where

ε is the strain at the time considered (in./in.), and

$\varepsilon_{initial}$ is the strain at prestress transfer (in./in.).

The results of this statistical analysis are shown in Table 6-3. The error statistics were calculated by girder and concrete type as well as strictly by concrete type for each prediction method used. A value closer to zero corresponds to a smaller error of the predicted time-dependent strains relative to the measured quantities.

Table 6-3: Unbiased Estimate of the Standard Deviation of the Prediction Errors for Bottom-Flange Strains

		SCC 54	SCC 72	CVC 54	CVC 72	All SCC	All CVC
AASHTO 2004	56 Day	0.19	0.26	0.29	0.40	0.22	0.34
	Erection	0.44	0.32	0.83	0.51	0.37	0.64
AASHTO 2010	56 Day	0.65	0.82	0.86	1.04	0.71	0.92
	Erection	0.80	0.68	1.14	0.84	0.71	0.95
ACI 209	56 Day	0.57	0.63	0.57	0.76	0.58	0.65
	Erection	0.91	0.59	0.98	0.71	0.74	0.81
MC 90	56 Day	0.33	0.31	0.27	0.21	0.31	0.23
	Erection	0.08	0.16	0.21	0.12	0.12	0.16
MC 90-KAV	56 Day	0.09	0.20	0.15	0.24	0.15	0.20
	Erection	0.36	0.17	0.54	0.26	0.27	0.39

The values reported in Table 6-3 seem to indicate that the MC 90 and MC 90-KAV models are the best predictors of internal strain growth over time in the bottom flange of the girders in this research. In addition, there is not an improved accuracy overall when predicting

strain growth in CVC girders versus SCC girders. In fact, in a majority of the prediction methods at both ages the SCC strain changes are somewhat better predicted than those in the CVC girders. Thus, the time-dependent behavior of the SCC is at least as predictable as the behavior of the CVC.

6.6 Prestress Losses

Prestress losses were not directly measured in this research. However, prestress losses were assumed based on the strain results from the VWSGs. The initial jacking stress was assumed to be 202.5 ksi in all of the prestressing steel with the exception of the lightly stressed top strands. However, effective prestress was only calculated at the level of the bottommost gauge in each girder, which corresponded closely to the centroid of the prestressing steel located in the bottom bulb of the girder at midspan. Relaxation of the strands between the time of jacking and transfer was calculated based on Equation 2-12 in a step-wise fashion. Therefore, the stress in the prestressing strands was assumed to be known just before transfer.

After transfer, strain readings were taken and corrected for temperature as reported in Section 6.5. Compatibility and the bond between the concrete and prestressing strand means that a strain change measured by the VWSG corresponds directly to a strain change in the prestressing strand at the level of the gauge. Furthermore, assuming linear-elastic behavior of the prestressing steel means that a change in strain corresponds directly to a change in stress in the strand. Therefore, the measured strains reported in Section 6.5 were used to directly calculate the effective prestress in the prestressing steel at various girder ages. Strand relaxation over time was also accounted for by using Equation 2-15 across each age.

The following figures show the measured stress in the prestressing steel as well as predicted stresses based on the different creep and shrinkage models used in predicting time-dependent deformations. The predictions and measured results are reported by casting group.

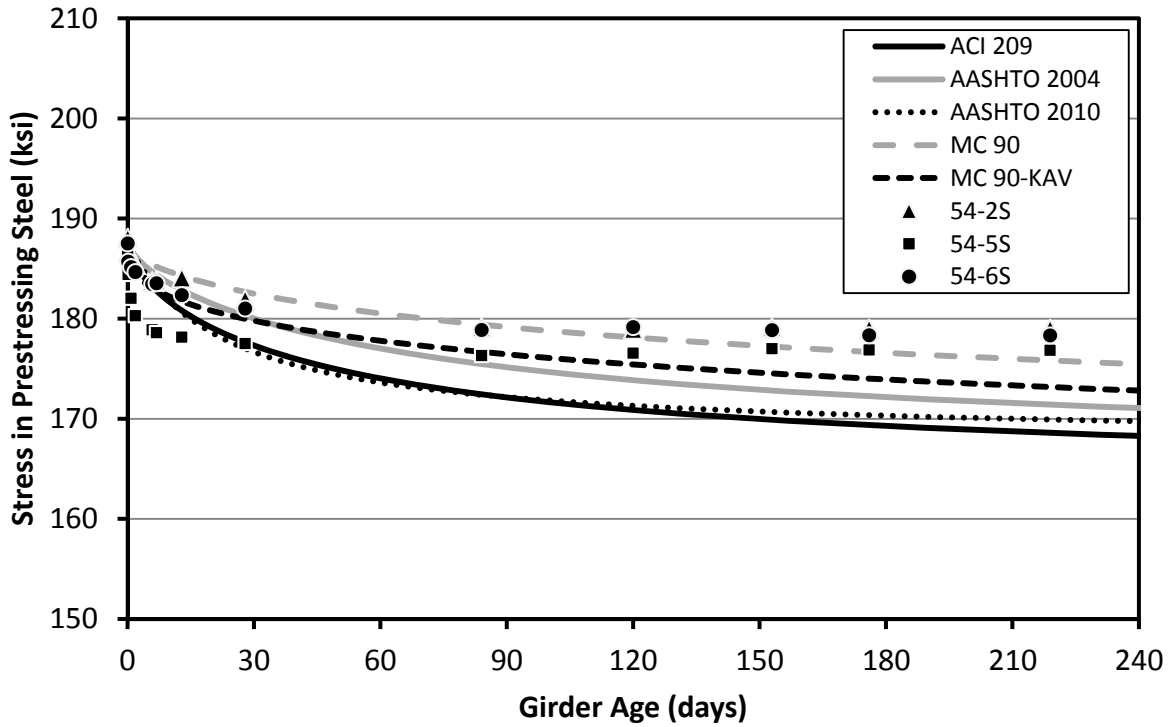


Figure 6-27: Prestress in Casting Group A (SCC)

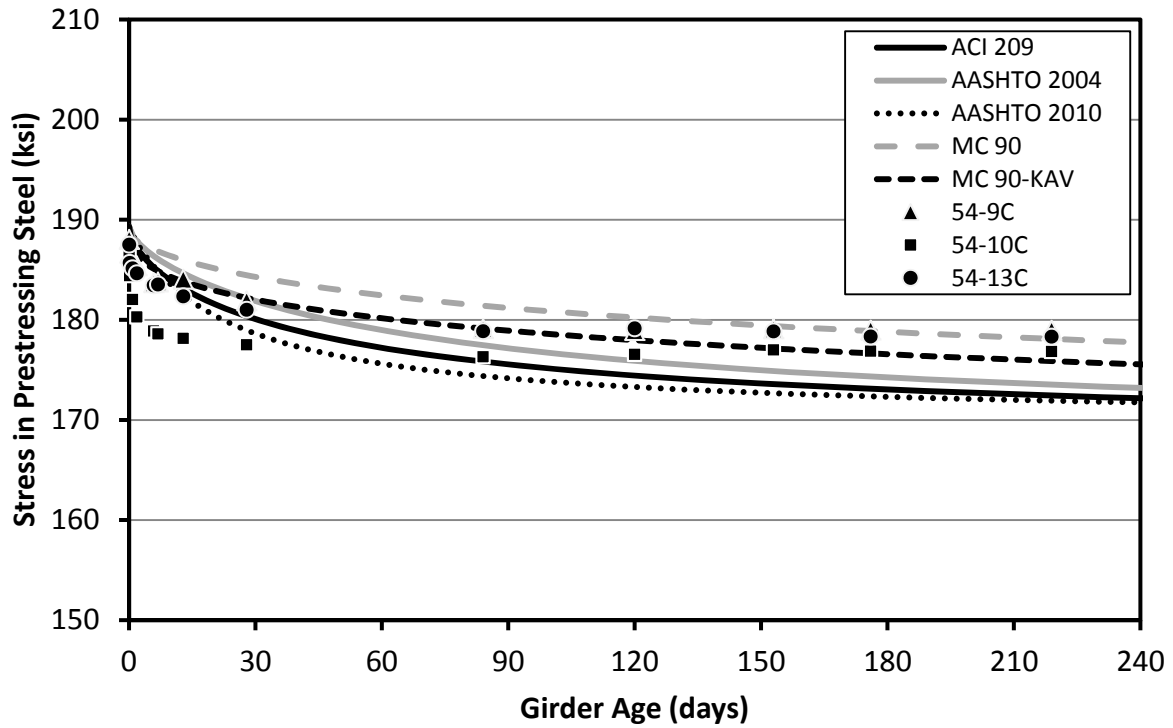


Figure 6-28: Prestress in Casting Group B (CVC)

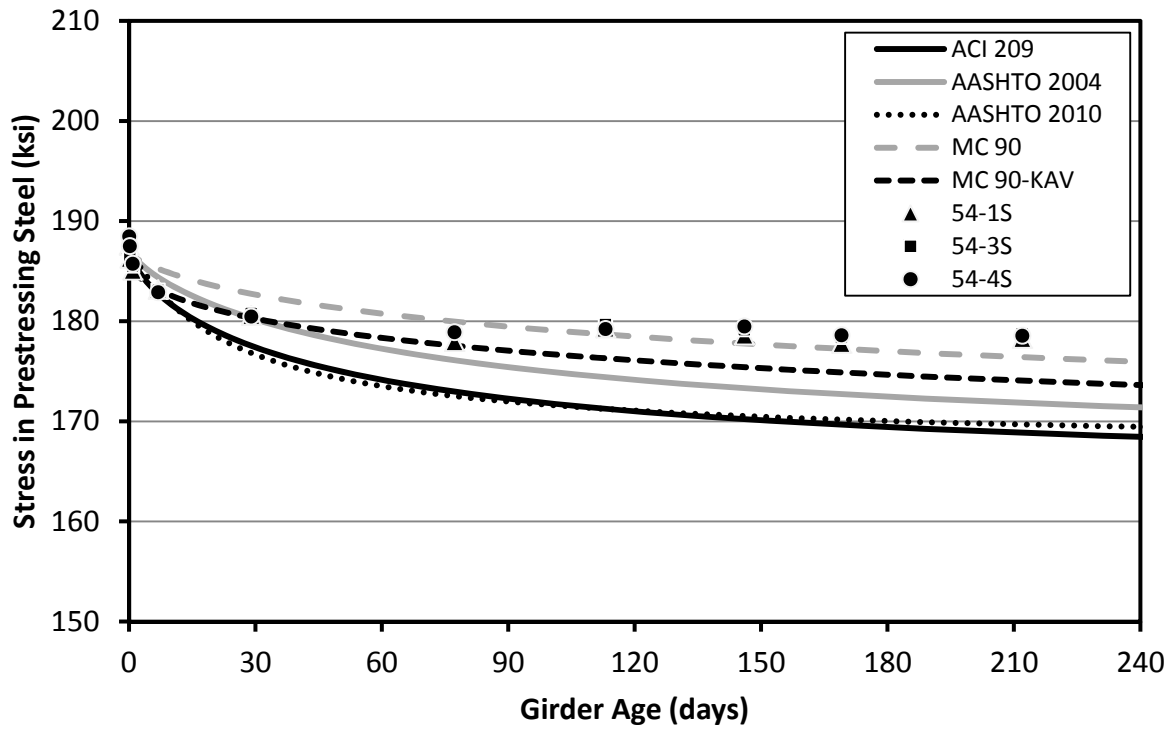


Figure 6-29: Prestress in Casting Group C (SCC)

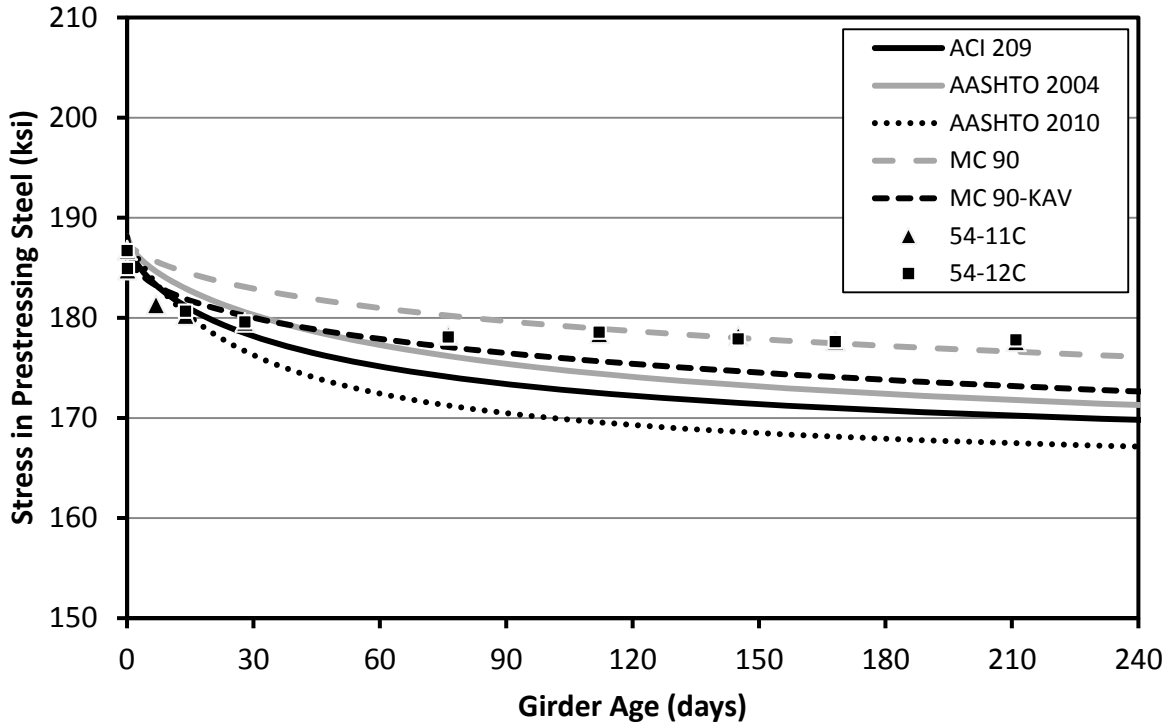


Figure 6-30: Prestress in Casting Group D (CVC)

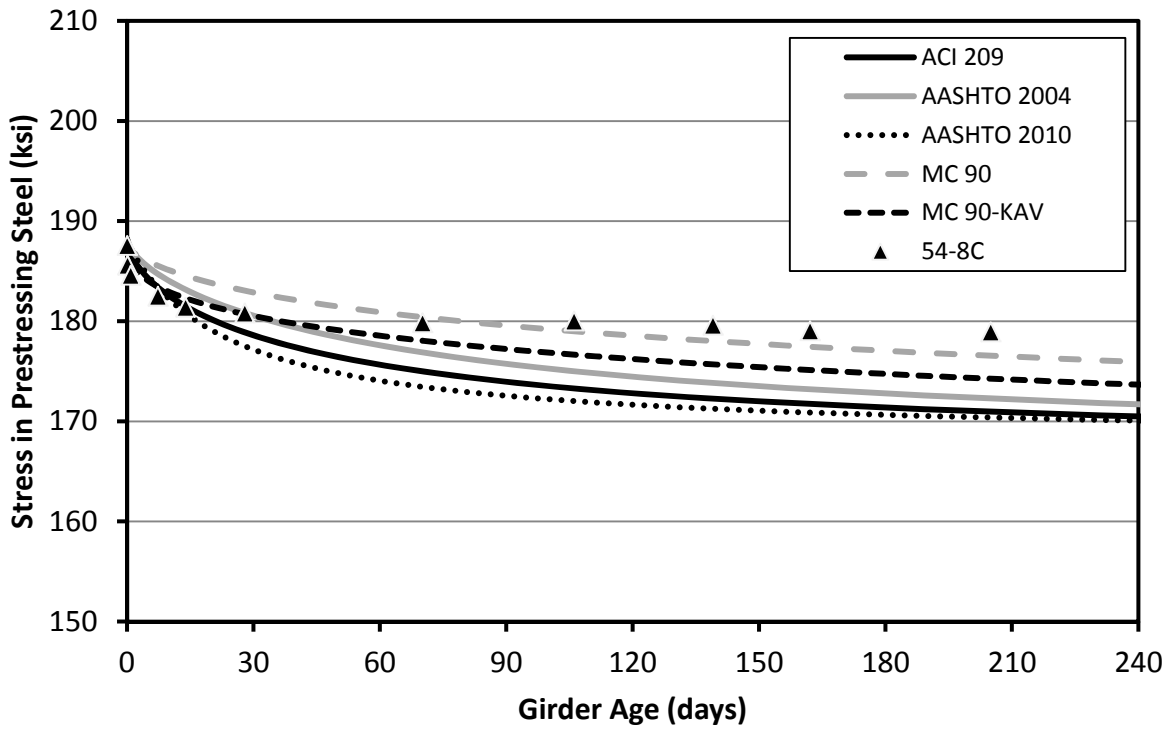


Figure 6-31: Prestress in Casting Group E (CVC)

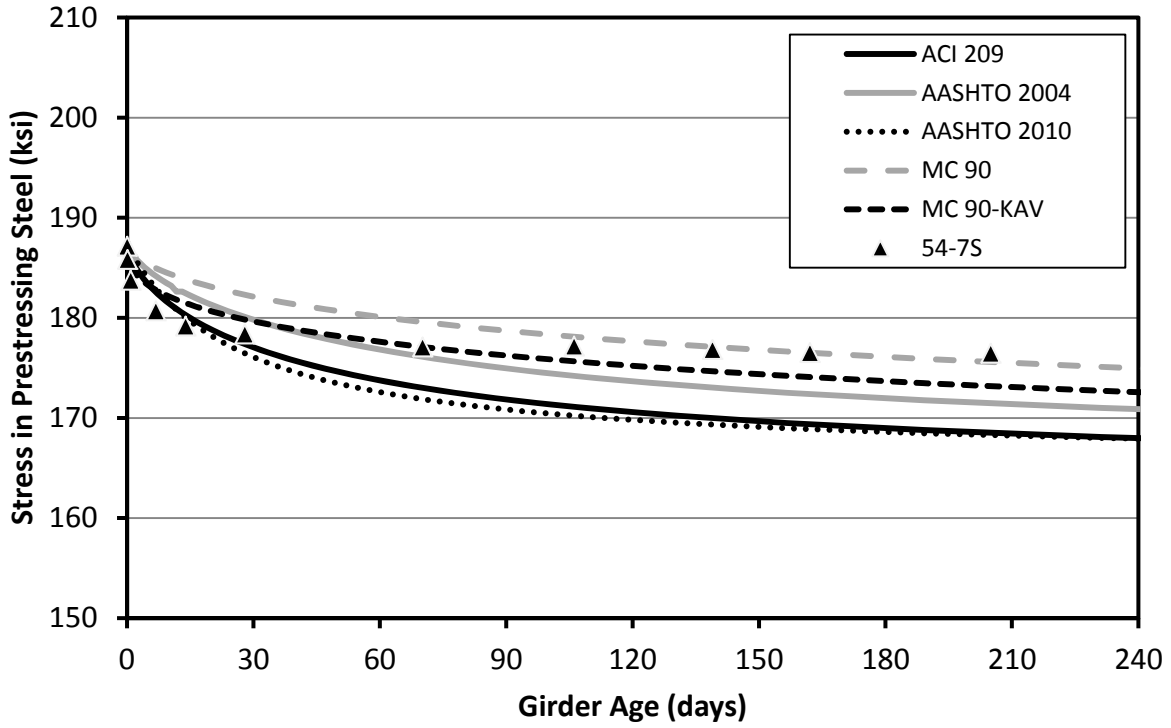


Figure 6-32: Prestress in Casting Group E (SCC)

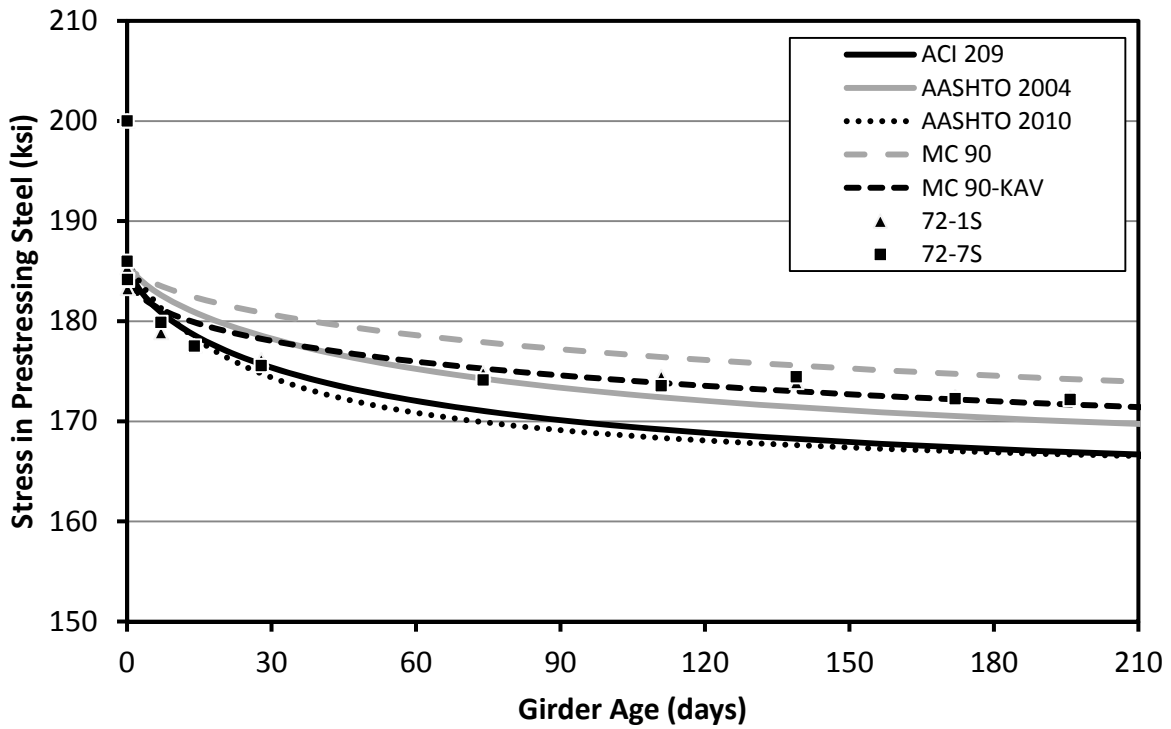


Figure 6-33: Prestress in Casting Group F (SCC)

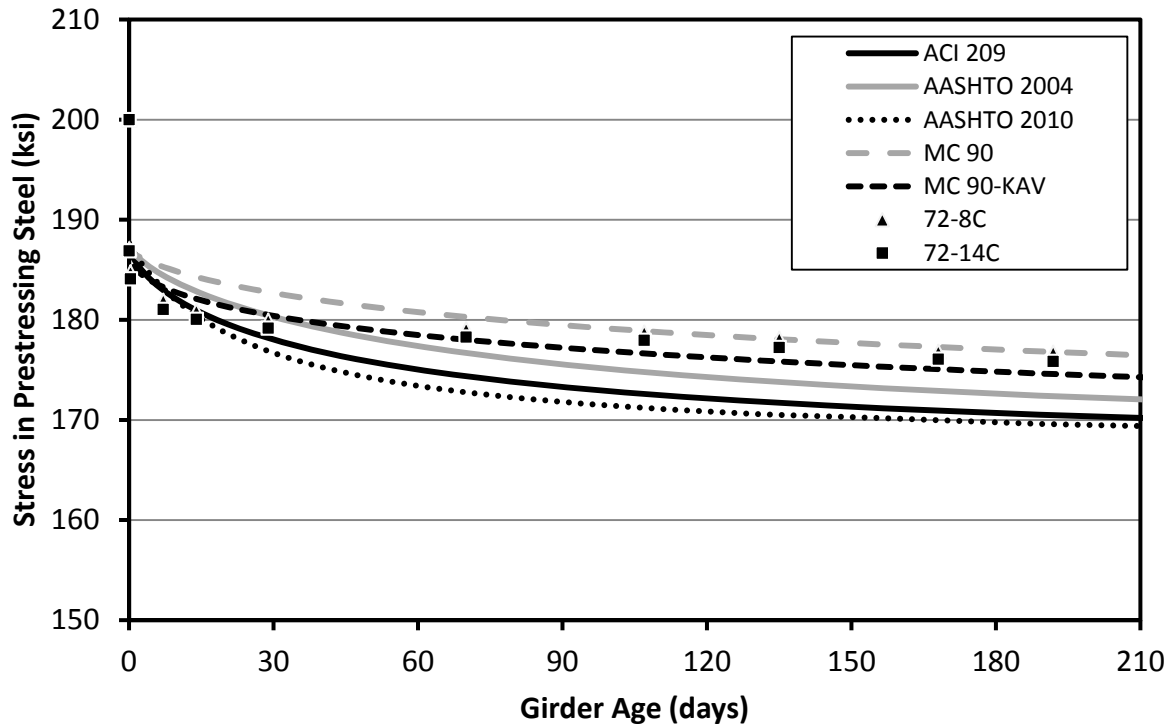


Figure 6-34: Prestress in Casting Group G (CVC)

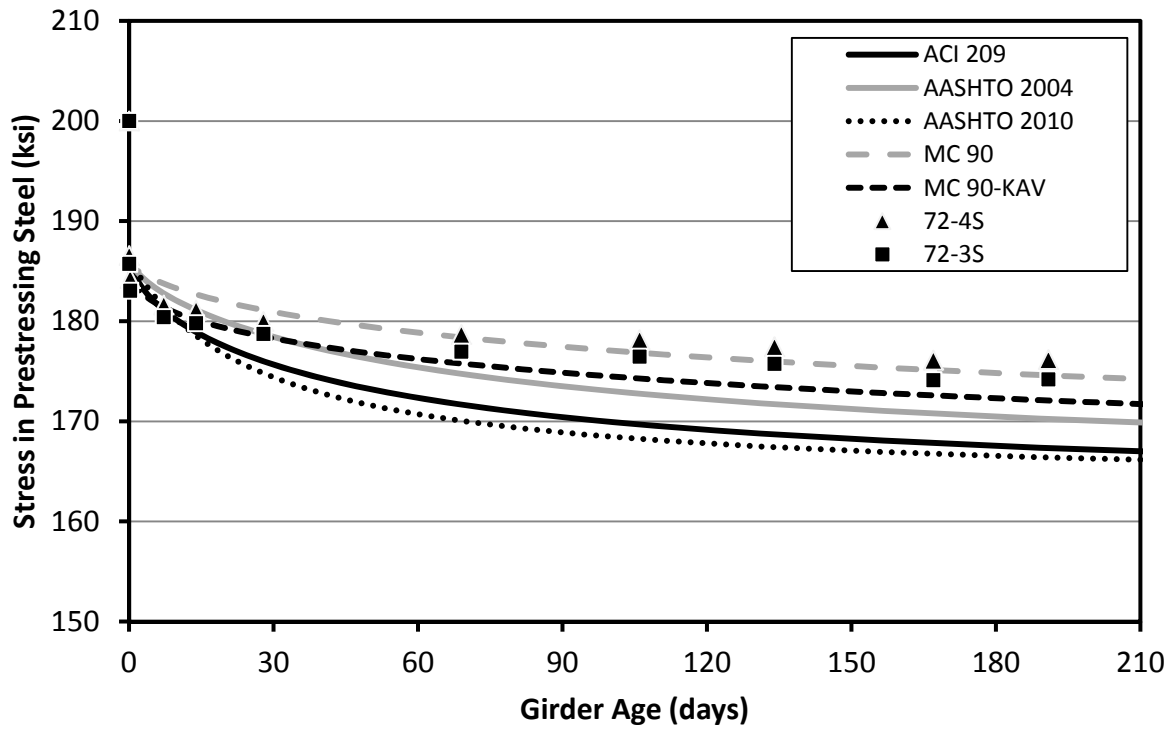


Figure 6-35: Prestress in Casting Group H (SCC)

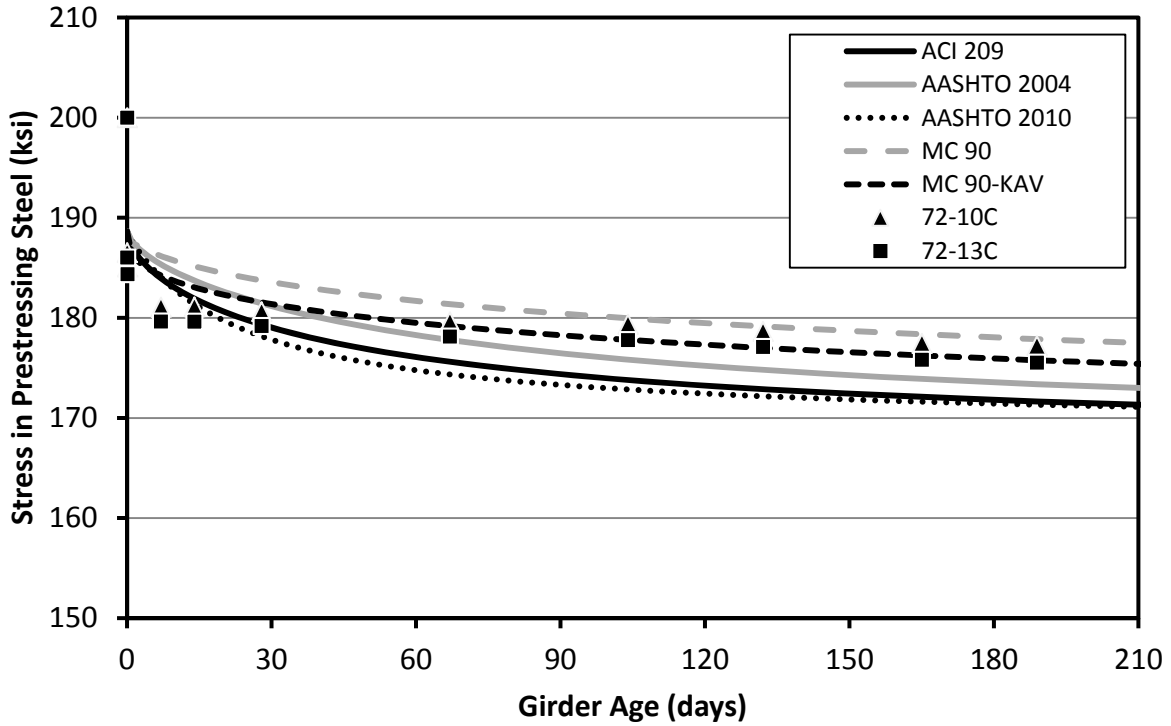


Figure 6-36: Prestress in Casting Group I (CVC)

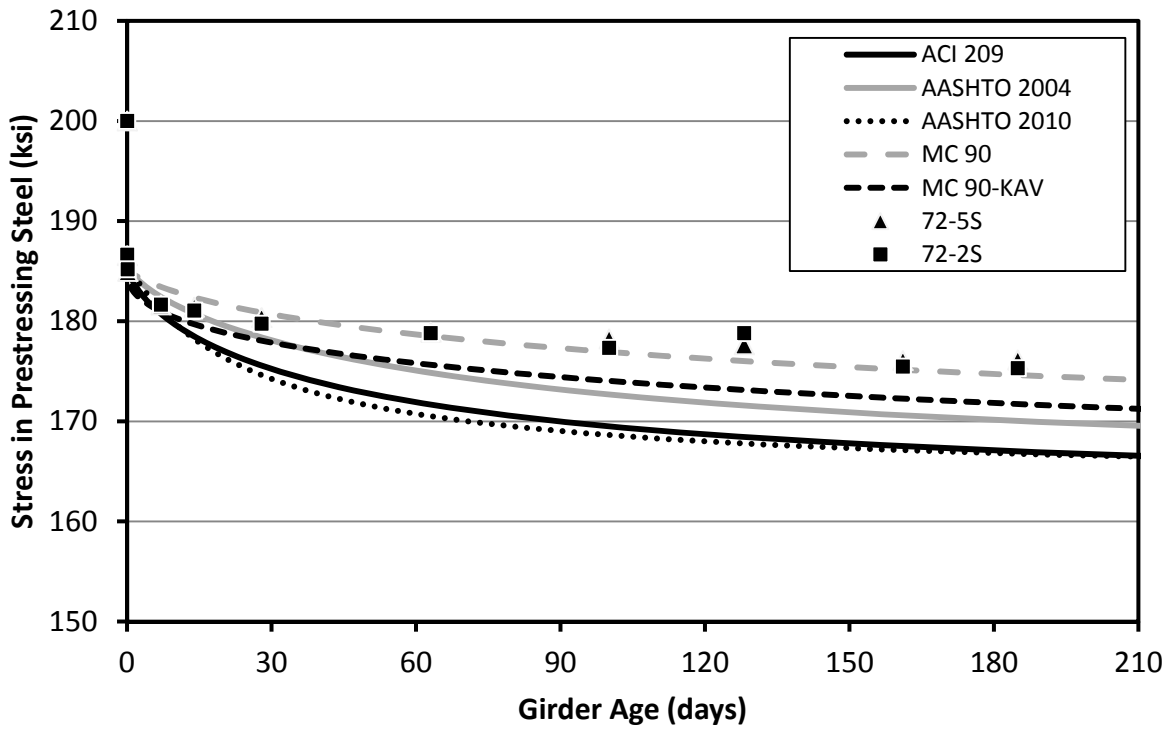


Figure 6-37: Prestress in Casting Group J (SCC)

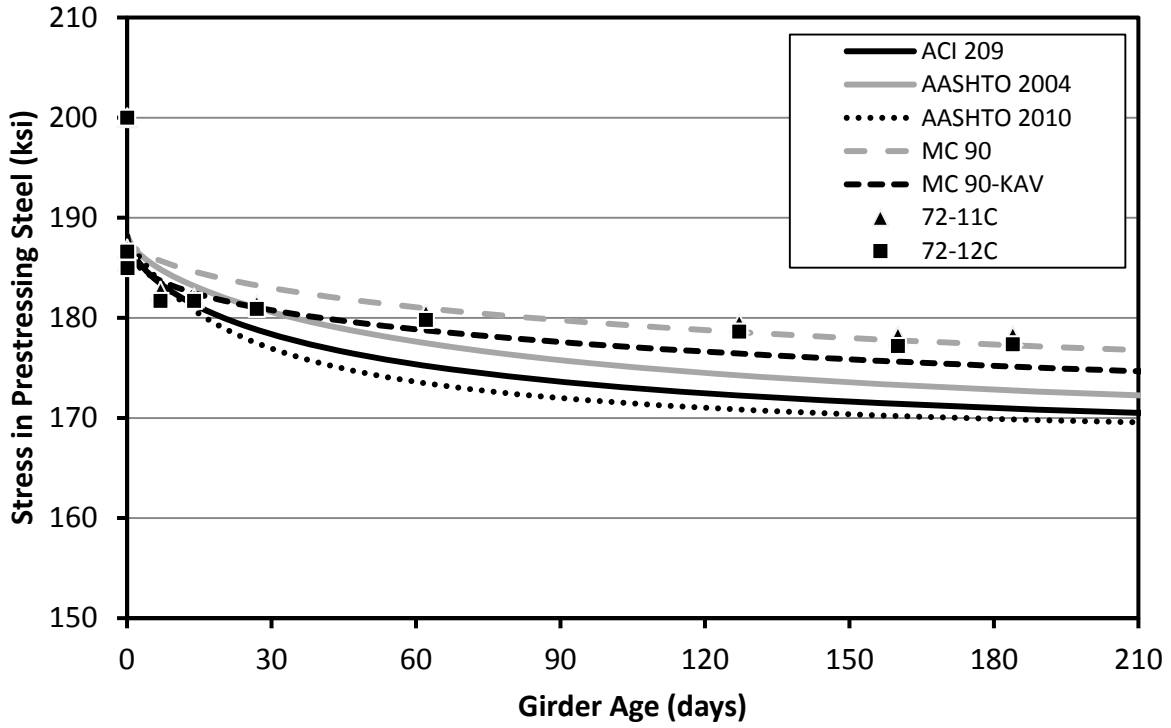


Figure 6-38: Prestress in Casting Group K (CVC)

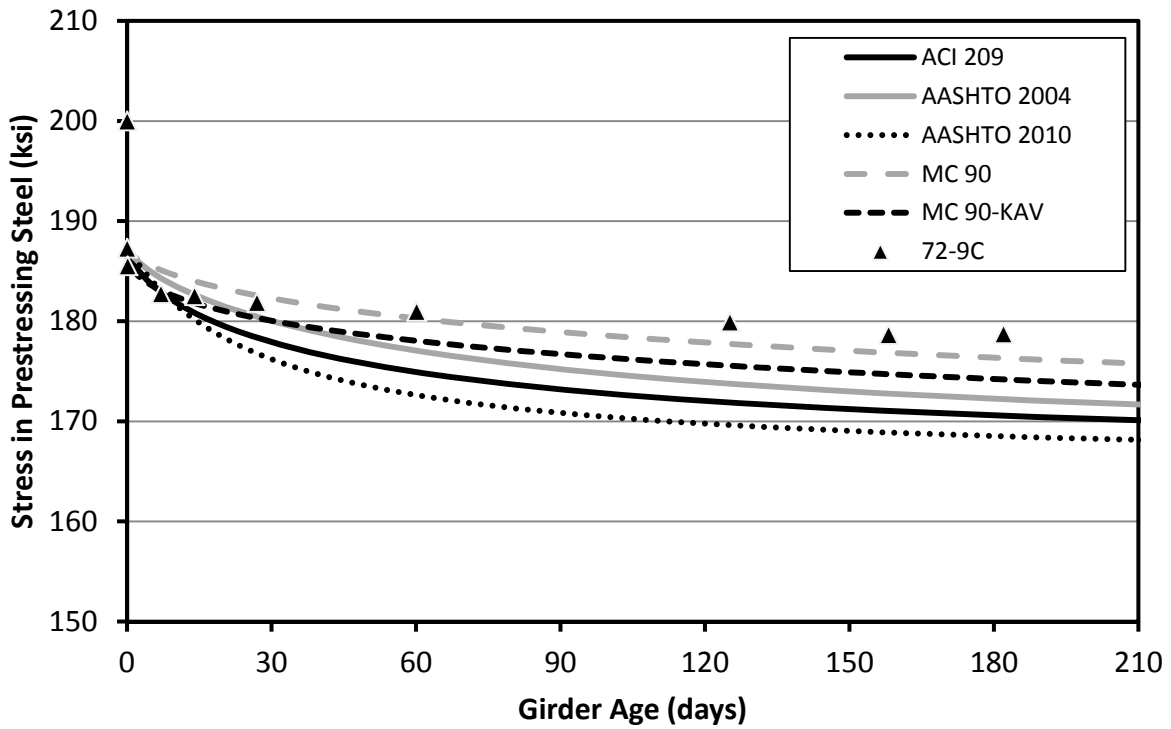


Figure 6-39: Prestress in Casting Group L (CVC)

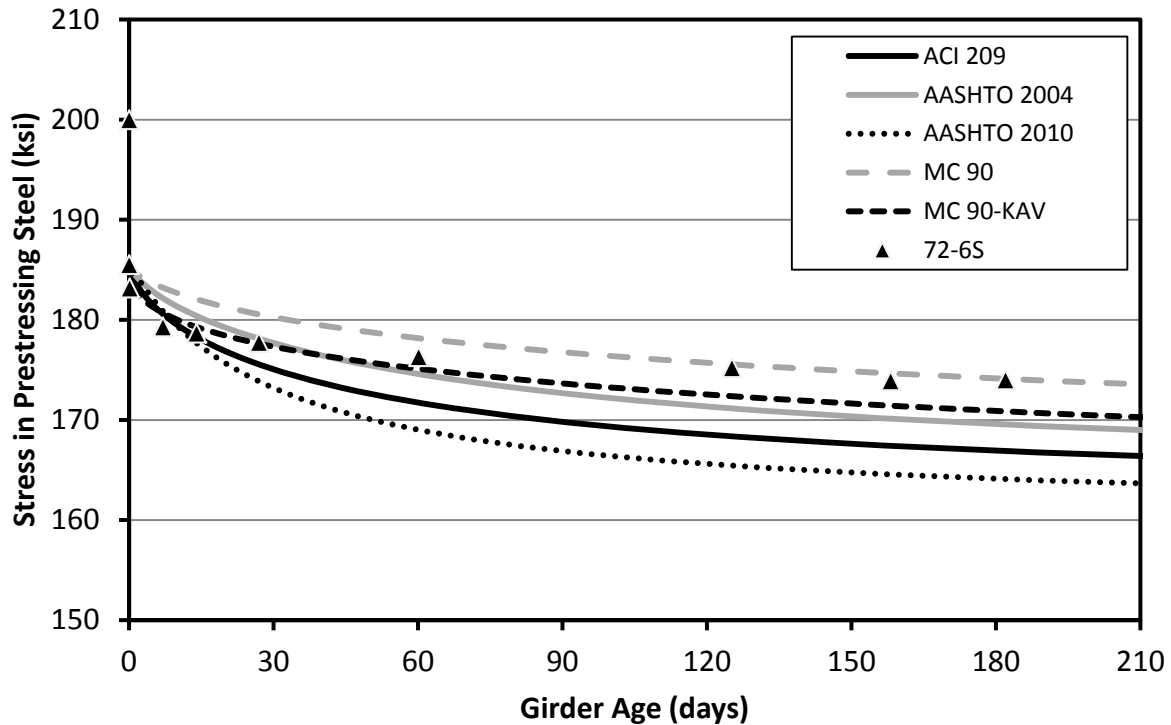


Figure 6-40: Prestress in Casting Group L (SCC)

A number of observations can be made from the above figures. The most obvious conclusion is that the effective prestress remaining in the prestressing steel at later girder ages seems to be accurately predicted by the MC 90 prediction method. In most cases, the prediction methods seem to predict less stress than what was actually measured at later ages. Some of these under-predictions are significant, especially by the ACI 209 and AASHTO 2010 methods. These under-predictions could cause more prestressing to be used in the design of a girder when in reality prestress losses at late ages are not as severe as they might be predicted to be. This could drive up the cost of the girders unnecessarily.

In early ages, though, many times the measured effective stress in the strands is less than predicted. This might be due to the severe temperature gradients present during prestress transfer, which are not accounted for in the prediction models.

6.7 Cambers

One of the major objectives of this research was to determine how predicted cambers for the girders in this project compared to the cambers measured in the field. Additionally, camber predictions using measured concrete material properties were compared to camber predictions using design concrete properties. Camber predictions were determined using the VB code developed by Schrantz (2012). The predictions were compared to measured cambers that were adjusted to account for transient temperature gradients as outlined in Section 6.2.1.

Figure 6-41, Figure 6-42, Figure 6-43, and Figure 6-44 all show the measured midspan cambers for all of the girders studied in this research. The last reading in each figure represents the camber measured just before the girders were placed on the bridge. Direct comparison of these cambers is somewhat useful, but the varying material properties (specifically the varying stiffness) among casting groups makes direct comparison of measured values more difficult. The camber differences between the SCC and CVC girders reflect the fact that the stiffness of the SCC girders is most often lower than the CVC girders. This is reflected in the somewhat higher measured and predicted cambers for the SCC girders.

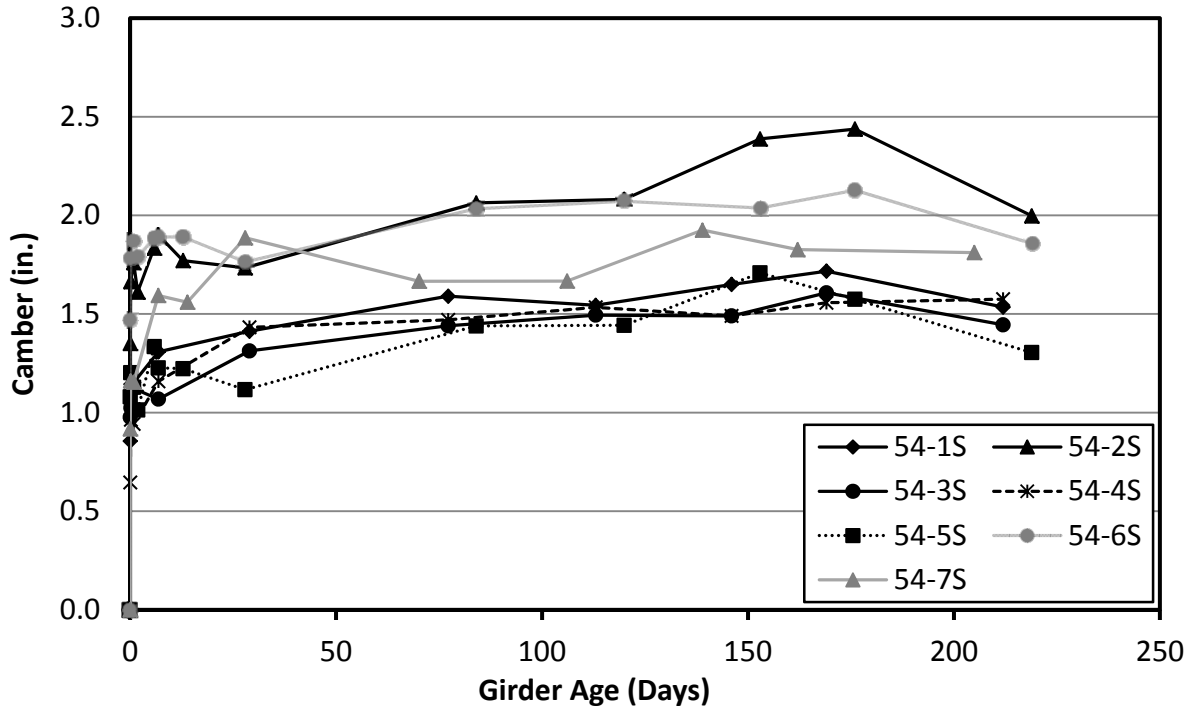


Figure 6-41: SCC BT-54 Measured Midspan Cambers

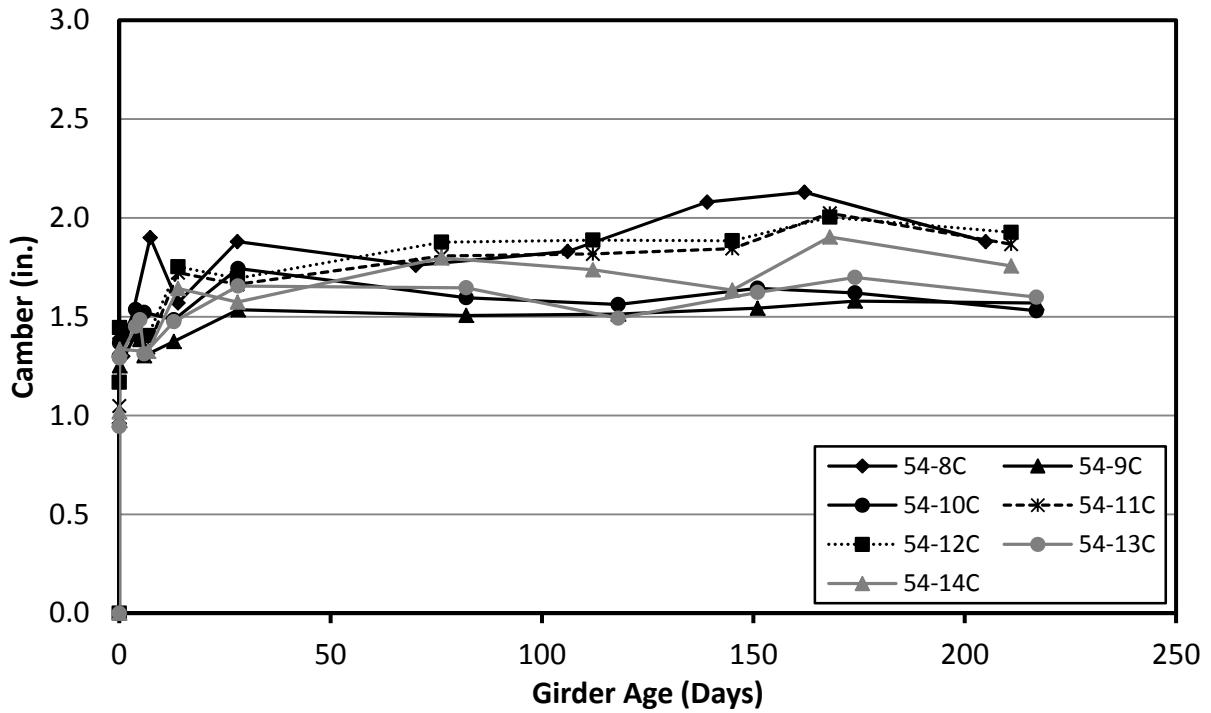


Figure 6-42: CVC BT-54 Measured Midspan Cambers

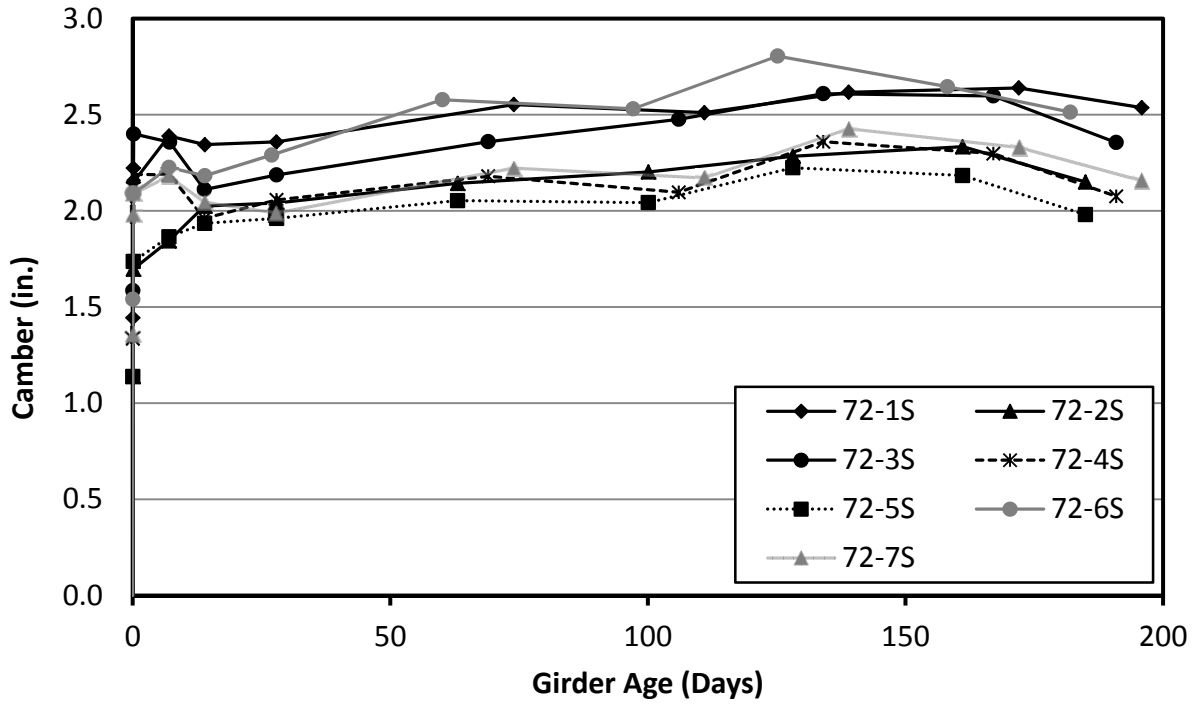


Figure 6-43: SCC BT-72 Measured Midspan Cambers

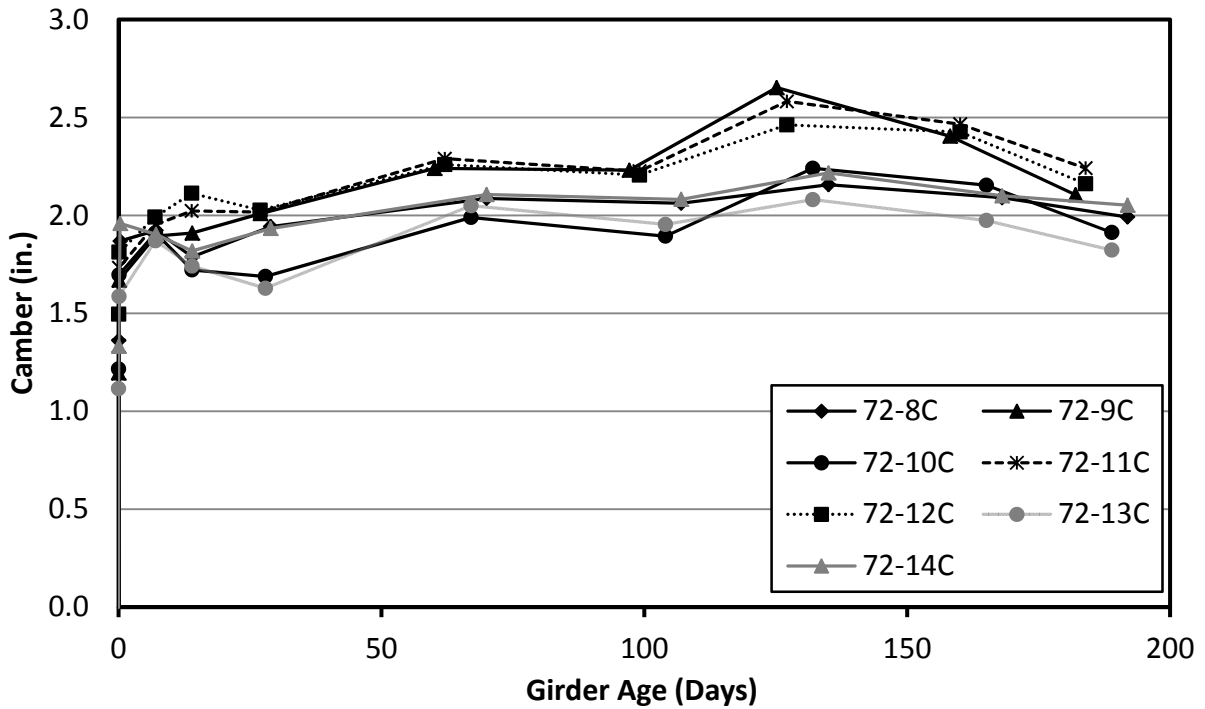


Figure 6-44: CVC BT-72 Measured Midspan Cambers

A comparison method including the predicted cambers for each girder has been applied, similar to the one used above for internal strains. Figure 6-45, Figure 6-46, Figure 6-47, and Figure 6-48 depict the measured versus predicted camber values for the girder ages of just after prestress transfer, 56 days, and erection. All of the prediction methods have the same predicted camber for each casting group at prestress transfer because it is assumed that creep and shrinkage have not occurred prior to prestress transfer. It is no surprise that a majority of the camber predictions in the following figures are over-predictions. This is consistent with the strains that were shown to be generally over-predicted.

In the case of the initial cambers, the disparity between the predicted and measured values may also be due to conditions on the casting bed. The cracking that was noted in the girders prior to prestress transfer that was likely due to the temperature gradient present after the forms were removed could have affected the initial camber readings. While a correction was applied to the camber readings to account for the temperature gradient, this correction did not account for any cracking that might have occurred due to these temperature gradients. Also, it was observed in many of the girders that the hold-down points occasionally got hung up in the casting bed during transfer. The hold-down points were flame-cut and there were times when it was obvious that the girder was trying to raise itself up off of the casting bed but was in fact pulling up on the entire base of the bed. The specific girders that were affected by this was not recorded because there were times when it was unclear whether or not the hold down was affecting the instantaneous camber reading.

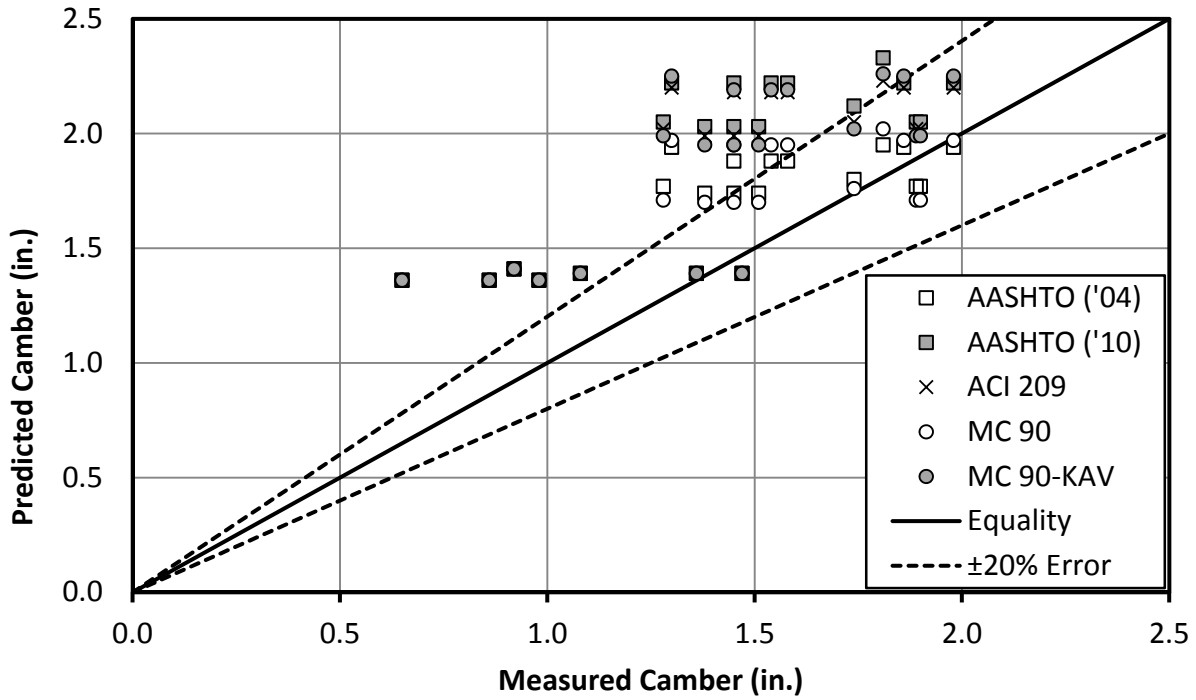


Figure 6-45: Measured Versus Predicted Camber – SCC BT-54

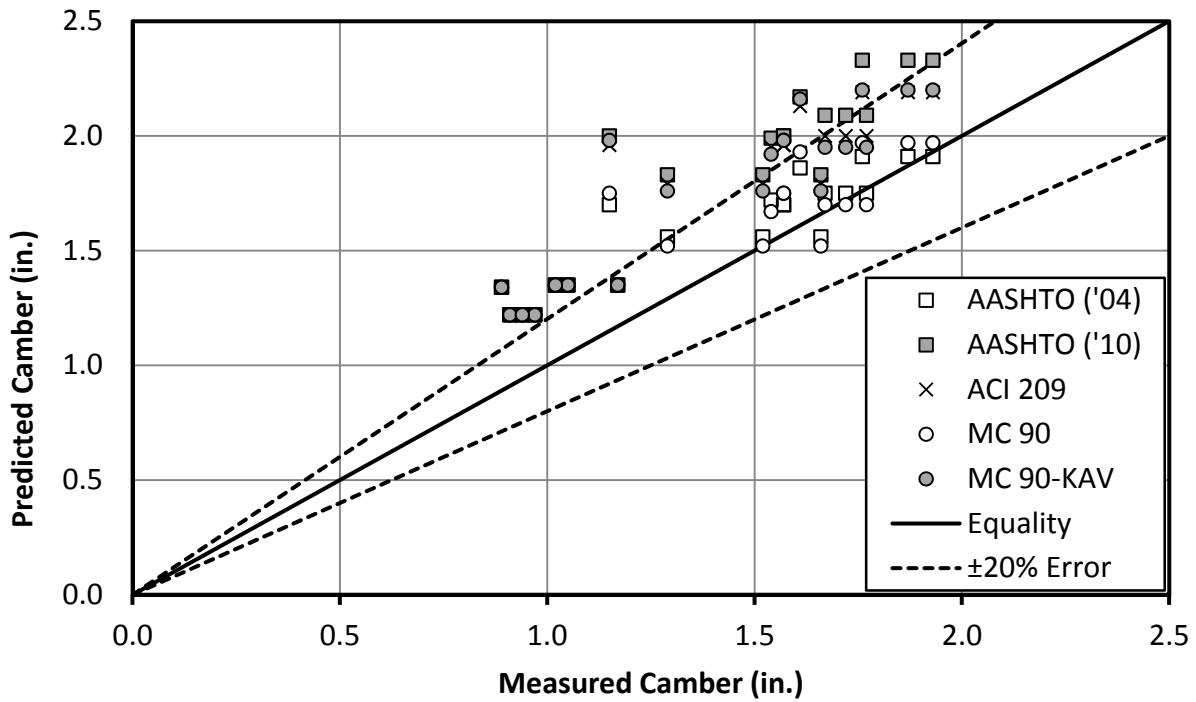


Figure 6-46: Measured Versus Predicted Camber – CVC BT-54

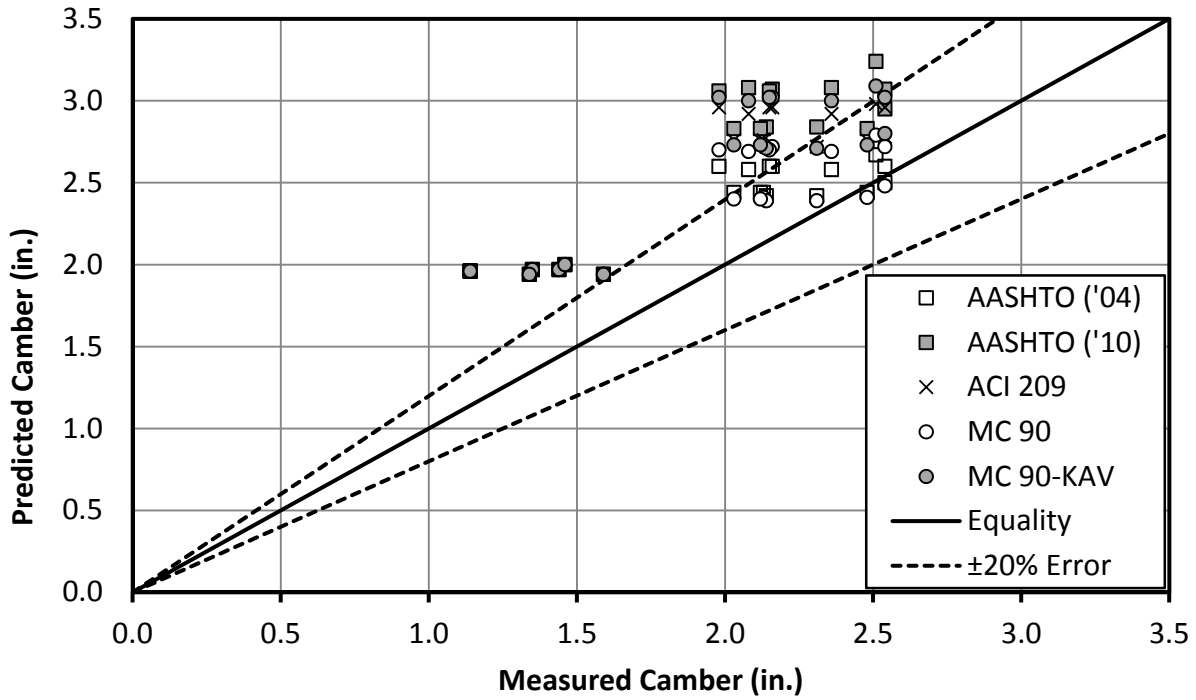


Figure 6-47: Measured Versus Predicted Camber – SCC BT-72

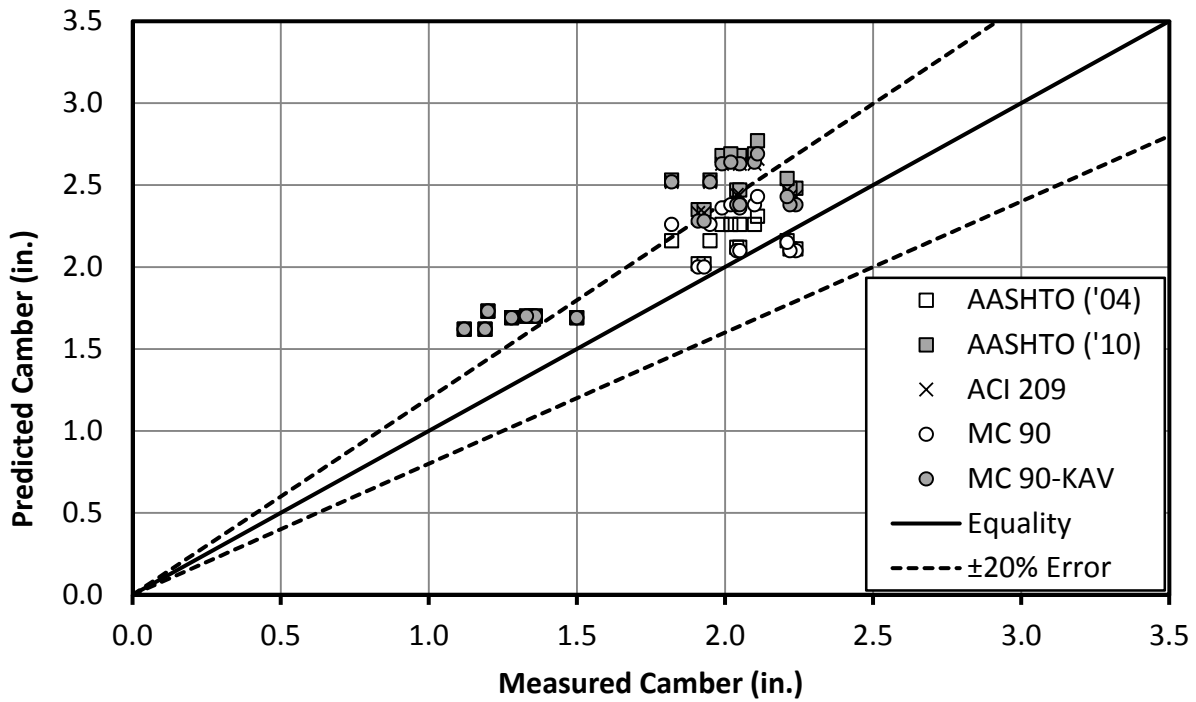


Figure 6-48: Measured Versus Predicted Camber – CVC BT-72

The camber predictions seem to fall into two groupings. The lowest predicted cambers for all girders occur when the MC 90 model is used, but the AASHTO 2004 model provides very similar predictions in all cases. The highest camber predictions come from the AASHTO 2010 model, although the ACI 209 and MC 90-KAV models were very similar in all of their predictions. For both girder sizes, the above plots indicate that the cambers were more accurately predicted for the CVC girders than for the SCC girders. The CVC girders have many more predictions within the 20 percent range than those of the SCC.

The instantaneous predictions have the most error in all of the groupings, with the largest error in readings occurring in the instantaneous readings for the SCC BT-54 set. However, the longer-term readings in all cases seem to have less overall error. This is probably due to the significant temperature gradient present at the time of the instantaneous camber measurement. At later ages, effort was made to measure camber early in the morning when the temperature across the height of the girder was more consistent. While the temperature gradient was corrected through the process described in Section 6.2.1, the simplifications involved in the correction including the simplified section geometry and linear temperature gradients reduced the accuracy of those instantaneous measurements.

An unbiased estimate of the standard deviation of the fractional error of the predicted time-dependent camber growth was calculated in a manner similar to the method used with the bottom-flange strains. Equation 6-16 and Equation 6-17 were used by replacing the strain values with camber values. Table 6-4 contains the descriptive statistics for the camber predictions. These standard deviations were used to determine how well a particular method was able to predict the growth of camber over time.

Table 6-4: Unbiased Estimate of the Standard Deviation of the Prediction Errors for Camber Growth

		SCC 54	SCC 72	CVC 54	CVC 72	SCC	CVC
AASHTO 2004	56 Day	0.52	0.50	0.41	0.52	0.49	0.45
	Erection	0.69	0.32	0.48	0.37	0.51	0.42
AASHTO 2010	56 Day	1.01	0.16	0.28	0.14	0.70	0.21
	Erection	1.28	0.36	0.95	0.50	0.90	0.73
ACI 209	56 Day	0.94	0.18	0.23	0.16	0.65	0.19
	Erection	1.23	0.22	0.86	0.43	0.85	0.65
MC 90	56 Day	0.50	0.52	0.48	0.52	0.49	0.48
	Erection	0.77	0.18	0.54	0.13	0.54	0.38
MC 90-KAV	56 Day	0.92	0.17	0.22	0.17	0.63	0.19
	Erection	1.39	0.34	0.96	0.51	0.97	0.74

The results of this analysis do not distinguish a particular method as obviously better than any other method. While the bottom-flange strain results showed that the MC 90 and MC 90-KAV models were the best methods, the camber results do not show the same thing. When comparing predictions for SCC and predictions for CVC, it appears that most methods predict camber growth of CVC girders slightly better than SCC camber growth. However, no method predicts camber growth very well at both ages for either type of concrete.

The larger relative errors seen in the camber predictions are not unexpected. The measured strains reflect the behavior of a single cross section at which the temperature gradient was also measured. However, the measured cambers reflect behavior of the entire girder length, but were corrected by using only the temperature gradient known at midspan and assuming that this gradient applied to every cross section along the length of the girder. Changes in the actual temperature gradient along the length of the girder are not actually reflected in the “measured” camber, and therefore lead to larger apparent errors between predicted and measured values.

6.8 Predictions Using Design versus Measured Concrete Strengths

One of the objectives of this research project was to demonstrate the importance of using accurate hardened concrete properties when attempting to predict time-dependent deformations. Predictions of time-dependent deformations were developed using three different sets of hardened concrete properties for one of the BT-72 girders made with CVC (72-8C). The only creep and shrinkage model used for the purpose of this exercise was the AASHTO 2010 method. The first set of predictions were developed in the same way as the results presented previously in this chapter. These predictions were based on the measured concrete strength and modulus of elasticity at transfer and at 28 days. The second set of predictions were determined by using the measured concrete strength at transfer and at 28 days, but calculating the predicted modulus of elasticity based on those measured strengths according to the AASHTO 2010 code, as shown in Equation 6-18.

$$E_c = 57000\sqrt{f'_c} \quad \text{Equation 6-18}$$

Where

E_c is the predicted module of elasticity of the concrete (psi), and
 f'_c is the compressive strength of the concrete (psi).

The third set of predictions were developed based on the design strengths specified for this bridge project and the corresponding modulus of elasticity values computed using the AASHTO expression at transfer and 28 days. Table 6-5 shows the compressive strength and modulus of elasticity values used in these predictions.

Table 6-5: Hardened Concrete Properties 72-8C

Concrete Properties	All Values Measured	Strength Measured, E Calculated	Strength Specified, E Calculated
f'_{ci} (psi)	8290	8290	5800
E_{ci} (ksi)	6700	5190	4340
f'_c (psi)	10770	10770	8000
E_c (ksi)	7000	5920	5100

The two time-dependent effects that were compared from these predictions were camber and effective prestress at midspan. Figure 6-49 contains the cambers predicted using the three possible sets of material inputs as well as the field-measured camber for 72-8C. It is obvious that the camber is being significantly over-predicted at later ages, especially when specified design strengths are used. In fact, the shop drawings provided by the girder manufacturer list a theoretical camber before placement of the bridge deck as 3¼ in. This value would seem to agree with the prediction based on the design strength and modulus of elasticity values at an age of 30 to 60 days, as is usually assumed for an erection age.

The error between the predicted and measured values shown in the plot below arises from different sources. In the case of the predictions using the measured strengths and measured modulus of elasticity values, the primary source of the error arises from the uncertainty of the time-dependent behavior of the girder. These errors were discussed in previous sections and have to do with the accuracy of predicting creep and shrinkage. In the case of the line in which the modulus of elasticity was assumed based on the measured strength, another source of error in that assumption is introduced, causing the prediction to be less accurate. Finally, the greatest over-prediction of camber occurs when the specified design strength is used with an estimated modulus of elasticity. The differences between the conservatively low design strength and

measured values are significant, and this difference is compounded over time as time-dependent deformations are calculated based on already inaccurate values.

The errors resulting from using assumed or predicted values for strength and modulus of elasticity as opposed to measured values is much more significant than the errors discussed in previous sections resulting from using different creep and shrinkage prediction models with measured concrete strength and modulus of elasticity values.

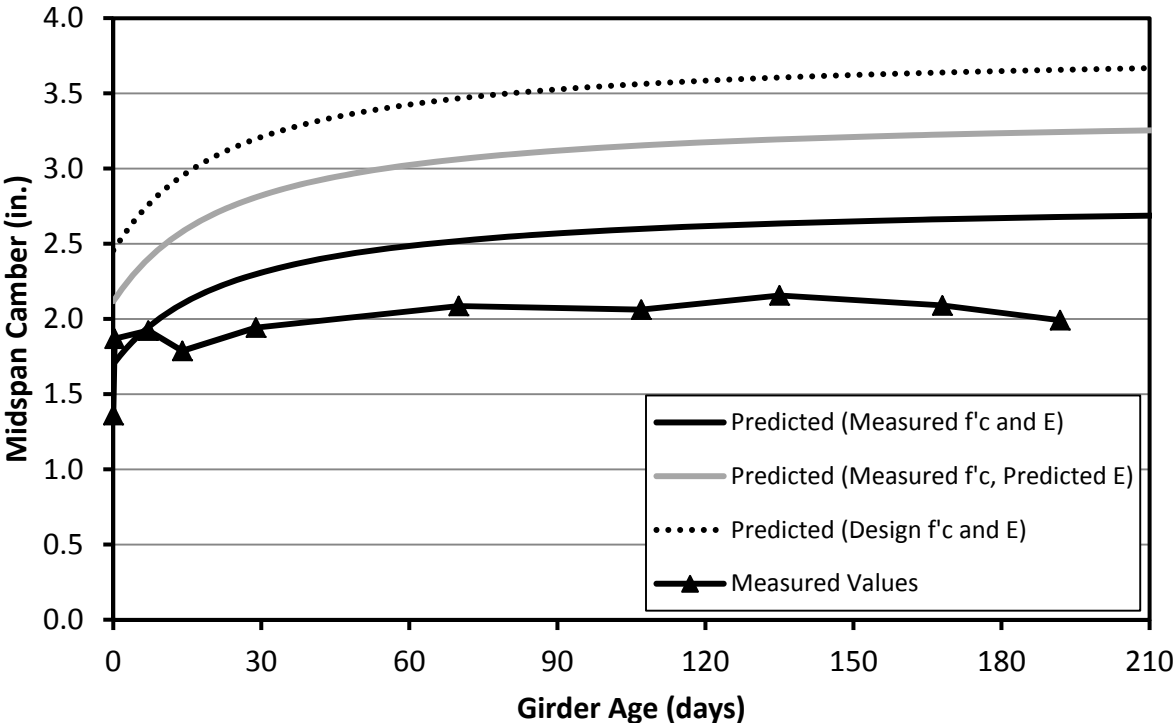


Figure 6-49: Predicted and Measured Camber of 72-8C

The effective prestress at midspan was also predicted based on each set of these conditions. The effective prestress was calculated for 72-8C based on the measured internal strains as discussed in Section 6.6. These predictions are shown in Figure 6-50. In the same way that camber was over-predicted, the effective prestress was under-predicted as the girder aged.

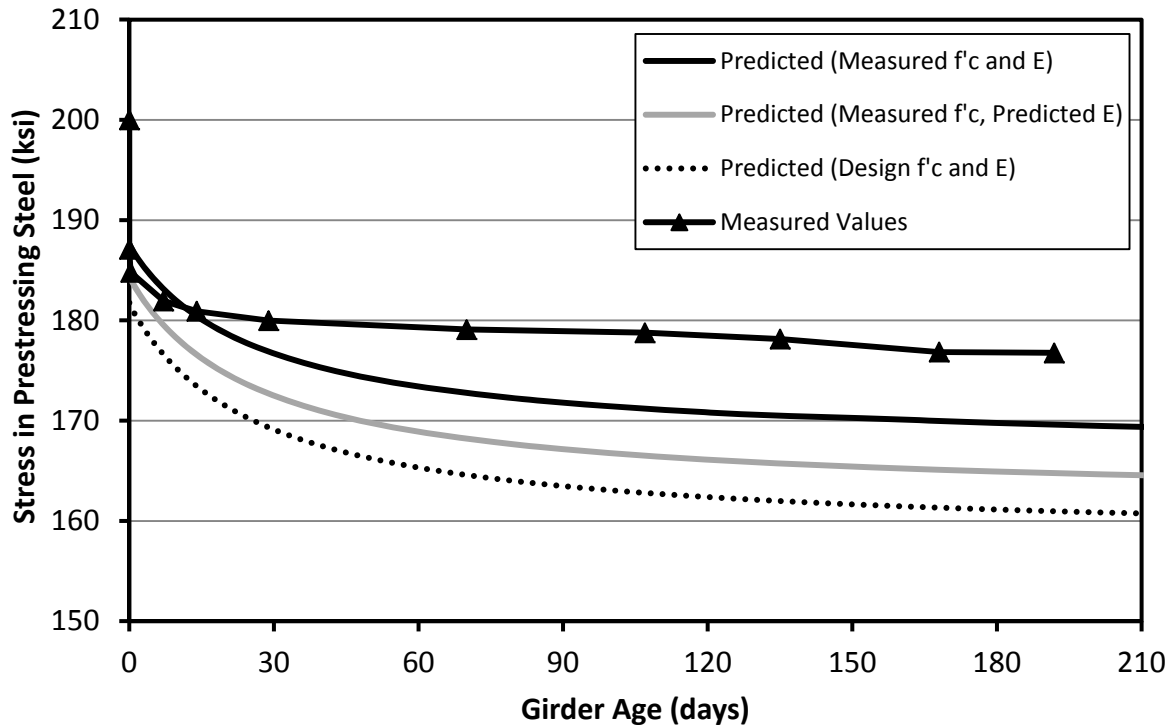


Figure 6-50: Predicted and Measured Effective Prestress for 72-8C

The difference between the measured effective prestress and the predicted effective prestress using design concrete strengths is about 10%, or about 16 ksi. Improved predictions based on more accurate material properties could be used to improve the girder design. If prestress losses are not as significant as initially thought, less prestress force could be used. This means that less prestressing strands would be used, and the cost of manufacturing the girder would decrease. Stallings et al. (2003) made it clear that under-predicted prestress values at later girder ages might discourage some designers from using high-performance concrete in long-span prestressed bridge girders. This is true regardless of whether the concrete is CVC or SCC.

Chapter 7 Summary and Conclusions

7.1 Summary

The use of advanced concretes including high-strength concrete in precast, prestressed bridge girders is widespread throughout the state of Alabama. In addition, precast concrete producers would like to implement SCC for the same applications. The effects of time-dependent deformations, including camber and the loss of prestress, are important responses that need to be addressed during the design of the girders. The accurate prediction of time-dependent deformations is an essential part of providing an efficient design for prestressed bridge girders in order to keep manufacturing and construction costs to a minimum.

The most difficult time-dependent properties to predict for prestressed bridge girders include the creep and shrinkage properties of the concrete. The creep and shrinkage properties directly affect long term deformations in the girders including camber and the loss of prestress force. For this reason, the AASHTO LRFD Bridge Design Specifications allow for the use of a number of different creep and shrinkage models to predict girder response. The main purpose of this study was to determine the accuracy of these prediction methods in full-scale bulb-tee girders that contained both CVC and SCC.

A time-step prediction procedure was developed in previous research and put into a Visual Basic computer program. This program was used to predict time-dependent deformations for 28 bulb-tee girders manufactured for use in a replacement bridge on State Route 22 over Hillabee Creek in Tallapoosa County, Alabama. Two spans of this bridge consisted of girders manufactured using CVC and the remaining two spans consisted of girders manufactured with

SCC. The bridge girders were instrumented with VWSGs to measure internal strain at specific cross sections and were also measured for camber at regular intervals.

Comparisons between the predicted deformations and measured deformations were made in order to determine the accuracy of the different creep and shrinkage prediction methods as well as to compare the CVC to the SCC. A second component to this research involved the comparison of predictions made using measured material properties versus design material properties. Specifically, measured concrete strengths and modulus of elasticity values at prestress transfer and 28 days were used for all of the creep and shrinkage prediction models to see which models matched measured deformations the most closely. An investigation was also performed in which predictions were developed for a specific girder using different combinations of design and measured concrete strength and modulus of elasticity values to see how sensitive the predictions were to these changes.

7.2 Conclusions

The following conclusions were made regarding the use of SCC versus CVC in the precast, prestressed bridge girders observed in this study:

- Measured initial bottom-flange strains and cambers of SCC girders were slightly larger than for CVC girders because of the slightly smaller modulus of elasticity of the SCC at prestress transfer.
- Measured initial bottom-flange strains and corresponding prestress losses were accurately predicted for both SCC and CVC girders.
- Measured time-dependent strains and corresponding prestress losses in SCC girders were predicted at least as well as corresponding values in CVC girders.

- Measured time-dependent camber growth of SCC girders was predicted with slightly less accuracy than camber growth of CVC girders.
- Based on time-dependent behavior, there is no reason to deter the implementation of SCC for precast, prestressed girders when produced as specified for the Hillabee Creek Bridge project.

The following conclusions were made concerning the prediction of bottom-flange strain, prestress losses, and camber in the girders observed in this study:

- All of the creep and shrinkage models investigated were reasonably accurate in predicting bottom-flange strain, with the MC 90 and MC-90 KAV models being the best.
- All of the methods investigated over-predicted internal strain at later girder ages with the exception of the MC 90 method, which consistently under-predicted internal strain.
- All of the prediction methods over-predicted effective prestress in the first months after transfer while mostly under-predicting effective prestress at later girder ages.
- The ACI 209 and AASHTO 2010 methods significantly under-predicted effective prestress at later girder ages.
- Measured cambers were generally less than predicted for ages up to approximately 200 days.
- None of the models predicted time-dependent camber growth particularly well.

The following conclusion was made regarding time-dependent deformation predictions developed using specified concrete strength and computed stiffness values versus using measured strength and stiffness values:

- A significant reduction in the accuracy of predictions occurs when specified strength and computed stiffness values for concrete were used. The resulting prediction errors are at least as large as the errors associated with creep and shrinkage models. This applies to both CVC and SCC.

7.3 Recommendations for Future Study

After completion of the study, the following recommendations can be made for future investigations:

- A more in-depth study of the distribution of temperatures across girder cross sections could be used to make better adjustments to measured values.
- Additional creep and shrinkage models should be investigated for prediction of the time-dependent deformations for precast, prestressed girders.

The following recommendations can be made regarding the computer program used to develop the time-dependent deformation predictions:

- The program should be updated to allow the input of either specified or mean concrete compressive strengths.
- The ability to generate output files that can be saved to a spreadsheet file would greatly enhance the program.
- The program could be modified to produce plots of the predicted growth of camber or the loss of prestress over time.

References

- AASHTO. 2004. *AASHTO LRFD Bridge Design Specifications*. 5th ed. Washington D.C.: American Association of State Highway and Transportation Officials (AASHTO).
- AASHTO. 2010. *AASHTO LRFD Bridge Design Specifications*. 5th ed. Washington D.C.: American Association of State Highway and Transportation Officials (AASHTO).
- ACI 209. 1992. "Prediction of Creep, Shrinkage, and Temperature Effects in Concrete Structures." Farmington Hills, Michigan: American Concrete Institute, 209R-92 (Reapproved 1997).
- ACI 209. 2008. "Guide for Modeling and Calculating Shrinkage and Creep in Hardened Concrete." Farmington Hills, Michigan: American Concrete Institute, 209.2R-08.
- Al-Manaseer, A., Lam, J.P. 2005. Statistical Evaluation of Shrinkage and Creep Models. *ACI Materials Journal* 102, no. 3: 170-176.
- Al-Omaishi, N., M.K Tadros, and S.J. Seguirant. 2009. Elastic modulus, shrinkage, and creep of high strength concrete as adopted by AASHTO. *PCI Journal*, Summer 2009: 44-63.
- ASTM C 39. 2005. "Standard Test Method for Compressive Strength of Cylindrical Concrete Specimens." *Annual Book of ASTM Standards*. Vol 4: Concrete and Aggregates: 21-25.
- ASTM C 469-02. 2005. "Standard Test Method for Static Modulus of Elasticity and Poisson's Ratio of Concrete in Compression." *Annual Book of ASTM Standards*. Vol 4: Concrete and Aggregates.

- Barr, P.J., B.M. Kukay, and M.W. Halling. 2008. Comparison of Prestress Losses for a Prestress Concrete Bridge Made with High-Performance Concrete. *Journal of Bridge Engineering*, ASCE. September/October: 468-475.
- CEB. 1990. "Creep and Shrinkage". In *CEB-FIP Model Code 1990*. Lausanne, Switzerland: Comite Euro-International du Beton (CEB).
- Collins, Michael P. and Dennis Mitchell. 1991. *Prestressed Concrete Structures*. Englewood Cliffs, N.J.: Prentice Hall.
- Dunham, Emily L. 2011. Transfer Length in Bulb-Tee Girders Constructed with Self-Consolidating Concrete. M.S. Thesis, Auburn University.
- Ellis, Morgan A. 2012. Time-Dependent Deformations of Concrete for Precast/Prestressed Bridge Components. M.S. Thesis, Auburn University.
- Geokon Instruction Manual. Model 4200/4204/4210 Vibrating Wire Strain Gauges. Rev N, 8/10.
- Gross, Shawn P. and Ned H. Burns. Field Performance of Prestressed High Performance Concrete Highway Bridges in Texas. Federal Highway Administration Report No. FHWA/TX-05/9-580/589-2. February 2000.
- Hinkle, Stephen D. 2006. Investigation of Time-Dependent Deflection in Long Span, High Strength, Prestressed Concrete Bridge Beams. M.S. Thesis, Virginia Polytechnic Institute and State University.
- Huo, X.S., N. Al-Omaishi, and M.K. Tadros. 2001. Creep, Shrinkage, Modulus of Elasticity of High-Performance Concrete. *ACI Materials Journal* 98, no. 6: 440- 449.
- Kavanaugh, Bryan P. 2008. Creep Behavior of Self-Consolidating Concrete. M.S. Thesis, Auburn University.

- Labonte, T. and H.R. Hamilton III. 2005. Self-Consolidating Concrete (SCC) Structural Investigation. Florida Department of Transportation Report No. BD545, RPWO No. 21.
- Levy, K.R., Barnes, R.W., and A.K. Schindler. 2010. Time-Dependent Deformations of Pretensioned, Self-Consolidating Concrete. In Think Globally, Build Locally: Proceedings of the Third International fib (International Federation for Structural Concrete) Congress and Exhibition in Washington, D.C. 29 May-2 June 2010. Chicago: Precast/Prestressed Concrete Institute.
- McCuen, R.H. 1985. *Statistical Methods for Engineers*. Prentice-Hall. 439 pp.
- Mokhtarzadeh, A. and C. French. 2000. Time-Dependent Properties of High-Strength Concrete with Consideration for Precast Applications. *ACI Materials Journal* 97, no. 3: 263-271.
- Neville, Adam . 1997. "Aggregate Bond and Modulus of Elasticity of Concrete". *PCI Journal* 95, no. 1: 71-74.
- Nilson, Arthur H. *Design of Prestressed Concrete (2nd ed.)*. John Wiley and Sons Inc. New York, New York. 1987.
- Roberts, James B. 2005. Evaluation of Self-Consolidating Concrete for Use in Prestressed Girder Applications. M.S. Thesis, Auburn University.
- Schranz, Claire E. 2012. Development of a User-Guided Program for Predicting Time-Dependent Deformations in Prestressed Bridge Girders. M.S. Thesis, Auburn University.
- Stallings, J.M., R.W. Barnes, and S. Eskildsen. 2003. Camber and Prestress Losses in Alabama HPC Bridge Girders. *PCI Journal* 48, no. 5: 90-104.
- Tadros, M.K., N. Al-Omaishi, S.J. Seguirant, and J.T. Gallt. 2003. Prestress Losses in Pretensioned High-Strength Concrete Bridge Girders. NCHRP Report 496, National Cooperative Highway Research Program (NCHRP).

Trent, Justin D. 2007. Transfer Length, Development Length, Flexural Strength, and Prestress Loss Evaluation in Pretensioned Self-Consolidating Concrete Members. M.S. Thesis, Virginia Polytechnic Institute and State University.

Appendix A Notation

A	area of cross section
A_c	area of concrete
A_p	area of prestressing steel
E_c	modulus of elasticity of concrete
E_{ci}	modulus of elasticity of concrete at time of initial prestress
E_p	modulus of elasticity of prestressing steel
f'_c	compressive strength of concrete
f'_{ci}	compressive strength of concrete at time of initial prestress
f_p	stress in prestressing steel
f_{pu}	ultimate strength of prestressing steel
f_{py}	yield strength of prestressing steel
h	depth of girder cross section
I	moment of inertia of cross section
i	time interval
K_L	factor accounting for type of prestressing steel
L	length of girder
y	distance from the centroid of a cross section
$\Delta\varepsilon_{cen}$	change in strain at centroid of a cross section
$\Delta\phi$	change in curvature of a cross section

Appendix B Prediction Program Input Values

Table B-1: Section Geometric Property Prediction Program Inputs

Geometric Properties	BT-54	BT-72
Area (in²)	659	767
Moment of Inertia (in⁴)	268077	545894
y_{bot} (in.)	27.63	36.60
h (in.)	54	72
L (in.)	1174	1620
V/S (in.)	3.01	3.01
Notional Size (mm)	153	153

Table B-2: Concrete Strength and Modulus of Elasticity

Casting Group	f'ci (psi)	f'c (psi)	Eci (ksi)	Ec (ksi)	MC 90 f'ci (psi)	MC 90 f'c (psi)
A	9010	10240	6200	6400	8067	9297
B	8790	10590	7100	7400	7847	9647
C	8680	10800	6300	6600	7737	9857
D	7860	9670	6700	6900	6917	8727
E (SCC)	7940	10180	6100	6200	6997	9237
E (CVC)	8760	10360	6400	6800	7817	9417
F	8120	10490	5800	6300	7177	9547
G	8290	10770	6700	7000	7347	9827
H	7860	10770	5900	6400	6917	9827
I	8770	10850	7100	7300	7827	9907
J	8220	10550	5800	6400	7277	9607
K	8320	11050	6800	7700	7377	10107
L (SCC)	6930	10070	5700	6000	5987	9127
L (CVC)	7710	10510	6600	6900	6767	9567

Table B-3: Concrete Mixture Properties

Casting Group	Adjusted Slump (in.)	Cement Content (pcy)	Air Content (%)	Fine Agg. Ratio (% by weight)	Cement Type
A	0.0	892	4.10	48.0	RS
B	0.5	820	4.00	38.0	RS
C	0.0	892	3.40	48.0	RS
D	0.5	820	4.50	38.0	RS
E (SCC)	0.0	892	4.90	48.0	RS
E (CVC)	0.5	820	4.20	38.0	RS
F	0.0	895	4.00	47.0	RS
G	0.5	833	3.90	38.0	RS
H	0.0	895	4.10	47.0	RS
I	0.5	833	2.90	38.0	RS
J	0.0	895	3.90	47.0	RS
K	0.5	833	3.40	38.0	RS
L (SCC)	0.0	895	3.80	47.0	RS
L (CVC)	0.5	833	2.70	38.0	RS

Table B-4: Time of Events, Curing, and Maturity Information

Casting Group	Time of Jacking (hrs before casting)	Time of Transfer (hrs after casting)	Steam Curing Duration (hrs)	Maturity at Transfer for MC 90 (days)	Maturity at Transfer for MC 90-KAV (days)	RH (%)
A	26.00	22.50	12.0	5.35	10.40	70
B	23.83	22.80	12.0	4.38	7.82	70
C	99.50	23.20	12.0	3.89	6.66	70
D	26.75	21.95	12.0	3.33	5.45	70
E (SCC)	24.50	23.40	12.0	3.64	6.13	70
E (CVC)	23.70	24.20	12.0	3.58	5.86	70
F	23.58	23.65	14.0	3.62	6.01	70
G	72.67	22.30	12.0	3.29	5.29	70
H	23.67	18.90	12.0	3.55	6.44	70
I	22.75	21.85	14.0	3.34	5.46	70
J	73.50	22.20	16.0	3.89	6.77	70
K	22.25	19.85	13.0	2.95	4.80	70
L (SCC)	48.75	18.50	12.0	2.32	3.56	70
L (CVC)	47.42	19.83	12.0	2.67	3.94	70

Table B-5: Analysis Intervals

Analysis Intervals	BT-54	BT-72
Cross Sections	40	40
Time Intervals	40	40
Maximum Age (days)	365	365

Appendix C Strain Predictions and Measurements

Table C-1: Measured Gauge 1 Strains and AASHTO 2004 Predicted Strains

Casting Group	Girder	Measured Strains			AASHTO ('04)		
		Initial	56 day	Erection	Initial	56 day	Erection
A	54-2S	-418	-670	-733	-430	-750	-940
	54-5S	-465	-797	-807	-430	-750	-940
	54-6S	-436	-691	-755	-430	-750	-940
B	54-9C	-404	-653	-678	-378	-685	-870
	54-10C	-417	-632	-656	-378	-685	-870
	54-13C	-436	-708	-735	-378	-685	-870
C	54-1S	-433	-711	-757	-422	-737	-785
	54-3S	-437	-692	-741	-422	-737	-785
	54-4S	-402	-696	-748	-422	-737	-785
D	54-11C	-463	-728	-780	-417	-741	-930
	54-12C	-464	-731	-774	-417	-741	-930
	54-14C	--	--	--	-417	-741	-930
E (SCC)	54-7S	-448	-780	-820	-436	-760	-943
E (CVC)	54-8C	-434	-686	-734	-416	-733	-914
F	72-1S	-490	-880	-972	-496	-828	-1004
	72-7S	-512	-860	-964	-496	-828	-1004
G	72-8C	-451	-715	-811	-431	-747	-918
	72-14C	-458	-743	-843	-431	-747	-918
H	72-3S	-499	-781	-901	-488	-823	-998
	72-4S	-470	-724	-832	-488	-823	-998
I	72-10C	-471	-695	-795	-410	-719	-886
	72-13C	-488	-746	-854	-410	-719	-886
J	72-2S	-467	-724	-862	-494	-829	-1004
	72-5S	-470	-716	-833	-494	-829	-1004
K	72-11C	-458	-668	-761	-426	-743	-913
	72-12C	-467	-687	-790	-426	-743	-913
L (SCC)	72-6S	-506	-819	-907	-503	-848	-1026
L (CVC)	72-9C	-444	-655	-742	-437	-760	-931

Table C-2: Predicted Gauge 1 Strains AASHTO 2010 and ACI 209

Casting Group	Girder	AASHTO ('10)			ACI 209		
		Initial	56 day	Erection	Initial	56 day	Erection
A	54-2S	-430	-870	-990	-430	-852	-1040
	54-5S	-430	-870	-990	-430	-852	-1040
	54-6S	-430	-870	-990	-430	-852	-1040
B	54-9C	-378	-802	-923	-378	-745	-904
	54-10C	-378	-802	-923	-378	-745	-904
	54-13C	-378	-802	-923	-378	-745	-904
C	54-1S	-422	-868	-998	-422	-847	-1025
	54-3S	-422	-868	-998	-422	-847	-1025
	54-4S	-422	-868	-998	-422	-847	-1025
D	54-11C	-417	-908	-1080	-417	-816	-985
	54-12C	-417	-908	-1080	-417	-816	-985
	54-14C	-417	-908	-1080	-417	-816	-985
E (SCC)	54-7S	-436	-907	-1053	-436	-866	-1046
E (CVC)	54-8C	-416	-855	-979	-416	-800	-960
F	72-1S	-496	-982	-1128	-496	-940	-1118
	72-7S	-496	-982	-1128	-496	-940	-1118
G	72-8C	-431	-887	-1019	-431	-830	-987
	72-14C	-431	-887	-1019	-431	-830	-987
H	72-3S	-488	-988	-1136	-488	-931	-1102
	72-4S	-488	-988	-1136	-488	-931	-1102
I	72-10C	-410	-844	-960	-410	-798	-948
	72-13C	-410	-844	-960	-410	-798	-948
J	72-2S	-494	-982	-1120	-494	-939	-1113
	72-5S	-494	-982	-1120	-494	-939	-1113
K	72-11C	-426	-885	-1015	-426	-824	-978
	72-12C	-426	-885	-1015	-426	-824	-978
L (SCC)	72-6S	-503	-1042	-1220	-503	-950	-1121
L (CVC)	72-9C	-437	-916	-1061	-437	-837	-990

Table C-3: Predicted Gauge 1 Strains MC 90 and MC 90-KAV

Casting Group	Girder	MC 90			MC 90-KAV		
		Initial	56 day	Erection	Initial	56 day	Erection
A	54-2S	-430	-631	-782	-430	-728	-878
	54-5S	-430	-631	-782	-430	-728	-878
	54-6S	-430	-631	-782	-430	-728	-878
B	54-9C	-378	-562	-704	-378	-643	-780
	54-10C	-378	-562	-704	-378	-643	-780
	54-13C	-378	-562	-704	-378	-643	-780
C	54-1S	-422	-616	-760	-422	-700	-845
	54-3S	-422	-616	-760	-422	-700	-845
	54-4S	-422	-616	-760	-422	-700	-845
D	54-11C	-417	-615	-760	-417	-722	-882
	54-12C	-417	-615	-760	-417	-722	-882
	54-14C	-417	-615	-760	-417	-722	-882
E (SCC)	54-7S	-436	-645	-795	-436	-733	-881
E (CVC)	54-8C	-416	-617	-762	-416	-700	-838
F	72-1S	-496	-709	-857	-496	-803	-949
	72-7S	-496	-709	-857	-496	-803	-949
G	72-8C	-431	-628	-761	-431	-709	-840
	72-14C	-431	-628	-761	-431	-709	-840
H	72-3S	-488	-704	-843	-488	-796	-933
	72-4S	-488	-704	-843	-488	-796	-933
I	72-10C	-410	-602	-725	-410	-678	-802
	72-13C	-410	-602	-725	-410	-678	-802
J	72-2S	-494	-704	-841	-494	-806	-945
	72-5S	-494	-704	-841	-494	-806	-945
K	72-11C	-426	-624	-752	-426	-703	-828
	72-12C	-426	-624	-752	-426	-703	-828
L (SCC)	72-6S	-503	-723	-864	-503	-832	-981
L (CVC)	72-9C	-437	-648	-784	-437	-728	-861

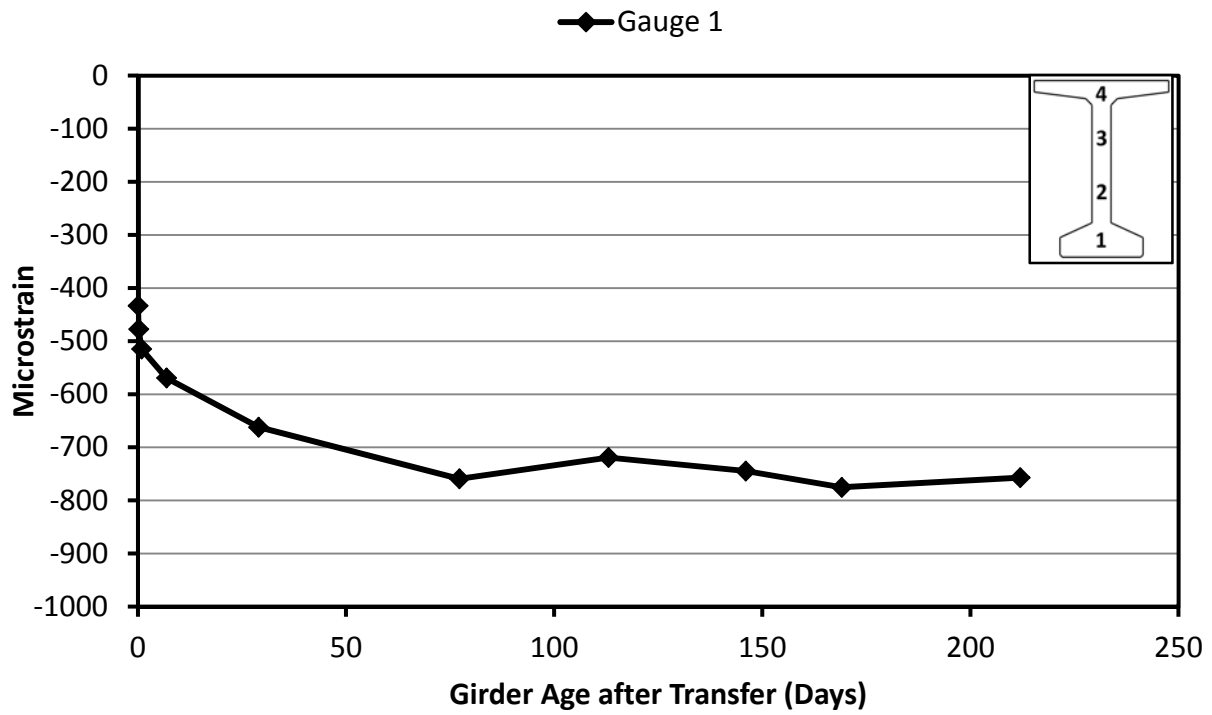


Figure C-1: Measured Strain 54-1S

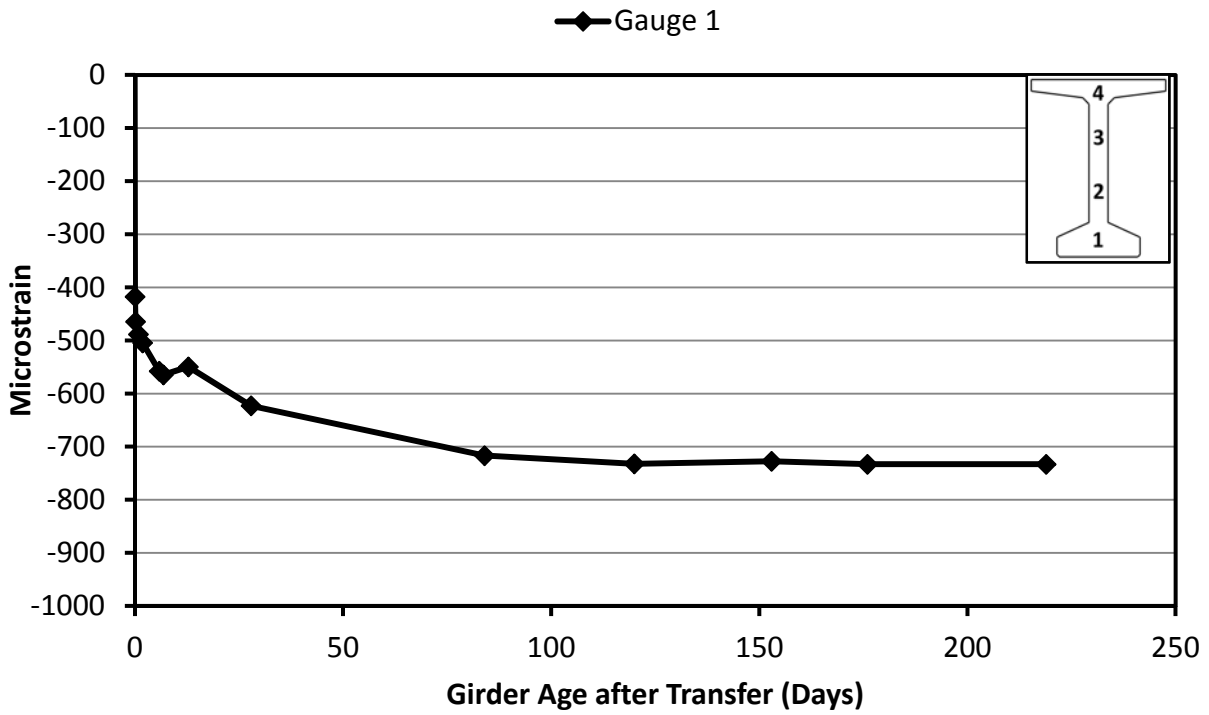


Figure C-2: Measured Strain 54-2S

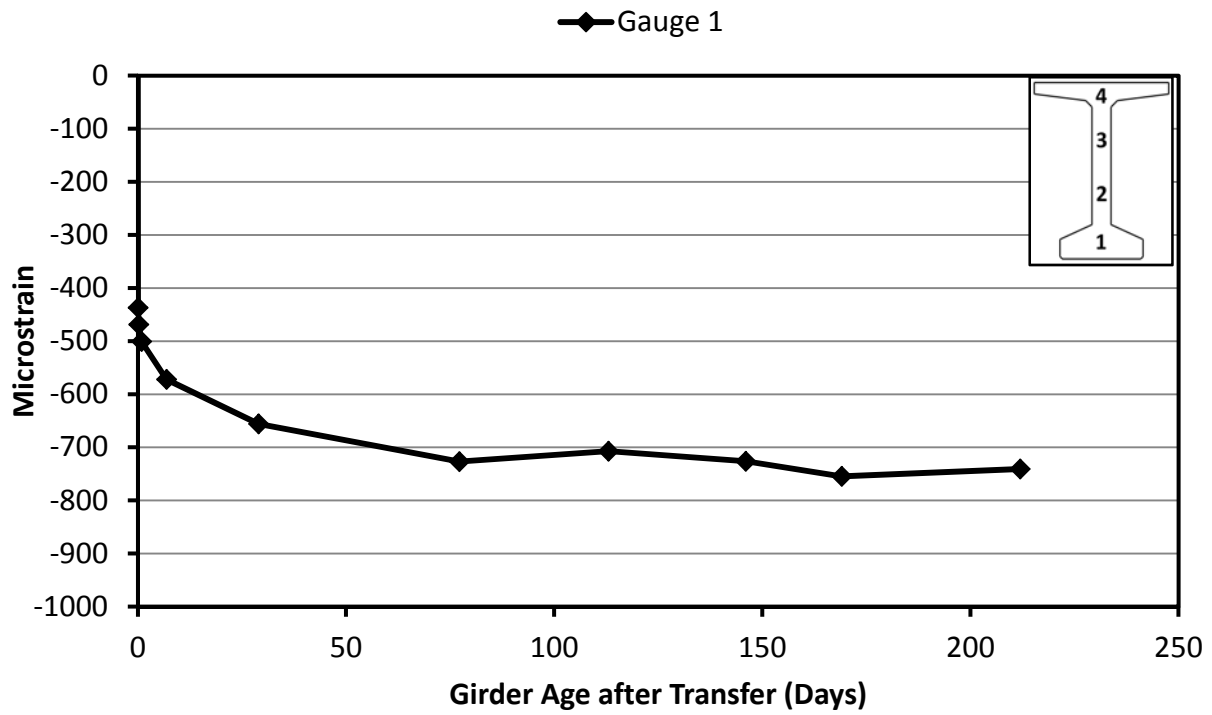


Figure C-3: Measured Strain 54-3S

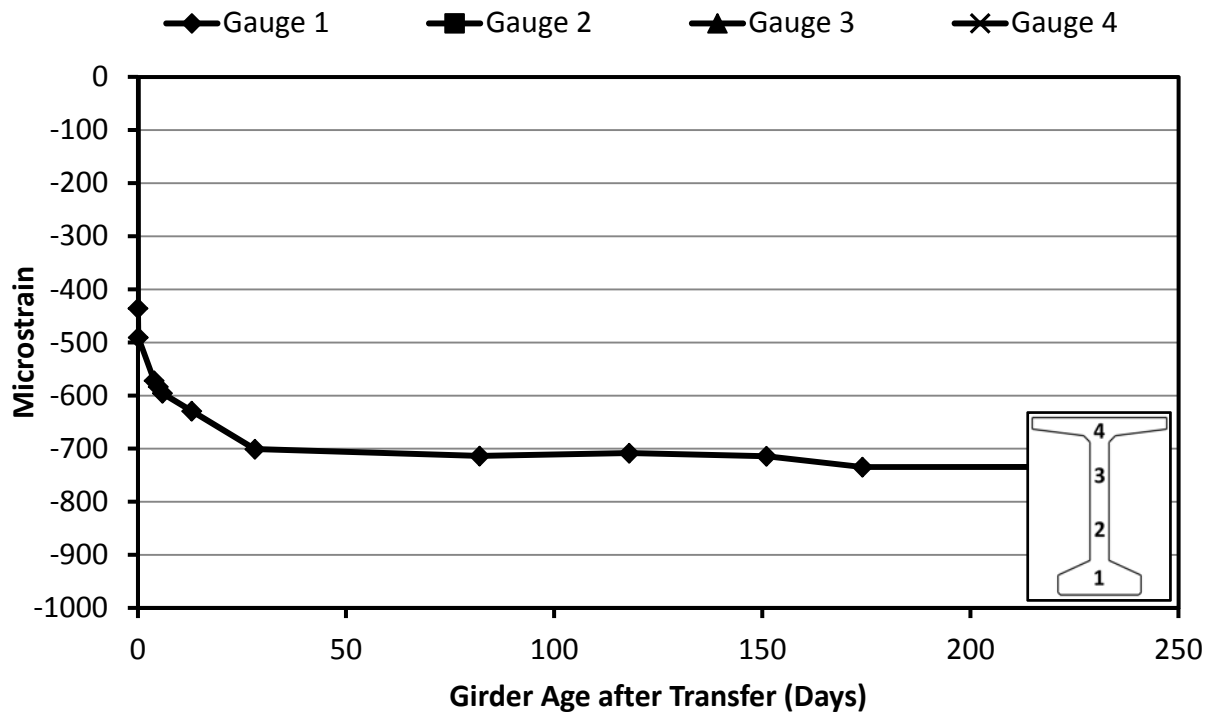


Figure C-4: Measured Strain 54-4S

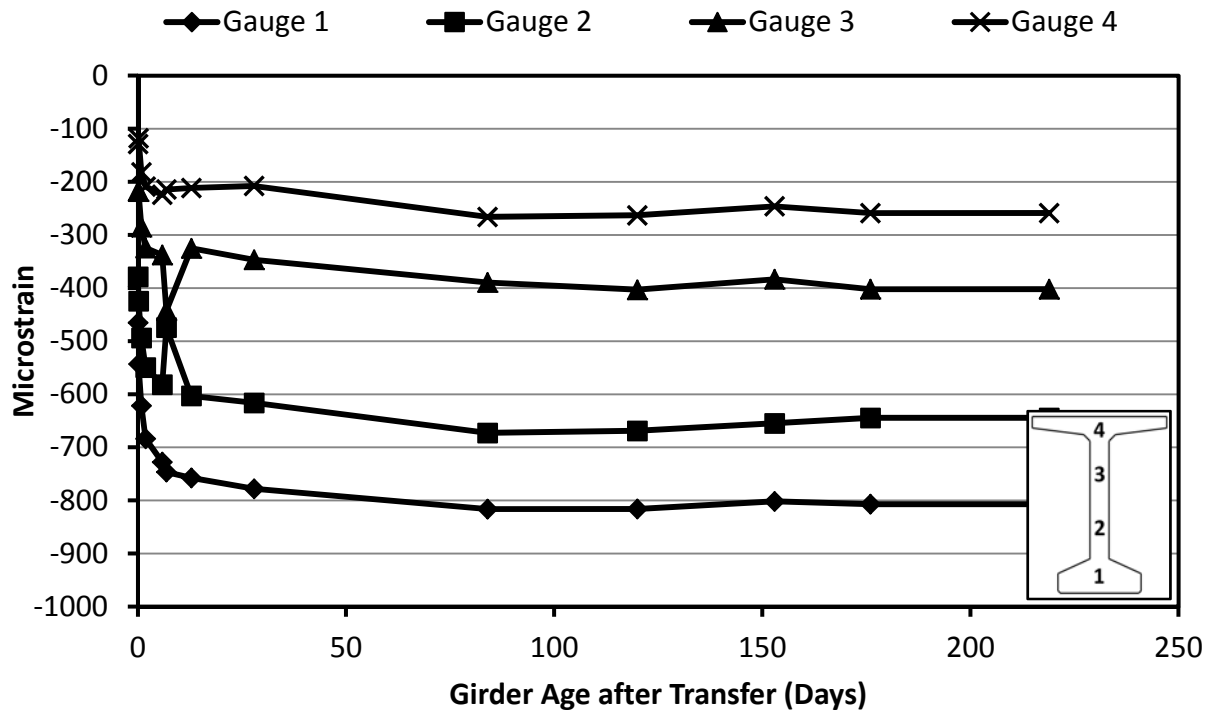


Figure C-5: Measured Strain 54-5S

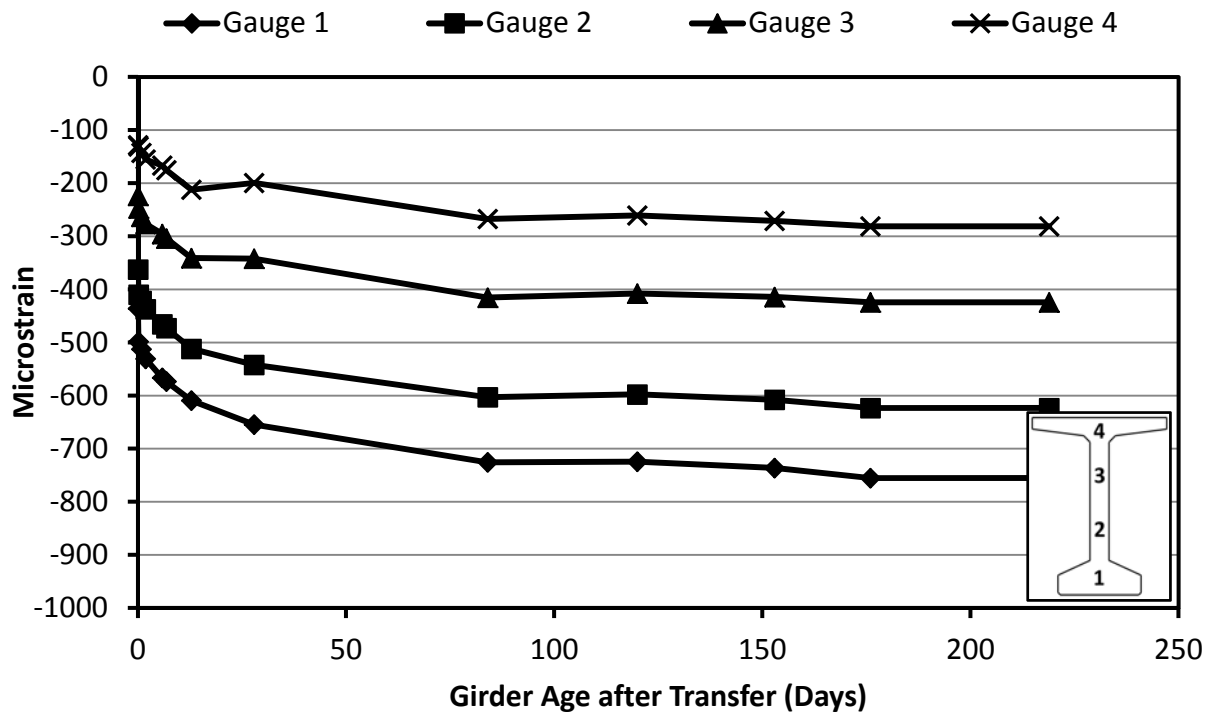


Figure C-6: Measured Strain 54-6S

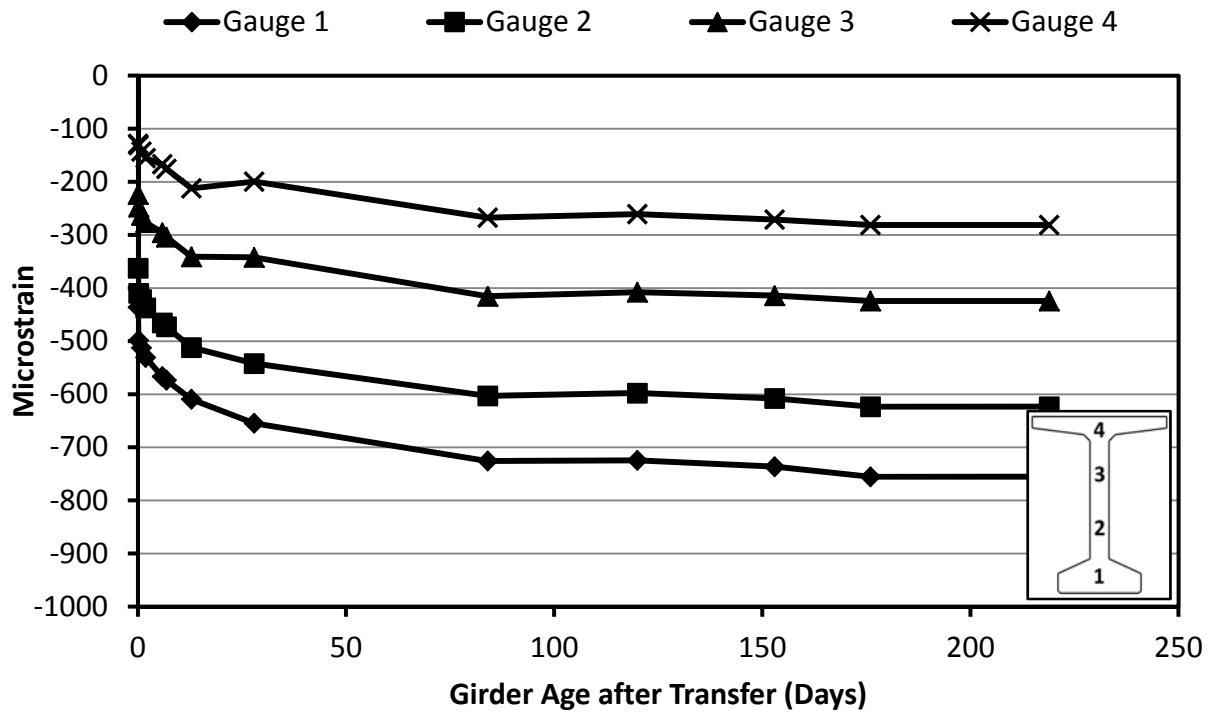


Figure C-7: Measured Strain 54-7S

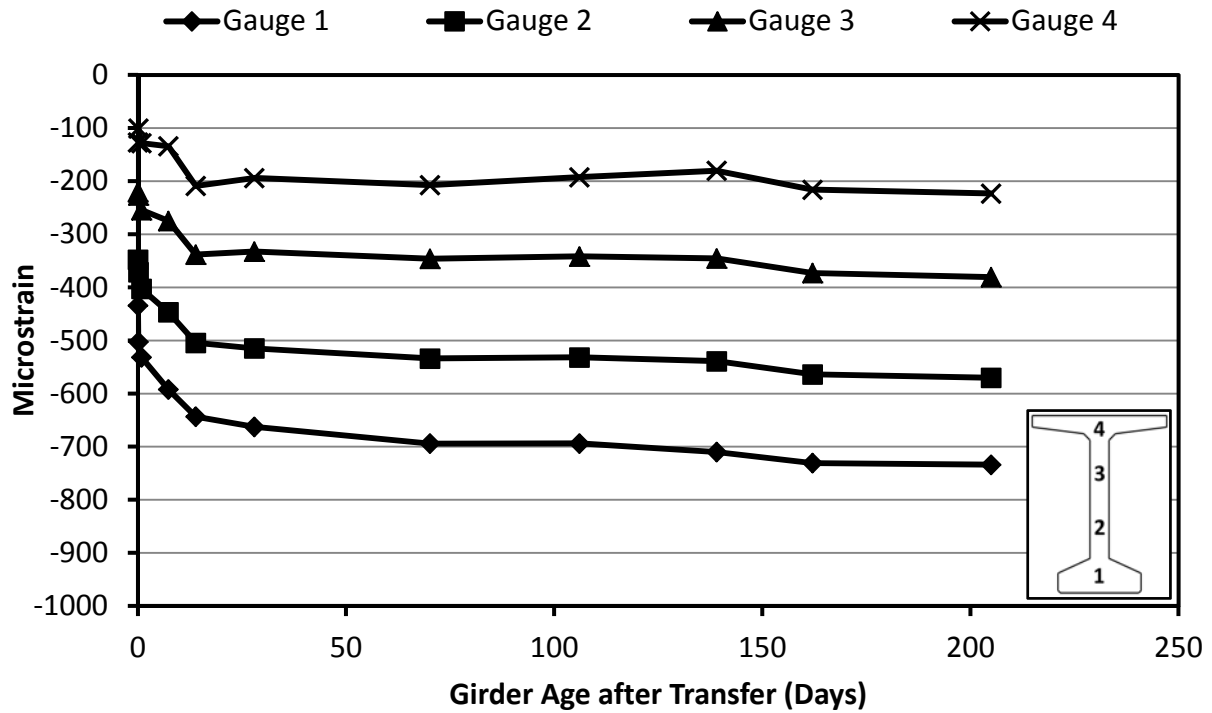


Figure C-8: Measured Strain 54-8C

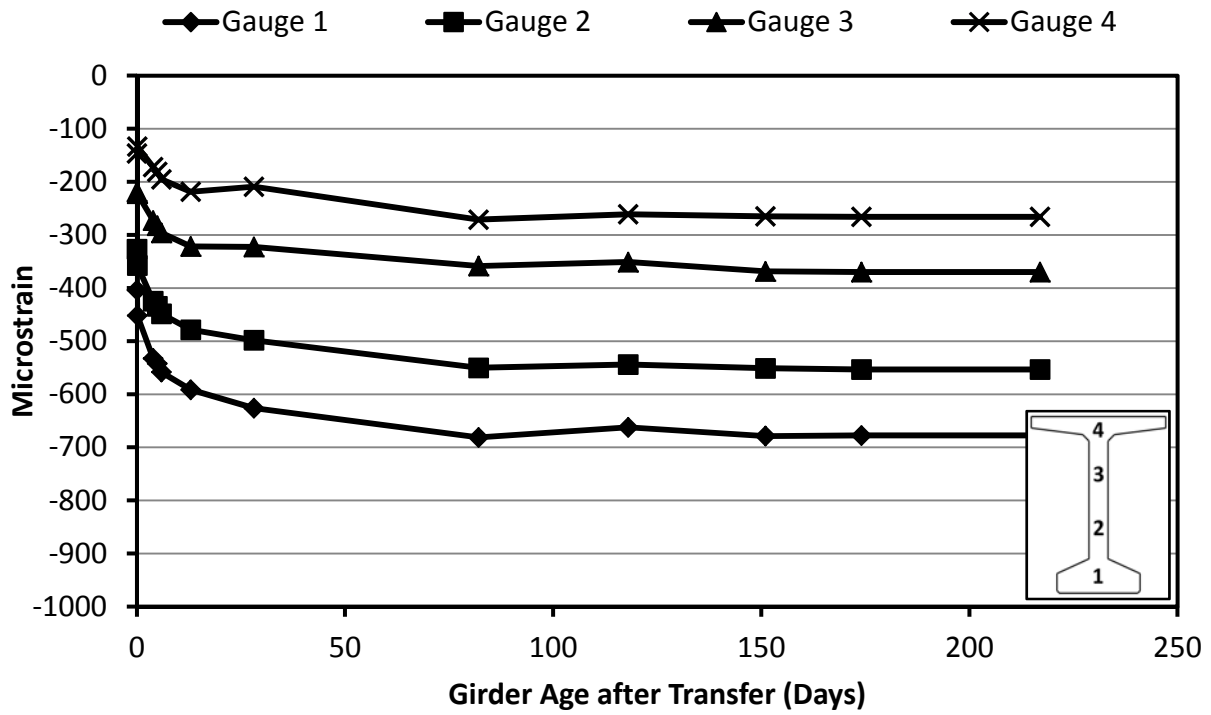


Figure C-9: Measured Strain 54-9C

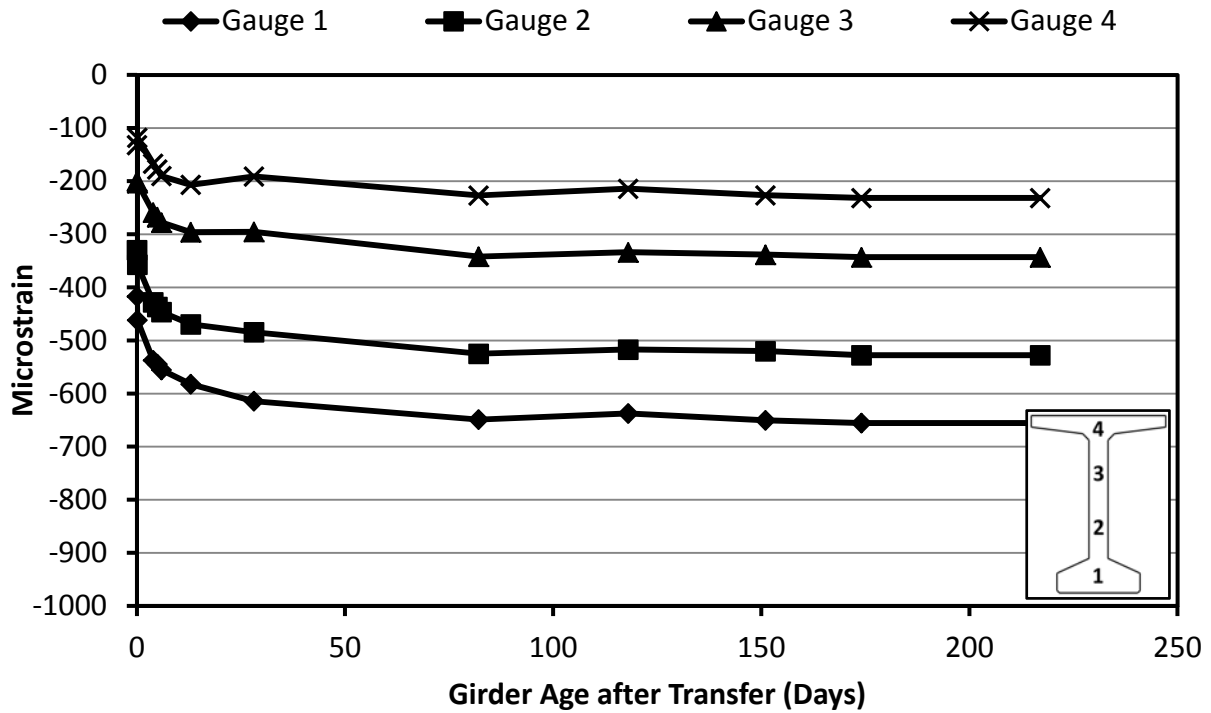


Figure C-10: Measured Strain 54-10C

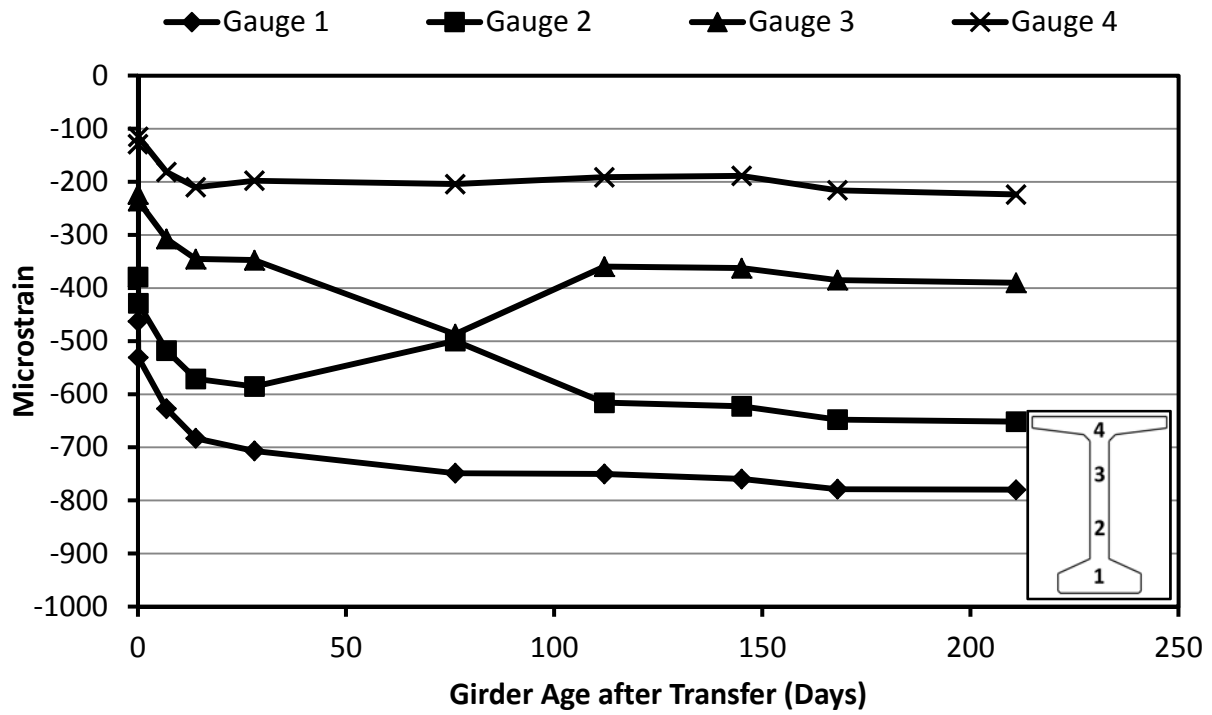


Figure C-11: Measured Strain 54-11C

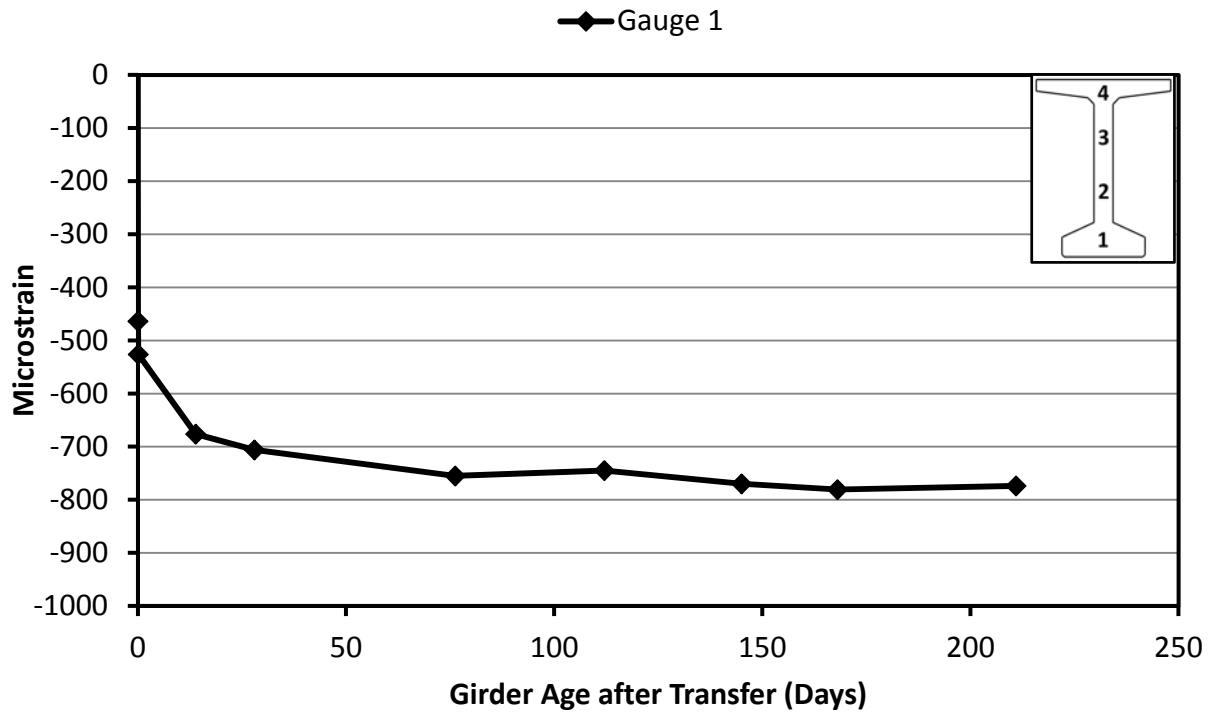


Figure C-12: Measured Strain 54-12C

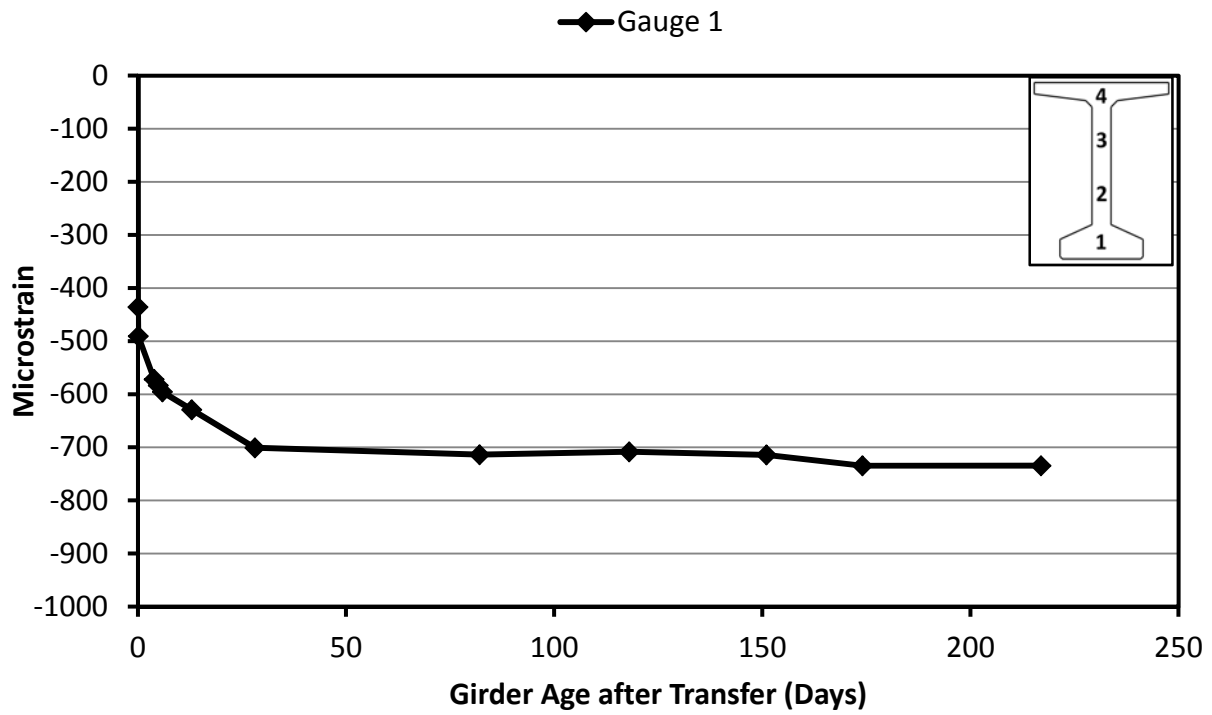


Figure C-13: Measured Strain 54-13C

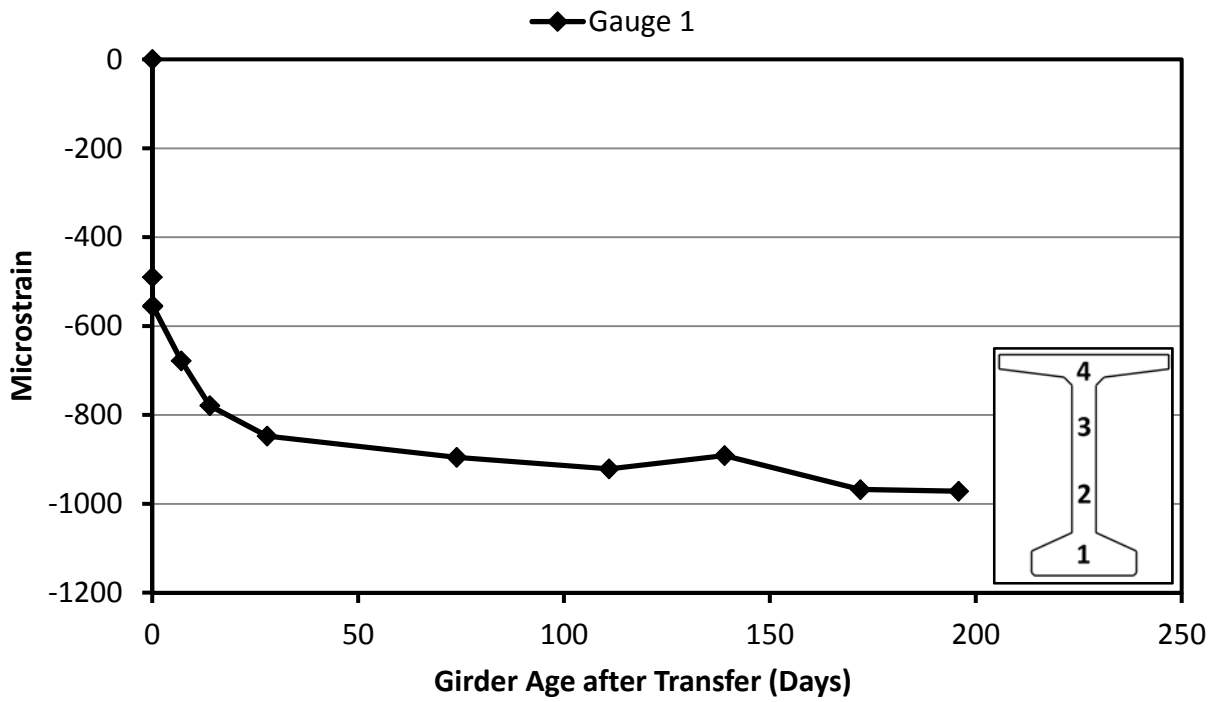


Figure C-14: Measured Strain 72-1S

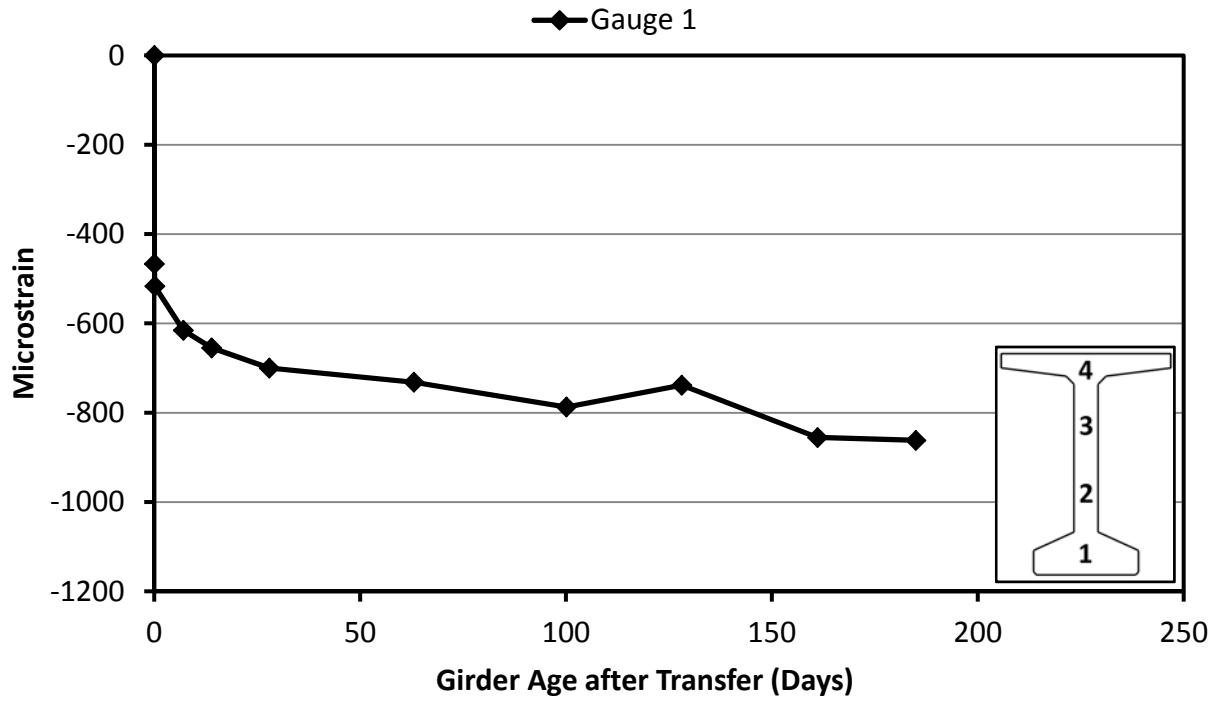


Figure C-15: Measured Strain 72-2S

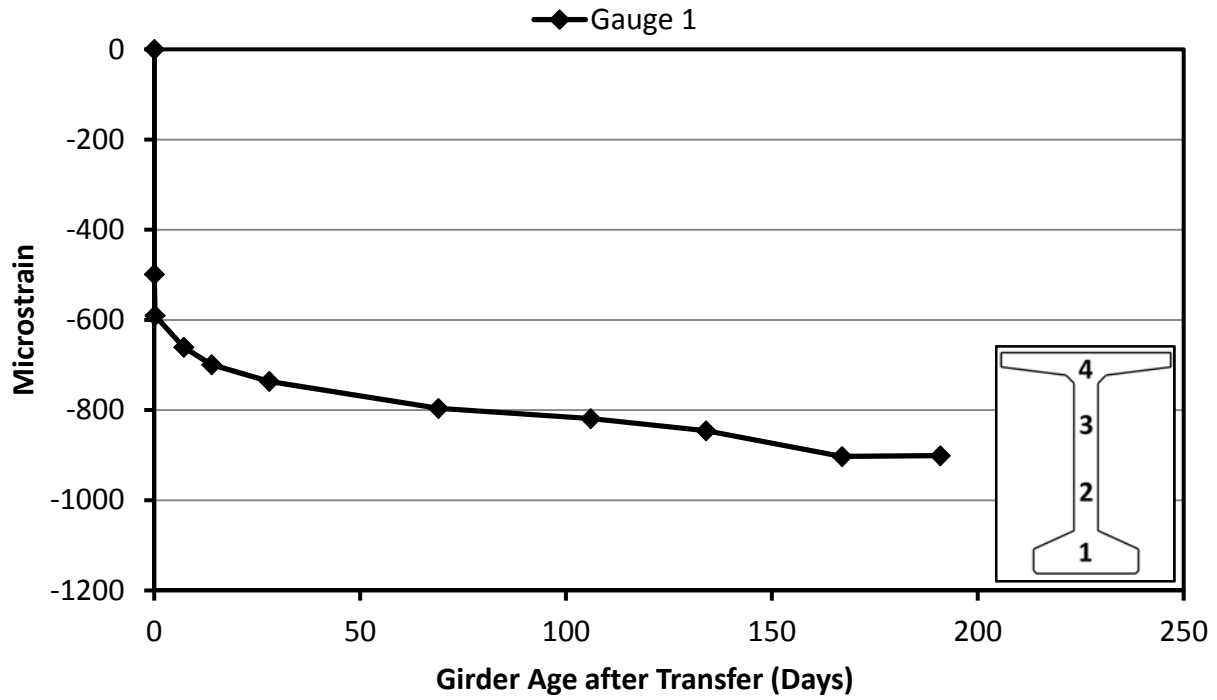


Figure C-16: Measured Strain 72-3S

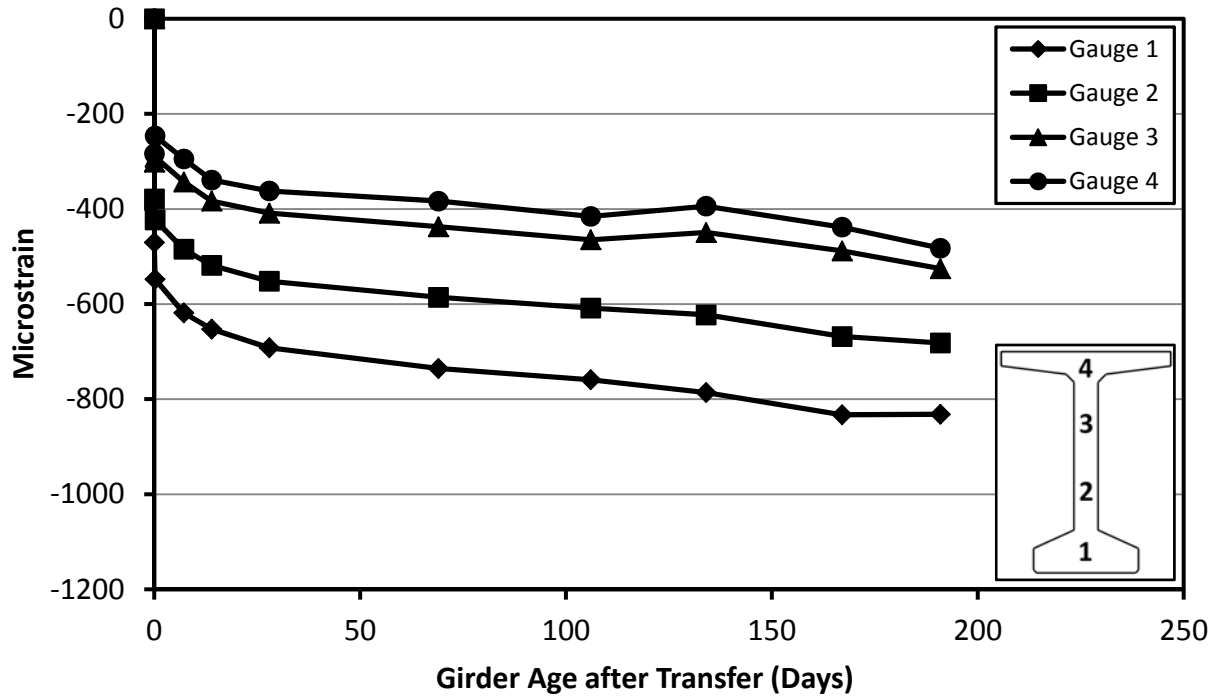


Figure C-17: Measured Strain 72-4S

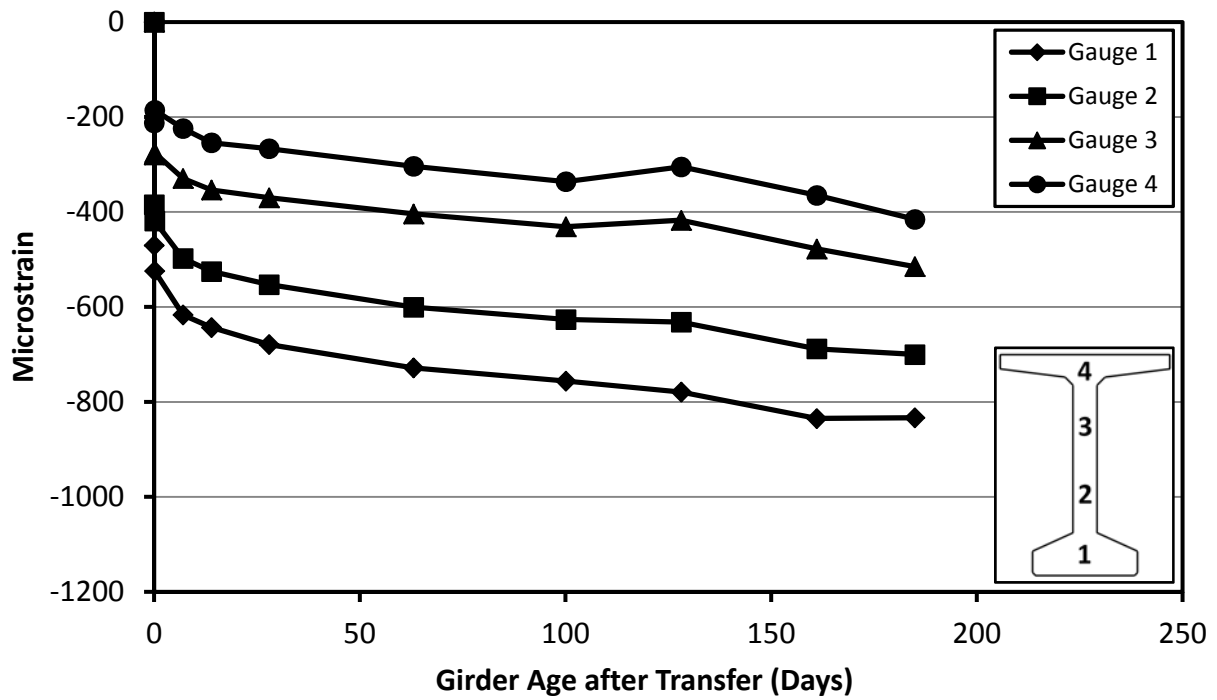


Figure C-18: Measured Strain 72-5S

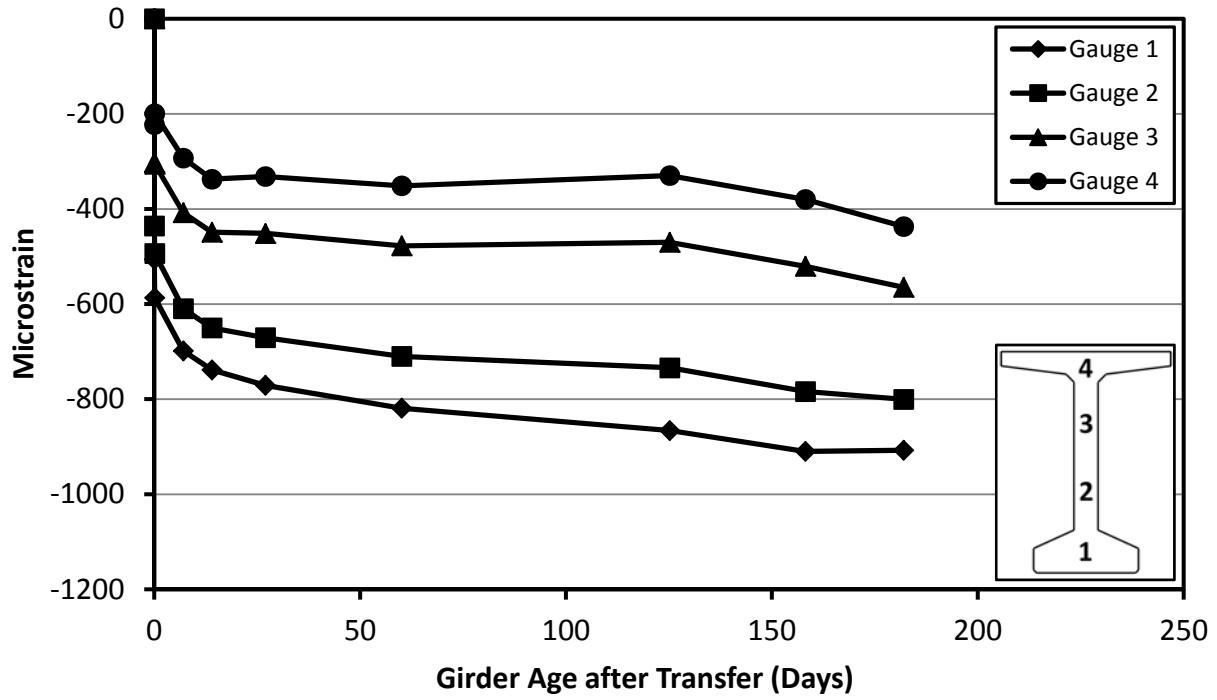


Figure C-19: Measured Strain 72-6S

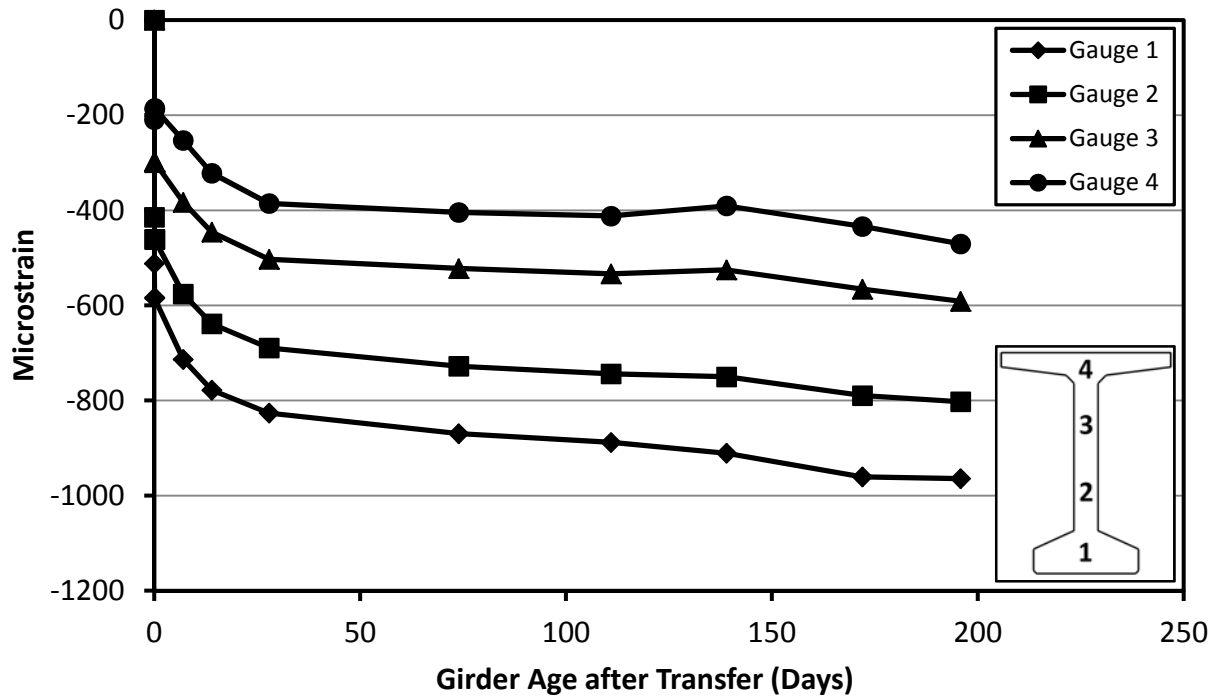


Figure C-20: Measured Strain 72-7S

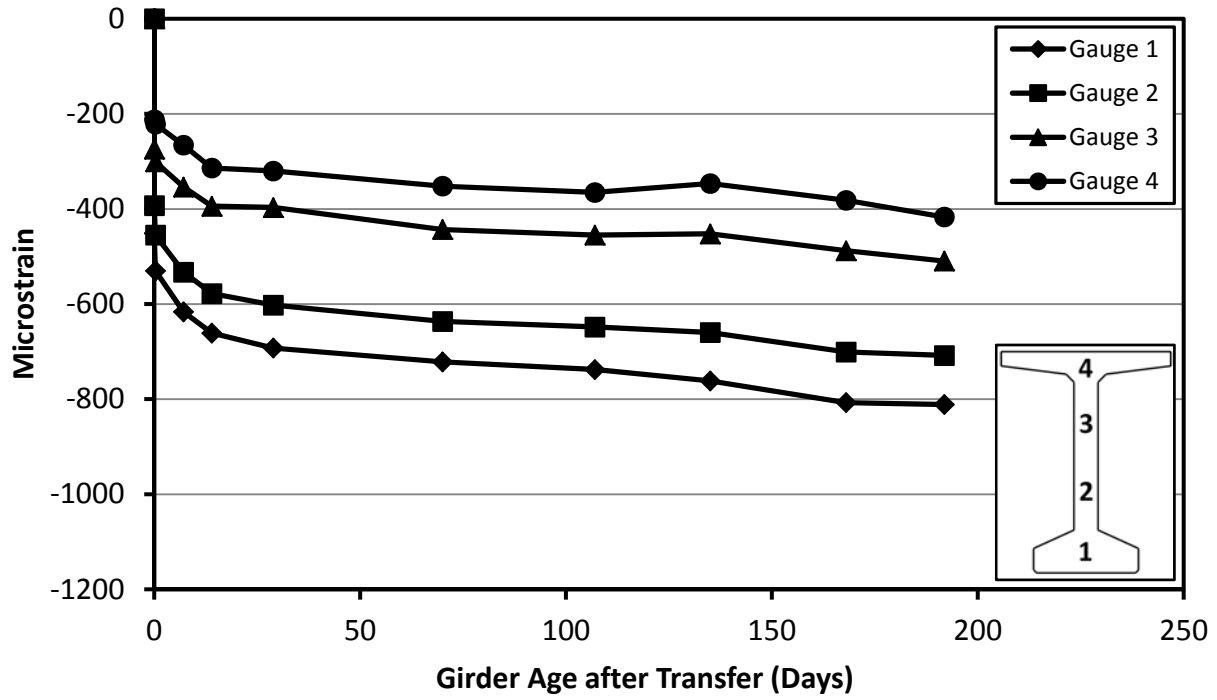


Figure C-21: Measured Strain 72-8C

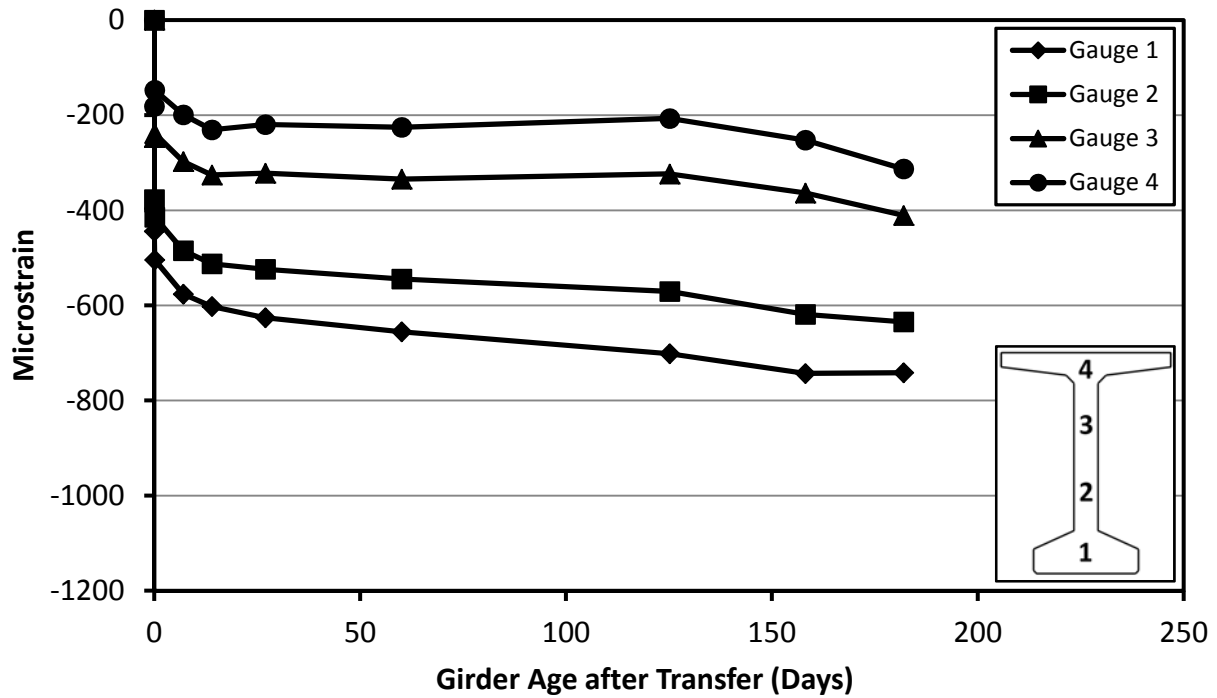


Figure C-22: Measured Strain 72-9C

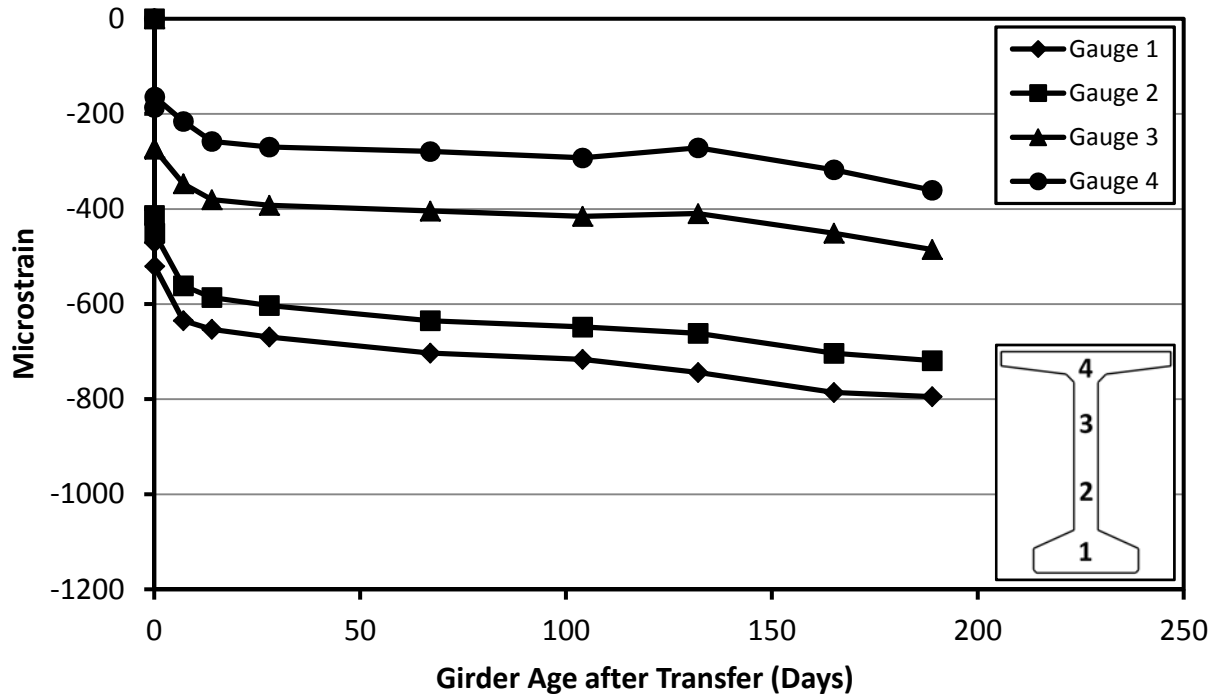


Figure C-23: Measured Strain 72-10C

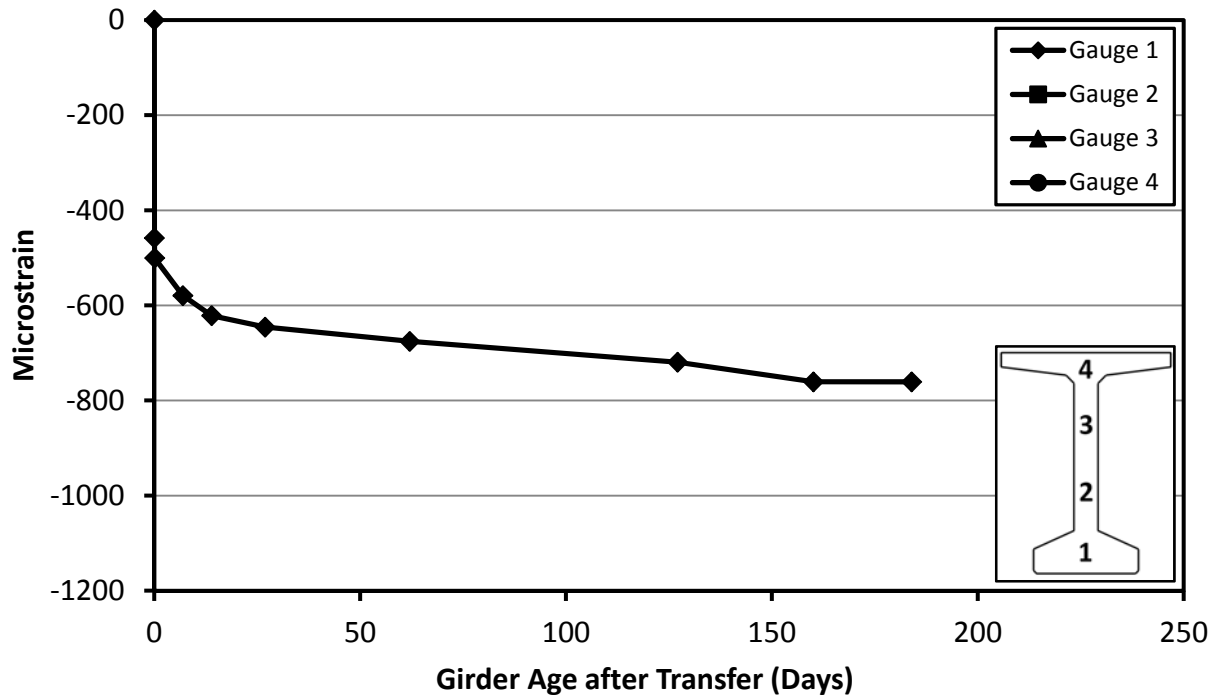


Figure C-24: Measured Strain 72-11C



Figure C-25: Measured Strain 72-12C

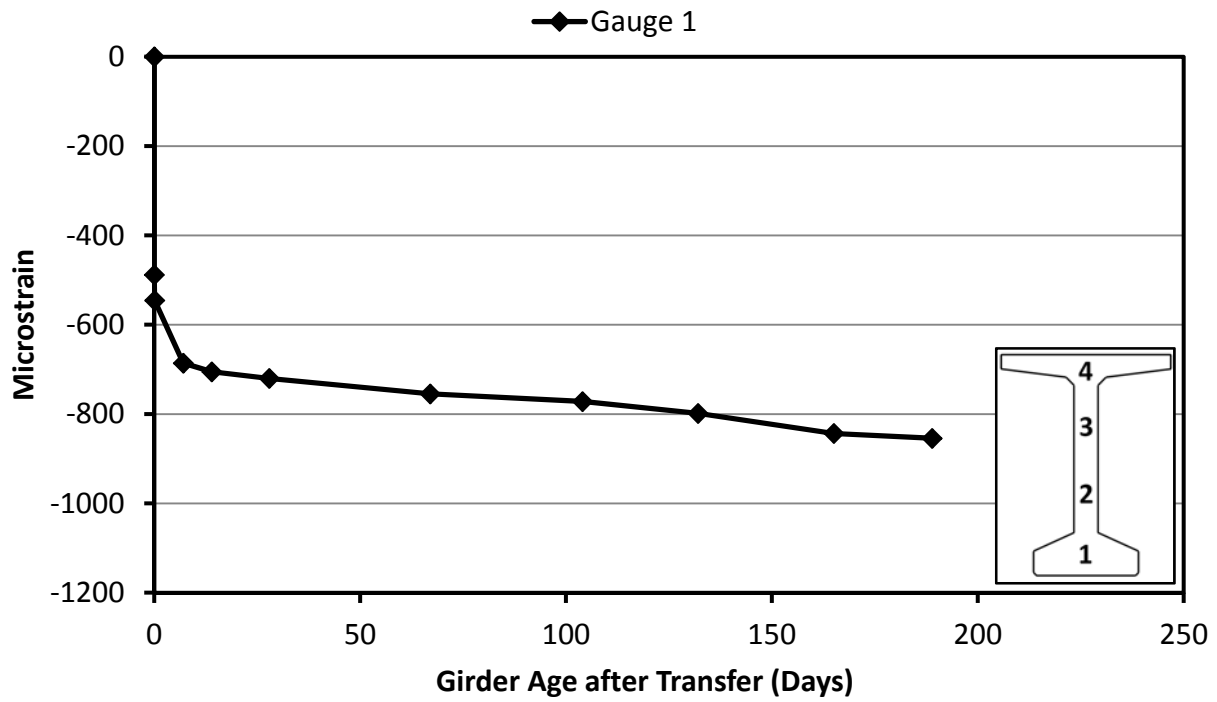


Figure C-26: Measured Strain 72-13C

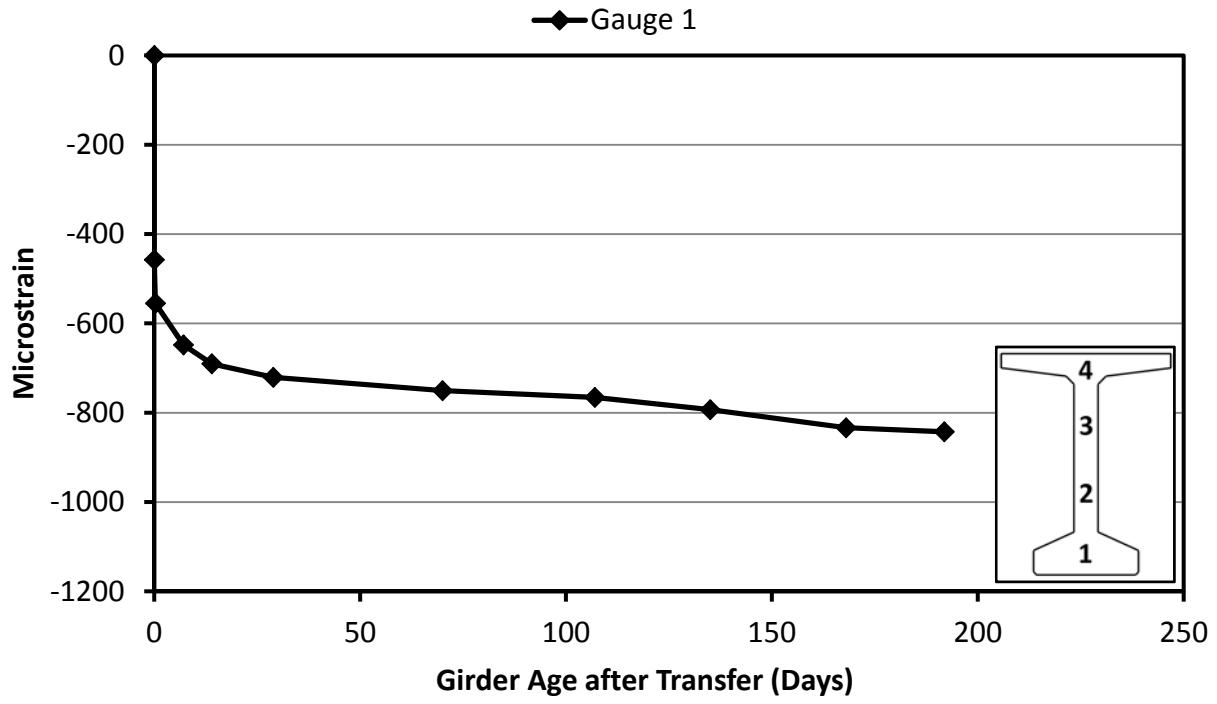


Figure C-27: Measured Strain 72-14C

Appendix D Camber Predictions and Measurements

Table D-1: Measured Camber and AASHTO 2004 Predicted Cambers

Casting Group	Girder	Measured Cambers			AASHTO ('04)		
		Initial	56 day	Erection	Initial	56 day	Erection
A	54-2S	1.36	1.89	1.98	1.39	1.77	1.94
	54-5S	1.08	1.28	1.30	1.39	1.77	1.94
	54-6S	1.47	1.90	1.86	1.39	1.77	1.94
B	54-9C	0.97	1.52	1.57	1.22	1.56	1.70
	54-10C	0.91	1.29	1.15	1.22	1.56	1.70
	54-13C	0.94	1.66	1.57	1.22	1.56	1.70
C	54-1S	0.86	1.51	1.54	1.36	1.74	1.88
	54-3S	0.98	1.38	1.45	1.36	1.74	1.88
	54-4S	0.65	1.45	1.58	1.36	1.74	1.88
D	54-11C	1.05	1.72	1.87	1.35	1.75	1.91
	54-12C	1.17	1.77	1.93	1.35	1.75	1.91
	54-14C	1.02	1.67	1.76	1.35	1.75	1.91
E (SCC)	54-7S	0.92	1.74	1.81	1.41	1.80	1.95
E (CVC)	54-8C	0.89	1.54	1.61	1.34	1.72	1.86
F	72-1S	1.44	2.48	2.54	1.97	2.44	2.60
	72-7S	1.35	2.13	2.16	1.97	2.44	2.60
G	72-8C	1.36	2.04	1.99	1.70	2.12	2.26
	72-14C	1.33	2.05	2.05	1.70	2.12	2.26
H	72-3S	1.59	2.31	2.36	1.94	2.42	2.58
	72-4S	1.34	2.14	2.08	1.94	2.42	2.58
I	72-10C	1.19	1.91	1.95	1.62	2.02	2.16
	72-13C	1.12	1.93	1.82	1.62	2.02	2.16
J	72-2S	1.14	2.12	2.15	1.96	2.44	2.60
	72-5S	1.14	2.03	1.98	1.96	2.44	2.60
K	72-11C	1.28	2.24	2.10	1.69	2.11	2.26
	72-12C	1.50	2.22	2.02	1.69	2.11	2.26
L (SCC)	72-6S	1.46	2.54	2.51	2.00	2.50	2.67
L (CVC)	72-9C	1.20	2.21	2.11	1.73	2.16	3.31

Table D-2: AASHTO 2010 and ACI 209 Predicted Cambers

Casting Group	Girder	AASHTO ('10)			ACI 209		
		Initial	56 day	Erection	Initial	56 day	Erection
A	54-2S	1.39	2.05	2.22	1.39	2.02	2.20
	54-5S	1.39	2.05	2.22	1.39	2.02	2.20
	54-6S	1.39	2.05	2.22	1.39	2.02	2.20
B	54-9C	1.22	1.83	2.00	1.22	1.79	1.96
	54-10C	1.22	1.83	2.00	1.22	1.79	1.96
	54-13C	1.22	1.83	2.00	1.22	1.79	1.96
C	54-1S	1.36	2.03	2.22	1.36	1.99	2.18
	54-3S	1.36	2.03	2.22	1.36	1.99	2.18
	54-4S	1.36	2.03	2.22	1.36	1.99	2.18
D	54-11C	1.35	2.09	2.33	1.35	2.00	2.19
	54-12C	1.35	2.09	2.33	1.35	2.00	2.19
	54-14C	1.35	2.09	2.33	1.35	2.00	2.19
E (SCC)	54-7S	1.41	2.12	2.33	1.41	2.05	2.23
E (CVC)	54-8C	1.34	1.99	2.17	1.34	1.95	2.13
F	72-1S	1.97	2.83	3.07	1.97	2.76	2.96
	72-7S	1.97	2.83	3.07	1.97	2.76	2.96
G	72-8C	1.70	2.47	2.68	1.70	2.44	2.63
	72-14C	1.70	2.47	2.68	1.70	2.44	2.63
H	72-3S	1.94	2.84	3.08	1.94	2.72	2.92
	72-4S	1.94	2.84	3.08	1.94	2.72	2.92
I	72-10C	1.62	2.35	2.53	1.62	2.33	2.52
	72-13C	1.62	2.35	2.53	1.62	2.33	2.52
J	72-2S	1.96	2.83	3.06	1.96	2.76	2.96
	72-5S	1.96	2.83	3.06	1.96	2.76	2.96
K	72-11C	1.69	2.48	2.69	1.69	2.43	2.63
	72-12C	1.69	2.48	2.69	1.69	2.43	2.63
L (SCC)	72-6S	2.00	2.95	3.24	2.00	2.78	2.98
L (CVC)	72-9C	1.73	2.54	2.77	1.73	2.47	2.66

Table D-3: MC 90 and MC 90-KAV Predicted Cambers

Casting Group	Girder	MC 90			MC 90-KAV		
		Initial	56 day	Erection	Initial	56 day	Erection
A	54-2S	1.39	1.73	1.99	1.39	2.01	2.27
	54-5S	1.39	1.73	1.99	1.39	2.01	2.27
	54-6S	1.39	1.73	1.99	1.39	2.01	2.27
B	54-9C	1.22	1.53	1.76	1.22	1.78	2.01
	54-10C	1.22	1.53	1.76	1.22	1.78	2.01
	54-13C	1.22	1.53	1.76	1.22	1.78	2.01
C	54-1S	1.36	1.71	1.98	1.36	1.97	2.22
	54-3S	1.36	1.71	1.98	1.36	1.97	2.22
	54-4S	1.36	1.71	1.98	1.36	1.97	2.22
D	54-11C	1.35	1.70	1.97	1.35	1.99	2.24
	54-12C	1.35	1.70	1.97	1.35	1.99	2.24
	54-14C	1.35	1.70	1.97	1.35	1.99	2.24
E (SCC)	54-7S	1.41	1.77	2.03	1.41	2.03	2.29
E (CVC)	54-8C	1.34	1.68	1.94	1.34	1.94	2.18
F	72-1S	1.97	2.42	2.75	1.97	2.75	3.05
	72-7S	1.97	2.42	2.75	1.97	2.75	3.05
G	72-8C	1.70	2.11	2.40	1.70	2.40	2.69
	72-14C	1.70	2.11	2.40	1.70	2.40	2.69
H	72-3S	1.94	2.41	2.74	1.94	2.75	3.05
	72-4S	1.94	2.41	2.74	1.94	2.75	3.05
I	72-10C	1.62	2.01	2.30	1.62	2.30	2.57
	72-13C	1.62	2.01	2.30	1.62	2.30	2.57
J	72-2S	1.96	2.42	2.74	1.96	2.76	3.07
	72-5S	1.96	2.42	2.74	1.96	2.76	3.07
K	72-11C	1.69	2.12	2.41	1.69	2.41	2.69
	72-12C	1.69	2.12	2.41	1.69	2.41	2.69
L (SCC)	72-6S	2.00	2.50	2.81	2.00	2.82	3.13
L (CVC)	72-9C	1.73	2.17	2.46	1.73	2.45	2.72